

ICCESEN-2022

9th International Conference on Computational and Experimental Science and Engineering

Antalya-TURKEY

29-31 October 2022

Proceedings of ICCESEN-2022

EDITORS

Prof.Dr. İskender AKKURT

Dr. Kadir GÜNOĞLU

Dr. Hakan AKYILDIRIM

ISBN : 978-605-68728-9-1

2022.iccesen.org iccesen2022@gmail.com

ICCESSEN-2022

9th International Conference on Computational and Experimental Science and Engineering

Antalya-TURKEY
29-31 October 2022

Proceedings

of

ICCESSEN-2022

Editors:

Prof.Dr. İskender AKKURT

Dr. Kadir GÜNOĞLU

Dr. Hakan AKYILDIRIM

ISBN: 978-605-68728-9-1

Proceedings of ICCESSEN-2022 ,

9th International Conference on Computational and Eperimental Science and Engineering (**ICCESSEN-2022**)

29-31 October 2022, Antalya-TURKEY

Editors:

Prof. Dr. İskender AKKURT

Dr. Kadir GÜNOĞLU

Dr. Hakan AKYILDIRIM

Published : 30 December 2022

ISBN: 978-605-68728-9-1

This work is subject to copyright. All rights are reserved, whether the whole or part of the material is concerned. Nothing from this publication may be translated, reproduced, stored in a computerized system or published in any form or in any manner, including, but not limited to electronic, mechanical, reprographic or photographic, without prior written permission from the Publisher 2022.iccesen.org. Pls contact at iccesen2022@gmail.com.

The individual contributions in this publication and any liabilities arising from them remain the responsibility of the authors. The publisher is not responsible for possible damages, which could be a result of content derived from this publication.

TABLE OF CONTENTS

TABLE OF CONTENTS	i
FOREWORD	iii
ORGANISATION COMMITTEE	iv
SCIENTIFIC COMMITTEE	v
INVITED SPEAKERS	vii
Mohammed A. ALMOMANI, Bilal R MELHEM “Review on the effect of reinforcement particle type, shape, and volume fraction on the porosity content of metal matrix composite”	1-5
Fırat EVİRGEN, Esmehan UÇAR and Necati ÖZDEMİR “Impact of Fractal Fractional Derivative on a Plant Disease Model with Vector Borne”	6-15
Kadir GÜNOĞLU, Hatice VAROL ÖZKAVAK, İskender AKKURT “Radiation attenuation coefficients of stainless steels containing different proportions of boron carbide”	16-20
Nurdan KARPUZ “Gamma Strength Functions for Some Medical Radioisotopes”	21-25
Özgül KARATAŞ “Use of ESR Spectroscopy on Identification of the Radiation-Induced Radicals in Gamma Irradiated Bone”	26-29
Abolfazl MAJNOONI-HERIS, Ahmad FAKHERI-FARD, Maryam VAEZ-MADANI, and Saeed SAMADIANFARD “Effects of precipitation, Wet and Drought Periods on Rainfed Wheat Yield in a Semi-Arid Region”	30-36
Taner KAVAS, Huseyin Ozkan TOPLAN, Iskender AKKURT , Kadir GUNOGLU, Recep KURTULUS, Melda IPLIKCIOGLU “Some theoretical radiation shielding calculations via Phy-X/PSD for investigating the effect of doping Gd ₂ O ₃ into a barium-calcium-boro-silicate glass system”	37-43
Serap ÖZHAN DOĞAN, Burak Galip ANIK, Umut GÖKTAŞ “Design And Analysis Of The Boarding Ladder Used On Ships By Finite Element Method”	44-50
Serap YİĞİT GEZGİN, Yasemin GÜNDOĞDU and Hamdi Şükür KILIÇ “Numerical study for the quaternary semiconductor based heterojunction solar cell modelled with the SCAPS-1D program”	51-60
Şemsettin KILINÇARSLAN, Yasemin ŞİMŞEK TÜRKER “Investigation of Flexural Properties of Solid and Composite Wood Materials”	61-65
Yasemin ŞİMŞEK TÜRKER*, Şemsettin KILINÇARSLAN “Investigation of Flexural Properties of Glulam Beams”	66-69
Osman GÜNAY, Kadir GÜNOĞLU, İskender AKKURT “Determination of radium-226 activity concentration in sand samples from Doğançalı beach”	70-73
Yasemin GÜNDOĞDU, Amina HOUMI, Serap YİĞİT GEZGIN, Hamdi Şükür KILIÇ “Effects of Nonlinear Optical Absorption Properties on Na and Li doped Cu ₂ SnS ₃ (CTS) Thin Films”	74-81
Song WANG, Lixiao XIAO, Huiyong YU, Jiayan LI, Jun HU “Optimization of S-wave Prediction Method in Mahu Area and Its Influence on Calculation of Rock Mechanics Parameters”	82-90
“Osman GÜNAY, Hakan AKYILDIRIM, Kadir GÜNOĞLU, İskender AKKURT “Investigation of interaction of some iron minerals with gamma rays using XCOM database”	91-94

Ning CHENG, Lixiao XIAO, Song WANG, Wei TANG, Lin TANG “Study on dynamic variation law of stress field in a well area of Mahu and application of proppant selection”	95-103
Alper ÖZSEVEN, İskender AKKURT, Kadir GÜNOĞLU “Evaluation of heavy metal distributions in surface waters and sediments of Eğirdir Lake”	104-108
Hamdi Şükür KILIÇ, Yasemin GÜNDOĞDU and Serap YİĞİT GEZGİN “Nonlinear Optical Properties of IGZO Thin Films Prepared by Pulse Laser Deposition”	109-117
Hasan ŞAHİN, Halit ÖZTEKİN “Türkiye’de Yapay Zeka Alanında Lisansüstü Tezlerde Güncel Konular (1984-2021)”	118-131
Osman GÜNAY “Determination of Ra-226 concentration at Suadiye beach in Istanbul”	132-135
Osman GÜNAY “Determination of Ra-226 radioactivity level in Goztepe Beach”	136-139
Mehmet Ali KAYGUSUZ and Vilda PURUTÇUOĞLU “Detection of Anomalies via Robust Artificial Neural Networks and Gaussian Mixture Models”	140-147
Mehmet Ali KAYGUSUZ and Vilda PURUTÇUOĞLU “Conditional Randomization Test for Causal Additive Models in Biological Networks”	148-151
Jiexian XIAO, Deli GAO, Zhengxu WANG, Xuelin DONG and Qingfeng GUO “Research on temperature distribution of heavy oil reservoir in situ heated by electromagnetic radiation”	152-164
Yusuf CEYLAN “Experimental Approach for Natural Radioactivity Measurement”	165-166
Chengwei ZHANG, Shiqing CHENG, Wei ZHANG, Lang ZHU, Tingting JIANG, Longquan HU, Dengke SHI, Sha LU “A p3D Discrete Fracture-Matrix Simulation for Production Data Analysis in Vertically Fractured Well in Tight Gas Reservoirs”	167-170

FOREWORD



Dear Colleagues,

It is a great honor for me to host you all in “**9th International Conference on Computational and Experimental Science and Engineering (ICCESSEN-2022)**” was taken place in Antalya-TURKEY in the period of 27-31 October 2022.

We are also happy to publish the proceeding of ICCESSEN-2022. All papers have been reviewed by two reviewers.

Prof. Dr. İskender AKKURT

Chair for ICCESSEN-2022

Editor for Proceedings of ICCESSEN-2022

ORGANISATION COMMITTEE

Prof.Dr. Iskender AKKURT (Chair)	Suleyman Demirel University, Isparta -Turkey
Dr. Kadir GÜNOĞLU (secretary)	Isparta Uygulamalı Bilimler University, Isparta -Turkey
Dr. Hakan AKYILDIRIM	Suleyman Demirel University, Isparta -Turkey
Dr. Ahmet BEYÇİOĞLU	Düzce University, Düzce -Turkey
Dr. Nilgün DEMİR	Uludag University, Bursa -Turkey
Dr. Nurdan KARPUZ DEMİR	Suleyman Demirel University, Isparta -Turkey
Dr. Özge Kozguş GÜLDÜ	Ege University,İzmir-Turkey
Dr. Ümit KARA	Suleyman Demirel University, Isparta -Turkey
Dr. Feride KULALI	Üsküdar University, Istanbul-Turkey
Dr. Zehra Nur KULUÖZTÜRK	Bitliseren University, Bitlis-Turkey
Dr. M. Fatih KULUÖZTÜRK	Bitliseren University, Bitlis-Turkey
Dr. Hüseyin Ozan TEKİN	Üsküdar University, Istanbul-Turkey

SCIENTIFIC COMMITTEE

Prof.Dr. Iskender AKKURT (Chair)	Suleyman Demirel University, Isparta –Turkey
Prof.Dr. Majid ABBASPOUR	Sharif University of Technology-Iran
Prof.Dr. Zahid Hussain ABRA	Quadi-E-Awam University, Sindh-Pakistan
Prof.Dr. Abdullah ALAMRI	King Saud University, Saudi Arabia
Prof.Dr. Nezam Mahdavi-AMIRI	Sharif University Iran
Dr. John R.M.ANNAND	Glasgow University, Glasgow-Scotland (UK)
Dr. Majda AOUITITEN	Abdelmalek Essaadi University-Morocco
Prof.Dr. Mohamed Kheireddine AROUA	University of Malaya-Malaysia
Dr. Rachid BELKADA	CRSTSE -Algeria
Dr. Radhey S BENIWAL	CSIR-NISCAIR, New Delhi 110012, India
Dr. Mahmoud Abdullah BENNASER	Kuwait University-Kuwait
Dr. Djoudi BOUHAFS	Centre de Recherche en Technologie -Algeria
Prof. Oleg BURDAKOV	Linköping University Linköping, Sweden
Dr. Yusuf CEYLAN	Selcuk University, Konya-Turkey
Prof.Dr. Lotfi CHOUGHANE	Weill Cornell Medical College-Qatar
Dr. Manju D CHOUDHARY	Niscair-India
Dr. Nermin DEMİRKOL	Kocaeli University, Kocaeli –Turkey
Prof.Dr. İbrahim DİNÇER	University of Ontario Institute of Technology (UOIT)-Canada
Prof. Dr. Mitra DJAMAL	Institute Teknologi Bandung-Indonesia
Prof.Dr. Mahmut DOĞRU	Bitlis Eren University, Bitlis-Turkey
Prof.Dr. Mohammed Mostafa EL TOKHI	United Arab Emirates University-UAE
Dr. Zuhair ER	Istanbul Technical University, Istanbul-Turkey
Prof.Dr. Mustafa EROL	Dokuz Eylul University, İzmir-Turkey
Prof.Dr. Madjid FATHI	Dept. of EECS University of Siegen- Germany
Prof.Dr. Jan FELBA	Wroclaw University of Technology-Poland
Prof.Dr. S. Mostafa GHIAASIAAN	Mechanical/Nuclear Engineering, Georgia Tech USA
Prof.Dr. Mustafa GÜNAL	Gaziantep University, Gaziantep-Turkey
Prof. Dr. Amir HUSSAIN	University of Stirling- Scotland(UK)
Dr. Nabi IBADOV	Warsaw University of Technology-Poland
Prof.Dr. Fatma KARİPCİN	Nevşehir Hacı Bektaş Veli University-Turkey
Prof.Dr. Hamdi Ş. KILIÇ	Selcuk University, Konya-Turkey
Dr. Menekşe V. KILIÇARSLAN	İstanbul Aydın University, Istanbul-Turkey

Prof.Dr. Ziya Erdem KOÇ	Selcuk University, Konya-Turkey
Prof. Dr. İsmail KOYUNCU	Istanbul Technical University, Istanbul-Turkey
Dr. Irida MARKJA	Polytechnic University, Tirana-Albania
Dr. F. Zümrüt Biber MÜFTÜLER	Ege University, Izmir-Turkey
Dr. Susan Shukur NOORI	Kirkuk University, Kirkuk-Iraq
Prof.Dr. Ravindra NUGGEHALLI	New Jersey Institute of Technology-USA
Prof.Dr. İbrahim ÖRÜN	Aksaray University, Aksaray-Turkey
Prof.Dr. Necati ÖZDEMİR	Balıkesir University, Balıkesir-Turkey
Dr. Zeynep PARLAR	Istanbul Technical University, Istanbul-Turkey
Prof.Dr. Ioana G. Petrisor	ToxStrategies, Inc., Mission Viejo, CA
Dr. Tomasz PIOTROWSKI	Warsaw University of Technology, Warsaw-Poland
Prof.Dr. Javad RAHIGHI	AEOI, Tehran-Iran.
Dr. Abdelmadjid RECIQUI	University of Boumerdes-Algeria
Prof.Dr. Osman SAGDIÇ	Yıldız Technical University, Istanbul-Turkey
Prof.Dr. Miljko SATARIC	Faculty of Technical Sciences Novi Sad-Serbia
Prof.Dr. Saleh SULTANSOY	TOBB University, Ankara-Turkey
Dr. Naim SYLA	University of Prishtina-Kosova
Prof. Dr. Mustafa TAVASLI	Uludag University, Bursa-Turkey
Dr. Huseyin TOROS	Istanbul Technical University, Istanbul-Turkey
Prof.Dr. Ahmad UMAR	Najran University-Saudi Arabia
Prof.Dr. Gerhard-Wilhelm WEBER	Middle East Technical University Ankara-Turkey
Prof.Dr. Erol YAŞAR	Mersin University, Mersin-Turkey

INVITED SPEAKERS

	<p style="text-align: center;">Dr. Jana LIPKOVSKI</p> <p style="text-align: center;"><i>University of Belgrade, SERBIA</i></p> <p>Title: Sustainable development of dense urban areas in correlation with planning requirements of educational facilities and belonging open spaces – an issue of social welfare</p>
	<p style="text-align: center;">Prof. Dr. Madjid FATHI</p> <p style="text-align: center;"><i>Dept. of EECS University of Siegen, GERMANY</i></p> <p>Title: A beneficiary for advance in Knowledge graph for cyber technology</p>
	<p style="text-align: center;">Dr. Hayat ARBOUZ</p> <p style="text-align: center;"><i>University of Blida1-ALGERIA</i></p> <p>Title: Optimization of Lead-Free CsSnI₃-based Perovskite Solar Cell structure</p>
	<p style="text-align: center;">Prof. Dr. Gerhard-Wilhelm WEBER</p> <p style="text-align: center;"><i>Poznan University of Technology-POLAND</i></p> <p>Title: New Contributions to Aggregate Production Planning with Outsourcing under Uncertain Seasonal Demand - Supported by Human</p>
	<p style="text-align: center;">Prof. Dr. M. Shaheer AKHTAR</p> <p style="text-align: center;"><i>Chonbuk National University, SOUTH KOREA</i></p> <p>Title: Efficient Hole Transporting Materials for Perovskite Solar Cells</p>

Review on the effect of reinforcement particle type, shape, and volume fraction on the porosity content of metal matrix composite

Mohammed A. ALMOMANI*¹, Bilal R MELHEM²

^{1,2}Jordan University of Science and Technology, Faculty of Engineering, Industrial Engineering Department, 22110, Irbid-Jordan
maalmomani7@just.edu.jo

ABSTRACT

The porosity contents in metal matrix composite materials (MMCs) is one of the important factors that affect the composite final properties. Thus, this topic had caught the focus of many researchers. However, several factors affect the porosity content in this class of materials, including: reinforcement particle type, shape, and volume fraction. No single article covers the effect of the aforementioned factors on porosity contents in MMCs. Hence, this article is designed to summarize this effect to cover this gap in the literature.

KEYWORDS: *Porosity content, Metal matrix composites*

1. INTRODUCTION

Particulate metal matrix composites (MMCs) in which the second phase reinforcement is in the form of particles had caught more attention when compared with other types of composites (fibrous, and structural) composites due to its cost effectiveness, and their isotropic properties. Stir casting (SC) and powder metallurgy (PM) are among the most widely used techniques to produce MMCs. The constituent materials of MMCs are used in the form of powders/particles in powder metallurgy. Stir casting technique is similar to traditional casting in which solid reinforcement particles are added to the molten metal matrix and stirring action is used to disperse them in the matrix [1].

The development and production of this class of composites led to a technological advancement resulting from enhancement of various properties of the matrix properties. However, the formation of porosities during production presents a challenge that had caught the attention of many researchers, especially that the porosities affect most of the MMCs' properties; including: mechanical (yield strength (σ_y), ultimate tensile strength (UTS), Poisson ratio (ν), ductility, fatigue life, and elastic modulus) and thermal. Most studies agreed that increasing the porosity content results in a decrease of UTS, σ_y , ν and fatigue strength. Furthermore, the increase of porosity causes an increase of the damping capacity, and a decrease of thermal conductivity of MMCs [2-11]. In stir casting, porosities form either from gas entrapment during mixing, vapor surrounding reinforcement particles, or shrinkage during solidification. On the other hand, porosities form during compaction process in powder metallurgy. Studies showed that the porosity content in stir casting is much lower for the corresponding MMCs made by powder metallurgy at all levels of volume fraction of reinforcements.

SiC is one of the most frequently used reinforcement. However, other types of reinforcement particles and in some cases two or more kind of particles are used.

Weight fraction of reinforcements varied from very small amount (~0.1 wt.%), and it was not exceeding 15 or 20 wt.% in most cases. Different particle sizes and shapes were also used. Nano to micro size particles were used, and the shape varied from regular spherical to other non-regular shapes.

Weight or volume fraction, size, shape, and type of reinforcements affect the porosity content in MMCs. The aim of this article is to provide a summary of the effect of each one of these factors on porosity contents in MMCs.

2. EFFECT OF REINFORCEMENT ON POROSITY CONTENT

2.1 Effect of Volume Fraction

Several researchers have examined the effect of volume fraction of ceramic reinforcements on the porosity content in MMC. All of the studies reported that the porosity content increased with increase of volume fraction as a result of the increase of reinforcement surface area, which accompanied by increase of the gases that surround particles [2,3, 5, 7-9].

2.2 Effect of Size

The size of the reinforcement particle is one of the important factors that affect porosity content of MMC. The use of small reinforcement particles with a large surface area results in a reduction of their wettability in the molten matrix. High surface energy of the nanoparticles cause an increase of their agglomeration. Hence, the porosity content increased with decreasing particle size [5, 10].

2.3 Effect of Shape

The shape of the reinforcement ceramic particles affects their compaction, and thus the density and porosity content of MMC. The method of powder preparation process affects the size and shape of the attained particles. It was found that the use of particles with irregular shape cause an increase of the porosity content as they may mechanically interlock and entangle with each other. On the other hand, the use of spherical particles results in a more homogenous distribution of particles and thus producing denser MMC with low porosity content [6, 11].

Table 1. Summary of the effect of volume fraction, size, and shape of reinforcements on the porosity content of MMC.

Composite	Volume fraction of reinforcement	Particle size	Processing	Reference
A356.1-B ₄ C A356.1-TiB ₂ A356.1-ZrSiO ₄	5, 10, 15	Micron sized particles	SC	2
Porosity content increases with increase of volume fraction of reinforcements as a result of increase of surface area of the particles. Thus, increasing the gas layer surrounded them, which increases heterogeneous pore nucleation.				
Composite	Volume fraction of reinforcement	Particle size	Processing	Reference
A356.1-MgO	1.5, 2.5, 5	Nano sized particles	SC	3
Porosity content increases with increase of volume fraction of reinforcements, due to: <ol style="list-style-type: none"> 1. decrease of particles wettability in the matrix material, which result in their agglomeration. 2. Increase of the induced tensile stress generated from the mismatch of thermal expansion coefficient between matrix material and reinforcement particles, which would promote porosity formation. 				
Composite	Volume fraction of reinforcement	Particle size	Processing	Reference

A356-Al ₂ O ₃	1, 2, 3	50 nm	SC	5
	1, 3, 5, 10	20 μm	SC	5
The porosity contents increase with increase of the volume fraction and decrease of particle size due to the accompanying decrease of wettability that result from increase of surface area of the particles in contact with air.				
Composite	Volume fraction of reinforcement	Particle size	Processing	Reference
Ti-TiB ₂	5 wt. %	3.5-6 μm	Selective laser melting	6
The use of irregular shape particles caused less compaction of powder, which increase the porosity content as they may interlock and entangle with each other. On the other hand, particles with spherical morphology have higher degree of flowability, and they caused a decrease of porosity content.				
Composite	Volume fraction of reinforcement	Particle size	Processing	Reference
Al-SiC	10, 15, 20	< 100 nm	PM	7
Porosity content increases with increasing volume fraction of reinforcements, because of the restriction of plastic deformation in the hard ceramic reinforcement particles (poor compressibility) as compared with the ductile matrix material. This mismatch in the elastic-plastic deformation reduces the wettability of the particles in the matrix resulting in weak bonding.				
Composite	Volume fraction of reinforcement	Particle size	Processing	Reference
A356-MgO	1.2, 2.5, 5	70 nm	PM	8
Porosity content increases with increasing volume fraction of reinforcements (decrease of wettability) as a result of formation of rigid network of MgO reinforcement in the matrix. This lessen the compaction efficiency of the composite structure, and increasing porosity contents.				
Composite	Volume fraction of reinforcement	Particle size	Processing	Reference
Al-MgO	5, 10, 15	105 μm	SC	9
Porosity content increases with increasing volume fraction of reinforcements as a result of reduction of ceramic reinforcement particles wettability in the molten matrix.				
Composite	Volume fraction of reinforcement	Particle size	Processing	Reference
Al-SiC	10	2 μm 40 μm	Accumulative roll bonding	10

The use of large reinforcement particles results in higher quality of bonding and lower porosity contents as compared with the small size reinforcement particles.				
Composite	Volume fraction of reinforcement	Particle size	Processing	Reference
Cu-CNT		3 μm	PM	11
		10 μm		
		45 μm		
Cu alloy- CNT		45 μm	PM	
Increasing the particle size will increase the porosity content in the composite.				
The use of regular spherical shape particles gives less porosity than the use of dendritic shape particles				

3. CONCLUSION

The main conclusions of this article are summarized as follows:

- Increasing the volume fractions of reinforcement results in an increase of the porosity content in MMCs.
- The porosity content increased with decreasing reinforcement particle size.
- Regular shape of reinforcement particles like spherical and rectangular tend to form less porosity than other irregular shapes.

REFERENCES

- [1] W. D. Callister, D.G. Rethwisch, *Materials Science and Engineering: An Introduction*, 8th Edition.
- [2] K. Shirvanimoghaddam, H. Khayyam, H. Abdizadeh, M. Karbalaee Akbari, A. Pakseresht, F. Abdi, A. Abbasi, M. Naebe, Effect of B4C, TiB2 and ZrSiO4 ceramic particles on mechanical properties of aluminium matrix composites: Experimental investigation and predictive modelling, *Ceramics International* 42(5) (2016), 6206-6220.
- [3] A. Ansary Yar, M. Montazerian, H. Abdizadeh, H.R. Baharvandi, Microstructure and mechanical properties of aluminium alloy matrix composite reinforced with nano-particle MgO, *Journal of Alloys and Compound* 484(2009), 400-404.
- [4] S.N. Aqida, M.I. Ghazali, J. Hashim, Effect of porosity on mechanical properties of metal matrix composite: an overview, *Jurnal Teknologi*, 40(1) (2004), 17-32.
- [5] S.A. Sajjadi, H.R. Ezatpour, H. Beygi, Microstructure and mechanical properties of Al–Al2O3 micro and nano composites fabricated by stir casting, *Materials Science and Engineering: A*, 528(29-30) (2011), 8765-8771.
- [6] H. Attar, K.G. Prashanth, L. Zhang, M. Calin, I. V. Okulov, S. Scudino, C. Yang, J. Eckert, Effect of powder particle shape on the properties of in situ Ti–TiB composite materials produced by selective laser melting, *Journal of Materials Science & Technology*, 31(10) (2015), 1001-1005.
- [7] A. Iqbal A, N. Amierah, Effect of reinforcement volume fraction on the mechanical properties of the Al-SiC nanocomposite materials. *IOP Conference Series: Materials Science and Engineering*. 2017;226.
- [8] H. Abdizadeh, R. Ebrahimifard, M.A. Baghchesara, Investigation of microstructure and mechanical properties of nano MgO reinforced Al composites manufactured by stir casting and

- powder metallurgy methods: A comparative study, *Composites Part B: Engineering*, 56(2014), 217-221.
- [9] R. Calin, M. Pul, Z. O. Pehlivanli, The effect of reinforcement volume ratio on porosity and thermal conductivity in Al-Mgo composites, *Materials Research*, 15(6) (2012), 1057-1063.
- [10] R. Jamaati, S. Amir Khanlou, M.R. Toroghinejad, B. Niroumand, Effect of particle size on microstructure and mechanical properties of composites produced by ARB process, *Materials Science and Engineering: A*, 528(4-5) (2011), 2143-2148.
- [11] S.M. Uddin, T. Mahmud, C. Wolf, C. Glanz, I. Kolaric, C. Volkmer, H. Höller, U. Wienecke, [12] S. Roth, H. Fecht, Effect of size and shape of metal particles to improve hardness and electrical properties of carbon nanotube reinforced copper and copper alloy composites, *Composites Science and Technology*, 70(16) (2010), 2253-2257.

Impact of Fractal Fractional Derivative on a Plant Disease Model with Vector Borne

Fırat EVİRGEN, Esmehan UÇAR and Necati ÖZDEMİR*

Balıkesir University, Department of Mathematics, Balıkesir, TURKEY

*nozdemir@balikesir.edu.tr

ABSTRACT

Plant diseases caused by a variety of factors have historically had a negative impact on the world's ecology and economy. The most important of these is the Maize Streak Virus (genus *Mastrevirus*; family *Geminiviridae*) (MSV), which is the causal agent of Maize Streak disease (MSD). This virus is caused the most important and widespread maize disease in Sub-Saharan Africa. In this study, an eco-epidemiological deterministic model for the transmission dynamics of Maize Streak virus (MSV) is first remodeled with Fractal Fractional (FF) Caputo derivative. The recently-presented FF notion of differentiation comprises an operator possessing two orders; the fractional order and the fractal dimension, respectively. We deeply investigate the numerical properties of this fractal fractional model, furthermore, acquire several numeric graphs involving this MSV model in order to forecast and survey intricate phenomena.

KEYWORDS - *Fractal fractional derivative, Plant disease, Maize streak virus.*

1. INTRODUCTION

Plants are one of the indispensable building blocks of our world's ecosystem. Diseases that occur in plants, which are in the food chain of people and have great economic value, cause great losses in many respects. For example, some bacterial vector-borne infections have significantly harmed the citrus, grape, and olive sectors in recent years [1]. Maize is another plant that can be damaged by plant diseases. The biggest factor that makes the diseases on this species important is that it is a basic food element in almost all of sub-Saharan Africa [2]. One of the most important diseases affecting maize is maize streak disease (MSD) caused by the maize streak virus (MSV) in the *Mastrevirus* genus of the *Geminiviridae* family. It is spread by the genus *Cicadulina* of leafhopper vectors [2]. Mathematical modeling is of great importance in understanding plant disease dynamics, planning and implementing the necessary measures to prevent the devastating consequences of the disease. Some mathematical models related to Maize Streak disease can be accessed from [3,4]. Recently, fractional derivatives have been used to obtain more realistic behavior of systems [5,6,7]. This study aims to analyze the influence of memory and heritability effects on the spread of the disease by applying the new fractal-fractional Caputo derivative to the Maize streak disease model. Our model divides the Maize population and the leafhopper vector population into sub-two classes under the interaction of MSV pathogen $P(t)$. The model comprising the typical derivative is represented by the reference [4] as follows.

$$\frac{dS(t)}{dt} = rS \left(1 - \frac{S + I}{K} \right) - \frac{\beta_1 SY}{A + S},$$

$$\frac{dI(t)}{dt} = \frac{\beta_1 SY}{A + S} - (\mu_1 + \delta)I,$$

$$\begin{aligned} \frac{dH(t)}{dt} &= q - H \left(\frac{\beta_2 I}{C + I} + \frac{\beta_3 P}{D + P} \right) - \mu_2 H, \\ \frac{dY(t)}{dt} &= b_1 H \left(\frac{\beta_2 I}{C + I} + \frac{\beta_3 P}{D + P} \right) - \mu_3 Y, \\ \frac{dP(t)}{dt} &= \gamma + \delta I - \mu_4 P, \\ S(0) = S_0 \geq 0, \quad I(0) = I_0 \geq 0, \quad H(0) = H_0 \geq 0, \quad Y(0) = Y_0 \geq 0 \quad \text{and} \quad P(0) = P_0 \geq 0 \end{aligned} \tag{1}$$

where $S(t)$ susceptible maize, $I(t)$ infected maize, $H(t)$ susceptible leafhopper and $Y(t)$ infected leafhopper populations. Table 1 provides descriptions and values for each parameter in the Maize streak disease model.

Table 1. The explanations and values of all parameters in the Maize streak disease model (1) [4].

Parameter	Description	Value
β_1	Predation and infection rate of Infected Leafhopper on Susceptible Maize plant	0.45
β_2	Predation and infection rate of Susceptible Leafhopper on Infected Maize plant	0.04
β_3	Infection rate of Susceptible Leafhopper by MSV Pathogen from grasses and other plants	0.25
q	Recuriment rate of leafhopper	0.02
K	Carrying capacity	10
μ_1	Death rate of infected maize	0.008
μ_2	Death rate of susceptible leafhopper	0.0303
μ_3	Death rate of infected leafhopper	0.0303
b_1	Conversion rate of Infected Leafhopper	0.45
δ	Production rate of MSV pathogen by Infected Maize plant	0.018
A	Half saturation rate of Susceptible maize with Infected plant	0.4
C	Half saturation rate of Susceptible Leafhopper with Infected Maize plant	0.6
D	Half saturation rate of Susceptible Leafhopper with pathogen	0.5
r	Intrinsic growth rate of Maize	0.0005
μ_4	Death rate of a pathogen	0.0005

Some preliminaries

In this section, we give essential new concepts of fractal fractional (FF) Caputo derivative.

Definition 1 [8] Let $g(t)$ a continuous and differentiable function over the interval (a, b) with the order \mathcal{K} , the FF derivative of $g(t)$ having fractional order ρ in Riemann-Liouville type with power law kernel is defined by:

$${}^{FFP}D_{0,t}^{\rho,\kappa}(g(t)) = \frac{1}{\Gamma(m-\rho)} \frac{d}{dt^\kappa} \int_0^t (t-\lambda)^{m-\rho-1} g(\lambda) d(\lambda), \tag{2}$$

with $m-1 < \rho, \kappa \leq m \in \mathbb{N}$ and $\frac{dg(s)}{ds^\kappa} = \lim_{t \rightarrow s} \frac{g(t) - g(s)}{t^\kappa - s^\kappa}$.

Definition 2 [8] Let $g(t)$ a continuous function over the interval (a, b) , the definition of FF integral of $g(t)$ with order ρ having power law type kernel is defined as:

$${}^{FFP}J_{0,t}^\rho(g(t)) = \frac{\kappa}{\Gamma(\rho)} \int_0^t (t-\lambda)^{\rho-1} \lambda^{\kappa-1} g(\lambda) d(\lambda). \tag{3}$$

2. FRACTAL FRACTIONAL MSV MODEL

We model the system by replacing the ordinary time derivative with the newly introduced fractal fractional derivative operator FF in the sense of Caputo FFC. Consequently, the fractal fractional version of the mathematical model (1) takes the following form:

$$\begin{aligned} {}^{FFP}D_{0,t}^{\rho,\kappa}(S(t)) &= rS \left(1 - \frac{S+I}{K} \right) - \frac{\beta_1 SY}{A+S}, \\ {}^{FFP}D_{0,t}^{\rho,\kappa}(I(t)) &= \frac{\beta_1 SY}{A+S} - (\mu_1 + \delta)I, \\ {}^{FFP}D_{0,t}^{\rho,\kappa}(H(t)) &= q - H \left(\frac{\beta_2 I}{C+I} + \frac{\beta_3 P}{D+P} \right) - \mu_2 H, \\ {}^{FFP}D_{0,t}^{\rho,\kappa}(Y(t)) &= b_1 H \left(\frac{\beta_2 I}{C+I} + \frac{\beta_3 P}{D+P} \right) - \mu_3 Y, \\ {}^{FFP}D_{0,t}^{\rho,\kappa}(P(t)) &= \gamma + \delta I - \mu_4 P. \end{aligned} \tag{4}$$

3. NUMERICAL RESULTS

In this section, we solve our fractal fractional MSV model (4) using a numerical method [9] as follows:

$$\begin{aligned} \frac{1}{\Gamma(1-\rho)} \int_0^t (t-\sigma)^{-\rho} \left(\frac{d}{d\sigma^\kappa} S(\sigma) \right) d\sigma &= g_1(t, S(t), I(t), H(t), Y(t), P(t)), \\ \frac{1}{\Gamma(1-\rho)} \int_0^t (t-\sigma)^{-\rho} \left(\frac{d}{d\sigma^\kappa} I(\sigma) \right) d\sigma &= g_2(t, S(t), I(t), H(t), Y(t), P(t)), \\ \frac{1}{\Gamma(1-\rho)} \int_0^t (t-\sigma)^{-\rho} \left(\frac{d}{d\sigma^\kappa} H(\sigma) \right) d\sigma &= g_3(t, S(t), I(t), H(t), Y(t), P(t)), \quad (5) \\ \frac{1}{\Gamma(1-\rho)} \int_0^t (t-\sigma)^{-\rho} \left(\frac{d}{d\sigma^\kappa} Y(\sigma) \right) d\sigma &= g_4(t, S(t), I(t), H(t), Y(t), P(t)), \\ \frac{1}{\Gamma(1-\rho)} \int_0^t (t-\sigma)^{-\rho} \left(\frac{d}{d\sigma^\kappa} P(\sigma) \right) d\sigma &= g_5(t, S(t), I(t), H(t), Y(t), P(t)). \end{aligned}$$

where g_1, g_2, \dots, g_5 are the right hand side of the Eq. (4). Then the right hand side of Eq. (5) can

be convert to Riemann-Liouville type by using $\frac{1}{\Gamma(1-\rho)} \frac{d}{dt} \int_0^t (t-\sigma)^\rho g(\sigma) d\sigma \frac{1}{\kappa t^{\kappa-1}}$

relation such that [9,10]:

$$\begin{aligned} {}^{RL}D_{0,t}^\rho (S(t)) &= \kappa t^{\kappa-1} g_1(t, S(t), I(t), H(t), Y(t), P(t)), \\ {}^{RL}D_{0,t}^\rho (I(t)) &= \kappa t^{\kappa-1} g_2(t, S(t), I(t), H(t), Y(t), P(t)), \\ {}^{RL}D_{0,t}^\rho (H(t)) &= \kappa t^{\kappa-1} g_3(t, S(t), I(t), H(t), Y(t), P(t)), \quad (6) \\ {}^{RL}D_{0,t}^\rho (Y(t)) &= \kappa t^{\kappa-1} g_4(t, S(t), I(t), H(t), Y(t), P(t)), \\ {}^{RL}D_{0,t}^\rho (P(t)) &= \kappa t^{\kappa-1} g_5(t, S(t), I(t), H(t), Y(t), P(t)). \end{aligned}$$

We change place RL derivative to Caputo derivative for the purpose of integer-order initial conditions. Implementing the Riemann-Liouville fractional integral, we achieve

$$\begin{aligned}
 S(t) &= S(0) + \frac{\kappa}{\Gamma(\rho)} \int_0^t \sigma^{\kappa-1} (t-\sigma)^{\rho-1} g_1(\sigma, S, I, H, Y, P) d\sigma, \\
 I(t) &= I(0) + \frac{\kappa}{\Gamma(\rho)} \int_0^t \sigma^{\kappa-1} (t-\sigma)^{\rho-1} g_2(\sigma, S, I, H, Y, P) d\sigma, \\
 H(t) &= H(0) + \frac{\kappa}{\Gamma(\rho)} \int_0^t \sigma^{\kappa-1} (t-\sigma)^{\rho-1} g_3(\sigma, S, I, H, Y, P) d\sigma, \\
 Y(t) &= Y(0) + \frac{\kappa}{\Gamma(\rho)} \int_0^t \sigma^{\kappa-1} (t-\sigma)^{\rho-1} g_4(\sigma, S, I, H, Y, P) d\sigma, \\
 P(t) &= P(0) + \frac{\kappa}{\Gamma(\rho)} \int_0^t \sigma^{\kappa-1} (t-\sigma)^{\rho-1} g_5(\sigma, S, I, H, Y, P) d\sigma.
 \end{aligned}
 \tag{7}$$

Benefiting from approach at t_{n+1} , we can give

$$\begin{aligned}
 S_{n+1}(t) &= S_0 + \frac{\kappa}{\Gamma(\rho)} \int_0^{t_{n+1}} \sigma^{\kappa-1} (t_{n+1}-\sigma)^{\rho-1} g_1(\sigma, S, I, H, Y, P) d\sigma, \\
 I_{n+1}(t) &= I_0 + \frac{\kappa}{\Gamma(\rho)} \int_0^{t_{n+1}} \sigma^{\kappa-1} (t_{n+1}-\sigma)^{\rho-1} g_2(\sigma, S, I, H, Y, P) d\sigma, \\
 H_{n+1}(t) &= H_0 + \frac{\kappa}{\Gamma(\rho)} \int_0^{t_{n+1}} \sigma^{\kappa-1} (t_{n+1}-\sigma)^{\rho-1} g_3(\sigma, S, I, H, Y, P) d\sigma, \\
 Y_{n+1}(t) &= Y_0 + \frac{\kappa}{\Gamma(\rho)} \int_0^{t_{n+1}} \sigma^{\kappa-1} (t_{n+1}-\sigma)^{\rho-1} g_4(\sigma, S, I, H, Y, P) d\sigma, \\
 P_{n+1}(t) &= P_0 + \frac{\kappa}{\Gamma(\rho)} \int_0^{t_{n+1}} \sigma^{\kappa-1} (t_{n+1}-\sigma)^{\rho-1} g_5(\sigma, S, I, H, Y, P) d\sigma,
 \end{aligned}
 \tag{8}$$

and

$$\begin{aligned}
 S_{n+1}(t) &= S_0 + \left(\frac{\kappa}{\Gamma(\rho)} \sum_{i=0}^n \int_{t_j}^{t_{j+1}} \sigma^{\kappa-1} (t_{n+1} - \sigma)^{\rho-1} g_1(\sigma, S, I, H, Y, P) d\sigma \right), \\
 I_{n+1}(t) &= I_0 + \left(\frac{\kappa}{\Gamma(\rho)} \sum_{i=0}^n \int_{t_j}^{t_{j+1}} \sigma^{\kappa-1} (t_{n+1} - \sigma)^{\rho-1} g_2(\sigma, S, I, H, Y, P) d\sigma \right), \\
 H_{n+1}(t) &= H_0 + \left(\frac{\kappa}{\Gamma(\rho)} \sum_{i=0}^n \int_{t_j}^{t_{j+1}} \sigma^{\kappa-1} (t_{n+1} - \sigma)^{\rho-1} g_3(\sigma, S, I, H, Y, P) d\sigma \right), \quad (9) \\
 Y_{n+1}(t) &= Y_0 + \left(\frac{\kappa}{\Gamma(\rho)} \sum_{i=0}^n \int_{t_j}^{t_{j+1}} \sigma^{\kappa-1} (t_{n+1} - \sigma)^{\rho-1} g_4(\sigma, S, I, H, Y, P) d\sigma \right), \\
 P_{n+1}(t) &= P_0 + \left(\frac{\kappa}{\Gamma(\rho)} \sum_{i=0}^n \int_{t_j}^{t_{j+1}} \sigma^{\kappa-1} (t_{n+1} - \sigma)^{\rho-1} g_5(\sigma, S, I, H, Y, P) d\sigma \right).
 \end{aligned}$$

Benefiting from Lagrangian piece-wise interpolation, in the interval $[t_i, t_{i+1}]$, approximating the function $\sigma^{\kappa-1} g_i(t, S, I, H, Y, P)$ we obtain

$$\begin{aligned}
 P_i(\sigma) &= \frac{\sigma - t_{i-1}}{t_i - t_{i-1}} t_i^{\kappa-1} g_1(t_i, S_i, I_i, H_i, Y_i, P_i) - \frac{\sigma - t_i}{t_i - t_{i-1}} t_{i-1}^{\kappa-1} g_1(t_{i-1}, S_{i-1}, I_{i-1}, H_{i-1}, Y_{i-1}, P_{i-1}), \\
 Y_i(\sigma) &= \frac{\sigma - t_{i-1}}{t_i - t_{i-1}} t_i^{\kappa-1} g_2(t_i, S_i, I_i, H_i, Y_i, P_i) - \frac{\sigma - t_i}{t_i - t_{i-1}} t_{i-1}^{\kappa-1} g_2(t_{i-1}, S_{i-1}, I_{i-1}, H_{i-1}, Y_{i-1}, P_{i-1}), \\
 Z_i(\sigma) &= \frac{\sigma - t_{i-1}}{t_i - t_{i-1}} t_i^{\kappa-1} g_3(t_i, S_i, I_i, H_i, Y_i, P_i) - \frac{\sigma - t_i}{t_i - t_{i-1}} t_{i-1}^{\kappa-1} g_3(t_{i-1}, S_{i-1}, I_{i-1}, H_{i-1}, Y_{i-1}, P_{i-1}), \\
 T_i(\sigma) &= \frac{\sigma - t_{i-1}}{t_i - t_{i-1}} t_i^{\kappa-1} g_4(t_i, S_i, I_i, H_i, Y_i, P_i) - \frac{\sigma - t_i}{t_i - t_{i-1}} t_{i-1}^{\kappa-1} g_4(t_{i-1}, S_{i-1}, I_{i-1}, H_{i-1}, Y_{i-1}, P_{i-1}), \\
 U_i(\sigma) &= \frac{\sigma - t_{i-1}}{t_i - t_{i-1}} t_i^{\kappa-1} g_5(t_i, S_i, I_i, H_i, Y_i, P_i) - \frac{\sigma - t_i}{t_i - t_{i-1}} t_{i-1}^{\kappa-1} g_5(t_{i-1}, S_{i-1}, I_{i-1}, H_{i-1}, Y_{i-1}, P_{i-1}).
 \end{aligned} \quad (10)$$

Thus, we get

$$\begin{aligned}
 S_{n+1} &= S_0 + \frac{\kappa}{\Gamma(\rho)} \sum_{i=0}^n \int_{t_i}^{t_{i+1}} \sigma^{\kappa-1} (t_{n+1} - \sigma)^{\rho-1} P_i(\sigma) d\sigma, \\
 E_{n+1} &= E_0 + \frac{\kappa}{\Gamma(\rho)} \sum_{i=0}^n \int_{t_i}^{t_{i+1}} \sigma^{\kappa-1} (t_{n+1} - \sigma)^{\rho-1} Y_i(\sigma) d\sigma, \\
 A_{n+1} &= A_0 + \frac{\kappa}{\Gamma(\rho)} \sum_{i=0}^n \int_{t_i}^{t_{i+1}} \sigma^{\kappa-1} (t_{n+1} - \sigma)^{\rho-1} Z_i(\sigma) d\sigma, \\
 B_{n+1} &= B_0 + \frac{\kappa}{\Gamma(\rho)} \sum_{i=0}^n \int_{t_i}^{t_{i+1}} \sigma^{\kappa-1} (t_{n+1} - \sigma)^{\rho-1} T_i(\sigma) d\sigma, \\
 R_{n+1} &= R_0 + \frac{\kappa}{\Gamma(\rho)} \sum_{i=0}^n \int_{t_i}^{t_{i+1}} \sigma^{\kappa-1} (t_{n+1} - \sigma)^{\rho-1} U_i(\sigma) d\sigma. \tag{11}
 \end{aligned}$$

After elimination of the integrals, we present the numerical method for the fractal fractional Caputo MSV model

$$\begin{aligned}
 S_{n+1} &= S_0 + \frac{K(\Delta t)^\rho}{\Gamma(\rho+2)} \sum_{i=0}^n \left[t_i^{\kappa-1} g_1(t_i, S_i, I_i, H_i, Y_i, P_i) \begin{pmatrix} (n+1-i)^\rho (n-j+2+\rho) \\ -(n-i)^\rho (n-i+2+2\rho) \end{pmatrix} \right. \\
 &\quad \left. - t_{i-1}^{\kappa-1} g_1(t_{i-1}, S_{i-1}, I_{i-1}, H_{i-1}, Y_{i-1}, P_{i-1}) \left((n+1-i)^{\rho+1} - (n-i)^\rho (n-i+1+\rho) \right) \right], \\
 I_{n+1} &= I_0 + \frac{K(\Delta t)^\rho}{\Gamma(\rho+2)} \sum_{i=0}^n \left[t_i^{\kappa-1} g_2(t_i, S_i, I_i, H_i, Y_i, P_i) \begin{pmatrix} (n+1-i)^\rho (n-j+2+\rho) \\ -(n-i)^\rho (n-i+2+2\rho) \end{pmatrix} \right. \\
 &\quad \left. - t_{i-1}^{\kappa-1} g_2(t_{i-1}, S_{i-1}, I_{i-1}, H_{i-1}, Y_{i-1}, P_{i-1}) \left((n+1-i)^{\rho+1} - (n-i)^\rho (n-i+1+\rho) \right) \right], \\
 H_{n+1} &= H_0 + \frac{K(\Delta t)^\rho}{\Gamma(\rho+2)} \sum_{i=0}^n \left[t_i^{\kappa-1} g_3(t_i, S_i, I_i, H_i, Y_i, P_i) \begin{pmatrix} (n+1-i)^\rho (n-j+2+\rho) \\ -(n-i)^\rho (n-i+2+2\rho) \end{pmatrix} \right. \\
 &\quad \left. - t_{i-1}^{\kappa-1} g_3(t_{i-1}, S_{i-1}, I_{i-1}, H_{i-1}, Y_{i-1}, P_{i-1}) \left((n+1-i)^{\rho+1} - (n-i)^\rho (n-i+1+\rho) \right) \right], \\
 Y_{n+1} &= Y_0 + \frac{K(\Delta t)^\rho}{\Gamma(\rho+2)} \sum_{i=0}^n \left[t_i^{\kappa-1} g_4(t_i, S_i, I_i, H_i, Y_i, P_i) \begin{pmatrix} (n+1-i)^\rho (n-j+2+\rho) \\ -(n-i)^\rho (n-i+2+2\rho) \end{pmatrix} \right. \\
 &\quad \left. - t_{i-1}^{\kappa-1} g_4(t_{i-1}, S_{i-1}, I_{i-1}, H_{i-1}, Y_{i-1}, P_{i-1}) \left((n+1-i)^{\rho+1} - (n-i)^\rho (n-i+1+\rho) \right) \right], \\
 P_{n+1} &= P_0 + \frac{K(\Delta t)^\rho}{\Gamma(\rho+2)} \sum_{i=0}^n \left[t_i^{\kappa-1} g_5(t_i, S_i, I_i, H_i, Y_i, P_i) \begin{pmatrix} (n+1-i)^\rho (n-j+2+\rho) \\ -(n-i)^\rho (n-i+2+2\rho) \end{pmatrix} \right. \\
 &\quad \left. - t_{i-1}^{\kappa-1} g_5(t_{i-1}, S_{i-1}, I_{i-1}, H_{i-1}, Y_{i-1}, P_{i-1}) \left((n+1-i)^{\rho+1} - (n-i)^\rho (n-i+1+\rho) \right) \right].
 \end{aligned}
 \tag{12}$$

The initial conditions $S(0) = 1000$, $I(0) = 20$, $H(0) = 100$, $Y(0) = 0$, $P(0) = 1000$ and the parameters found in Table 1 are used to display the numerical outputs that result from the fractal-fractional Caputo model. Figure 1 shows the computational results when the fractal and fractional order remain constant as $\kappa = 0.8$ and $\rho = 0.9$, respectively.

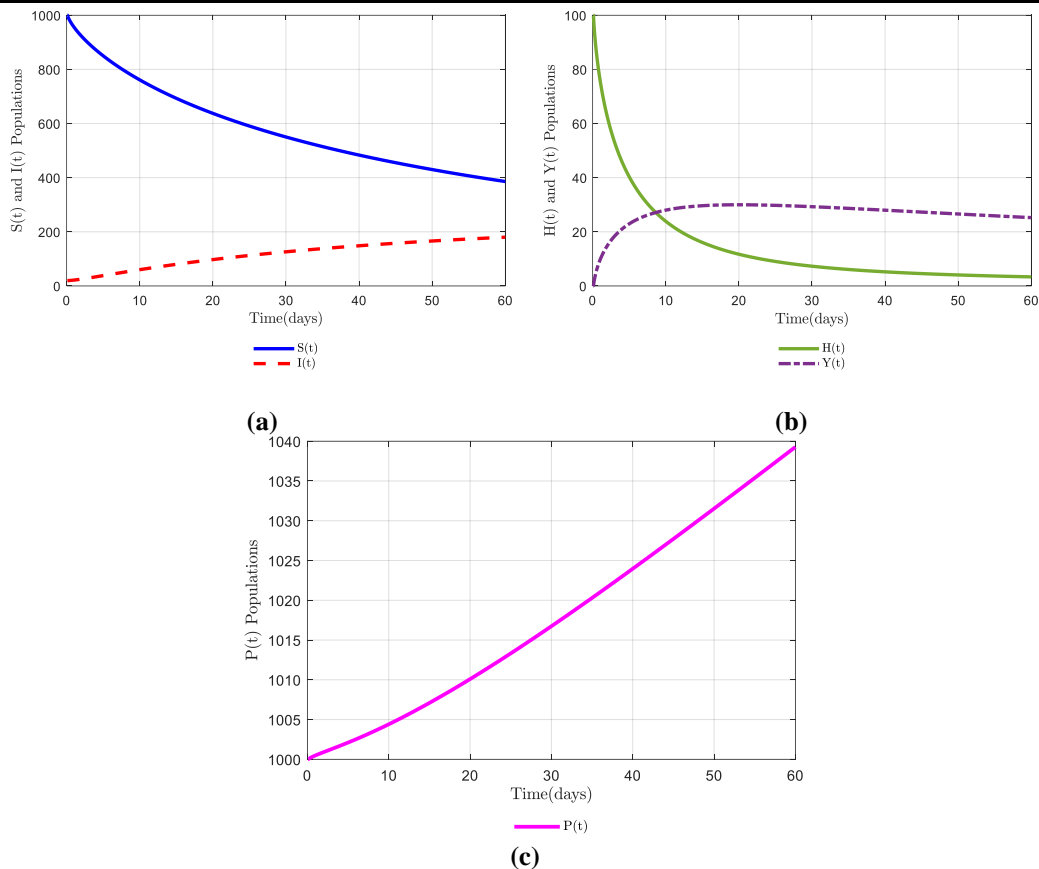


Figure 1. Visualization of Susceptible Maize $S(t)$, Infected Maize $I(t)$, Susceptible Leafhopper $H(t)$, Infected Leafhopper $Y(t)$, and MSV Pathogen $P(t)$ under the fractal and fractional operator.

4. CONCLUSION

In this paper, the fractal fractional derivative operator which is a new concept in the literature has been applied to a plant disease model. For this purpose, a Maize Streak Virus (MSV) model is handled by taking into account the vector-borne and MSV pathogen. We interpreted the dynamic system handled by applying fractal fractional derivative in terms of memory effect and fractal size.

ACKNOWLEDGMENTS:

This study is supported by Balikesir University Research Grant No. BAP 2021/121.

REFERENCES

[1] W. Huang, P. Reyes-Caldas, M. Mann, S. Seifbarghi, A. Kahn, R.P. Almeida, L. Beven, M. Heck, S.E. Hogenhout & G. Coaker, Bacterial vector-borne plant diseases: unanswered questions and future directions, *Molecular Plant* 13(10) (2020) 1379-1393. DOI:10.1016/j.molp.2020.08.010

[2] N.A. Bosque-Pérez, Eight decades of maize streak virus research, *Virus Research* 71(1-2) (2000) 107-121. DOI:10.1016/S0168-1702(00)00192-1

[3] H.T. Alemneh, O.D. Makinde, & D. Mwangi Theuri, Ecoepidemiological model and analysis of MSV disease transmission dynamics in maize plant, *International Journal of Mathematics and Mathematical Sciences* Article ID 7965232 (2019). DOI:10.1155/2019/7965232

-
- [4] H.T. Alemneh, O.D. Makinde, & D.M. Theuri, Mathematical modelling of msv pathogen interaction with pest invasion on maize plant, *Global Journal of Pure and Applied Mathematics* 15(1) (2019) 55-79.
- [5] H. Joshi, B.K. Jha, Chaos of calcium diffusion in Parkinson's infectious disease model and treatment mechanism via Hilfer fractional derivative, *Mathematical Modelling and Numerical Simulation with Applications* 1(2) (2021), 84-94. DOI: 10.53391/mmnsa.2021.01.008.
- [6] P.A. Naik, Z. Eskandari, M. Yavuz, J. Zu, Complex dynamics of a discrete-time Bazykin–Berezovskaya prey-predator model with a strong Allee effect, *Journal of Computational and Applied Mathematics* 413 (2022). DOI: 10.1016/j.cam.2022.114401.
- [7] N. Özdemir, E. Uçar, Investigating of an immune system-cancer mathematical model with Mittag-Leffler kernel, *AIMS Mathematics* 5(2) (2020) 1519-1531. DOI:10.3934/math.2020104
- [8] A. Atangana, Fractal-fractional differentiation and integration: connecting fractal calculus and fractional calculus to predict complex system, *Chaos, Solitons Fractals* 102 (2017) 396–406. DOI:10.1016/j.chaos.2017.04.027
- [9] A. Atangana, S. Qureshi, Modeling attractors of chaotic dynamical systems with fractal fractional operators, *Chaos Solitons Fractals* 123 (2019), 320–337. DOI:10.1016/j.chaos.2019.04.020
- [10] S. Uçar, Analysis of hepatitis B disease with fractal–fractional Caputo derivative using real data from Turkey, *Journal of Computational and Applied Mathematics* 419 (2023) 114692. DOI:10.1016/j.cam.2022.114692

Radiation attenuation coefficients of stainless steels containing different proportions of boron carbide

Kadir GÜNOĞLU¹, Hatice VAROL ÖZKAVAK^{1*}, İskender AKKURT²

¹ Isparta Applied Science University, Technical Sciences Vocational School, Isparta TURKEY

² Suleyman Demirel University, Science Faculty, Physics Department, Isparta-TURKEY

*haticevarol@isparta.edu.tr

ABSTRACT

The linear attenuation coefficients (μ , cm^{-1}) for AISI 316 stainless steel having boron carbide (B_4C) in different concentrations have been investigated. The boron carbide (B_4C) concentrations investigated in the work were 0%, 10%, and 20% in AISI 316 stainless steel. The measurements were made using a gamma spectrometer that contains a NaI(Tl) detector and Multi-Channel-Analyser (MCA) connected to a PC. Three different gamma rays energies have been used at 511 and 1275 keV which are obtained from ^{22}Na radioactive source.

KEYWORDS: AISI 316 stainless steel, boron carbide (B_4C), Linear attenuation coefficient, Gamma spectroscopy

1. INTRODUCTION

Stainless steels, known as materials that do not stain or corrode, are defined as steels that contain at least 10% chromium by combining various metals in different proportions. AISI 316 steel, which is classified as austenitic stainless steel, is used in areas and applications such as engine parts of many vehicles that require corrosion-resistant materials, pharmaceutical production areas, equipment using chemical materials, machines used in purification processes and devices used for medical applications [1-3]. AISI 316 austenitic stainless steels consist 16.5-18.5% Chromium (^{24}Cr), 10-13% Nickel (^{28}Ni), 2-3% Molybdenum (^{42}Mo), 2% Manganese (^{25}Mn), 1% Silicon (^{14}Si) and small amounts of Carbon (^{6}C), Phosphorus (^{15}P), Sulfur (^{16}S). The remaining part of these elements in AISI 316 stainless steel is iron. Many researchers have conducted studies to investigate the physical and mechanical properties of stainless steel [4-6].

Boron carbide is a non-oxide ceramic material that has a special place in the important hard nonmetal group such as SiC, Si_3N_4 , diamond, alumina [7]. Boron carbide has good mechanical properties, high melting temperature, high hardness, low density, high radiation absorption. In addition, it is highly resistant to chemical substances. Boron carbide comes after diamond and cubic boron nitride in the hardest materials ranking. The main areas of use of boron carbide include spray nozzles, mold materials used in wire drawing, absorbent materials in nuclear reactors [8]. In addition, due to some superior properties such as low density, high elastic modulus and hardness, boron carbide-based ceramic-metal composites used in armor material have become the focus of attention of researchers [9-12].

With technological developments, today radiation has a wide range of uses such as industrial applications, scientific studies, agricultural activities, medicine (radiotherapy applications and imaging). Ionizing radiation used in these areas directly (radioactive sources, natural radioactivity, etc.) or indirectly (leakage, scatter, etc.) exposure affects the health of living things and the environment. For this reason, the issue of radiation protection has gained great importance in terms of health. Time, distance and shielding are the three basic principles of radiation protection. The principle of shielding is the use of barrier material between the radiation source and the system to be protected in order to attenuate or hold different types of radiation (X-ray, gamma ray, particle, etc.). The best known traditional material in terms of radiation shield is lead (Pb). Lead is not used much because of its disadvantages such as poor mechanical properties, high cost, Pb toxicity for humans and the environment. For this reason, the production of new types of materials for radiation protection is increasing. In the literature, many physicists and materials scientists have produced

many different types of materials as radiation shielding materials and examined the radiation shielding properties of these materials [13-21].

This study aims to investigate the variation of linear attenuation coefficient for gamma rays with different energies by adding different ratios of boron carbide to AISI 316 stainless steel, experimentally using gamma spectroscopy system and theoretically using WinXCom software [22].

2. MATERIAL AND METHOD

2.1. Production Of Steel Samples

Cylindrical specimens with a diameter of 35 mm and a thickness of 5 mm were prepared by Powder Metallurgy method to be used in experimental studies. AISI 316 Austenitic Stainless Steel powder has been chosen as the matrix material. In order to prepare samples with different compositions, different proportions of boron carbide powder were added to the stainless steel powder. Powder compositions by weight of the prepared samples are given in Table 1.

Table 1. Powder Composition of Test Sample Groups

Sample Group Number	AISI 316 Stainless Steel Powder (% weight)	Boron carbide Powder (%weight)
1	100	0
2	90	10
3	80	20

In the present work commercially available AISI 316 ASS powders were produced by gas atomization method. The powders have a size range of 80-100 μm and a spherical shape. Boron carbide was added to the ASS powder in the proportions given in Table 1 and mixed in a double-sided conical mixer for 10 minutes. The homogeneously obtained powder mixture was carried appropriately and the cold pressing stage was initiated. The mixed powder; cold compressed in a double acting press using lubricated mold with an inner diameter of 35 mm. The green density value after cold compression was determined as $93 \pm 0.5\%$. Demoulded samples has been used as it is.

2.2. Experimental gamma ray attenuation measurements

LACs of AISI 316 stainless steel samples produced by adding boron carbide at different rates were measured to determine their gamma ray shielding properties using a low level gamma counting spectroscopy system containing a NaI (TI) detector. Gamma spectroscopy system consists of electronic parts such as High Voltage (HV), Amplifier, Multi-Channel Analyzer (MCA). The experiments were performed at 662, 1173 and 1332 keV gamma rays which were obtained from ^{137}Cs and ^{60}Co radioactive sources [23,24].

As a result of the interaction of gamma rays with matter, some of the rays are absorbed, some of them are transmitted directly without interaction and some of them are scattered in different directions. The realization of these interactions depends on the properties of the shield material, the incoming gamma energy and the measurement geometry. In order for the results of the experimental measurements to be accurate, an ideal experimental geometry called narrow beam geometry was created. The electronic components and geometry of the gamma counting spectroscopy system used in this study are shown in Figure 1. The multi-channel analyzer in the system creates spectra with digital signal processing techniques and the areas of these obtained spectra are calculated using MAESTRO-32 software.

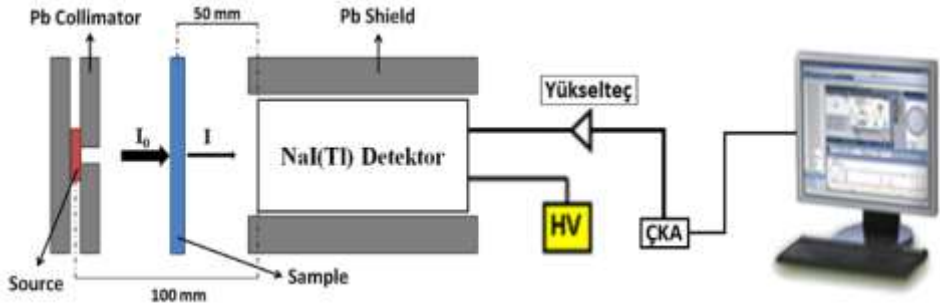


Figure 1. The electronic components and geometry of the gamma counting spectroscopy system

LACs μ (cm^{-1}) is obtained by the following equation [25]:

$$\mu = \frac{1}{x} \ln \frac{N_0}{N} \tag{1}$$

where x is the thickness of the absorbent material, and N and N_0 are the counts obtained with and without absorber material between the radioactive gamma source and the detector, respectively. The mass attenuation coefficient (MAS) was calculated with the help of the WinXCom software [22], which uses the chemical content of the absorbent material as input. The linear attenuation coefficient was calculated by multiplying the calculated MAS (μ / ρ) with the density of the absorbent material.

3. RESULTS AND DISCUSSIONS

As stated in the experimental gamma ray attenuation measurement section, the gamma spectroscopy system was used to measure the LACs of the steel samples produced by doping different amounts of boron carbide. LACs values were measured for gamma energies of 511 and 1275 keV emitted from ^{22}Na radioactive source. The results obtained are shown in Figure 2. As seen in Figure 2, the linear attenuation coefficient of the steel decreases against increasing gamma ray energy. Similar to this result, it was observed that the LACs values decreased as the boron carbide ratio in the steel increased.

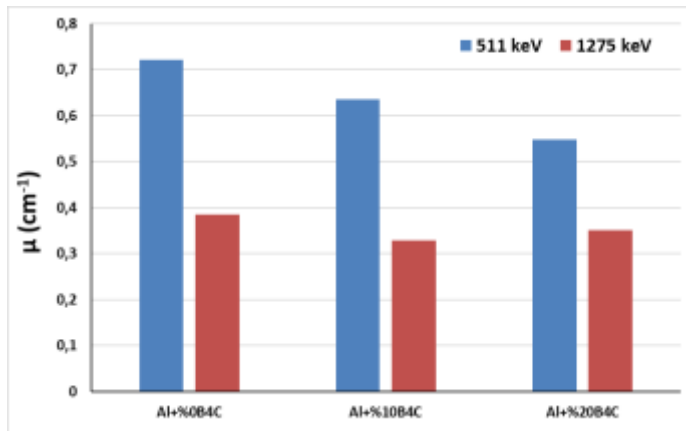


Figure 2. Measured LAC values

Within the scope of the study, LACs for gamma energies ranging from 1 keV to 100 GeV were calculated with the WinXCom software by using the chemical contents of steels produced by doping different amounts of B₄C. The results of LACs calculated and experimentally measured with the WinXCom software are shown in Figure 3. When these results are compared in Figure 3, it is seen that there is agreement between the LACs values.

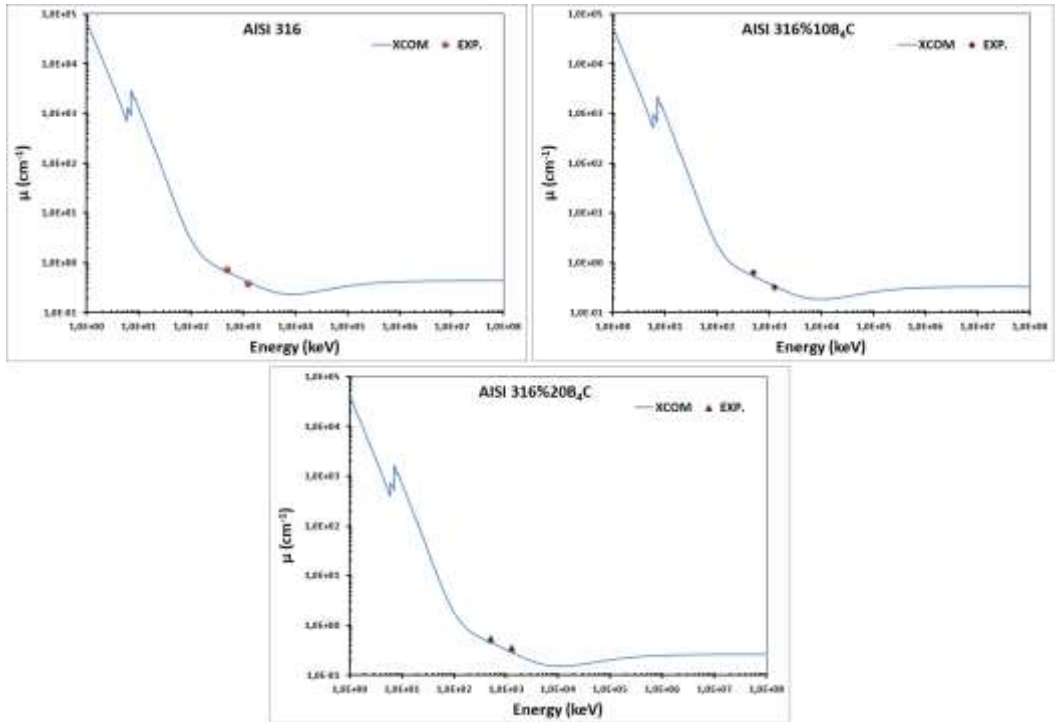


Figure 3. Comparison of calculated and measured LAC values

REFERENCE

- [1] Toro, W. Misiolek, A.P. Tschiptschin, Correlations between microstructure and surface properties in a high nitrogen martensitic stainless steel. *Acta Mater.* 51 (2003) 3363–3374.
- [2] T. Bell, C.X. Li, Stainless steel low temperature nitriding and carburizing, *Adv. Mater. Process.* 160 (2002) 49–51.
- [3] P. Srisattayakul, C. Saikaew, A. Wisitsoraat, D. Phokharatkul, Reciprocating two-body abrasive wear behavior of DC magnetron sputtered Mo-based coatings on hard-chrome plated AISI 316 stainless steel, *Wear* 378-379 (2017) 96–105
- [4] C.X. Li, T. Bell, sliding wear properties of active screen plasma nitrided 316 austenitic stainless steel, *Wear* 256 (2004) 1144–1152.
- [5] F. Borgioli, E. Galvanetto, G. Pradelli, Glow-discharge nitriding of AISI 316L austenitic stainless steel: influence of treatment temperature, *Surf. Coat. Technol.* 200 (2005) 2474–2480.
- [6] Q.S. Jun, Microstructure and wear resistance of 35MnVN, 40MnVTi microalloyed engineering steels after warm forging, *Heat Treat. Met.* 31 (2006) 40–43.
- [7] Alp, E., Karacay, E., Cabbar, H.C., “Low Temperature Production of Boron Carbide And Its Characterization”, *Journal Of The Faculty Of Engineering And Architecture Of Gazi University*, 28(2), 293-302, 2013.

- [8] Arslan, D., Gürü, M., Mekanokimyasal Yöntemle Bor Karbür Sentezi Ve Alüminyum Matrisli Kompozit Malzemede Kullanılabilirliğinin İncelenmesi. Journal of the Faculty of Engineering and Architecture of Gazi University, Vol 28, No 4, 875-883, 2013
- [9] R. Pandiyarajan, S. Marimuthu, Dry Sliding Wear Behaviour of aluminium Matrix Composite Materials, Test Eng. Manag. 83 (2020) 15086–15089.
- [10] I. Mehmet, N. Amin, A. Sabri, Mechanical characterization of B4C reinforced aluminum matrix composites produced by squeeze casting, J. Mater. Res. 32 (3) (2017) 599–605.
- [11] P. Moslem, O. Olatunji, R. Hamid, H. Akbar, Influence of multi-pass FSP on the microstructure, mechanical properties and tribological characterization of Al/B4C composite fabricated by accumulative roll bonding (ARB), Surf. Coat. Technol. 361 (2019) 159–169.
- [12] B. Subramaniam, B. Natarajan, B. Kaliyaperumal, Investigation on mechanical properties of aluminium 7075 - boron carbide - coconut shell fly ash reinforced hybrid metal matrix composites, China Foundry 15 (2018) 449–456.
- [13] Akkurt, I., 2009. Effective atomic and electron numbers of some steels at different energies. Ann. Nucl. Energy 36, 1702–1705.
- [14] Akkurt, I., Calik, A., Akyildirim, H., 2011. The boronizing effect on the radiation shielding and magnetization properties of AISI 316L austenitic stainless steel. Nucl. Eng. Des. 241, 55–58.
- [15] Akkurt, I., Akyildirim, H., Mavi, B., Kilincarslan, S., Basyigit, C., 2010. Gamma-ray shielding properties of concrete including barite at different energies. Prog. Nucl. Energy 52 (7), 620–623.
- [16] Akkurt, I., Altindag, R., Gunoglu, K., Sarikaya, H., 2012. Photon attenuation coefficients of concrete including marble aggregates. Ann. Nucl. Energy 43, 56–60.
- [17] Akman, F., Kaçal, M.R., Sayyed, M.I., Karataş, H.A., 2019. Study of gamma radiation attenuation properties of some selected ternary alloys. J. Alloy. Comp. 782, 315–322.
- [18] Srinivasan, K., James, E., Samuel, J., 2017. Evaluation of radiation shielding properties of the polyvinyl alcohol/iron oxide polymer composite. J. Med. Phys. 42, 273–278.
- [19] R. Kurtulus, T. Kavas, I. Akkurt, and K. Gunoglu, “An experimental study and WinXCom calculations on X-ray photon characteristics of Bi2O3- and Sb2O3- added waste soda-lime-silica glass,” Ceram. Int., no. April, pp. 1–8, 2020
- [20] Büyükyıldız, M., 2017. Estimation of radiological properties of common ion implantation materials for different heavy ions. Radiat. Eff. Defect Solid 172, 531–543.
- [21] Demir, D., Keleş, G., 2006. Radiation transmission of concrete including boron waste for 59.54 and 80.99 keV gamma rays. Nucl. Instrum. Methods B 245, 501–504.
- [22] M. Berger, J. Hubbell, “XCOM: photon cross sections on a personal computer,” Natl. Bur. Stand. Washington, DC (USA), Cent. Radiat. Res. (1987) 1–28,
- [23] Akkurt, I., Akyıldırım, H., Mavi, B., Kilincarslan, S., Basyigit, C., 2010. Radiation shielding of concrete containing zeolite. Radiat. Meas. 45 (7), 827–830.
- [24] I. Akkurt, K. Gunoglu, S.S. Arda, Detection efficiency of NaI(Tl) detector in 511-1332 keV energy range, Sci. Technol. Nucl. Install. (1) (2014) 6–11,
- [25] Bashter, I.I., 1997. Calculation of radiation attenuation coefficients for shielding concretes. Ann. Nucl. Energy 24, 1389.

Gamma Strength Functions for Some Medical Radioisotopes

Nurdan KARPUZ✉

Amasya University, Sabuncuoğlu Şerefeddin Vocational School of Health Services, Amasya-TURKEY
nurdankarpuz@amasya.edu.tr

ABSTRACT

Energy and reaction cross section values are required in theoretical calculations. The reaction-induced cross section value, which can be described as the possibility of a reaction occurring, can be obtained by theoretical calculations, while the result can be affected by many parameters. In the calculation of the reaction cross-section, the gamma strength function is an important input as well as the nuclear level density. In addition to the very important role of radioisotopes in the field of nuclear medicine, especially in imaging and therapeutic applications; radioisotopes also occupy a large place in diagnostics in radiotherapy and nuclear medicine. In this study, it was intended to investigate the effects of gamma-ray strength functions on different gamma-ray strength functions and cross-section calculations. The cross section calculation simulations were performed with the version 1.95 of the TALYS Monte Carlo code. The data obtained were analysed graphically against available experimental data from the EXFOR library.

KEYWORDS: *Gamma strength functions, TALYS, EXFOR*

1. INTRODUCTION

Nuclear reactions, which are very important from the point of view of human health, may occur during the production of the radiation sources, used in radiotherapy. The nuclear reaction data are needed in the radioisotope production procedure. The total cross section is also important in accelerator technology, in view of radiation protection and safety (Noori et al., 2017).

The cross section is an important quantity in studying the nuclear reaction, where it helps to calculate the probability of nuclear reaction, therefore, it became the main concern since the beginning of nuclear reaction studies (Abdullah et al. 2020). The cross section is a mathematical version of describing the probability of a nuclear reaction occurring. Physically, the possibility of a reaction is described in an amount called a nuclear cross section. The cross-sectional value of a reaction can be expressed as the value that clearly indicates the probability of that reaction occurring.

The use of systematics for nuclear reaction cross section evaluation is important, if experimental data are absent or results of nuclear model calculation are not reliable. Systematics of cross sections has a special importance as an additional tool for the cross section evaluation (Tel et al. 2016). Studies of excitation functions of nuclear reactions are of considerable importance for testing nuclear models as well as for practical applications (Sudar et al. 2006).

It is essential to nuclear industry such as medical isotope production and radiation applications (Kavun and Makwana, 2020). Radioisotopes play very important roles in nuclear medicine for imaging and therapeutic applications.

Gamma strength function describes the (average) energy distribution of photon emission from highlyexcited states or cross section of photon absorption (principle of detailed balance) (Martin, 2012).

Nuclear reaction codes for the degradation of the compound nucleus are an advantage way to guess and evaluate yield for dissimilar reactions. Based on this; there are experimental (Vagena and Stoulos 2017), (Ghergherehchi et al. 2012), (Hu et al. 2022), (Sziki et al. 2006), (Usman et al. 2016), (Usman et al. 2017), (Usman et al. 2016), (Usman et al. 2020) and theoretical (Kaplan et al. 2014), (Aydın et al. 2015), (Kaplan et al. 2015), (Özdoğan et al. 2018), (Artun 2018), (Artun 2019), (Sarpün et al. 2019), (Canbula et al. 2014), (Canbula 2020), (Noori et al. 2019), (Noori et al. 2017), (Karpuz Demir 2017), (Noori et al. 2016), (Karpuz 2016), (Noori et al. 2018), (Kavun and Makwana 2021),

(Kavun et al. 2020), (Kavun and Makwana 2020) nuclear reaction section studies in the literature that conducted in the light of this direction.

In this study, (γ , n) reaction have been investigated and gama strength functions. Calculations were performed with version 1.95 of the TALYS nuclear code (Koning et al. 2019). The calculation results obtained and the experimental data of the reaction obtained from the experimental database were compared.

2. MATERIAL AND METHOD

Nuclear reaction calculations require complete (Koning et al. 2008). Gamma strength function describes the (average) energy distribution of photon emission from highlyexcited states or cross section of photon absorption (principle of detailed balance). There are five models (Kopecky-Uhl generalized Lorentzian, Brink-Axel Lorentzian, Hartree-Fock BCS tables, Hartree-Fock-Bogolyubov tables, Goriely's hybrid model) for E1 gamma-ray strength function in TALYS. Calculations of theoretical cross section are based on these gamma-ray strength function models. Current study was performed for energy range of the giant dipole resonance region (GDR) (Karpuz Demir et al. 2017).

TALYS Computer Programme

TALYS, is one of the widely used computer programs for the cross-section computations of nuclear reactions. It is a program that can simulate nuclear reactions involving protons, neutrons, deuterones, tritons, alpha particles, and gamma rays in the energy range of 1 keV to 1 GeV. TALYS is preferred in both basic and applied sciences. It is written in Fortran 77 programming language. Over time, continuous updates were made to eliminate the deficiencies seen on TALYS. In this study, dissimilar nuclear level intensity models were calculated using the latest version of TALYS.

3. RESULTS AND DISCUSSIONS

In this study, the impact section values of ^{12}C that is important with its different practices in science and technology, and the production impact section calculations of ^{11}C was calculated with TALYS 1.95 computer program (Koning et al. 2019) using gamma strength functions. Comparison of all theoretical calculated results obtained from the models with both each other and with the experimental data, valid in the EXFOR (Int Kyn. 1) database in literature. Figures 1 represent calculated cross section effects with the all of level density models and gamma strength function models for ^{12}C all the known medical materials respectively.

My main aim is here to demonstrate the predictive power of different models calculations and this comparison may be considered as starting point for the future improvements in the theoretical models. The computation cross section results with gamma strength functions, (Kopecky-Uhl generalized Lorentzian, Brink-Axel Lorentzian, Hartree-Fock BCS tables, Hartree-Fock-Bogolyubov tables, Goriely's hybrid model), for the radionuclide of ^{11}C is indicated in Fig. 1. These calculated results are checked against with the experimental results in the literature (Cohen et al. 1959), (Del Bianco et al. 1962), (Lochstet et al. 1966). For this reaction, value of maximum calculated cross section is 22 MeV. The experimental cross section results are convenient to the conclusion of Brink-Axel Lorentzian model in the area between 20 MeV and 28 MeV.

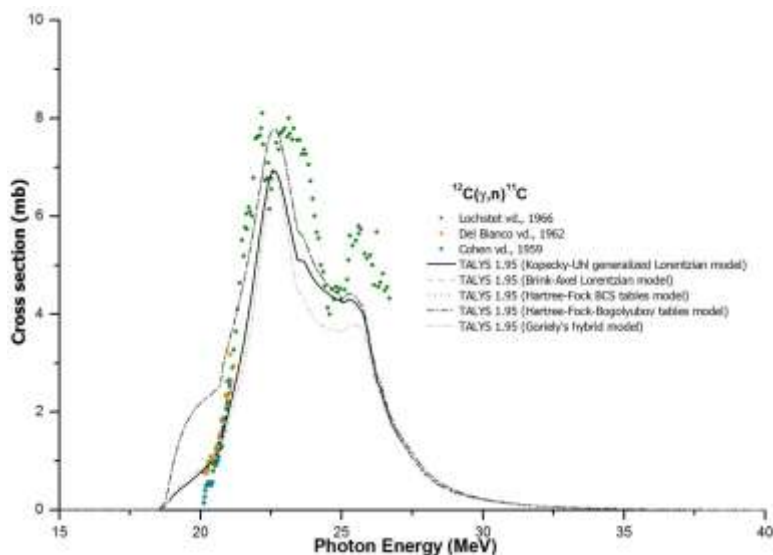


Fig. 1. Calculated cross section for $^{12}\text{C}(\gamma,n)^{11}\text{C}$ reaction with gamma strength function models

4. CONCLUSIONS

In this article where I examined the effect of gamma strength function models on ^{12}C radionuclides. According to the calculated theoretical results, Brink-Axel Lorentzian model is the most coherent model with the experimental data. The theoretical cross sections of reactions, obtained using the TALYS 1.95 models, clearly demonstrate the GDR effect. And however, all level density models give close cross section results with the each other.

The data I have calculated cross sections that occur in the process of performing a reaction on the basis of nuclear reactions; will be able to benefit studies aimed at developing materials to be used in different application areas, providing preliminary information to experimental and theoretical studies on nuclear reactions and creating a theoretical database.

REFERENCES

- Abdullah, A. M., Salloum, A. D., 2020. A comparison between the theoretical cross section based on the partial level density formulae calculated by the exciton model with the experimental data for ^{197}Au nucleus. *Baghdad Science Journal*, 18, 1, 1, 139-143. doi.org/10.21123/Bsj.2021.18.1.0139.
- Artun, O., 2018. Calculation of productions of PET radioisotopes via phenomenological level density models. *Radiation Physics and Chemistry*, 149, 73-83. doi.org/10.1016/j.radphyschem.2018.03.018.
- Artun, O., 2019. Calculation of productions of medical ^{201}Pb , ^{198}Au , ^{186}Re , ^{111}Ag , ^{103}Pd , ^{90}Y , ^{89}Sr , ^{77}Kr , ^{77}As , ^{67}Cu , ^{64}Cu , ^{47}Sc and ^{32}P nuclei used in cancer therapy via phenomenological and microscopic level density models. *Applied Radiation and Isotopes*, 144, 64-79. doi.org/10.1016/j.apradiso.2018.11.011.
- Aydın, A., Pekdoğan, H., Kaplan, A., Sarpün, İ. H., Tel, E., Demir, B., 2015. Comparison of level density models for the $^{60,61,62,64}\text{Ni}$ (p, n) reactions of structural fusion material nickel from threshold to 30 MeV. *Journal of Fusion Energy*, 34(5), 1105-1108. doi: 10.1007/s10894-015-9927-2.

- Canbula, B., Bulur, R., Canbula, D., Babacan, H., 2014. A Laplace like formula for the energy dependence of the nuclear level density parameter. Nuclear Physics A, 929, 54-70. doi.org/10.1016/j.nuclphysa.2014.05.020.
- Canbula, B., 2020. 55Mn izotopunun fotonükleer tesir kesitleri üzerinde kollektif nükleer seviye yoğunluğunun etkisi. Süleyman Demirel Üniversitesi Fen Bilimleri Enstitüsü Dergisi, 24, 138-142. doi: 10.19113/sdufenbed.639828.
- Ghergherehchi, M., Afarideh, H., Kim, Y.S., Park, S.Y., Lee, S.B., Shin, D.H., Chai, J.S., Mu, X.J., Lee, B.N., 2012. Dosimetry and microdosimetry of 10-220 MeV proton beams with CR-39 and their verifications by calculation of reaction cross sections using ALICE, TALYS and GEANT4 codes. Radiation Measurements, 47, 6, 410-416. doi.org/10.1016/j.radmeas.2012.03.008.
- Hu, H., Guo, W-L., Su, J., Wang, W., Yuan, C., 2022. Implementation of residual nucleus de-excitations associated with proton decays in ^{12}C based on the GENIE generator and TALYS code. Physics Letters B, 831, 137183. doi.org/10.1016/j.physletb.2022.137183.
- Kaplan, A., Özdoğan, H., Aydın, A., Tel, E. 2014. Photo-neutron cross-section calculations of $^{142,143,144,145,146,150}\text{Nd}$ rare-earth isotopes for (γ, n) reaction. Physics of Atomic Nuclei, 77(11), 1371-1377. doi:10.1134/S1063778814100081.
- Kaplan, A., Sarpün, İ. H., Aydın, A., Tel, E., Çapalı, V., Özdoğan, H., 2015. $(\gamma, 2n)$ -Reaction cross-section calculations of several even-even lanthanide nuclei using different level density models. Physics of Atomic Nuclei, 78(1), 53-64. doi: 10.1134/S106377881501010X.
- Karpuz, N., 2016. Effect of the Level Density Parameter Ratio on the Cross Sections of Fission of Uranium Isotopes. Acta Physica Polonica A, 130, 1, 306-308. doi: 10.12693/APhysPolA.130.306.
- Karpuz Demir, N., 2017. Detailed Analysis of Differential Cross Sections of Elastic Scattering for $n+^{208}\text{Pb}$ Reaction. Acta Physica Polonica A, 132, 3-II, 1189-1191. doi: 10.12693/APhysPolA.132.1189.
- Kavun, Y., Makwana R., 2020. Study of (γ, p) reaction cross-section calculations of ^{52}Cr , ^{54}Fe , ^{60}Ni and ^{64}Zn isotopes. Nuclear Inst. and Methods in Physics Research B, 472, 72-77. doi:10.1016/j.nimb.2020.03.036.
- Kavun, Y., Makwana R., 2021. Effects of some level density models and γ -ray strength functions on production cross-section calculations of $^{16,18}\text{O}$ and $^{24,26}\text{Mg}$ radioisotopes. Journal Kerntechnik, 86(6), 411-418. doi:10.1515/kern-2021-1018.
- Kavun, Y., Parashari S., Tel E., 2020. Investigation of (γ, p) reaction cross-section calculations of ^{40}Ca , ^{70}Ge and ^{90}Zr isotopes. Applied Radiation and Isotopes, 164. doi:10.1016/j.apradiso.2020.109318.
- Koning, A. J., Hilaire, S., Goriely, S., 2008. Global and local level density models, Nuclear Physics A 810, 13-76. doi:10.1016/j.nuclphysa.2008.06.005.
- Koning, A.J., Hilaire, S., and Goriely, S., 2019. TALYS 1.95 Nuclear Research and Consultancy Group (NRG), The Netherlands.
- Martin, D., 2012. Do we understand gamma strength functions? The case of ^{96}Mo , Institut für Kernphysik Technische Universität Darmstadt. Available on: inis.iaea.org/search/search.aspx, ref. No. 45081928.
- Noori, S. S., Karpuz, N., Akkurt, İ., 2016. Excitation Functions of (d, n) Reactions on Some Light Nuclei. Acta Physica Polonica A, 129, 1, 484-486. doi: 10.12693/APhysPolA.130.484.
- Noori, S. S., Akkurt, İ., Karpuz Demir, N., 2017. Comparison of Excitation Functions of Longer and Shorter Lived Radionuclides. Acta Physica Polonica A, 132, 3-II, 1186-1188. doi: 10.12693/APhysPolA.132.1186.
- Noori, S. S., Akkurt, İ., Karpuz Demir, N., 2018. Excitation functions of proton induced reactions of some radioisotopes used in medicine. Open Chemistry, 16, 810-816. doi: 10.1515/chem-2018-0085.

- Noori, S. S., Akkurt, İ., Karpuz Demir, N., 2019. Excitation Functions for the Proton Irradiation on ^{45}Sc Target. *International Journal of Computational and Experimental Science and Engineering*, 5, 2, 61-64. doi: 10.22399/ijcesen.547000.
- Özdoğan, H., Şekerçi, M., Sarpün, İ. H., Kaplan, A., 2018. Investigation of level density parameter effects on (p,n) and (p,2n) reaction cross-sections for the fusion structural materials ^{48}Ti , ^{63}Cu and ^{90}Zr . *Applied Radiation and Isotopes*, 140, 29-34. doi.org/10.1016/j.apradiso.2018.06.013.
- Sarpün, İ. H., Özdoğan, H., Taşdöven, K., Yalim, H. A., Kaplan, A., 2019. Theoretical photoneutron crosssection calculations on Osmium isotopes by Talys and Empire codes. *Modern Physics Letters A*, 34(26),1950210. doi.org/10.1142/S0217732319502109.
- Sudar, S., and Qaim, S. M., 2006. Cross sections for the formation of ^{195}Hg , ^{197}Hg , ^{196}Au , ^{197}Au , and ^{196}Au , ^{197}Au in α and ^3He -particle induced reactions on Pt: effect of level density parameters on the calculated isomeric cross-section ratio. *Physical Review C*, 73(3), 034613. doi.org/10.1103/PhysRevC.73.034613.
- Sziki, G.A., Simon, A., Szikszai, Z., Kertész, Zs., Dobos, E., 2006. Gamma ray production cross-sections of deuteron induced nuclear reactions for light element analysis. *Nuclear Instruments and Methods in Physics Research B*, 251, 2, 343–351. doi.org/10.1016/j.nimb.2006.07.008.
- Tel, E., Akça, S., Sahan, M., Depedelen, M., Sarpün, İ.H., 2016. The comparison of (n,p), (n, α), (n,2n) and (α ,n) reaction cross sections for ^7Li and ^9Be target nuclei, *Journal of Fusion Energy*, 35(4):709-714, doi.org/10.1007/S10894-016-0094-X.
- Usman, A. R., Khandaker, M. U., Haba, H., Otuka, N., Murakami, M., 2020. Production cross sections of thulium radioisotopes for alpha-particle induced reactions on holmium. *Nuclear Inst. and Methods in Physics Research B*, 469, 42-48. doi.org/10.1016/j.nimb.2020.02.036.
- Usman, A. R., Khandaker, M. U., Haba, H., Otuka, N., Murakami, M., Komori, Y., 2016. Production cross-sections of radionuclides from α -induced reactions on natural copper up to 50 MeV. *Applied Radiation and Isotopes*, 114, 104-113. doi.org/10.1016/j.apradiso.2016.04.027.
- Usman, A. R., Khandaker, M. U., Haba, H., Otuka, N., Murakami, M., 2017. Excitation functions of alpha particles induced nuclear reactions on natural titanium in the energy range of 10.4-50.2 MeV. *Nuclear Instruments and Methods in Physics Research B*, 399, 34-47. doi.org/10.1016/j.nimb.2017.03.120.
- Usman, A. R., Khandaker, M. U., Haba, H., Murakami, M., Otuka, N., 2016. Measurements of deuteron-induced reaction cross-sections on natural nickel up to 24 MeV. *Nuclear Instruments and Methods in Physics Research B*, 368, 112-119. doi.org/10.1016/j.nimb.2015.10.077.
- Vagena, E., ve Stoulos, S., 2017. Average cross section measurement for ^{162}Er (γ ,n) reaction compared with theoretical calculations using TALYS. *Nuclear Physics A*, 957, 259-273. doi.org/10.1016/j.nuclphysa.2016.09.007.

Internet references

1-<http://www.nds.iaea.org/exfor/> (01.09.2022)

Use of ESR Spectroscopy on Identification of the Radiation-Induced Radicals in Gamma Irradiated Bone

Özgül KARATAŞ*

Konya Technical University/Electricity and Energy Department - Nuclear Technology and Radiation Safety Program, Konya, TURKEY

*okaratas@ktun.edu.tr

ABSTRACT

It is well established that electron spin resonance (ESR) is a useful spectroscopic method to identify the paramagnetic radical species resulting from the degradation in some cases, such as irradiation. The bone is a uniform material which consists of almost 50% hydroxyapatite mineral in the inorganic constituent. This mineral is sensitive to radiation effects and produces a signal which can be analysed by ESR method. In this case, the ESR deals with the accumulation of radiation-induced radicals in the defects of this mineral crystalline lattice.

Herein, the radical concentrations and radiation centers formed in the bone structure after gamma irradiation was studied using the ESR spectroscopy. For this purpose, selected fossil animal bone (sheep) sample was subjected to combination of cleaning and grinding in the laboratory. The obtained sample was irradiated with 10Gy, 50Gy, 1000Gy and 2000Gy radiation doses by ^{60}Co - γ source, respectively and then the ESR measurements were performed using X-band ESR spectrometer at 300K, separately. This sample was also analysed for mineralogical composition and elemental concentration using X-ray diffraction (XRD) and scanning electron microscopy coupled with energy-dispersive X-ray measurements (SEM-EDX), respectively. As a conclusion, the XRD and the SEM-EDX results showed that this sample had a poorly hydroxyapatite which is microcrystalline hexagonal mineral. From the ESR measurements, it was observed that the signal amplitudes and shapes were changed as a function of applied radiation doses. Also, the stable carbonate-containing paramagnetic radical was determined only high irradiation doses.

KEYWORDS - Bone, ESR, XRD, SEM-EDX, Irradiation, Paramagnetic radical

1. INTRODUCTION

Bone is one of the hardest tissues in the body [1, 2]. It occurs an organic component composed of collagen predominantly and an inorganic component containing hydroxyapatite crystals [3, 4]. This inorganic structure, which includes high amounts of calcium and phosphate, constitutes approximately 50% of the bone. In addition to calcium and phosphate, this structure also contains magnesium, bicarbonate, sodium, hydroxyl, potassium, chlorine, citrate and fluorine [1].

The inorganic component is capable of forming stable paramagnetic species, induced by irradiation in the bone. So, the most reliable method to choice for investigation the paramagnetic centers in this structure is electron spin resonance (ESR) spectroscopy. The ESR spectroscopy is a very suitable method for investigation of biological materials exposed to ionizing radiation due to its accuracy, reproducible, sensitivity, non-destructive, low cost and fast measuring procedure [5-7]. Especially teeth and bone materials, where stable paramagnetic species can be produced easily by irradiation, can be used as ESR dosimeters for radiation research and radiation technologies [8-10].

In this paper, the chemical and structural changes of fossil bone sample were checked by experimental methods (XRD and SEM-EDX), firstly, and then X-band ESR measurements of gamma irradiated fossil bone sample were investigated in order to identify paramagnetic centres the contributing to ESR signals at room temperature.

2. MATERIAL AND METHODS

2.1 Sample Preparation

In this study, a fossil animal bone (sheep) was used for investigation. This sample was stored in a light-tight box in the laboratory. It was protected from direct sunlight and other possible agents that could induce radicals in the bone. In the laboratory, firstly, bone sample was washed with distilled water in ultrasonic bath and then oven-dried at 30°C. After cleaning, this sample was grinded carefully with an agate mortar and pestle to get powder samples. These powdered samples were divided into five equal parts and placed in different sample containers for measurements. Four powdered samples were irradiated using cobalt-60 gamma source with the following multiply doses: 10, 50, 1000 and 2000 Gy.

2.2 Characterization and ESR Measurements

The X-ray diffraction (XRD) patterns were recorded using XRD diffractometer, Rigaku MiniFlex model, with CuK α radiation. The X-ray generator worked at a power 30 kV and 15 mA. The powder patterns were collected in the angular range 5°– 140° in 2 θ , with scan-speed 3°/min, and 0.02 mm steps. The scanning electron microscopy (SEM) coupled with energy-dispersive X-ray (EDX) measurements were performed using Zeiss Evoma15 Model microscope and Inca and AzTec Software, respectively. Operating conditions of SEM were 15 kV accelerating voltage, 5 - 15 mA current and 10 - 20 s counting time for each element.

The electron spin resonance (ESR) spectra of this sample were recorded in the Bruker model X-Band ESR Spectrometer at 300K to verify the presence of the radical induced by ionizing radiation. During the measurement, the microwave power was set at 20 mW with modulation amplitude of 0.2 mT at 100 kHz.

3. RESULTS AND DISCUSSION

The bone has a high reactive surface area than other dental tissues, and the significant alteration can be observed in the structure depend on the interactions with the sedimentary environments. So, in this study the chemical and structural changes of fossil bone sample were checked by experimental methods (XRD and SEM-EDX) and then investigated by ESR spectroscopy.

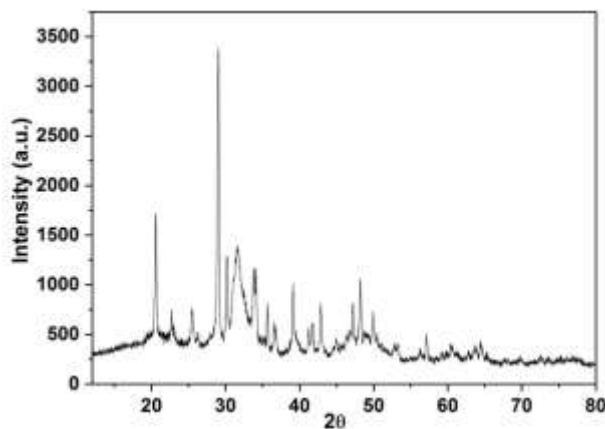


Figure 1. The XRD patterns of powdered fossil bone sample

The XRD was used to determine the mineralogical composition of the fossil bone structure. This analysis was carried out from natural bone that was powdered after sample preparation. The XRD patterns of powdered fossil bone sample is presented in Figure 1. The XRD results showed that the hydroxyapatite was the major component of analyzed bone. In addition, some characteristic peaks of impurities were observed and some residuary amounts of organic matter present as collagen was

2000 Gy irradiated bone ESR signals with $g=2.0020$ and $g=2.0023$ values were related to orthorhombic CO_2^- radical in hydroxyapatite structure in bone [12].

4. CONCLUSION

The XRD, the SEM-EDX and the ESR methods were used for investigation the fossil bone sample. The chemical and structural analyzes were revealed the presence of the hydroxyapatite mineral in the bone structure. The stable radiation defects created in hydroxylapatite in bone were determined. The obtained ESR spectra were analysed by g anisotropy the resolution of g components.

REFERENCES

- [1] H. F. Çay, N. Sezer, A review over bone structure and turnover, *Fiziksel Tıp* 5(3) (2002) 177-184.
- [2] T. Tütken, T. W. Vennemann, Fossil bones and teeth: Preservation or alteration of biogenic compositions, *Palaeogeography, Palaeoclimatology, Palaeoecology* 310(1-2) (2011) 1-8.
- [3] K. J. Dennison, B. M. Peake, ESR Bone Dating In New Zealand, *Quaternary Science Reviews* 11 (1992) 251-255.
- [4] J. Sadlo, J. Michalik, W. Stachowicz, G. Strzelczak, A. Dziedzic-Goclawska, K. Ostrowski, EPR study on biominerals as materials for retrospective dosimetry, *Nukleonika* 51(2006) S95-S100.
- [5] A. Kinoshita, O. Baffa, S. Mascarenhas, Electron spin resonance (ESR) dose measurement in bone of Hiroshima A-bomb victim, *Plos one* 13(2) (2018) e0192444, 1-11.
- [6] G. Strzelczak, J. Sadlo, J. Michalik, X- and Q-band EPR study on dosimetric biomaterials, *Nukleonika* 54(4) (2009) 247-250.
- [7] M. Ikeya, Use of electron spin resonance dating and dosimetry: A review, *Analytical Sciences* 5 (1989) 5-12.
- [8] Y. Liritzis, Y. Maniatis, ESR experiments on quaternary calcites and bones for dating purposes, *Journal of Radioanalytical and Nuclear Chemistry* 129(1) (1989) 3-21.
- [9] V. Balter, V., A. Zazzo, Bone and enamel diagenesis: From the crystal to the environment — A tribute to Jean-François Saliège, *Palaeogeography, Palaeoclimatology, Palaeoecology* 416 (2014) 1–3.
- [10] S. Egersdörfer, A. Wieser, A. Müller, Tooth enamel as a detector material for retrospective EPR dosimetry, *Applied Radiation and Isotopes* 47(11–12) (1996) 1299-1303.
- [11] K. J. Dennison, B. M. Peake, ESR bone dating in New Zealand, *Quaternary Science Reviews* 11(1992), 251 – 255.
- [12] R. Ramya, G. Velraj, Electron spin resonance dating and XRD analysis of archaeological bone samples recently excavated in Karnataka, India, *Elixir Chem. Phys.* 41 (2011) 5750 – 5754.

Effects of precipitation, Wet and Drought Periods on Rainfed Wheat Yield in a Semi-Arid Region

Abolfazl MAJNOONI-HERIS*, Ahmad FAKHERI-FARD, Maryam VAEZ-MADANI, and Saeed SAMADIANFARD

Dept. of Water Engineering, Faculty of Agriculture, University of Tabriz, Tabriz, IRAN

**majnooni@tabrizu.ac.ir*

ABSTRACT

It is observed that most continents around the globe have experienced frequent droughts in the last three decades and this condition is being aggravated due to growing water demands with limited source of water as well as spatiotemporal changes in climatic patterns. In this study, the impacts of droughts and wet spells on rainfed wheat yield were investigated using the Herbst method. The study area is Tabriz plain in the northwestern Iran with statistical period of last 40 years. Drought analysis showed 19 events, with the longest event of 81 months. Yield reduction due to the impact of droughts in annual were estimated 19.30% in the study period. The results showed that there is a significant relationship between rainfall, drought and wet periods with the yield. Also, it was comprehended that spring rainfall was the most effective parameter in the growing of the rainfed wheat.

KEYWORDS: *climatic variables, drought spells, Meteorological drought, yield variations, wet spells.*

1. INTRODUCTION

Wheat is the second highest consumed crop after rice and meets the most food requirement in developing countries (Hossain and Teixeira da Silva, 2012). As one of the important strategic grains, it plays a key role in energy supply and food security across the world. Wheat covers approximately 22% of the world's agricultural lands under cultivation (Licker et al., 2010) and provides about 20% of daily calorie intake (Ramirez-Rodrigues et al., 2016). Because climate change is global concern of these days (Ya-nan et al., 2014), its impact on a variety of crops grown in different parts of the world has been analyzed in umpteen studies (Lobell et al., 2011; Ju et al., 2013). According to IPCC (2007), climate change has a significant relationship with crop yield. Under climate change, the factors affecting the yield have been identified as temperature, precipitation and concentration of atmospheric carbon dioxide (Holden et al., 2003). In recent decades, the production of a variety of products, such as rice, wheat, and maize, has experienced a decreasing trend in different parts of Asia due to increased water stress and temperature, and the decrease in the number of rainy days (Bates et al., 2008). Incidences of drought during 1999-2000 heavily affected some 60 million people of central and southwest Asia, particularly Iran, West Afghanistan, Tajikistan, Uzbekistan and Turkmenistan (Mishra and Singh, 2010). At the global scale, the wheat production in developing countries is expected to undergo a 20 to 30% decline by 2050 as a result of 2 to 3°C rise in temperature (Hossain and Teixeira da Silva, 2012). On the other hand, the demand for wheat in Iran will exceed 20 MtYear⁻¹ upto year 2025 (Nassiri et al., 2006). This is so when 60% to 65% of the area under wheat cultivation in the country is rainfed and meets 30% to 35% of the national demand (Mousavi-Baygiet al., 2016). Atmospheric conditions, especially incidences of droughts, induce risks in agricultural production (Nejedlik and Orlandini, 2008; Mkhabela et al., 2010; Mir et al., 2012). Many drought indices have been developed, and each one has pros and cons and widely used to interpret the severity and duration of droughts. Some of these indices include Palmer Drought Severity Index (PDSI; Palmer, 1965), Herbst method (Herbst et al., 1966), Crop Moisture Index (CMI; Palmer, 1968), Standardized Precipitation Index (SPI; McKee et al., 1993, 1995) and Reclamation Drought Index (RDI; Weghorst, 1996).

Herbst proposed a method for meteorological drought. The method is based on the analysis of monthly precipitation data in which a seasonal drought period with a certain intensity and duration

occurs due to the changes in mean monthly rainfall, this kind of drought is not considered harmful. Therefore, as an important advantage, this method differentiates a conventional drought from harmful droughts, which can be mitigated with the regulation of water consumption (Herbst et al., 1966). The plant response to drought, in terms of yield, is low after the completion of growth stage (Hakim et al., 2012). Nassiri et al. (2006) predicted that Iran would be sensitive to climate change and the vulnerability and damage would rise with the incidence of drought, especially in areas with semi-arid climate which is dominant, as the country is situated in the desert belt of the world and receives low rainfall. The global climate tends to indicate rainfall reduction in many arid and semiarid regions. At the same time, rainfed agricultural production and in particular wheat seems necessary to achieve food security by mitigating the threat of water resources scarcity. Despite widespread occurrence of high frequency droughts in many arid and semi-arid areas, development of relationships between droughts with yield has not yet been the main focus of research programs. It is in this framework that the main objective of this study is to address the impacts of precipitation, drought and wet periods on rainfed wheat yield in the semi-arid regions.

2. MATERIALS AND METHODS

Study site, weather and yield data

The study site, Tabriz plain situated in the northwest part of the Iran, covers an area of over 100,000 ha (geographic coordinates of 37°56' to 38°17' N latitude and 45°30' to 46°15' E longitude). Also, Tabriz meteorological station is located 1364 m above mean sea level at a latitude and longitude of 38°04'47" N and 46°17'30" E, respectively. According to De Martonne method, the climate of the region is considered semi-arid with a long-term average annual precipitation of 261mm, which is low in comparison with the average rainfall in the world and Asia. Monthly synoptic data (1951-2016) consisting of precipitation (mm) for Tabriz station were obtained from Iranian Meteorological Organization (IRIMO).

In the Tabriz Plain, different varieties of wheat have been cultivated in recent decades. Thus, the data relating to wheat yield pertain to the average yield of common varieties. The sowing date is determined by the Ministry of Agriculture (MOA) in the study area and based on the normal situation the sowing date is in last decade of September and varied to October 20. In addition, temperature in the early summer and late spring determines the harvest date (Bannayan et al., 2010). The long-term records (1977-2016) of rainfed wheat yield in the Tabriz Plain, obtained from MOA, were used to study relationships between yield and climate data.

Herbst method

This method is based on monthly rainfall data from which the duration and intensity of droughts and their months of onset and termination are determined; a drought index is also calculated which enables the intensity of droughts to be compared irrespective of their seasonal occurrence. Computational steps and determination of drought parameters using this method are as follows (Herbst et al., 1966):

- i. The weight for precipitation impact of the previous month on the current month was calculated for each months using a transmission factor of the i th month (W_i , dimensionless) as:

$$W_i = 0.1 \left[1 + \frac{M_i}{\frac{1}{12}MAR} \right] \quad (1)$$

where, M_i and MAR represent the monthly average precipitation of the i th month and the annual average precipitation in mm, respectively.

- ii. The effective precipitation of the i th month and the j th year (E_{ij}) in mm was estimated by equation 2. In the first month under study, the actual precipitation was considered to be the effective rainfall.

$$E_{ij} = [R_{(i-1)j} - M_{(i-1)}]W_i + R_{ij} \quad (2)$$

- iii. The precipitation of the i th month and the j th year is shown by R_{ij} . Monthly Deficit of rainfall in the i th month of the j th year (MD_{ij}) for all months was calculated as:

$$MD_{ij} = (E_{ij} - M_i) \quad (3)$$

- iv. The ordinary Mean Monthly Deficit of i th month (MMD_i) during N years was calculated as:

$$MMD_i = \frac{1}{N} \sum_{j=1}^N MD_{ij} \quad (4)$$

The values of $MD_i > 0$ (wet periods) were not considered deficient, they were included in the calculation of mean values despite their zero values. In addition, drought periods were determined based on the values of $MD_i < 0$.

Then Mean Annual Deficit (MAD) will be:

$$MAD = \sum_{i=1}^{12} MMD_i \quad (5)$$

The shortcoming in the Herbst method is in the calculation of MMD, this is, it will be affected by high severity droughts events.

Yield analysis approach

The relationship among rainfed wheat yield and precipitation, as well as drought and wet criteria were determined. Also, the regression equations of seasonal precipitations (R_i), seasonal wet periods ($MD_i > 0$) and seasonal drought periods ($MD_i < 0$) with rainfed wheat yield were determined.

3. RESULTS AND DISCUSSION

Assessment of drought and wet periods of precipitation

Monitoring wet and drought periods were done using Herbst method, based on normal regime as the management line. The mere observation of the graphs is not sufficient for the determination of the onset and termination of drought time due to rainfall higher than normal regime in some months and their inability to compensate for drought. Thus, drought parameters were determined using the onset and termination tests of Herbst method mentioned in table 1.

Accordingly, the maximum, average and minimum severity values of drought were 1.32, 0.65 and 0.05, respectively. The continuity of their period was 7, 17 and 9 months. The minimum and maximum values of index (I) respectively belong to the drought No.3 (February 1958-November 1958, 9 months) and the drought No.13 (February 1995-November 2001, 81 months). Mirabbasi et al. (2012) showed that the longest and most severe drought occurred in 1998 at Sharafkhaneh port, located in the northwest part of the study region, with 6 months duration as per the SPI index this period is shorter than the maximum duration drought introduced in this study and situated within it. Since, the other methods do not separate wet periods that solely mitigate drought periods, without completely compensating the drought periods but Herbst method does.

Impact of drought and wet periods on wheat yield

The relationships of annual precipitation (R_A), annual wet period ($MD_A > 0$) and annual drought period ($MD_A < 0$) with wheat yield are shown in figures 1 to 3, having determination coefficients (R^2) of 0.82, 0.92 and 0.85, respectively. These three regression models show, an increase (decrease) in the amount of rainfall during wet (drought) period leading to an increase (decrease) of wheat yield. Table 2 shows the coefficients of the equations in the figures 1 to 3 with 95% confidence band; being 80% of data in this narrow band, indicates is a reason for low uncertainty.

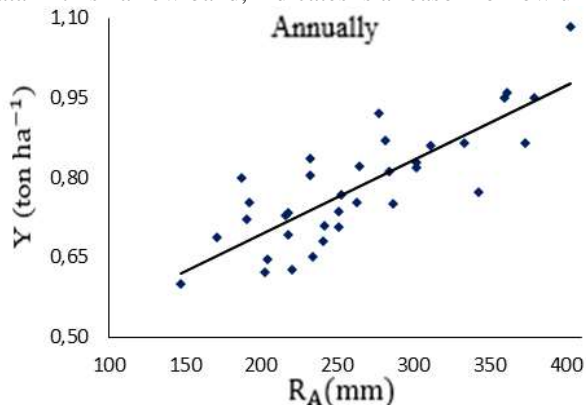


Figure 1- Relationship between annual precipitation and yield of rainfed wheat (1980-2015)

Table 1- Drought parameters of Tabriz station duringn 1950-2015

Period number	Onset of drought	Termination of drought	Drought length (L, month)	Drought Severity (K)	I = L × K
1.	May1952	January1953	8	0.44	3.54
2.	October1954	April1955	6	1.18	7.1
3.	February1958	November1958	9	0.05	0.53
4.	July1959	July1960	12	0.97	11.73
5.	May1961	April1962	11	1.17	12.97
6.	January1964	January1965	7	1.32	9.24
7.	October1974	September1975	11	0.38	4.24
8.	February1978	May1978	3	1.16	3.49
9.	February1983	September1984	19	0.59	11.23
10.	April1985	April1986	12	0.51	6.19
11.	April1987	October1987	6	0.82	4.94
12.	January1989	May1992	40	0.32	12.94
13.	February1995	November2001	81	0.21	16.99
14.	May2003	April2004	11	0.76	8.38
15.	March2006	October2006	7	0.51	3.59
16.	September 2007	April2011	43	0.32	13.96
17.	February2012	December2012	10	0.63	6.38
18.	March 2013	November 2013	8	0.39	3.18
19.	March 2015	Drought period continues until the end of the statistical period under review.			

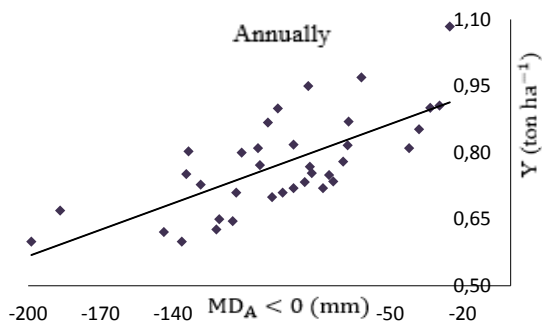


Figure 2- Relationship between annual dry and yield of rainfed wheat (1980-2015)

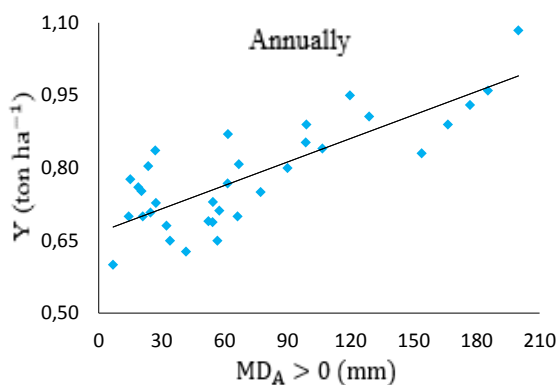


Figure 3- Relationship between annual wet periods with yield of rainfed wheat (1980-2015)

Table 2- Regression relations of historical precipitation, wet and drought spells with yield of rainfed wheat (1980- 2015)

Time scale	Model		
	Precipitation-yield	Wet period-yield (MD> 0)	Drought period-yield (MD <0)
Annual	$Y = 0.0014R_A + 0.4135$	$Y = 0.0016MD_A + 0.667$	$Y = 0.002MD_A + 0.9637$

The most important part of the wheat growing season in the study area is spring. According to National Weather Service, the right amount of rainfall in spring is 115 to 170 mm for the completion of reproductive growth stages. Based on figure 4, the highest and lowest seasonal normal precipitation occurred in spring and summer, 97.46 and 15.74 mm, respectively, on the other hand the deficit depth of spring precipitation [18-83 mm] is less than the amount that National Weather Service recommended. Therefore, a supplemental irrigation about 50 mm is suggested to compensate of spring rainfall limitation for more beneficial yield.

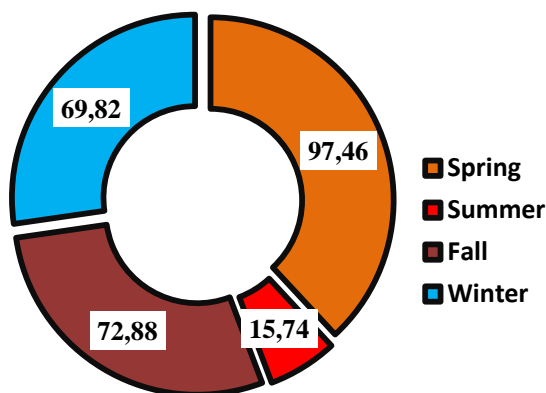


Figure 4. Mean value of long-term seasonal precipitation, mm (1980-2015)

4. CONCLUSION

Global experiences infrequent droughts during the last decades, growing water demands and limited source of water as well as spatiotemporal changes in climate patterns, call the methodologies for drought analysis and adjustment of crop production to water shortage. To investigate the influence of drought events on crop production, relationship between crop yield and water deficit during drought periods should be studied. The Herbst method was used to perform the analysis. According to our results in the last half century, 19 drought periods (with different durations) were identified. The longest duration of drought was 81 months from February 1995 to November 2001. Results showed that the effect of drought periods on rainfed wheat yield reduction was considerable, specifically during spring, because flowering and seed formation stages lied in spring season. Finally, it is recommended to investigate the effects of seasonal drought and wet periods and its effects on wheat and other crops yield.

REFERENCES

- Bannayan, M., Sanjani, S., Alizadeh, A., SadeghiLotfabadi, S., Mohammadian, A., 2010. Association between climate indices, aridity index and rainfed crop yield in northeast of Iran. *Field Crops Res.* 118, 105–114.
- Bates, B.C., Kundzewicz, Z.W., Wu, S., Palutikof, J.P. (Eds.), 2008. *Climate change and water. Technical Paper.* International Panel on Climate Change (IPCC) Secretariat, Geneva.
- Hakim, M.A., Hossain, A., Teixeira da Silva, J., Zvolinsky, V.P., Khan, M.M., 2012. Yield, protein and starch content of 20 wheat (*Triticumaestivum* L.) genotypes exposed to high temperature under late sowing conditions. *J. Sci. Res.* 4 (2), 477–489.
- Herbst, P.H., Bredenkamp, D.B., Barker, H.M. G., 1966. A technique for the evaluation of drought from rainfall data. *J. Hydrol.* 4, 264-272.
- Holden, N.M., Brereton, A.J., Fealy, R., Sweeney, J., 2003. Possible change in Irish climate and its impact on barley and potato yields. *Agric. Forest. Meteorol.* 116, 181–196.
- Hossain, A., Teixeira da Silva, J., 2012. Phenology, growth and yield of three wheat (*Triticumaestivum* L.) varieties as affected by high temperature stress. *Not. Sci. Biol.* 4 (3), 97–109.
- Intergovernmental Panel on Climate Change (IPCC), 2007. *Climate Change 2007: Synthesis Report, Contribution of Working Groups I, II and III to the Fourth Assessment Report of the Intergovernmental Panel on Climate Chang [Core Writing Team, Pachauri RK, Reisinger A (Eds.)].* IPCC: Geneva, Switzerland, 104 pp.

- Licker, R., Johnston, M., Foley, A., Barford, C., Kucharik, C.J., Monfreda, Ch., Ramankutty, N., 2010. Mind the gap: how do climate and agricultural management explain the 'yield gap' of croplands around the world? *Glob. Ecol. Biogeogr.* 19 (6), 769–782.
- Lobell, D.B., Schlenker, W., Costa-Roberts, J., 2011. Climate trends and global crop production since 1980. *Science*.333, 616-620.
- McKee, T.B., Doesken, N.J., Kleist, J., 1993. The Relationship of Drought Frequency and Duration to Time Scales, Paper Presented at 8th Conference on Applied Climatology. American Meteorological Society, Anaheim, CA.
- Mirabbasi, R., Fakheri-Fard, A., Dinpashoh, Y., 2012. Bivariate drought frequency analysis using the copula method. *Theor. Appl. Climatol.* 108, 191- 206.
- Mishra, A.K., Singh, V.P., 2010. A review of drought concepts. *J. Hydrol.* 391, 202-216.
- Mkhabela, M., Bullock, P., Gervais, M., Finlay, G., Sapirstein, H., 2010. Assessing indicators of agricultural drought impacts on spring wheat yield and quality on the Canadian prairies. *Agric. Forest Meteorol.* 150, 399- 410.
- Mousavi-Baygi, M., Bannayan, M., Ashraf, B., AsadiOskuei, E., 2016. Assessment of climatic indices limiting rainfed wheat yield. *Ecol. Indic.* 62, 298-305.
- Nassiri, M., Koochechi, A., Kamali, G.A., Shahandeh, H., 2006. Potential impact of climate change on rainfed wheat production in Iran. *Arch. Agron. Soil Sci.* 52, 1–12.
- Nejedlik, P., Orlandini, S., 2008. Survey of Agrometeorological Practices and Applications in Europe Regarding Climate Change Impacts, Impact of Climate Change and Variability on European Agriculture. Copisteria Sangallo Press, Bologna, Italia.
- Palmer, W.C., 1965. Meteorologic drought. US Department of Commerce, Weather Bureau, Research Paper No. 45, p. 58.
- Ramirez-Rodrigues, M.A., Alderman, Ph. D., Stefanova, L, Cossani, C.M., Flores, D., Asseng, S., 2016. The value of seasonal forecasts for irrigated, supplementary irrigated, and rainfed wheat cropping systems in northwest Mexico. *Agric. Syst.* 147, 76-86.
- Weghorst, K.M., 1996. The reclamation drought index: guidelines and practical applications. Bureau of reclamation, denver, co, p. 6 (available from bureau of reclamation, D-8530, box 25007, lakewood, co 80226).
- Ya-nan, H., Ying-jie, L., Hua-jun, T., Yin-long, X., Jie, P., 2014. Contribution of drought to potential crop yield reduction in a Wheat-Maize rotation region in the north China plain. *J. Integr. Agric.* 13 (7), 1509-1519.

Some theoretical radiation shielding calculations via Phy-X/PSD for investigating the effect of doping Gd₂O₃ into a barium-calcium-boro-silicate glass system

Taner KAVAS^{1*}, Huseyin Ozkan TOPLAN², Iskender AKKURT³, Kadir GUNOGLU⁴,
Recep KURTULUS¹, Melda IPLIKCIOGLU¹

¹ Afyon Kocatepe University, Materials Science and Engineering Department, Afyonkarahisar-TURKEY

² Sakarya University, Metallurgy and Materials Engineering Department, Sakarya- TURKEY

³ Suleyman Demirel University, Physics Department, Isparta- TURKEY

⁴ Isparta Applied Science University, Technical Sciences Vocational School, Isparta- TURKEY

* tkavas@aku.edu.tr

ABSTRACT

Many researchers have been developing glass materials for radiation protection applications. This study addresses a barium-calcium-boro-silicate (BCBS) glass to obtain high-performance radiation shielding glass. Within the concept of this work, the effect of doping Gd₂O₃ into the BCBS glass network was evaluated in terms of theoretical radiation shielding characteristics. The glass (50-x)SiO₂+10B₂O₃+10Na₂O+10CaO+15BaO+5ZnO+xGd₂O₃, where x notifies 0, 5, and 10 mol%, was accordingly designed. Besides that, some physical properties such as density and molar volume were theoretically calculated to estimate the alterations. As a result of Phy-X/PSD calculations, one can say that the additive-Gd₂O₃ resulted in enhanced radiation protection against low and high photon energies. That is, mass attenuation coefficient (MAC) and effective atomic number (Z_{eff}) increased while the tenth-value layer (TVL) decreased when Gd₂O₃ entered the glass network. On the other hand, glass density and molar volume parameters ascended from 3.2705 to 3.7465 g/cm³ and from 23.20 to 28.32 cm³/mol in subjection to the increasing Gd₂O₃ doping rate. Finally, the comparison among alternative radiation shielding materials clearly demonstrated that Gd₂O₃ containing BCBS glass system has a promising result to compete with the others.

KEYWORDS: Gd₂O₃, Phy-X/PSD, Radiation protection, Glass density, Glass, Borosilicate

1. INTRODUCTION

The essentiality of radiation protection due to its hazardous impacts on human health is unquestionable [1]. Researchers have relentlessly endeavored to develop alternative material systems so that utmost protection can be guaranteed effectively. Despite the prevalence and dominance of metallic lead, different materials such as alloys, polymers, or composites are proposed by scientists [2], [3]. This is because metallic lead has a severe drawback: its toxicity to humans and the environment. At least the scientific community has been evaluating various material systems to eliminate metallic lead preference at lower or intermediate photon energy levels. Thus, it is critical to say that great efforts have latterly been adored in radiation shielding applications.

If one searches for radiation shielding topics in different databases, it is not surprising to encounter that the number of investigations has exponentially increased from the past to now. These studies have probed multifarious materials, wide-ranging photon energy levels, and diverse irradiation in terms of experimental, theoretical, and simulation perspectives. Among these, glass materials have potentially emerged on account of their great advantages, including ease of preparation, compositional variations, advanced optical features, and being environmentally friendly [4], [5]. Most specifically, its transparency in the visible light ensures glass materials be suggested as an observation window; for instance, radiotherapy rooms equipped with a device capable of irradiation must involve an openness to monitor the person inside [6]. Therefore, the authors can briefly state that glass use in radiation shielding applications is mission critical.

After providing the importance of glass materials in radiation protection applications, it is worth addressing different glass types preferred by researchers in the existing literature. At the beginning

of the investigations, many tried to compose lead oxide-containing glass recipes to exploit its high-density value; however, the trend has progressively been changing toward lead-free compositions, yet again, due to the harmful impacts of lead content [7], [8]. Borates, silicates, tellurites, or phosphates have been explored as alternative glass types regarding radiation protection efficiency; nevertheless, scientists have still continued to determine the optimum glass composition for serving the needs against various irradiation sources and photon energies. In this sense, a familiar glass system, boro-silicate (BS), seems a good choice because researchers have gained many experiences in the BS system for nearly half a century [9]. Additionally, adding barium oxide and calcium oxide into the BS glass network shall be regarded as an effective way to enhance glass properties. In the final scenario, one can compose a barium-calcium-boro-silicate (BCBS) glass formulation for fostering lead-free radiation shielding glass. Indeed, certain numbers of literature reports on BS glass containing heavy-oxide contents are available, which is a strong motivation for the authors [10], [11].

Based upon given facts about the BS glass system within the field of radiation protection, this preliminary study comprises the glass formulation as follows:

$(50-x)\text{SiO}_2+10\text{B}_2\text{O}_3+10\text{Na}_2\text{O}+10\text{CaO}+15\text{BaO}+5\text{ZnO}+x\text{Gd}_2\text{O}_3$, where x : 0, 5, and 10 mol%.

After deciding on the glass design, some theoretical calculations on glass density and molar volume were performed, while radiation shielding characteristics against different photon energies ranging from 0.015 to 15 MeV were estimated via Phy-X/PSD. Further to those, a comparison among alternative radiation shielding glass materials was fulfilled to highlight the superiorities of the intended glass samples. Eventually, the authors revealed their findings with proper illustrations and detailed discussions for extending the existing literature on lead-free glass systems.

2. MATERIALS & METHODS

Equations 1 and 2 were applied to calculate glass density and molar volume parameters within the scope of theoretical physical property determinations.

$$\rho_{\text{glass}} = \rho_i \cdot f_i \quad (1)$$

where ρ_i and f_i denote the density and molar fraction of the i th constituent, respectively.

$$V_m = \frac{AMW}{\rho_{\text{glass}}} \quad (2)$$

where AMW is the average molecular weight of the glass system.

To estimate the theoretical behavior of glass series against ionizing photons, we readily inputted the glass formulas and the corresponding glass density values to the Phy-X/PSD software [12]. Afterward, the software computed the attenuation characteristics within 0.015 to 15 MeV photon energy level. The formulas used for calculating mass attenuation coefficient (MAC), tenth-value layer (TVL), and effective atomic number (Z_{eff}) were principally figured out via Equations 3 to 5, respectively.

$$LAC = MAC \cdot \rho_{\text{glass}} \quad (3)$$

where LAC and MAC signify linear attenuation coefficient and mass attenuation coefficient, respectively.

$$TVL = \frac{2.303}{LAC} \tag{4}$$

$$Z_{eff} = \frac{\sum_i f_i A_i \left(\frac{LAC}{\rho}\right)_i}{\sum_i f_i \left(\frac{A_i}{Z_i}\right) \left(\frac{LAC}{\rho}\right)_i} \tag{5}$$

where A_i , f_i , and Z_i , represent atomic weight, fraction of i th element, and atomic number, respectively.

3. RESULTS & DISCUSSIONS

Determining physical properties, particularly glass density (ρ_{glass}), is essential before understanding the radiation shielding characteristics. This is because the radiation shielding computations primarily use glass formulation and the corresponding ρ_{glass} value. From this perspective, we theoretically calculated ρ_{glass} and molar volume (V_m) parameters for our glass systems, and the illustrations can be found in Figure 1. It is sharp enough that both parameters behave in a similar trend toward increasing values as Gd_2O_3 replaces SiO_2 in the BCBS glass network. In a numerical sense, ρ_{glass} increases from 3.27 to 3.75 g.cm⁻³ while V_m rises from 23.20 to 28.32 cm³.mol⁻¹. For the case of ρ_{glass} increment, we can simply associate it with the density differences between the dopant and the substituted contents. On the other hand, the increase in V_m as a function of Gd_2O_3 concentration may be attributed to the network modifier role of Gd_2O_3 in the BCBS glass system. In the upshot, adding Gd_2O_3 to enhance physical properties is sensible.

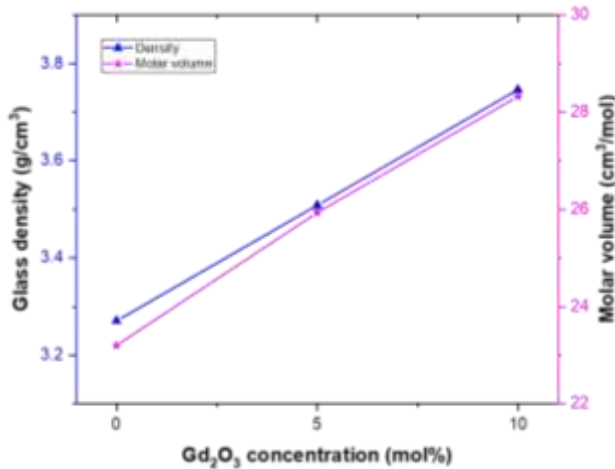


Figure 1. The variations in glass density and molar volume as a function of Gd_2O_3 concentration.

After presenting the physical property findings, one can discuss radiation shielding abilities based on Phy-X/PSD computations. Figure 2 plots the change in MAC parameter against varying photon energies for our glass series. The increasing photon energy from 0.015 to 15 MeV occasionate the MAC parameter to decrease. The MAC parameter is high, namely around 60 cm²/g, in the lower photon energy; however, a sharp decrease is visible in the intermediate and high photon energy levels. On the other hand, the decrement can decelerate due to introducing Gd_2O_3 content to the BCBS glass network. According to the illustration, the G3 sample has a higher MAC value at almost all photon energies, which is highly desired for effective protection. One can find analogical reports regarding the Gd_2O_3 effect on MAC increment in the literature studies [13], [14]. Last but not least, the reason for this increment can be linked to the higher molecular weight of Gd_2O_3 (362.50 g.mol⁻¹).

1) compared to SiO₂ (60.08 g.mol⁻¹) content. Therefore, we can conclude that Gd₂O₃ improves the protection abilities against photon energies.

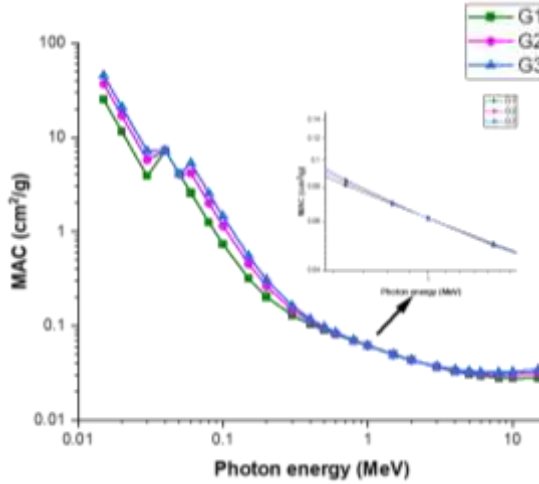


Figure 2. The change in MAC parameter against varying photon energies for our glass series.

Many other parameters can be derived based on LAC and MAC findings in the radiation shielding concept. One of the noteworthy parameters, the tenth-value layer (TVL), is used for attaining the thickness value at which the incident photon's initial energy is attenuated down to 90% [15]. Figure 3 demonstrates photon energy versus TVL thickness for our glass systems in this regard. We observe an increasing trend in TVL values as a function of increasing photon energy, this phenomenon occurs to attenuate more photons. When it comes to assessing the benefits of Gd₂O₃ addition, we can say that it vails to decrease the TVL thickness, which is a fairly optable consequence. As a result, inserting Gd₂O₃ aids TVL to decrease, which in turn, more photons can effectively be attenuated.

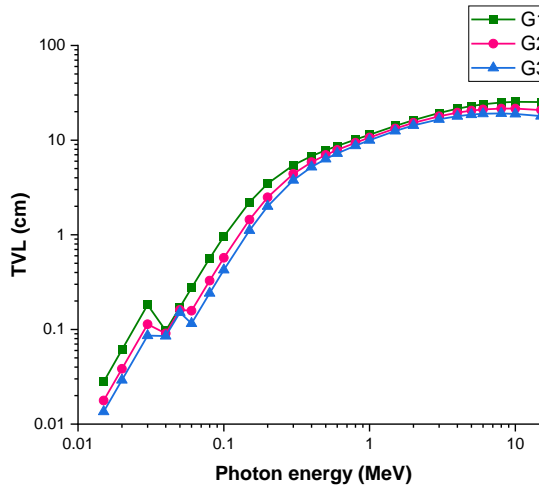


Figure 3. Photon energy versus TVL thickness for our glass systems.

When heavy-oxide contents are introduced to the glass network in radiation shielding applications, the effective atomic number (Z_{eff}) parameter is supposed to be evaluated. In addition, we know that the parameter Z_{eff} is expected to be as high as possible because this will lead to enhancement in more photon-matter interaction. In Figure 4, we draw the variations in Z_{eff} as a variable of

increasing photon energy level in our glass series. It is essential to mention that Z_{eff} behaves in an increasing trend as low photon energies emerge; however, this trend changes towards intermediate photon energies. Finally, Z_{eff} begins to increase through high photon energies. These alternations may be attributed to the photoelectric effect, Compton scattering, and pair production processes [16]. From the point of Gd_2O_3 addition, we can mention its effectiveness on Z_{eff} improvement since G3 has higher Z_{eff} values than others in all photon energy levels. For this reason, Z_{eff} can be advanced by adding Gd_2O_3 .

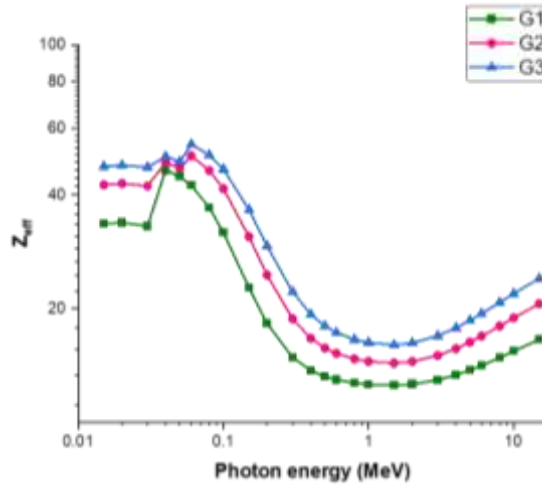


Figure 4. The variations in Z_{eff} as a variable of increasing photon energy level in our glass series.

Thus far, we theoretically estimated some notable radiation shielding parameters by evaluating the alterations as functions of photon energy level and Gd_2O_3 insertion ratio. Nonetheless, it is critical to compare the findings with commercially available radiation shielding glass materials for more clarification. To achieve this aim, Figure 5 reveals a benchmarking diagram, for Schott products (RS360 and RS 323 G19), ordinary soda-lime glass (SLS), and our targetted glass series, with respect to the TVL thicknesses at 662 keV photon energy level [17], [18]. Apparently observed that G3 has a lower TVL thickness, except for RS360 (containing lead oxide), compared to the others. That, on the other hand, means it has a good potential to replace existing commercial products, indeed, with a lead-free glass formulation. Therefore, we can emphasize its promising potency for radiation protection purposes.

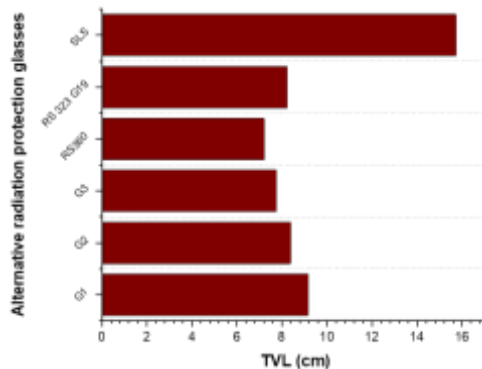


Figure 5. A benchmarking diagram with respect to the TVL thicknesses at 662 keV photon energy level.

4. CONCLUSIONS

In this study, we addressed a barium-calcium-boro-silicate (BCBS) glass system and doped Gd₂O₃ content into the BCBS glass network theoretically. After designing glass formulations, we theoretically performed glass density and molar volume calculations while Phy-X/PSD software provided to estimate some essential radiation protection parameters. We found that ρ_{glass} increases from 3.27 to 3.75 g.cm⁻³ while V_m rises from 23.20 to 28.32 cm³.mol⁻¹. On the other hand, the increasing photon energy from 0.015 to 15 MeV occasionated the MAC parameter to decrease. This decrement could be decelerated due to introducing Gd₂O₃ content to the BCBS glass network. When assessing the benefits of Gd₂O₃ addition, we reported that it vailed to decrease the TVL thickness, which was a fairly optable consequence. From the point of Gd₂O₃ addition, we mentioned its effectiveness on Zeff improvement since G3 had higher Zeff values than others in all photon energy levels. Lastly, a benchmarking diagram, for Schott products (RS360 and RS 323 G19), ordinary soda-lime glass (SLS), and our targetted glass series, with respect to the TVL thicknesses at 662 keV photon energy level was carried out. We concluded that the G3 sample had a good potential to replace existing commercial products, indeed, with a lead-free glass formulation.

ACKNOWLEDGMENT

The authors would like to thank the financial support from The Scientific and Technological Research Council of Turkey (TÜBİTAK) with the program of 1005-National New Ideas and New Products Research Funding Program under contract number 121M096.

REFERENCES

- [1] G. Lakshminarayana et al., “Detailed inspection of γ -ray, fast and thermal neutrons shielding competence of calcium oxide or strontium oxide comprising bismuth borate glasses,” *Materials (Basel)*, vol. 14, no. 9, May 2021, doi: 10.3390/MA14092265.
- [2] S. M. Hulbert and K. A. Carlson, “Is lead dust within nuclear medicine departments a hazard to pediatric patients?,” *J. Nucl. Med. Technol.*, vol. 37, no. 3, pp. 170–172, Sep. 2009, doi: 10.2967/jnmt.109.062281.
- [3] M. F. Turhan et al., “Gamma radiation shielding performance of CuxAg(1-x)-alloys: Experimental, theoretical and simulation results,” *Prog. Nucl. Energy*, vol. 143, p. 104036, Jan. 2022, doi: 10.1016/J.PNUCENE.2021.104036.
- [4] Z. Nur, K. Recep, K. Nilgun, and D. Taner, “Barium - lead - borosilicate glass containing lanthanum oxide : fabrication , physical properties , and photon shielding characteristics,” *Appl. Phys. A*, pp. 1–10, 2022, doi: 10.1007/s00339-022-05285-7.
- [5] R. Kurtulus, C. Kurtulus, and T. Kavas, “Nuclear radiation shielding characteristics and physical, optical, mechanical, and thermal properties of lithium-borotellurite glass doped with Rb₂O,” *Prog. Nucl. Energy*, vol. 141, Nov. 2021, doi: 10.1016/J.PNUCENE.2021.103961.
- [6] M. Almatari, “Gamma radiation shielding properties of glasses within the TeO₂-TiO₂-ZnO system,” *Radiochim. Acta*, vol. 107, no. 6, pp. 517–522, 2019, doi: 10.1515/ract-2018-3058.
- [7] N. Singh, K. J. Singh, K. Singh, and H. Singh, “Gamma-ray attenuation studies of PbO-BaO-B₂O₃ glass system,” *Radiat. Meas.*, vol. 41, no. 1, pp. 84–88, 2006, doi: 10.1016/j.radmeas.2004.09.009.
- [8] J. Kaewkhao, A. Pokaipisit, and P. Limsuwan, “Study on borate glass system containing with Bi₂O₃ and BaO for gamma-rays shielding materials: Comparison with PbO,” *J. Nucl. Mater.*, vol. 399, no. 1, pp. 38–40, Apr. 2010, doi: 10.1016/j.jnucmat.2009.12.020.
- [9] B. KARASU, O. BERKET, E. BİRYAN, and D. SANOĞLU, “The Latest Developments in Glass Science and Technology,” *El-Cezeri Fen ve Mühendislik Derg.*, vol. 4, no. 2, pp. 209–233, 2017, doi: 10.31202/ecjse.318204.

- [10] V. E. Eremyashev, D. A. Zhrebtsov, L. M. Osipova, and M. V. Brazhnikov, "Effect of Calcium, Barium, and Strontium on the Thermal Properties of Borosilicate Glasses," *Glas. Ceram. (English Transl. Steklo i Keramika)*, vol. 74, pp. 1–4, 2018, doi: 10.1007/s10717-018-9991-y.
- [11] R. Kurtulus, T. Kavas, I. Akkurt, K. Gunoglu, H. O. Tekin, and C. Kurtulus, "A comprehensive study on novel alumino-borosilicate glass reinforced with Bi₂O₃ for radiation shielding," *J. Mater. Sci. Mater. Electron.*, vol. 32, pp. 13882–13896, 2021.
- [12] E. Şakar, Ö. F. Özpolat, B. Alim, M. I. Sayyed, and M. Kurudirek, "Phy-X / PSD: Development of a user friendly online software for calculation of parameters relevant to radiation shielding and dosimetry," *Radiat. Phys. Chem.*, vol. 166, no. August 2019, 2020, doi: 10.1016/j.radphyschem.2019.108496.
- [13] E. Kaewnuam, N. Wantana, S. Tanusilp, K. Kurosaki, P. Limkitjaroenporn, and J. Kaewkhao, "The influence of Gd₂O₃ on shielding, thermal and luminescence properties of WO₃–Gd₂O₃–B₂O₃ glass for radiation shielding and detection material," *Radiat. Phys. Chem.*, vol. 190, Jan. 2022, doi: 10.1016/J.RADPHYSICHEM.2021.109805.
- [14] N. Intachai et al., "Effect of Gd₂O₃ on radiation shielding, physical and optical properties of sodium borosilicate glass system," *Radiat. Phys. Chem.*, vol. 199, p. 110361, Oct. 2022, doi: 10.1016/J.RADPHYSICHEM.2022.110361.
- [15] N. Al-Harbi et al., "Understanding the role of Bi₂O₃ in the P₂O₅–CaO–Na₂O–K₂O glass system in terms of physical, structural and radiation shielding properties," *J. Mater. Sci. Mater. Electron.*, pp. 11649–11665, 2021, doi: 10.1007/s10854-021-05775-z.
- [16] G. Lakshminarayana et al., "Comparative assessment of fast and thermal neutrons and gamma radiation protection qualities combined with mechanical factors of different borate-based glass systems," *Results Phys.*, vol. 37, Jun. 2022, doi: 10.1016/J.RINP.2022.105527.
- [17] Schott, "http://www.schott.com/advanced_optics/english/products/opticalmaterials/special-materials/radiation-shielding-glasses/index.html. (Accessed 03 September 2018), (2018). http://www.schott.com/advanced_optics/english/products/opticalmaterials/%0Aspecial-mate," 2018.
- [18] R. Kurtulus and T. Kavas, "Investigation on the physical properties, shielding parameters, glass formation ability, and cost analysis for waste soda-lime-silica (SLS) glass containing SrO," *Radiat. Phys. Chem.*, vol. 176, no. May, p. 109090, 2020, doi: 10.1016/j.radphyschem.2020.109090.

Design And Analysis Of The Boarding Ladder Used On Ships By Finite Element Method

Serap ÖZHAN DOĞAN^{1*}, Burak Galip ANIK², Umut GÖKTAŞ³

¹ Department of Mechanical Engineering, Beykent University, Istanbul/ TURKEY

² R&D Manager, Tersan Shipyards, Yalova/TURKEY

³ R&D Engineer, Tersan Shipyards, Yalova/TURKEY

erapdogan@beykent.edu.tr

ABSTRACT

Designing a ship must meet the standard requirements for the ship's class and be safe for the working crew and passengers. For this reason, the safety factor should be taken at the highest value. The aim of this research is to analyze the boarding ladder used on the NB 1093 and NB 1094 ships using the finite element method and to decide whether the ladder is safe or not as a result of this analysis. This research took place in several stages. First, the ladder was designed in real dimensions using Rhinoceros, a three-dimensional design program, then the HEXAGON finite element analysis program, the analysis type, the material to be used in the analysis were selected, the places where the ladder would be fixed were selected and the necessary force was applied to the ladder. The simulation was run, and the stress values and stress values were reached as a result of the simulation. After fixing the ladder from the determined points, a force of 4.00E-3 MPa was applied and as a result, a displacement of 4.34 mm in the whole structure and 2.21 mm on the step surface occurred. A maximum stress of 168 MPa occurred under a force of 4.00E-3 MPa (in the entire structure). On the step surface, the maximum stress value of 22.5 MPa was obtained. As a result of the calculations; The safety factor of the building was calculated as 2.1 and the safety factor for the stair step was calculated as 15.5. As a result of the analysis, it was determined that the safety factor of the boarding ladder was above 2. Thus, the designed system is correct and safe.

KEYWORDS: Boarding ladder, design and analysis, safety factor in boarding ladders

1. INTRODUCTION

Sea transportation is widely used especially in international transportation. Most of the world trade, around 90%, is carried out by maritime transport [1].

The boarding ladder is a ladder used to enter and exit a ship. Boarding ladders used on commercial ships, including cruise ships, ensure that passengers and crew are safely on board and off the ship [2].

The boarding ladder is a temporary access mechanism between the ship and the port or platform. It provides safe transfer of people. It can be produced from a variety of materials such as steel, aluminum, wood, fiberglass or carbon fiber. It can be operated using manual, hydraulic, pneumatic or electromechanical power systems. In addition, according to SOLAS (International Convention for the Safety of Life at Sea) to design requirements such as length, person or load capacity and safety factor; safety rules, adequate walking path width, lighting and handrails are taken into account [3].

ISO 5488:2015 specifies the requirements and test method for life ladders used on commercial ships (excluding passenger ships) to ensure safe embarkation and disembarkation of crew and pilots [4]. In this study, the design of the boarding ladder was made according to the scope of ISO-5488-2015 standards. Static analysis is a type of analysis widely used in many industrial areas such as aviation, robotics, vehicle, construction, machinery and shipbuilding industries to determine whether it is safe or not, allowing us to examine the load on the structure or the effect of any external effect on the structure [5]. In order to determine the safety of the design, static structural analyzes are made under the specified loads, and the results are examined and evaluated.

The safety factor is one of the most important factors that enable us to decide whether a structure is safe or not.

$$\text{Safety factor} = \frac{\sigma_{\text{yield}}}{\sigma_{\text{max Von-Mises}}}$$

The safety factor is found by dividing the yield strength (yield strength) of the material we use by the maximum Von Mises value occurring in the structure.

1.1. Boarding Ladder Types

Boarding ladder types are determined by building material, mounting position, walkway stages, and extra-specific purposes. The choice of material is as important as the design of the boarding ladders. Since there will be contact with water, the design and manufacture of the ladder should be made by choosing materials that are resistant to corrosion (rusting, decay, etc.), including fittings, nuts and bolts. In addition, the entire boarding ladder should be protected with a special galvanized paint.

1.1.1. Foldable Boarding Ladder

Foldable ladders provide the advantage of compactness thanks to folding mechanisms. They are generally used where space is limited. Figure 1 below shows a typical collapsible boarding ladder. This mechanism is formed by connecting two parts to each other at the joints.

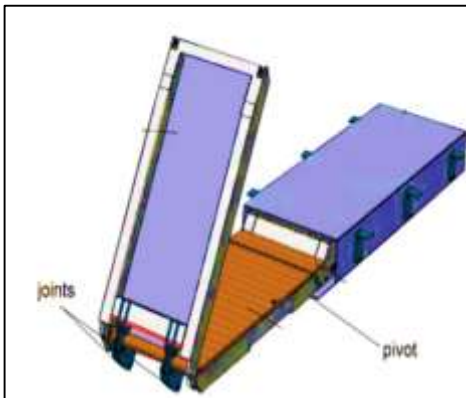


Figure 1: Foldable boarding ladder

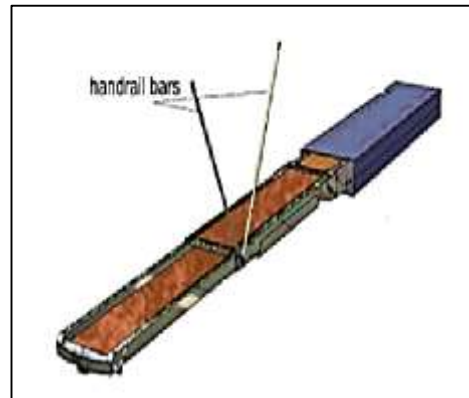


Figure 2: Telescopic boarding ladder

1.1.2. Telescopic Boarding Ladder

Telescopic boarding ladders take up the least space and are the most commonly used ladders on small ships. A simple telescopic ladder has at least two parts that slide longitudinally through an actuator (a type of motor that controls the mechanism). Thus, the length of the pier can be easily adjusted according to the space between the ship and the port. It shows a simple telescopic scaffold in Figure-2 below.

1.1.3. Spiral Boarding Ladder

The spiral boarding ladder is distinguished from the others by its ability to rotate. It basically consists of two concentrically interlocking parts, one of which is a fixed part with respect to the other, allowing the moving part to rotate via a rotary actuator mechanism. A typical spiral boarding ladder is shown in Figure-3 below.

2. DESIGN AND ANALYSIS OF BOARDING LADDER FOR NB 1093 AND NB 1094 SHIPS

Throughout this study, Rhinoceros was used as a computer aided design (CAD) program for 3D design and assembly.

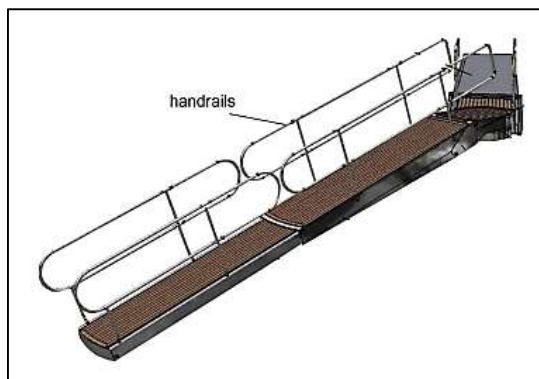


Figure 3: Spiral boarding ladder

2.1. Determining Design Requirements

This scaffolding was designed according to the scope of ISO-5488-2015 standards. The main criteria determined for the design are listed below.

- The inclination angle of the ladder shall not be greater than 55° unless there is a special situation.
- For the safe transportation of people, the width of the walkway will be at least 600mm and the height of the handrail will be at least 1000mm.
- The distance between adjacent piers shall not be more than 1500 mm.
- The connection points of the ladder and ladder will be designed in a way that can safely carry a load of 4000N/m² and the ladder's own weight.
- The height difference between the steps on the ladder shall not be less than 300mm and not more than 350mm.
- The safety factor shall not be less than 2 for the allowable voltage in the ladder design with the specified loading.
- It will be designed as an articulated ladder and in principle it will have a spiral boarding ladder system.

Below are the technical drawings of the designed boarding ladder.

2.2. Material Selection

Material selection was made taking into account seawater corrosion resistance, abrasion, strength, durability, machining, polishability and accessibility. Among them, water corrosion is an important issue for marine applications. Corrosion is an important factor affecting both the life of the designed product and the maintenance cost due to its mechanical and chemical effects. For this reason, the properties of the selected material are shared in Table-1 for the ladder and other parts.

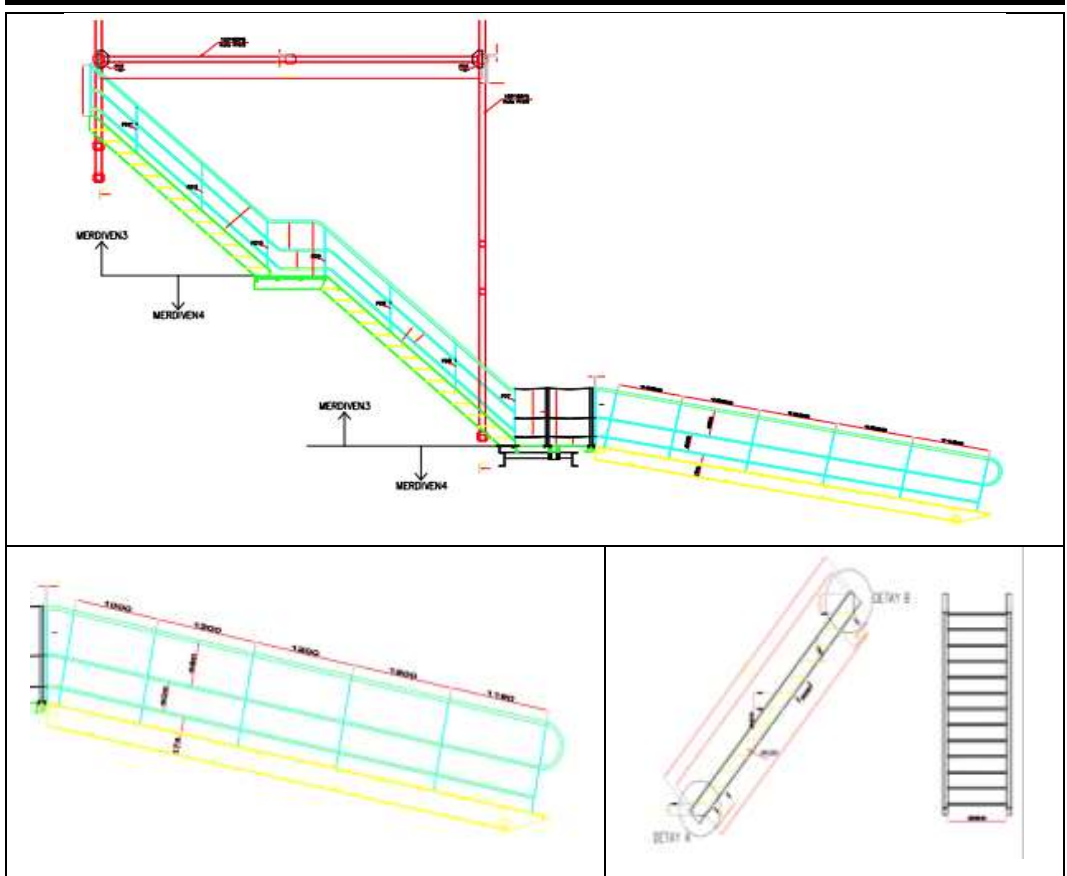


Figure 4: Technical drawing of boarding ladder

Table 1: Properties of the selected material

Physical Properties	Metric
Density	7.80g/cc
Physical Properties	Metric
Tensile Strength, Ultimate	490-620 MPa
Tensile Strength, Yield	360MPa
Elongation at Break	19%
	22%
Modulus of Elasticity	200GPa
Bulk Modulus	160GPa
Poissons Ratio	0.29
Shear Modulus	80.0 GPa

2.3. Static Analysis

The design of the pier used in NB 1093 – NB 1094 ships was made using static analysis. It should be noted that this process is an iterative process. In other words, the scaffolding design has been modified many times to meet the design requirements. In our designed work, position and force analysis is also done repeatedly until the design requirements are met. The analyzes made within the scope of the study were carried out using the HEXAGON analysis program.

Static structural analysis of the boarding ladder assembly designed with Rhinoceros was performed using the HEXAGON Workbench to determine the displacements in the scaffold, stresses due to gravity and external loading, and hence safety factors.

The selected materials were then defined on the ladder to be used on NB 1093 – NB 1094 ships. The next step is networking. To solve the mathematical model, the geometry must be discretized. For this purpose, the product geometry designed with the mesh creation tool is divided into finite elements. The nodes in the structure are connected by lines and form the mesh of complex geometry. Differential equations are solved numerically by the finite element method. Finally, the network model of the scaffold was obtained.

In the other stage, the points where the ladder will be fixed and the force and direction of force to be applied are selected. Force and force direction are applied according to the worst case scenario. According to ISO-5488-2015 rules, the safety factor should not be less than 2 when 4000Pa force is applied to the structure.

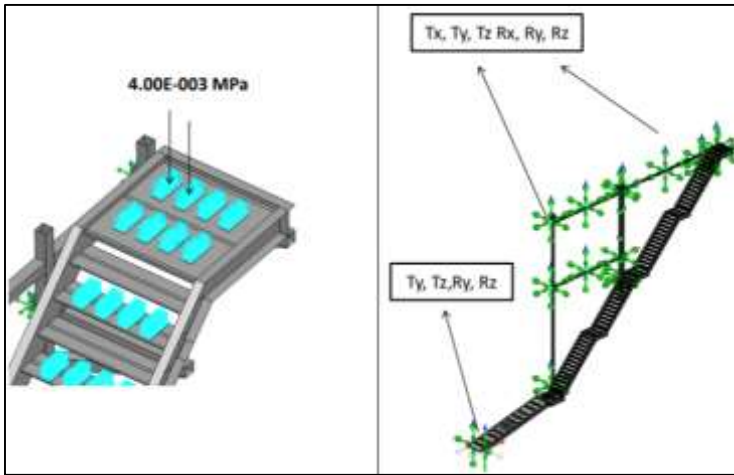


Figure 7: The points where the ladder is fixed and the force directions to be applied

3. RESULTS

Analyzes were made for validation studies on the designed product. Obtained results are given below.

3.1. Displacement

Displacement is the change in position of a particle or object. The first location of the designed product is accepted as a reference and the distance between the first and last location has been measured.

After the boarding ladder was fixed at the points indicated in Figure-7, a force of 4.00E-3 MPa was applied. As a result, a displacement of 4.34mm in the entire structure was achieved. A displacement of 2.21mm occurred on the step surface. These displacements are shared in Figure-8 and Figure-9.

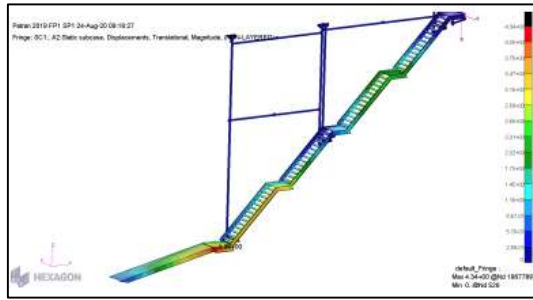


Figure 8: 4.34mm displacement seen in the whole structure

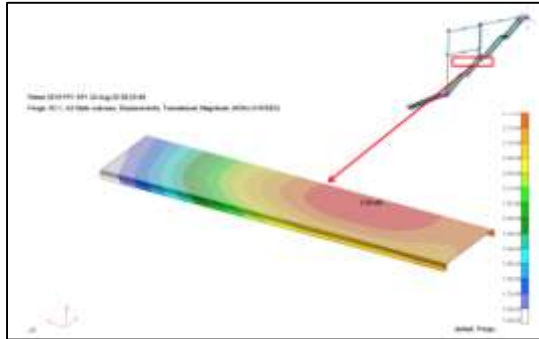


Figure 9: Max. displacement of 2.21mm on the rungs of the ladder

3.2. Stress – Strain

By applying a force of $4.00E-3$ MPa to the structure, its response under this load was examined. A maximum stress of 168MPa occurred throughout the structure. The result of this stress occurring in the entire structure is shared in Figure-10 below. The maximum stress obtained on the step surface was determined as 22.5MPa. This result is shared in Figure 11.

4. DISCUSSION

In order to understand whether a structure is safe or not, the safety factor of the structure can be calculated with the help of the formula shared above. In line with the results obtained, it was checked whether it met the safety factor.

The safety factor for the boarding ladder analyzed in the study is 2. After the calculation, if the safety factor is below 2, the building will be considered unsafe and the design of the building will be reviewed. If the safety factor is greater than 2, the building will be considered safe. Table-1 shows that the yield strength of the material we use in our construction is 350MPa. It was determined in the results obtained in Figure-10 that the maximum Von-Mises stress occurring in our structure was 168MPa. After the calculation, the safety factor of the building was calculated as 2.1. The ladder stress of the structure was determined as 22.5MPa in the results in Figure-11. In the calculation made with the same formula, the safety factor for the stair step was calculated as 15.5.

As a result of the analysis, it has been seen that the boarding ladder used in NB 1093 - NB 1094 ships will be used safely because the safety factor is above 2.

Numerical study for the quaternary semiconductor based heterojunction solar cell modelled with the SCAPS-1D program

Serap YİĞİT GEZGİN^{1*}, Yasemin GÜNDOĞDU² and Hamdi Şükür KILIÇ¹

¹ Department of Physics, Faculty of Science, University of Selçuk, 42031 Selçuklu, KONYA, TURKEY

² Department of Electric and Energy, Kadınhanı Faik İçil Vocational High School, University of Selçuk, 42031, Selçuklu, KONYA, TURKEY

³ Directorate of High Technology Research and Application Center, University of Selçuk, 2031 Selçuklu, Konya, Turkey

⁴ Directorate of Laser Induced Proton Therapy Application and Research Center, University of Selçuk, KONYA, TURKEY

*serap.gezgin@selcuk.edu.tr

ABSTRACT

In order to increase the efficiency of solar cells, tandem solar cells consisting of two or three solar cells have been studied in recent years. In order to obtain high efficiency tandem solar cells, the structure and quality of the sub solar cell are of great importance. Also, theoretical work is needed to confirm the efficiency of these sub-solar cells. At this point, the SCAPS-1D (Solar Cell Capacitance Simulator–one dimension) package program is used to calculate the photovoltaic parameters of heterojunction thin film solar cells.

In this study, we modelled the CZTS/ZnO thin film solar cell produced with CZTS thin film, whose contribution to the efficiency of the Si-based solar cell (produced using a pulse laser deposition system) was confirmed, using the SCAPS-1D program. It was determined that the generation rate characteristic of the thin film solar cell. In addition, the optimal photovoltaic parameters of the solar cell were calculated depending on the interface defect density, operating temperature and recombination coefficients.

KEYWORDS - thin film, solar cell, simulation program

1. INTRODUCTION

In recent years, $\text{Cu}_2\text{ZnSnS}_4$ (CZTS) is an alternative material to solar cells $\text{CuIn}_x\text{Ga}_{(1-x)}\text{S}_2$ (CIGS)[1] and CdTe, which is dominantly used in the photovoltaic market[2]. CZTS material is that p type semiconductor which is very advantageous to be used in the production of solar cells because it has a high absorption coefficient, low cost and environmental friendliness. Generally, CZTS forms a p-n heterojunction thin-film solar cell with n-type CdS semiconductor. In addition, CZTS material can be combined with n type semiconductor such as ZnO, ZnS to form p-n junction thin film solar cell. Furthermore, the heterojunction solar cell is produced by depositing the CZTS thin film on the n-type Si wafer[3].

Photovoltaic performances of solar cells can be determined using the SCAPS-1D simulation program. Photovoltaic parameters of the solar cell that can be calculated depending on physical parameters such as electron/hole capture coefficients of the layers forming solar cells, shallow acceptor/donor defect density, interlayer defect density, and operating temperature. Thus, the possible efficiency of the solar cells to be produced is calculated or the efficiency of the experimentally produced solar cells is verified [1, 4, 5].

In our previous publication, we produced a CZTS/n-Si heterojunction solar cell and theoretically verified the efficiency of the solar cell using the SCAPS-1D program[4]. In this study, we constructed the CZTS/n-ZnO heterojunction thin film solar cell by the same CZTS thin film that we produced in our previous study, using the SCAPS-1D program and calculated the its photovoltaic parameters. The possible performance of the solar cell is discussed in detail in the publication.

2. METHODOLOGY

The CZTS thin film used in CZTS/n-ZnO heterojunction solar cell that was produced by Pulse Laser Deposition (PLD) technique, and its experimental production details and morphological, crystalline and optical properties were given in detail in our previous article[4]. The equations and detailed information used in the SCAPS-1D program used in the modelling of CZTS/n-ZnO solar cell are also expressed in our previous study[4].

2.1 Modelling of Mo/CZTS/n-ZnO/AZO thin film solar cell by SCAPS-1S program



Figure. 1. **a)** Schematic view and **b)** structure of the modelled of Mo/CZTS/n-ZnO/AZO solar cell. In the study, Mo/CZTS/n-ZnO/AZO solar cell was modelled using the SCAPS-1d program, as seen in Figure. 1. In the layers that form this solar cell, Molybdenum (Mo) is back contact, CZTS is active layer, n-ZnO (Zinc Oxide) is buffer layer (n type transparent oxide semiconductor), AZO (Aluminium doped Zinc Oxide) is transparent conductivity oxide layer (electrode). The band gap of CZTS thin film in 212 nm thickness that is 1.56 eV. Film thickness, band gap, absorption coefficient file related to this thin film were determined experimentally and entered into SCAPS-1D program[4]. In addition, all physical parameters related to this and other semiconductors are given in Table 1.

Table 1. The layer’s physical parameter in modelled CZTS/n-ZnO heterojunction solar cell

Layers	AZO[6]	n-ZnO[7]	CZTS[4]
Band Gap (eV)	3.3	3.3	1.56
Electron affinity (eV)	4.6	4.6	3.9
Dielectric permittivity (relative)	9	9	6.5
CB effective density of states (cm⁻³)	2.20x10 ¹⁸	2.20x10 ¹⁸	2.20x10 ¹⁸
VB effective density of states (cm⁻³)	1.80x10 ¹⁹	1.80x10 ¹⁹	1.80x10 ¹⁹
Electron/Hole thermal velocity (cm/s)	1.00x10 ⁷	1.00x10 ⁷	1.00x10 ⁷
Electron/Hole mobility (cm²/Vs)	100/25	100/25	26/10
Shallow donor density (cm⁻³)	1.00x10 ²⁰	1.00x10 ¹⁸	0
Shallow acceptor density (cm⁻³)	0	0	8.00x10 ¹⁵
Thickness (nm)	100	50	210
Contacts		Back Contact (Mo)	
Metal work function(eV)		5.00	
Surface recombination velocity of electrons (cm/s)		1×10 ⁵	
Surface recombination velocity of holes (cm/s)		1×10 ⁷	

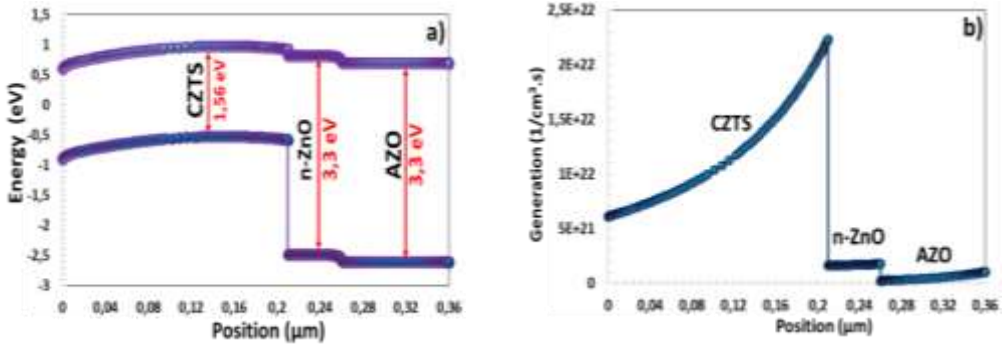


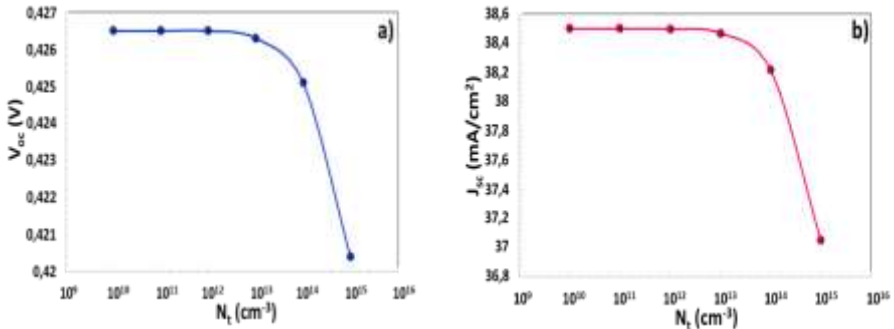
Fig. 2. a) Band diagram and b) the generation rate graph of Mo/CZTS/n-ZnO/AZO solar cell

2.2 Band gap diagram and the generation rate of Mo/CZTS/n-ZnO/AZO thin film solar cell

In the band diagram given in Figure. 2a, there is a cliff-like band structure between CZTS and n-ZnO semiconductors[8]. Electron charge transfer can easily occur from the conduction band of the CZTS semiconductor to the conduction band of the ZnO semiconductor. This increases charge aggregation in the solar cell. However, the charge transition from the valence band of ZnO semiconductor in 3.3 eV wide band gap to the valence band of the CZTS semiconductor in 1.56 eV band gap can be limited or recombination may occur and this can adversely affect charge aggregation.

According to the generation rate graph in Figure. 2b, a high number of photo-excited charge carriers were formed in the CZTS absorber layer. While the generation rate was 2.23×10^{22} $1/cm^3.s$ at the boundary of the depletion region and inside CZTS semiconductor, this ratio decreased to 6.22×10^{21} $1/cm^3.s$ behind the CZTS. Because, while more light diffuses into the depletion region, the light diffusivity behind the semiconductor is less and hence the number of photo-excited charge carriers is less[9, 10]. Since n-ZnO and AZO transparent oxide layers are very transparent and transmit light at a high rate, charge generation rates in these layers are very low.

2.3 The interface defect density (N_t)’s effect on CZTS/n-ZnO heterojunction solar cell



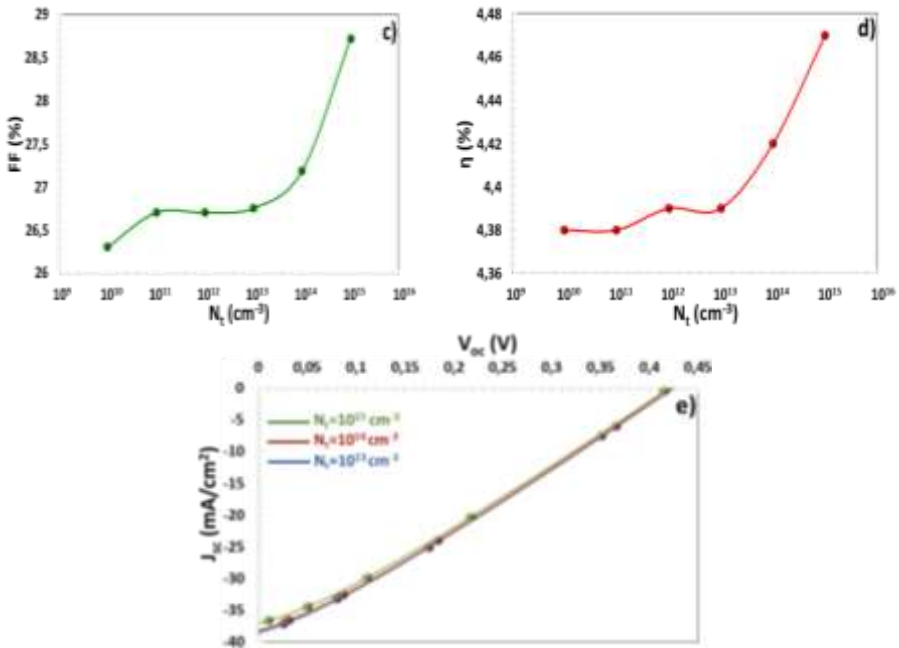
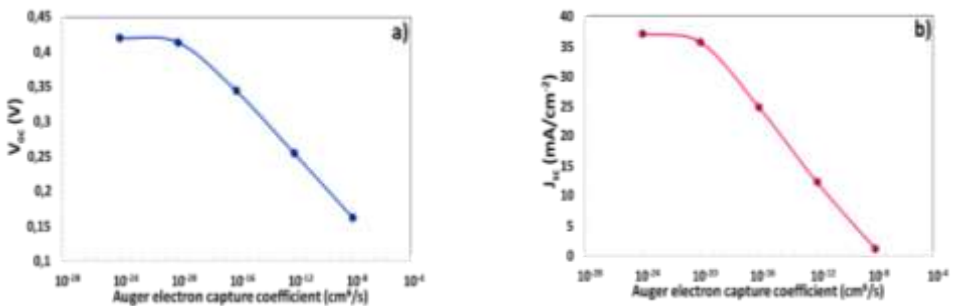


Figure. 3. Effects of N_t values on photovoltaic parameters of CZTS/n-ZnO solar cell

The interface defects can be caused by mismatch band alignment between two semiconductors, hanging bonds, and lattice mismatch between two semiconductors. The interface defect density has a significant effect on the photovoltaic parameters of the solar cell [11]. As seen in Figure. 3a and 3b, in $N_t = 10^{10}$ - 10^{13} cm^{-3} range, V_{oc} and J_{sc} values were almost constant at 0.4265 V and 38.49 mA/cm^2 , respectively. As the N_t value increased from 10^{13} - 10^{15} cm^{-3} , V_{oc} and J_{sc} decreased to 0.4204 V and to 37.05 mA/cm^2 , respectively [12-14]. When the N_t value risen from 10^{10} - 10^{15} cm^{-3} , the FF and η values increased from 26.31% to 28.72% and from 4.38% to 4.47% respectively. The possibility of a high maximum power point of the J-V curve can result in high FF and η values.

2.4 Auger electron/hole capture coefficient's effect on on CZTS/n-ZnO heterojunction solar cell



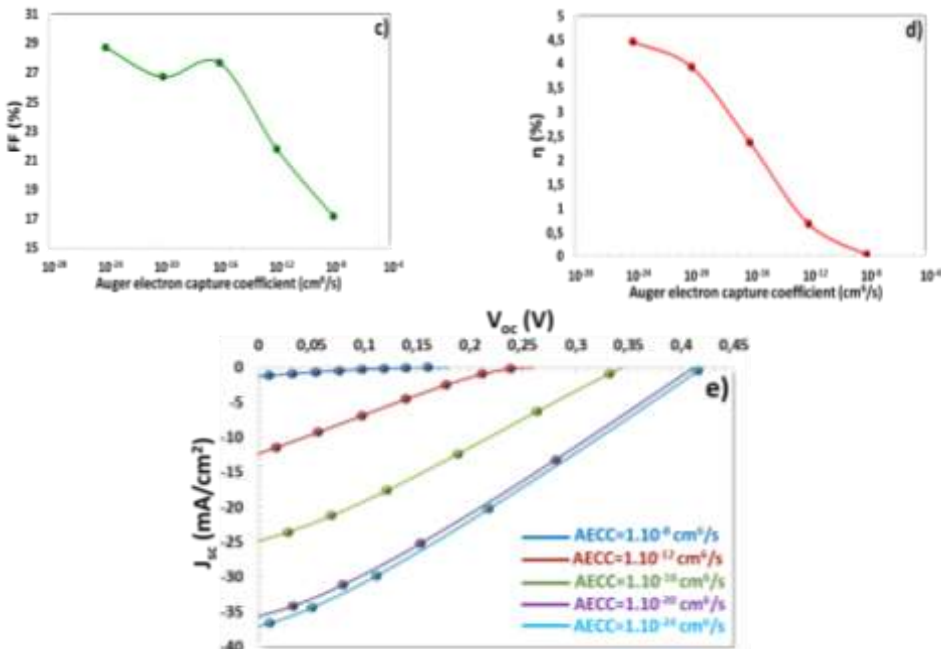
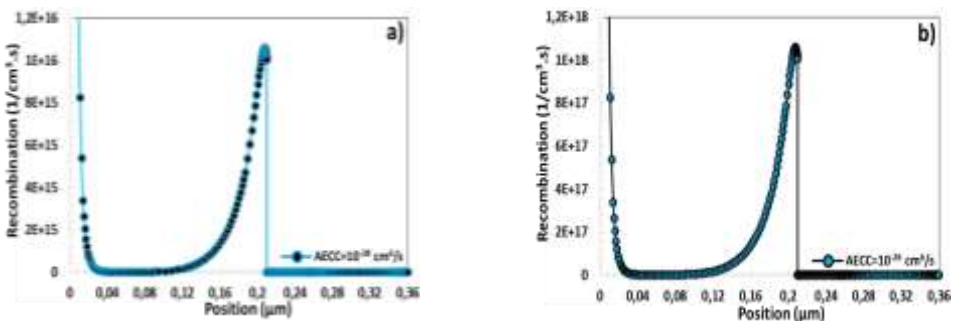


Figure. 4. The effect of Auger electron capture coefficient on the photovoltaic parameters of CZTS/n-ZnO heterojunction solar cell

Figure.4 which presents that the effect of Auger electron capture coefficient (AECC) on the photovoltaic parameter of the solar cell. When electrons and holes recombine, the generated excess energy is not transferred to photons, but to electrons and holes to be excited to higher energy states in the same band [15, 16]. No radiation occurs in this process and the event is called as the Auger recombination. For AECC, in the range of 10⁻²⁴ and 10⁻²⁰ cm⁶/s, V_{oc} and J_{sc} did not change significantly, but when AECC was increased from 10⁻²⁰ cm⁶/s to 10⁻⁸ cm⁶/s, they decreased to from 0.420 V and 0.162 V and from 37.05 mA/cm² to 1.25 mA/cm², respectively. AECC parameter was from 10⁻²⁴ cm⁶/s to 10⁻⁸ cm⁶/s, FF and η which were decreased from 28.72% to 17.2% and from 4.47% to 0.04%, respectively.



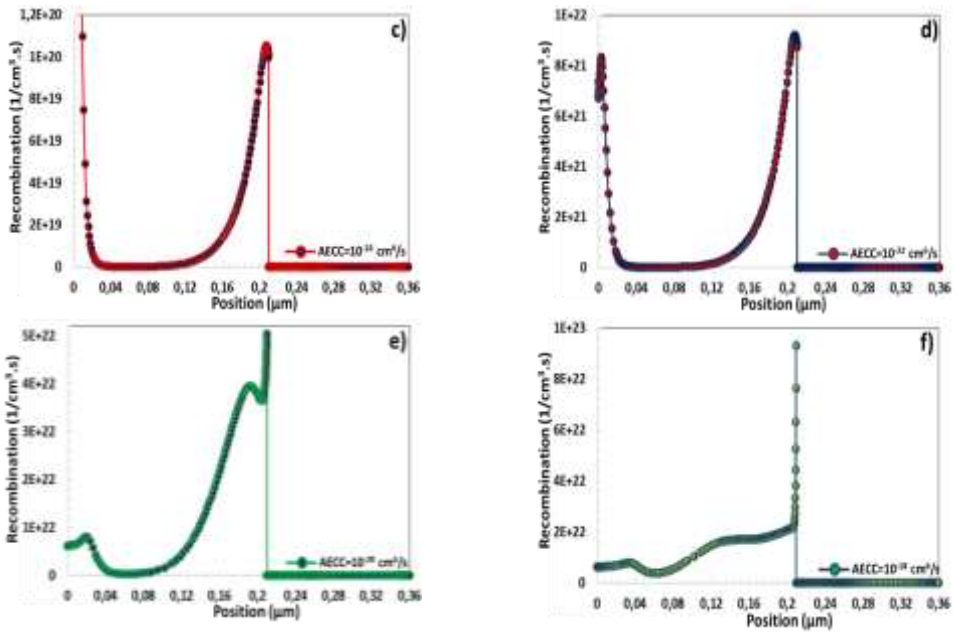
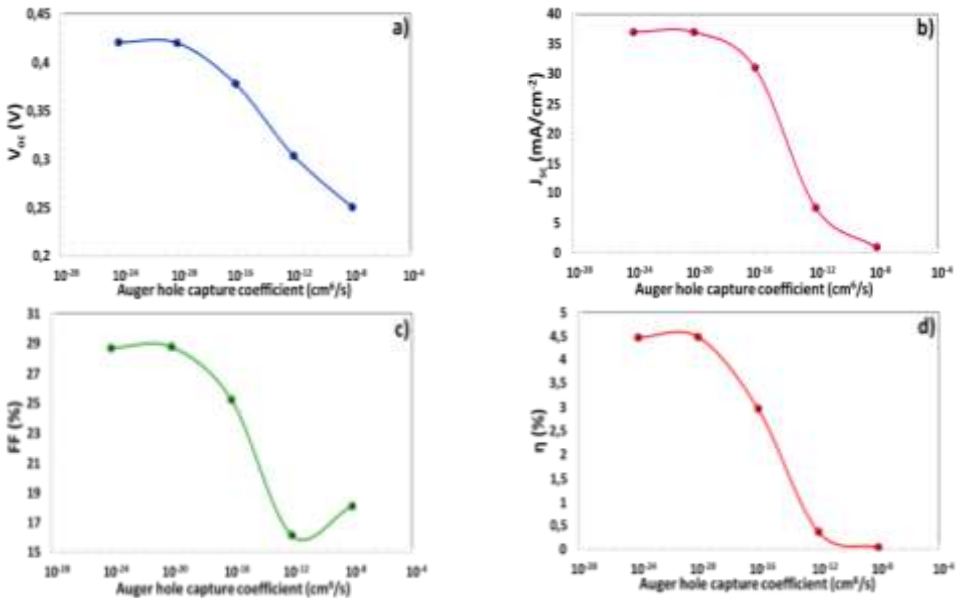


Figure. 5. The effect of AECC values on Recombination vs Position curve

According to Figure. 5 (a-d), For AECC= 10^{-28} , 10^{-26} , 10^{-24} , 10^{-22} cm^6/s , the maximum recombination values are obtained to be 1.0583×10^{16} , 1.0582×10^{18} , 1.0526×10^{20} , 9.214×10^{22} $1/\text{cm}^3.\text{s}$ on $x=0.207863$ μm position, respectively. For AECC= 10^{-20} , 10^{-18} cm^6/s , since the recombination values exceeded the charge formation values, the peaking on $x=0.207863$ μm that decreased and the maximum recombination were determined to be 5.0321×10^{22} $1/\text{cm}^3.\text{s}$ and 9.3139×10^{22} $1/\text{cm}^3.\text{s}$ on $x=0.210$ μm . As a result, while the AECC value increased, the recombination value increased significantly.



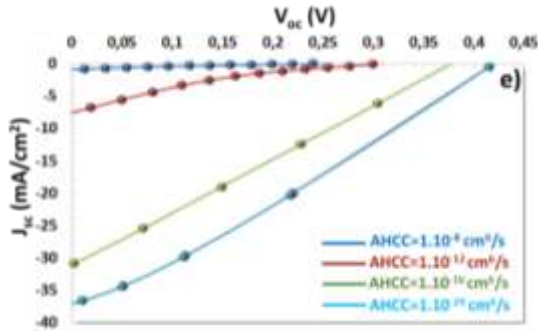
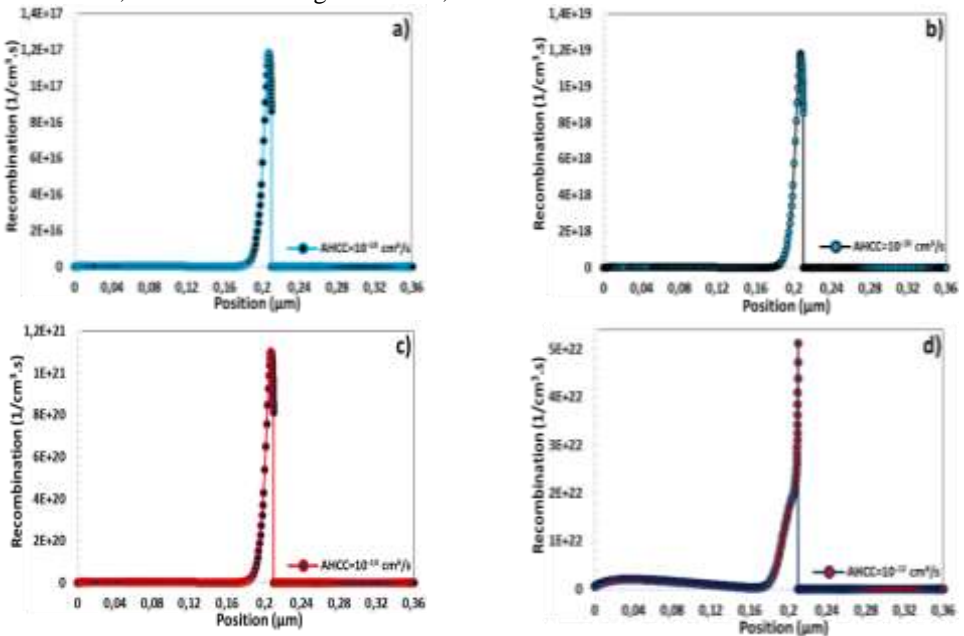


Figure. 6. The effect of Auger hole capture coefficient on the photovoltaic parameters of CZTS/n-ZnO heterojunction solar cell

The effect of Auger hole capture coefficient (AHCC) on the photovoltaic parameters of CZTS/n-ZnO heterojunction solar cell that is given in Figure. 6. While AHCC values were in the range of 10^{-24} - 10^{-20} cm^6/s , V_{oc} , J_{sc} , FF and η values did not change, when AHCC increased from 10^{-20} cm^6/s to 10^{-8} cm^6/s , these values decreased from 0.420 V to 0.250 V, from 37.05 mA/cm^2 to 0.91 mA/cm^2 , from 28.72% to 18.11% and from 4.47% to 0.04%, respectively.

As seen in Figure. 7, for AHCC= 10^{-18} , 10^{-16} and 10^{-14} cm^6/s , the recombination values are 1.1832×10^{17} , 1.1820×10^{19} , 1.1018×10^{21} $1/\text{cm}^3 \cdot \text{s}$ on $x=0.207594$ μm , respectively. To 10^{-12} , 10^{-10} and 10^{-8} cm^6/s , the recombination values that are determined to be 5.1135×10^{22} , 1.0829×10^{23} , 1.5031×10^{23} $1/\text{cm}^3 \cdot \text{s}$ on $x=0.210$ μm , respectively and the peaking on a decreased due to charge formation. Also, for AECC and higher AHCC, close recombination has occurred.



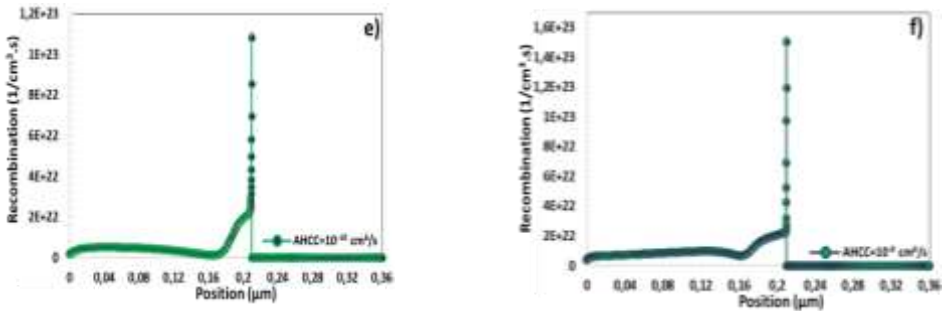
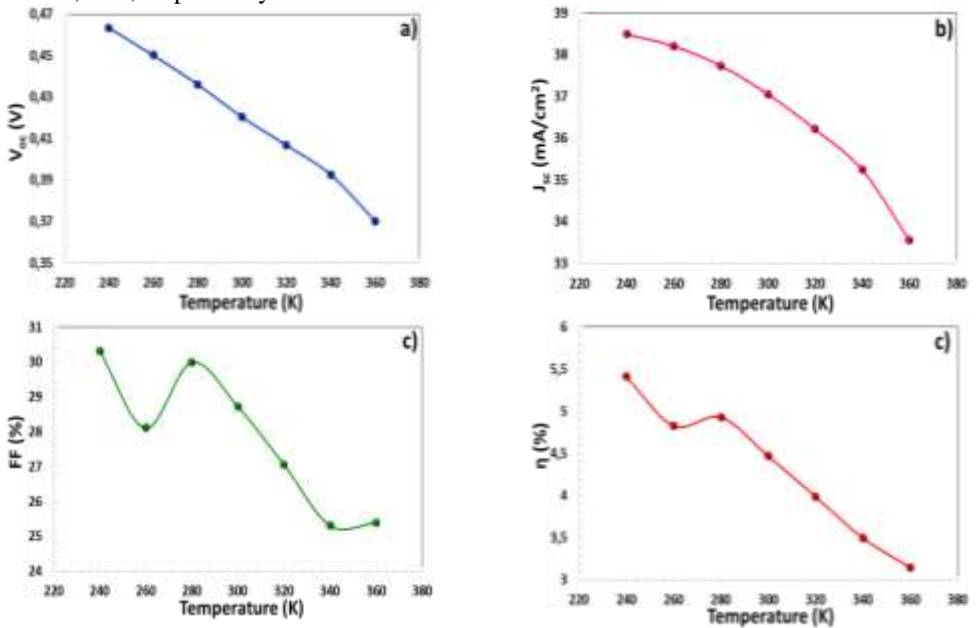


Figure. 7. The effect of AHCC values on Recombination vs Position curve

2.5 The operating temperature’s effect on the photovoltaic parameter of CZTS/n-ZnO heterojunction solar cell

As the operating temperature increases, the band gap and depletion width that decrease. Thus, recombination and charge accumulation at the depletion region can be reduced[17, 18]. Also, with increasing operating temperature, charge carriers can move inconsistently and form undesirable defects. As a result, these factors adversely affect the solar cell's operating performance and reduce its power conversion efficiency. At this point, as seen in the Figure. 8, as the operating temperature is increased from 240 K to 360 K, V_{oc} , J_{sc} , FF and η photovoltaic parameters that decrease from 0,4634 V to 0,3702 V, from 38,48 mA/cm² to 33,56 mA/cm², from 30,32% to 25,39% and from 5,41% to 3,15%, respectively



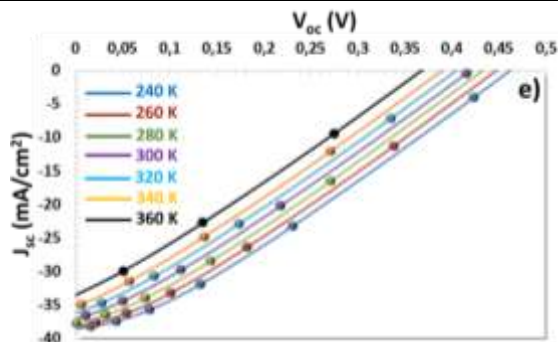


Figure. 8. The effect of AHCC values on Recombination vs Position curve

4. CONCLUSION

Mo/CZTS/n-ZnO/AZO solar cell has been modelled via SCAPS-1D program. A cliff-like band structure has been formed between the CZTS and n-ZnO semiconductors. While the generation rate was 2.23×10^{22} $1/\text{cm}^3 \cdot \text{s}$ at the boundary of the depletion region and inside CZTS semiconductor, this ratio decreased to 6.22×10^{21} $1/\text{cm}^3 \cdot \text{s}$ behind the CZTS. With the increase of N_d , V_{oc} and J_{sc} that decreased, FF and η that increased. While electron/hole capture coefficients are increased, the photovoltaic performance deteriorates and efficiency is reduced. High temperature causes a decrease in the efficiency of CZTS/n-ZnO solar cell.

ACKNOWLEDGEMENTS

Authors wish to kindly thank.

- Selçuk University, High Technology Research and Application Center.

- Selçuk University, Laser Induced Proton Therapy Application and Research Center.

- Dr. Marc Burgelman's group, University of Gent, Belgium for providing permission for us to use SCAPS-1D simulation program.

- Selçuk University, Scientific Research Projects Coordination (BAP) Unit for their financial support via projects with references of 18401178, 18401124 and 15201070.

REFERENCES

- [1] Gezgin, S.Y., Modelling and investigation of the electrical properties of CIGS/n-Si heterojunction solar cells. *Optical Materials*, 2022. 131: p. 112738. DOI:10.1016/j.optmat.2022.112738
- [2] Gezgin, S.Y. and H.Ş. Kılıç, The electrical characteristics of ITO/CZTS/ZnO/Al and ITO/ZnO/CZTS/Al heterojunction diodes. *Optik*, 2019. 182: p. 356-371. DOI:10.1016/j.ijleo.2019.01.014
- [3] Gezgin, S.Y., A. Houimi, and H.Ş. Kılıç, Production and photovoltaic characterisation of n-Si/p-CZTS heterojunction solar cells based on a CZTS ultrathin active layers. *Optik*, 2019. 199: p. 163370. DOI: 10.1016/j.ijleo.2019.163370
- [4] Houimi, A., et al., Numerical analysis of CZTS/n-Si solar cells using SCAPS-1D. A comparative study between experimental and calculated outputs. *Optical Materials*, 2021. 121: p. 111544. DOI:10.1016/j.optmat.2021.111544
- [5] Yiğit gezgin, S., A. Houimi, and h.ş. kiliç, Comparison of electrical and photovoltaic parameters of the hetero-junction solar cells based on CZTS and CIGS ultrathin films. *Materials Technology*, 2022. 37(10): p. 1573-1585. DOI:10.1080/10667857.2021.1964215
- [6] Adewoyin, A.D., et al., Development of CZTGS/CZTS tandem thin film solar cell using SCAPS-1D. *Optik*, 2019. 176: p. 132-142. DOI:10.1016/j.ijleo.2018.09.033

-
- [7] AlZoubi, T. and M. Moustafa, Numerical optimization of absorber and CdS buffer layers in CIGS solar cells using SCAPS. *Int. J. Smart Grid Clean Energy*, 2019. 8: p. 291-298. DOI: 10.12720/sgce.8.3.291-298
- [8] Ghorbani, E., On efficiency of earth-abundant chalcogenide photovoltaic materials buffered with CdS: the limiting effect of band alignment. *Journal of Physics: Energy*, 2020. 2(2): p. 025002. DOI: 10.1088/2515-7655/ab6942
- [9] Niane, D., et al., Generation and Recombination of a CIGSe Solar Cell under the Influence of the Thickness of a Potassium Fluoride (KF) Layer. *American Journal of Materials Science and Engineering*, 2018. 6(2): p. 26-30. DOI: 10.12691/ajmse-6-2-1
- [10] Abderrezek, M. and M.E. Djeghlal, Contribution to improve the performances of Cu₂ZnSnS₄ thin-film solar cell via a back surface field layer. *Optik*, 2019. 181: p. 220-230. DOI: 10.1016/j.ijleo.2018.12.048
- [11] Meher, S., L. Balakrishnan, and Z. Alex, Analysis of Cu₂ZnSnS₄/CdS based photovoltaic cell: a numerical simulation approach. *Superlattices and Microstructures*, 2016. 100: p. 703-722. DOI: 10.1016/j.spmi.2016.10.028
- [12] Elhmaidi, Z.O., et al. Pulsed laser deposition of CZTS thin films, their thermal annealing and integration into n-Si/CZTS photovoltaic devices. in 2016 International Renewable and Sustainable Energy Conference (IRSEC). 2016. IEEE. DOI: 10.1109/IRSEC.2016.7983988
- [13] Peksu, E. and H. Karaagac, A third generation solar cell based on wet-chemically etched Si nanowires and sol-gel derived Cu₂ZnSnS₄ thin films. *Journal of Alloys and Compounds*, 2019. 774: p. 1117-1122. DOI: 10.1016/j.jallcom.2018.10.012
- [14] Gupta, G.K. and A. Dixit, Simulation studies of CZT (S, Se) single and tandem junction solar cells towards possibilities for higher efficiencies up to 22%. *arXiv preprint arXiv:1801.08498*, 2018. DOI: 10.48550/arXiv.1801.08498
- [15] Adewoyin, A.D., M.A. Olopade, and M. Chendo, Enhancement of the conversion efficiency of Cu₂ZnSnS₄ thin film solar cell through the optimization of some device parameters. *Optik*, 2017. 133: p. 122-131. DOI: 10.1016/j.ijleo.2017.01.008
- [16] Fu, H. and Y. Zhao, Efficiency droop in GaInN/GaN LEDs, in *Nitride semiconductor light-emitting diodes (LEDs)*. 2018, Elsevier. p. 299-325. DOI: 10.1016/B978-0-08-101942-9.00009-5

Investigation of Flexural Properties of Solid and Composite Wood Materials

Şemsettin KILINÇARSLAN*, Yasemin ŞİMŞEK TÜRKER

Suleyman Demirel University, Civil Engineering Department, Isparta-TURKEY

*semsettinkilincarslan@sdu.edu.tr

ABSTRACT

In recent years, the use of concrete and steel construction materials has been increasing with the increasing need for construction. The use of laminated wood elements, especially in the construction of large buildings, provides a great advantage both from an environmental and technical point of view. Which is very rich in forests, the preference of wooden elements will not only support local economies, but also contribute to the country's economy, environmental health and architectural diversity. In parallel with the application of various techniques that allow the change of wood material within the body, the construction possibilities have also expanded. In a comparison to be made in terms of structural wood produced, it can be said that especially glued laminated wood has not yet fully developed, so traditional building systems still continue in construction organizations. In this context, national and international literature review of glued laminated wooden building elements was conducted. In the literature review, the usage areas, production stages and especially the experimental studies of glued laminated timber were emphasized. When the studies were examined, it was determined that the flexural properties of laminated beams were better than solid beams. Creating laminated wood elements with the lamination technique has significantly increased the value of wood material, thanks to its better physical and mechanical properties, by reducing the negative aspects of the natural growth process of wood.

KEYWORDS – Wood materials, glulam, flexural properties, composite materials

1. INTRODUCTION

Nowadays, plantation forestry constitutes a large part of modern world forestry. Natural forests with old trees are rapidly decreasing as a result of large amounts of harvest and destruction due to the increasing demand in the world, and these losses are tried to be compensated by plantations. This means that the need for industrial wood raw materials is mostly supplied from man-made forests. Annual increment in such forests; spacing, irrigation, fertilization, drainage, pruning, maintenance cuttings, etc. can be brought to the highest level with measures [1,2]. Although fast-growing species afforestation has an important potential to meet the ever-increasing wood raw material need of the forestry industry, there are generally quality problems in wood raw materials obtained from such afforestation. The main reason for the quality problems is that fast growing woods are mostly composed of young wood, have poor dimensional stability, low density and low flexural strength. For this reason, wood raw materials obtained from such afforestation are generally evaluated in the cellulose and fiber-chip industry [3].

Developments in glue and lamination technology have provided important opportunities for obtaining high quality and value-added products from low quality, low resistance and cheap wood raw materials. Lamination can be generally defined as a multi-layer material production technique [4]. The main purpose of this production is to improve the properties of the resulting composite product such as resistance, stability, sound and heat insulation, and appearance. Lamination has an important place in the production of engineered wood construction materials such as glulam, Laminated Veneer Lumber (LVL), Particle Strand Lumber (PSL) and Laminated Strand Lumber (LSL) [5]. In addition to the above-mentioned benefits, lamination in wood to be used structurally is extremely important in that it allows the use of low-quality and low-resistance and therefore cheap wood raw materials with high-quality, high-resistance and expensive wood raw materials to a certain extent. It is an accepted practice to use low quality and cheap lamellas from the same or different

wood species in the inner layers of laminated building timbers, and high quality and expensive lamellas in the surface layers [6,7]. The low quality of the lamellas used in the middle layer does not cause a significant loss of resistance, especially since a significant part of the stresses in the structural elements that try to bend are concentrated in the surface areas on the compressive and tensile sides and there are no significant stresses in the middle parts. Thus, while the resistance values of the structural element are largely preserved, its cost is significantly reduced and at the same time a lighter construction element is produced. In this study, it is aimed to evaluate the studies on the flexural properties of wooden solid and laminated composite beams.

2. STRUCTURAL LAMINATED WOOD ELEMENT

The lamination process is applied to solid wood elements in order to minimize the defects inherent in the wood, to spread it to other regions or to eliminate it, to enable it to be used as structural elements with large dimensions, to create a structural element with better properties and in different forms. This process is usually carried out by gluing wooden pieces with fiber directions parallel to each other with special binders such as glue in layers by pressure force. The material formed as a result of this process is called laminated wood. Laminated wood can be composed of wood of different grades or using one type of wood, depending on the intended use. The stratification of a material is important in terms of material properties. In the wood industry, the stratification of the material provides greater homogeneity, reducing the effect of damaging parts in critical areas under loading. This process also enables the use of higher quality wood species in the outer layers and lower quality wood species in the middle layers, where the material is subject to less stress [8]. In the early 1900s, the production and use of laminated wood became widespread in Europe, especially in Switzerland and Germany. It is used in hangar structures, churches and bridges. Especially since 2000, with the innovations in adhesive qualities and production processes, the use of laminated wood has become increasingly widespread in Europe. Since 2006, the European Union has been working on promoting the use of wood as a remedy for global warming and climate change [9].

3. PRODUCTION OF LAMINATED WOOD

Wooden elements to be laminated are subjected to drying process until they have the appropriate moisture content. Before gluing the parts that will form the laminated wood element, the impregnation process is performed. It can also be impregnated after the laminate processes are completed. However, the impregnation process of elements with large dimensions and different cross-sections can be difficult. For this reason, it is most appropriate to pre-impregnate the wooden elements that will form the laminated wood. With this process, water or oil-based chemicals are impregnated into the wood and the wood is protected against harmful external factors. The method and type of materials chosen in the impregnation process are effective on the adhesion resistance of wooden elements with glue. Therefore, care should be taken in this process [10, 11]. In order to determine for what purpose the laminated wood element will be used, it is first visually graded. Immediately afterwards, it is mechanically evaluated and classified for the determination of the modulus of elasticity. In order to create the parts to be laminated after classification, an appropriate one of the width or length joining methods shown in the figure is selected and each end connection point of these elements is tested and their combinations are made. Then, the laminate lengths are arranged according to the quality combination required for the element to be produced. A smooth surface is obtained by planing each laminate layer.

After the adhesive is applied between the laminate layers, it is pressed to obtain the desired configurations. After the gluing process, planing is done again to clean the glue that overflows from the joints of the laminates, and the laminated wood is cut to the desired size and made ready for use [5]. In order to obtain curved and different cross-section elements, hydraulic or manually operated clamps are placed around the element and contacted with steel apparatus pre-fixed to the supports

to provide the desired curvature or model. When pressure is applied, the laminations are adjusted for proper alignment and made ready for use.

In the production of laminated wood, the correct arrangement of the floors to be laminated is very important, especially in terms of bending strength and durability. Laminate layers should be arranged according to the location of the age rings. Because the wood material shows different properties in the tangential or radial direction to the age rings [12].

4. STUDIES RELATED TO LAYERED LAMINATED TIMBER

In general, there are studies on the flexural properties of laminated timber. In this study, especially the studies on the flexural properties of laminated timber are emphasized. Öztürk and Arıoğlu (2006) [13] produced laminated timber from scotch pine wood using various types of glue and performed static bending tests. As a result of the study, they stated that the wood material used is brought to the desired equilibrium humidity and if the appropriate glue material is used, the laminated timbers can give the best results. In general, they stated that the best result was obtained from laminated timbers produced with polyvinyl acetate glue with a bending strength of 75.24 MPa, and the worst result was obtained from layered laminated timbers produced with urea formaldehyde glue with a bending strength of 55.80 MPa. Kılınçarslan and Türker (2022) [14] strengthened 20x20x360 mm ash beams with basalt-based fiber-reinforced polymers. The bending test of the reference and reinforced beams was carried out. It was determined that the beams reinforced with basalt-based fiber reinforced polymer fabric have flexural strength (117.11 MPa) and modulus of elasticity (12845 MPa). It was determined that the reference beams had flexural strength (99.34 MPa) and modulus of elasticity (10320 MPa). It was determined that the flexural strength value of the reinforced beam increased by 18% and the elasticity modulus value increased by 25% compared to the reference beam. Güray et al. (2003) [15] investigated the effects of glue type and force direction on bending resistance in laminated wood material produced from stemmed oak (*Quercus Robur L.*) wood, and used a 2.5 mm thick peeling veneer. For this purpose, Polyvinylacetate (PVAc) and Polyurethane (PU) glues were preferred in the formation of laminates. In the experiment, two force directions were chosen, parallel and perpendicular to the glue line. A total of 80 test specimens were prepared according to the principles of TS 2474 standard and bending test tests were applied to these specimens in the direction perpendicular and parallel to the glue line. They determined that the highest bending strength was in the samples glued with polyurethane (PU) glue (121 MPa), and the lowest in the samples glued with polyvinylacetate (PVAc) glue (90.6 MPa). Kılınçarslan and Türker (2019) [16] tested laminated wooden beams with the same height and width of h by dividing them into 3 different groups. Variation in laminate layer thicknesses ($h/4$, $h/6$, $h/8$) or the number of glue lines did not have a significant effect on stiffness and flexural strengths, but differences in modulus of elasticity were observed. While the lowest elastic modulus values were observed in beams with the highest laminate layer thickness, approximately the same result was obtained in the samples with the highest layer thickness. The highest modulus of elasticity was obtained in the beam with medium laminate layer thickness. In this case, it may be more advantageous to prefer samples with higher laminate layer thickness. Because the reduction in the number of layers allows less glue to be used, saving labor, time and economically. Kılınçarslan and Şimşek Türker (2021) [17] investigated the effect of reinforcement with fiber reinforced polymers on the rotational behavior at the column-beam joint. They found that the load carrying capacity at the column-beam joint increased significantly.

5. CONCLUSION

Since their existence, people have used trees, which are natural materials, by shaping them to meet their need for shelter. Wood, whose raw material is wood, has long been preferred as a building material for aesthetic reasons, ease of processing and lightness. Wood material has had a more functional use with the discovery and development of glue. However, wood material has been used

massively for many years as a material with limitations due to its morphological structure, defects and irregular behavior. These limitations are caused by inherent features of the wood such as imperfections, knots, resin pockets and irregular wet rings. By laminating and gluing small solid wood pieces with adhesives such as glue, these defects are dissipated and the final product with better flexural strength properties is obtained. These laminated products can have much larger dimensions than solid wood. Creating laminated wood elements with the lamination technique has significantly increased the value of wood material, thanks to its better physical and mechanical properties, by reducing the negative aspects of the natural growth process of wood.

ACKNOWLEDGEMENTS

This study has been prepared within the scope of the thematic area of "Sustainable Building Materials and Technologies" with SDÜ BAP project with FDK-2019-6950 project code and YÖK 100/2000 doctoral program. The authors thank the SDU BAP unit, YÖK and YÖK100/2000 program staff.

REFERENCES

- [1] M. Erdem, O. Baykara, M. Dođru, F. Kuluöztürk, A novel shielding material prepared from solid waste containing lead for gamma ray. *Radiation Physics and Chemistry*, 79(9), (2010), 917-922. <https://doi.org/10.1016/j.radphyschem.2010.04.009>
- [1] H. Dirik, Conservation of genetic diversity and forest gene resources. *Journal of the Faculty of Forestry Istanbul University*, 44(3-4), (1994), 113-122.
- [2] Y. Göker, T. Dünder, The effects of young wood characteristics on wood quality and place of use. *Journal of the Faculty of Forestry Istanbul University*, 49 (1-2-3-4), (1999), 31-44.
- [3] S. Sađlam, Ü. Asan, Optimal structure problems of industrial plantations and their solutions. *Journal of the Faculty of Forestry Istanbul University*, 61(2), (2011), 115-138.
- [4] Ş. Kiliñarslan, Y. Şimşek Türker, Evaluation in terms of Sustainability of Wood Materials Reinforced with FRP. *Journal of Technical Sciences*, 10(1), (2020), 23-30. doi: 10.35354/tbed.615101
- [5] F. Mengelođlu, R. Kurt, Engineered Wood Products 1: Laminated Veneer Lumber (LVL) and Glued Laminated Timber (Glulam). *KSU Journal of Science and Engineering*, 7(1), (2004), 39-44.
- [6] C. A. Issa, Z. Kmeid, Advanced wood engineering: glulam beams. *Construction and Building Materials*, 19(2), (2005), 99-106. doi: 10.1016/j.conbuildmat.2004.05.013
- [7] M. Zor, E. Sozen, T. Bardak, Mechanical Performances of Laminated Wood and Determination of Deformation in the Bending Test with the Aid of Image Analysis Method. *Journal of Bartın Faculty of Forestry*, 18(2), (2016), 126-136. doi: 10.24011/barofd.268576
- [8] J. Gáborík, M. Gaff, D. Ruman, V. Záborský, V. Kašíčková, A. Sikora, Adhesive as a factor affecting the properties of laminated wood. *BioResources*, 11(4), (2016), 10565-10574.
- [9] S. Kayakiran, E. Kishali, The Investigation of the Glued Laminated Timber Elements from Past to Today and The Suggestions for the Use as Load-bearing in the Structures. *Journal of Architectural Sciences and Applications*, 4(1), (2019), 34-50. doi: 10.30785/mbud.450537
- [10] H. Yörür, D. Aydemir, B. Uysal, The factors affecting on bonding strength of impregnated wood material. *Journal of Bartın Faculty of Forestry*, 12(18), (2010), 99-106.
- [11] O. Perçin, G. Özbay, M. Ordu, The investigation of the mechanical properties of wooden materials laminated with various glues. *Journal of Science and Technology of Dumlupınar University*, (019), (2009), 109-120.
- [12] S. Karayilmazlar, Y. Çabuk, A. Atmaca, A. Aşkin, Lamination technique and its importance in lumber industry. *Journal of Bartın Faculty of Forestry*, 9(11), (2007), 78-86.
- [13] R. Beceren Öztürk, N. Ariođlu, Mechanical properties of laminated wood beams produced from Turkish *pinus silvestris*. *ITU Journal/a*, (2010), 5(2).

-
- [14] Ş. Kiliñarslan, Y. Şimşek Türker, Strengthening of solid beam with fiber reinforced polymers. Turkish Journal of Engineering, 7(3), (2022), 166-171. Doi: 10.31127/tuje.1026075
- [15] A. Güray, M. Kilic, G. Doğru, M.Özer, The effects of applying force direction and glue types on the bending strength of laminated wood material produced from brown oak (*Quercus Robur L.*), Thecnoloji, (2003), 6(1), (1-9).
- [16] Ş. Kiliñarslan, Y. Şimşek Türker, The Effect of Different Parameters on Strength Properties of Glulam Timber Beams. ICCESSEN-2019, Antalya-Turkey, (2019), 23-27.
- [17] Ş. Kilincarslan, Y. Şimşek Türker, Experimental investigation of the rotational behaviour of glulam column-beam joints reinforced with fiber reinforced polymer composites. Composite Structures, 262, (2021), 113612. Doi: 10.1016/j.compstruct.2021.113612

Investigation of Flexural Properties of Glulam Beams

Yasemin ŞİMŞEK TÜRKER*, Şemsettin KILINÇARSLAN

Suleyman Demirel University, Civil Engineering Department, Isparta-TURKEY

*yaseminturker@sdu.edu.tr

ABSTRACT

A wide range of structural members are made from sawn lumber, which is produced in a large number of sizes and grades. The size of the trees that can be used to make this kind of lumber, however, places a limit on the cross-sectional dimensions and lengths of these members. The main issues with using wood for structural members are its stiffness, ductility, and strength. In recent years, studies have been started to improve the mechanical properties of wooden beams by using materials such as steel plate and fiber reinforced polymers. One of the products made from wood as a derivative is glue-laminated timber. Glued laminated timber beams are complex engineering parts made from carefully chosen and positioned layers of lumber with different strengths and stiffnesses. Glued laminated timber beams are generally designed for and used in applications where they will be highly stressed under design loads. In this study, the production phase of glulam beams was emphasized and studies on the bending properties of glulam beams were examined. In addition, the effect of reinforcement with fiber-reinforced polymers on glulam flexural properties was investigated. As a result of the study, it was seen that the bending properties of glulam beams were higher than solid beams. It was determined that reinforcement with fiber-reinforced polymers significantly increased the bending properties of glulam beams.

KEYWORDS – Wood materials, glulam, flexural properties, composite materials

1. INTRODUCTION

Sawn lumber, which is manufactured in a wide range of sizes and grades, is used to make a wide variety of structural members. However, the cross-sectional sizes and lengths of these members are constrained by the size of the trees that can be used to produce this kind of lumber. Wood's stiffness, ductility, and strength are the main drawbacks to using it for structural members. The mechanical properties of wooden beams have recently been the subject of studies using [1].

One of the products made from wood as a derivative is glue-laminated timber. The process of making glulam involves gluing together layers of timber. Glulams are more advantageous when compared to sawn beams. The use of sawn lumber may become impractical as the span lengthens or as the load increases. In these circumstances, glue-laminated wood can be a wise option. Glued laminated timber beams are complex engineering parts made from carefully chosen and positioned layers of lumber with different strengths and stiffnesses. Beams made of glued-laminated wood are typically used in applications where they will be subjected to high design loads [2].

The tensile strength of the lamellae and the finger joints, which may be correlated, determine the bending strength of glulam. The characteristic bending strength of glulam can be calculated using only the characteristic tensile strength of the lamellae if the correlation is known. This results in the calculation model in [3] for softwood, where a linear relationship between the two values is provided. Based on the test procedures outlined in [4], the glulam's bending strength and the lamellae's tensile strength are determined. The so-called laminating effect is the result of these test methods. This indicates that glulam's bending strength is typically greater than lamellae's tensile strength. In this study, studies on the bending properties of glulam timbers were evaluated. In particular, the studies on the strengthening of glulam beams, which have been emphasized in recent years, have been emphasized.

2. STUDIES RELATED TO GLULAM TIMBER

Glulam, a crucial component of modern timber structures, not only addresses the traditional wood material's shortcomings of low lumber recovery and processing difficulty, but also offers a number of advantages over them, including fewer centralized defects, higher strength, a variety of cross sections and component shapes, and reasonable stress distribution [5]. However, the length of Glulam beams typically cannot satisfy the requirements of the continuous beams due to the size limitations of the raw materials and processing methods. The compressive strength cannot be fully utilized in the bending state because the failure always happens in the tensile zone [6]. In addition, because traditional Glulam connections have a limited ability to transmit bending moments, which would lead to inadequate joint stiffness, the majority of Glulam beams are simply supported beams. Previously, a variety of strengthening techniques were suggested to increase the capacity of timber structures. Numerous types of reinforced polymers, steel plates, and steel bars are used as typical reinforced materials to increase the ductility and flexural capacity and lessen deformation of Glulam beams. Griбанov et al. (2018) [7] studied the different laminar polymer composites for wooden structures and suggested the corresponding design suggestions. CFRP (carbon fiber-reinforced polymer) bars were used to improve the flexural capacity and the stiffness of Glulam beams by Yang et al. (2016) [8] The CFRP bar changed the failure mode from brittle tension failure to ductile compression failure, significantly improving the flexural capacity. After comparing the strengths of timber beams adhered to various steel plates, Nowak et al. (2016) [9] offered design recommendations. An experimental investigation on PBSL (parallel bamboo strand lumber) beams reinforced with AFRP was presented by Zhang et al. (2020) [10] (aramid fiber-reinforced polymer). The only studied variable was the cloth ratio, after which the tested beams' stiffness, flexural capacity, and load-carrying capacity were assessed. The findings indicated that bonding AFRP can make PBSL beams stiffer. Adopting the AFRP provision could significantly improve the ductility of the PBSL beams. Timber structures have been used with the NSM (near-surface mounted) technique in the interim [11]. Kılınçarslan and Türker (2019) [12] tested laminated wooden beams with the same height and width of h by dividing them into 3 different groups. Variation in laminate layer thicknesses ($h/4$, $h/6$, $h/8$) or the number of glue lines did not have a significant effect on stiffness and flexural strengths, but differences in modulus of elasticity were observed (Figure 2).

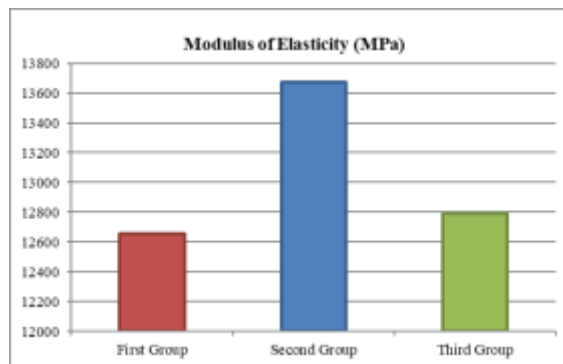


Figure 2. Modulus of elasticity of glulam beams belonging to three different groups [12]

While the lowest elastic modulus values were observed in beams with the highest laminate layer thickness, approximately the same result was obtained in the samples with the highest layer thickness. The highest modulus of elasticity was obtained in the beam with medium laminate layer thickness. In this case, it may be more advantageous to prefer samples with higher laminate layer thickness. Because the reduction in the number of layers allows less glue to be used, saving labor, time and economically. When Jorge et al. (2013) [11] investigated the bond between Glulam and

NSM CFRP laminates, they found that the bond length was the primary determining factor in the local bond stress-slip relationship and failure modes. A novel steel-reinforced PBSL beam was proposed by Wei et al. (2020) [13] in which prestressed steel bars or steel bars were embedded in bamboo-composite beams. The findings demonstrated that increasing reinforcement ratios and prestress increase the ultimate bearing capacity of reinforced beams, though prestress had a lesser impact than reinforced bar diameter. Kılınçarslan and Türker (2021) [14] strengthened 90x90x1300 mm glulam beams with carbon-based fiber reinforced polymers. The bending properties of the unreinforced reference sample (R-Glulam Timber) and reinforced beams (CFRP-Glulam Timber) were investigated. The graph obtained as a result of the experiment is given in Figure 3.

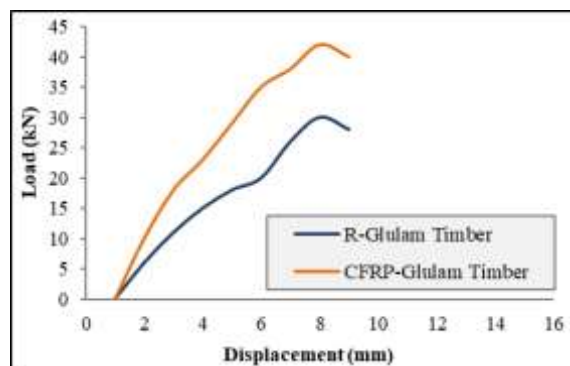


Figure 3. Graph obtained as a result of the experiment [14]

The load carrying capacity of glulam beams reinforced with carbon fiber reinforced polymer fabric increased significantly compared to the reference beams. The load carrying capacity of the reinforced beams increased by 42.85% and the displacement amount increased by 86.61% compared to the reference beams.

3. CONCLUSION

Glulams are more advantageous when compared to sawn beams. The use of sawn lumber may become impractical as the span lengthens or as the load increases. In these circumstances, glue-laminated wood can be a wise option. Glued laminated timber beams are complex engineering parts made from carefully chosen and positioned layers of lumber with different strengths and stiffnesses. Beams made of glued-laminated wood are typically used in applications where they will be subjected to high design loads. In addition, many studies have been conducted on the reinforcement of glulam beams with fiber-reinforced polymers and it has been determined that the load carrying capacity of glulam beams increases significantly with reinforcement. It has been observed that the load bearing capacity of the structure can be increased with the strengthening process in existing or newly constructed wooden structures.

ACKNOWLEDGEMENTS

This study has been prepared within the scope of the thematic area of "Sustainable Building Materials and Technologies" with SDÜ BAP project with FDK-2019-6950 project code and YÖK 100/2000 doctoral program. The authors thank the SDU BAP unit, YÖK and YÖK100/2000 program staff.

REFERENCES

- [1] G.P.A. Ardner, Reinforced glued laminated timber system. In: 2nd Pacific timber engineering conference., Auckland, New Zealand; August, vol 2, (1989), 295– 300.
- [2] Z. W. Guan, P. D. Rodd, D. J. Pope, Study of glulam beams pre-stressed with pultruded GRP, Computers & Structures, 83, (2005), 2476–2487. Doi: 10.1016/j.compstruc.2005.03.021

-
- [3] EN 1194, Ausgabe April 1999. Brettschichtholz–Festigkeits-klassen und Bestimmung charakteristischer Werte – Glued laminated timber – Strength classes and determination of characteristic values.
- [4] EN 408, Ausgabe April 1996. Bauholz für tragende Zwecke und Brettschichtholz – Bestimmung einiger physikalischer und mechanischer Eigenschaften – Structural timber and glued laminated timber – Determination of some physical and mechanical properties
- [5] X. Y. Zhou, L. Cao, D. Zeng, Flexural capacity analysis of glulam beams, *Building Structure*, 45 (22), (2008), 91–96.
- [6] C. A. Issa and Z. Kmeid, Advanced wood engineering: glulam beams, *Construction and Building Materials*, 19(2), (2005), 99–106. Doi: 10.1016/j.conbuildmat.2004.05.013
- [7] A. S. Gribanov, S. I. Roshchina, M. V. Popova, M. S. Sergeev, Laminar polymer composites for wooden structures, *Magazine of Civil Engineering*, 83 (7), (2018), 3–11. Doi: 10.18720/MCE.83.1
- [8] H. Yang, D. Ju, W. Liu, W. Lu, Prestressed glulam beams reinforced with CFRP bars, *Construction and Building Materials*, 109, (2016), 73–83. Doi: 10.1016/j.conbuildmat.2016.02.008
- [9] T. Nowak, J. Jasienko, E. Kotwica, S. Krzosek, Strength enhancement of timber beams using steel plates-review and experimental tests, *Drewno*, 59 (196), (2016), 75–90. Doi: 10.12841/wood.1644-3985.150.06
- [10] J. Zhang, H. Shen, R. G. Qiu, Short-Term flexural behavior of prestressed glulam beams reinforced with curved tendons, *Journal of Structural Engineering*, 146 (6), (2020), Doi: 10.1061/(ASCE)ST.1943-541X.0002625
- [11] S. Jose, J. Marco, J. Branco, M. V., C. F. Cunha, Bond between glulam and NSM CFRP laminates, *Construction and Building Materials*, 40, (2013), 260–269. Doi: 10.1016/j.conbuildmat.2012.09.089
- [12] Ş. Kiliçarslan, Y. Şimşek Türker, The Effect of Different Parameters on Strength Properties of Glulam Timber Beams. ICCESSEN-2019, Antalya-Turkey, (2019), 23-27.
- [13] Y. Wei, S. C. Yan, K. Zhao, Experimental and theoretical investigation of steel-reinforced bamboo scrimber beams, *Engineering Structures*, 223, (2020). Doi: 10.1016/j.engstruct.2020.111179
- [14] Ş. Kiliçarslan, Y. Şimşek Türker, Reinforcement of Glulam Beams with Carbon-FRP. ICCESSEN-2021, Antalya-Turkey, (2021), 23-27.

Determination of radium-226 activity concentration in sand samples from Doğancalı beach

Osman GÜNAY^{1*}, Kadir GÜNOĞLU², İskender AKKURT³

¹ Yildiz Technical University, Faculty of Electrical and Electronics Engineering, Department of Biomedical Engineering, Istanbul- TURKEY

² Isparta Applied Science University, Technical Sciences Vocational School, Isparta- TURKEY

³ Suleyman Demirel University, Science Faculty, Physics Department, Isparta-TURKEY

*o.gunay@yildiz.edu.tr

ABSTRACT

Terrestrial radioactive elements constitute a large part of natural radioactivity. Radium-226 is a member of the Uranium-238 natural decay series and occurs at trace levels in almost all rocks, soil, water, and plants in the natural environment. The two isotopes of radium, Radium-226 and Radium-228, are very important for radiological protection because of their relatively long half-lives. Obligation to determine radium has become a public health concern due to its dangerous nature. In this study, Radium-226 activity concentration of sand samples collected from Doğancalı beach in Istanbul-Şile district was measured by using NaI (TI) detector gamma spectroscopy system. The activity concentrations obtained are compared with the determined world averages.

KEYWORDS: Radium-226 activity concentration, Doğancalı beach, Gamma spectroscopy,

1. INTRODUCTION

Radiation has always existed in nature. Generally, natural radiation is examined in two separate categories as cosmic and terrestrial radiation. There are basically three different radiations that make up the terrestrial radiation source. These are Ra-226, Th-232 and K-40. Terrestrial radiation level is very important for determining the radiation exposure of humans. For this reason, numerous studies have been conducted on both radiation protection and terrestrial radiation determination [1-15]. The main purpose of this study is to determine the Ra-226 radiation dose concentration level in Dogancali Beach in Istanbul.

2. MATERIALS AND METHODS

In this study, Ra-226 concentrations were determined in the sand samples of the Dogancali beach in Sile (Istanbul). For this, approximately 1 kg of sand samples were taken from 5 different points. These sand samples were first dried in the laboratory, then sieved. Then placed in airtight containers and kept for 40 to 50 days. After this stage, the radiation dose was calculated by using the NaI (TI) gamma detector to determine the Ra-226 dose level of the sand sample. Gamma radiation measurement experimental setup is shown in figure-1. The measurement level of gamma doses experimental set includes Spectrometer, Amplifier, MCA and Computer in general terms. The calibration curve is shown in Figure 2. The calibration of the experimental setup was made using Co-60 and Cs-137 sources.

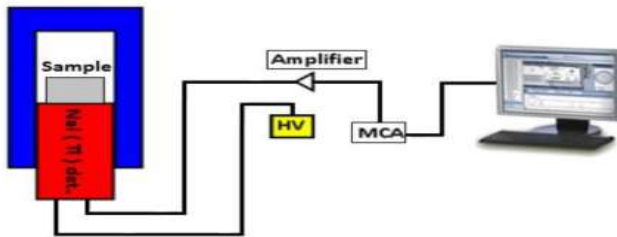


Figure 1. Experimental setup

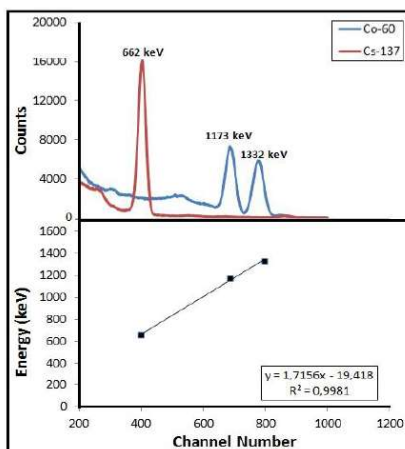


Figure 2. The gamma spectrum

3. RESULTS AND DICCUSSION

Ra-226 radiation concentrations are shown in table-1. The Ra-226 concentration was found to be the lowest at sample-3 (S3) with 28.15 ± 2.08 Bq/kg, and the highest at sample-1 (S1) with 34.45 ± 1.46 Bq/kg. The average Ra-226 concentration was calculated as 31.41 ± 1.93 Bq/kg. In fig-3, Ra-226 concentrations according to the sampling points are shown.

In a similar study conducted in Vietnam[16], the concentration of Ra-226 in the soil was 43 Bq/kg, in a study conducted in Yemen48 Bq/kg [17], in a study in India 27 Bq/kg [18], in a study in Iraq 14 Bq/kg[19] and in a study in Pakistan 26 Bq/kg[20]. The results obtained as a result of this study are similar to the results of studies conducted in other countries.

Table 1. Ra-226 Concentration

Sampling Point	Ra-226 Concentration (Bqkg ⁻¹)
S1	34.45±1.46
S2	29.54±1.12
S3	28.15±2.08
S4	32.12±1.64
S5	32.79±0.87
Mean	31.41±1.93

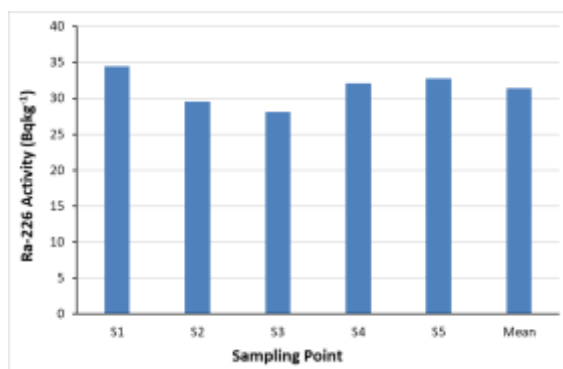


Figure 3. Ra-226 Concentration

4. CONCLUSION

In this study, Ra-226 radiation dose level in 5 different sand samples taken from Dogancili beach in sile (Istanbul) was determined using NaI(Tl) gamma detector. The Ra-226 radiation dose concentration found as a result of the study was compared with similar studies conducted in different countries. It has been observed that the average of the results obtained from this study and the average of the results obtained from the studies conducted in other countries are close to each other.

REFERENCES

- [1].Choudhary, M. D., Akkurt, I., Almisned, G., & Tekin, H. O. (2022). Radiation shielding properties for titanium dioxide added composites. *Emerging Materials Research*, 1-7.
- [2].Akkurt, I., & Tekin, H. O. (2020). Radiological parameters of bismuth oxide glasses using the Phy-X/PSD software. *Emerging Materials Research*, 9(3), 1020-1027.
- [3].Al-Obaidi, S., Akyıldırım, H., Gunoglu, K., & Akkurt, I. (2020). Neutron shielding calculation for barite-boron-water. *Acta Phys. Pol. A*, 137(4), 551.
- [4].Aközcan S, Kūlahcı F, Günay O, Özden S (2021) Radiological risk from activity concentrations of natural radionuclides: cumulative hazard index. *J Radioanal Nucl Chem* 327(1):105–122. <https://doi.org/10.1007/s10967-020-07474-1>
- [5].Akkurt I, Tekin HO (2020) Radiological parameters of bismuth oxide glasses using the Phy-X/PSD software. *Emerging Materials Research* 9(3):1020–1027. <https://doi.org/10.1680/jemmr.20.00209>
- [6].Akkurt I, Gunoglu K, Arda SS (2014) Detection efficiency of NaI (Tl) detector in 511–1332 keV energy range. *Science and Technology of Nuclear Installations*.
- [7].AKKURT I., N. Ayten UYANIK, Kadir GÜNOĞLU (2015).“ *International Journal of Computational and Experimental Science and Engineering* 1–1, 1–11 <https://doi.org/10.22399/ijcesen.194376>
- [8].Çelen YY, Evcin A (2020) Synthesis and characterizations of magnetite–borogypsum for radiation shielding. *Emerging Materials Research* 9(3):770–775. <https://doi.org/10.1680/jemmr.20.00098>
- [9].Çelen YY (2021) . *Emerging Materials Research* 10–2. (2021) <https://doi.org/10.1680/jemmr.21.00043>
- [10]. Çelen YY, Evcin A, Akkurt I, Bezir NÇ, Günoğlu K, Kutu N (2019) Evaluation of boron waste and barite against radiation. *Int J Environ Sci Technol* 16(9):5267–5274. <https://doi.org/10.1007/s13762-019-02333-3>
- [11]. El-Agawany F.I., Karem Abdel-Azeem Mahmoud, Hakan Akyildirim, El-Sayed Yousef, Huseyin Ozan Tekin, Yasser Saad Rammah. (2021). *Emerging Materials Research* 10–2, 227 <https://doi.org/10.1680/jemmr.20.00297>
- [12]. Günay O (2018) Assessment of lifetime cancer risk from natural radioactivity levels in Kadikoy and Uskudar District of Istanbul. *Arab J Geosci* 11(24):782
- [13]. Günay O, Saç MM, İçhedef M, Taşköprü C (2018) Natural radioactivity analysis of soil samples from Ganos fault (GF). *Int. J. Environ. Sci. Technol* 16:1735–1472
- [14]. Günay O, Eke C (2019) Determination of terrestrial radiation level and radiological parameters of soil samples from Sariyer-Istanbul in Turkey. *Arab J Geosci* 12(20):1–10. <https://doi.org/10.1007/s12517-019-4830-1>
- [15]. Kulali F (2020) Simulation studies on the radiological parameters of marble concrete. *Emerging Materials Research* 9(4):1341–1347. <https://doi.org/10.1680/jemmr.20.00307>
- [16]. Huy NQ, Hien PD, Luyen TV et al (2012) Natural radioactivity and external dose assessment of surface soils in Vietnam. *Radiat Prot Dosim* 151(3):522–531

- [17]. Harb S, El-Kamel AEH, Abbady AEB, Saleh II, El-Mageed AIA (2012) Specific activities of natural rocks and soils at quaternary intraplate volcanism north of Sana'a, Yemen. *J. Med. Phys. Assoc. Med. Phys. India* 37(1):54
- [18]. Reddy U, Ningappa C, Sannappa J (2017) Natural radioactivity level in soils around Kolar Gold Fields, Kolar district, Karnataka. *India J Radioanal Nucl Chem* 314:2037–2045
- [19]. Ahmed AI, Akrawy DT (2005) Measurement of natural radioactivity in soil samples from bekhma, Kurdistan region, Iraq. *International Journal of Recent Research and Review*, 8(4).
- [20]. Akhtar N, Tufail M, Ashraf M, Mohsi IM (2005) Measurement of environmental radioactivity for the estimation of radiation exposure from saline soil of Lahore. *Pakistan Radiat Meas* 39:11–14

Effects of Nonlinear Optical Absorption Properties on Na and Li doped Cu_2SnS_3 (CTS) Thin Films

Yasemin GÜNDOĞDU^{1,2,*}, Amina HOUMI³, Serap YİĞİT GEZGIN⁴, Hamdi Şükür KILIÇ^{2,4}

¹University of Selçuk, Department of Computer Technologies, Kadınhanı Faik İçil Vocational High School, Konya, TURKEY

²University of Selçuk, Directorate of Laser Induced Proton Therapy Application and Research Center, Konya, TURKEY

³University of Selçuk, Department of Nano-Technology and Advance Materials, Faculty of Science Konya, TURKEY

⁴University of Selçuk, Department of Physics, Faculty of Science, Konya, Turkey

*yasemingundogdu@selcuk.edu.tr

ABSTRACT

In this study, Cu_2SnS_3 (CTS) target have been synthesized using ball milling technique with Copper (Cu), Tin (Sn) and Sulphur (S) powders. After the production of CTS was prepared, the alkali metals including sodium (Na) and lithium (Li) were doped in it with %3 and % 1 concentration ratios. Homemade targets were used to production of thin films by pulsed laser deposition system. The linear optical properties and X-ray crystallography (XRD) patterns have been analysed and determined. The nonlinear parameters such as nonlinear absorption coefficient of CTS, Na doped CTS and Li doped CTS thin films were observed between 9.050×10^{-11} cm/W for pure CTS thin film and 0.164×10^{-11} cm/W for $\text{Na}_{0.03}$ doped CTS and Li doped CTS thin film, respectively,

KEYWORDS - CTS, Na, Li target, PLD, Nonlinear optic

1. INTRODUCTION

Ternary chalcogenide structured copper tin sulphide (Cu_2SnS_3 -CTS) has been investigated and it has been observed that CTS shows low energy band gap, high absorption coefficient with high photostability. Because of these promising properties such as low cost, nontoxicity, easy processing methods and user-friendly behaviours, CTS is used in studies such as solar cells and photocatalysis applications including light-matter interaction studies as an n-type semiconductor. CTS thin films and alkali metal doped CTS thin films attract very great interest of researchers and gains very common works on it. It has been observed that properties of alkali metals doped CTS thin films for several applications, for example, solar cell, the conversion efficiency has dramatically increased compared to pure CTS. Due to these properties, the need to reveal the optical, electronic and nonlinear optical properties of CTS thin film and alkali metal doped CTS thin films has emerged. CTS structure contains non-toxic elements in its and CTS is known as ternary semiconductor and less complicated composition with ternary structure, at the same time, it has similar crystal structure as in CZTS. CTS is especially used in solar cell technology because it contains fewer elements compared to CZTS. One of its biggest advantages is that it consists of non-toxic and abundant elements in the world[1-3]. Due to its chemical and physical advantages, CTS has many application areas such as optics, photonics and electronics including solar cells, photodiodes, transistors, etc. and the nonlinear properties in intense laser light should be revealed.

Copper-containing chalcogenides structures belong to I, IV and VI semiconductors groups which they considered as high absorbance ratios [4, 5]. These materials have some special properties with lower photon energy values and higher absorbance performances to use them in optoelectronic applications [6]. Another key property for Cu-Sn-S structure is good candidate for nonlinear optical area. CTS can be produced from ternary compound elements consists of Cu, Sn and S elements. There are some different phase structures for CTS including Cu_3SnS_4 , Cu_4SnS_4 , and Cu_2SnS_3 [7], however Cu_2SnS_3 , structure is the most investigated phase due to effective absorber layer, p-type

conductivity as well as it has convenient photon energy range between 0.8 eV and 1.7 eV with about 10^5 cm^{-1} optical absorption coefficient [8-11].

Pulsed laser deposition (PLD) method is a well-known physical deposition technique to utilize production of thin, ultrathin films with high quality standards depending on changing laser, pressure, and deposition conditions. In this method, a laser beam with high-power standards must be focused on a material with pellet or target forms to deposit a substrate on film in the vacuum chamber [12]. The laser beam during the ablation process on the target is observed as plasma plume which these vaporized particles include ionized nanoform of materials. This is very suitable to deposit on a film substrate. Generally, an inert atmosphere or a vacuum condition prefers as a background pressure depending on experimental process [8]. Thin film production with the PLD technique has superior properties due to its flexibility to change parameters, not harming the environment since it takes place in a vacuum chamber, and not requiring a complex experimental setup [12].

Identifying new areas of use of CTS thin films, which are used in solar cell technology, especially in nonlinear optics technology including lasing [13], the usage of waveguide and other nonlinear devices will increase, and new technologies will be created [14], will contribute positively to the development of the technology. Determining of nonlinear absorption properties is a popular approach for the emerging materials to examine and reveals their performance on saturable absorber which is a key point for a laser cavity design to generate mode locking and Q-switching in ultrashort laser pulses. With this aim, in this study fs laser z-scan nonlinearity determination method was utilized to calculate of nonlinear characterisation of CTS, Na doped CTs and Li doped CTS films, in details. Femtosecond (fs) laser z-scan nonlinearity method give promising approaches to study of materials nonlinearities due to minimal thermal effects during experimental section[15].

The sodium (Na) and lithium (Li) contributions to CTS has made a positive contribution to the increase of the efficiency of the solar cell. Hence, in this study Na and Li which is known as the alkali element, was doped into the CTS target with %5 and %3 molar ratios, respectively to investigate contribution of nonlinearity properties. The PLD was used to form thin films productions and fs laser z-scan method was used to measure nonlinear optical responses [16].

Investigation of the nonlinear optical properties of the CTS, Na and Li doped CTS were carried out to determine of nonlinear absorption coefficient as well as. The XRD graphs were obtained for these thin films. Linear absorbance range between 400 nm and 1200 nm was drawn and photon energy band gap values were determined for CTS, Na and Li doped CTS as 1.11 eV, 1.12 eV and 1.04 eV and respectively. Thin film forms of materials give different, promising approaches to various aspects of technology including lasing, optical limiting, optical data storage, computing and optical communications apparatus [17].

2. MATERIALS AND METHODS

2.1 Ball milling of Na-doped CTS

Copper (Cu), Tin (Sn) and Sulphur (S) powders with the ratio of 2:1:3 rate as represented in figure 1a) was prepared and mixed with the %99.9 pure ratio in a stainless-steel container with 10 ml ethanol. This wet powder mixture was mixed by a ball milling device for 6 hours and then dried in a quartz tube under Argon (Ar) gas flow about 24 hours. This powder mixture was put into a special designed mold and pressed by a hydraulic press device at 30 bar pressures with a 100 g of 3 mm diameter size target as presented in figure 1b.

Cu_2SnS_3 target pellets were annealed at 600 °C for 2 hours by placing 100 mg of sulphur powder next to them and giving Ar gas in a quartz tube. The ball milling system (Desktop high speed vibrating ball milling) with a fixed speed of 1400 rpm (round per minute) was used for a time duration of 6 hours. Doped CTS structures were carried out mixing powder %5 Na and %1 Li in Copper (Cu), Tin (Sn) and Sulphur (S) powders to forms $\text{Na}_{0.05}\text{CTS}$, $\text{Li}_{0.01}\text{CTS}$ targets were attached to the CTS powder before pressing it into targets.

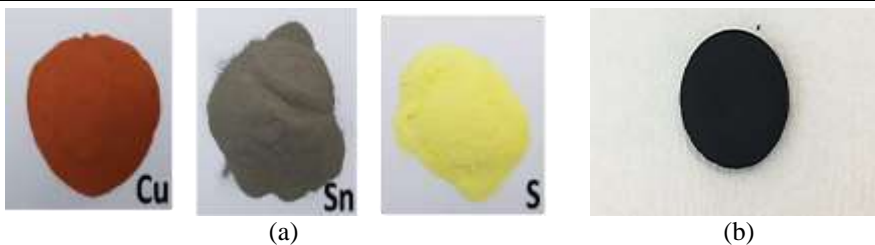


Figure 1. The images were taken from a) Cu, Sn and S powders and b) Cu_2SnS_3 target pellet

2.2. Pulsed Laser Deposition (PLD) System Details

The CTS, Na, Li doped CTS thin films was produced using homemade target which were prepared and synthesized ball milling technique. In this study, CTS, Na, Li doped CTS thin films were using a homemade PLD system are presented in figure 2a. The substrate was chosen as sodalime glass to deposit the targets of CTS, Na, Li doped CTS plasma. PLD system in high vacuum conditions was integrated to nanosecond (ns) Nd:YAG (Continuum, Surelite, NY, USA) laser system which has 5 ns pulse duration with a 10 Hz repetition rate by applying at 1064 nm laser beam wavelength. Experimental processes were given elsewhere in literature [18, 19]. Pulsed laser deposition details are given in table 1, in details.

Table 1. Pulsed laser deposition parameters

Parameters	Conditions for thin film production
Used laser type	Nd: YAG nanosecond laser system
Laser beam wavelength	1064 nm
Background Pressure of PLD vacuum chamber	10^{-6} mbar
Laser beam energy	15 mJ
Target- substrate distance	4 cm
Thin film deposition time	10 min
Annealing time, temperature, and atmosphere	10 min at 500°C with 50 mg of sulphur in evacuated oven

2.3. Femtosecond Laser Z-Scan Technique

In z-scan method, nonlinear optical properties of materials can be determined in two phenomenon self-focusing and self-defocusing processes. Different laser applications can be adapted to Quantronix, NY, Ti:Sapphire fs laser system. Figure 2b depicts the Z-scan setup in our lab, which typically comprises of two detector systems, open aperture studies, and closed aperture investigations. Before the z-scan operation began, incident laser power was measured using a reference detector. Moving the materials between the positive and negative ends of the optical axes in a stage along the optical axis to pass through the focus point of the Gaussian beam is how the z-scan measuring technique works. The sample's refractive index and absorption correlation both change as a function of the beam distribution.

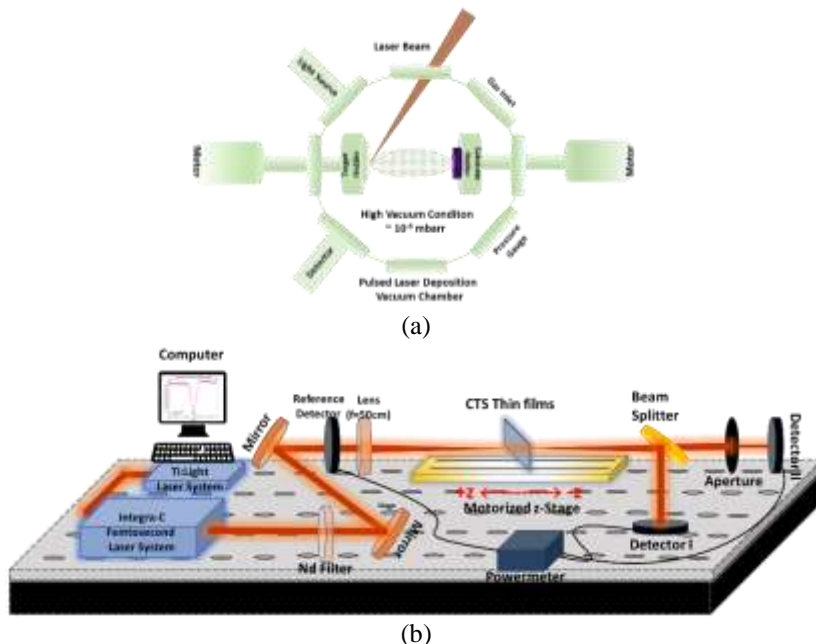


Figure 2. CTS, Na Doped CTS and Li Doped CTS Thin Films were produced using a) Pulsed laser deposition system, which is shown as schematic representation, and b) were characterized with fs laser z-scan technique which is represented experimental setup.

3. RESULTS AND DISCUSSION

3.1. UV-Vis-IR Absorbance Performance of CTS, Na Doped CTS and Li Doped CTS Thin Films

In this study, linear absorbance values have been calculated using UV-Vis spectroscopy to carry out of CTS, Na and Li doped CTS thin films linear optical properties. The spectra shows that these thin films absorbance range from 400 nm to 1200 nm wavelengths in fig. 3a. The absorption intensity in visible region is higher than that in the infrared region for all thin films. The Tauc equation as given in equation 1 was applied obtained absorbance spectra to determine photon energy band gap values. The band gap values of thin films are calculated using Tauc curve in equation 1,

$$(ahv)^2 = A(hv - E_g)^{1/2} \tag{1}$$

where E_g is called as photon energy band gap value of NPs, hv and A are photon energy value and constant value, E_g is determined by straight line of $(ahv)^2$ versus (hv) in Tauc plot in figure 3b. The photon energy band gap values have been determined using equation (1), which are calculated as 1.11 eV, 1.12 eV and 1.04 eV for CTS, Na and Li doped CTS, respectively.

3.2. X-ray crystallography (XRD) Structures of CTS, Na_{0.03} Doped CTS and Li_{0.01} Doped CTS Thin films

Fig. 4 (a-b) shows the deposited CTS, Na_{0.03} Doped CTS and Li_{0.01} Doped CTS Thin films XRD patterns which they obtained annealing process in evacuated oven at 500 °C about 10 minutes with 50 mg sulphur medium. The crystallization of the pure, Na and Li doped CTS thin films presents as main peaks in $2\theta = 28.9^\circ, 33.4^\circ, 47.8^\circ$ and 56.6° degrees consistent with (112/222), (200/040), (220/044) and (321/262), respectively.

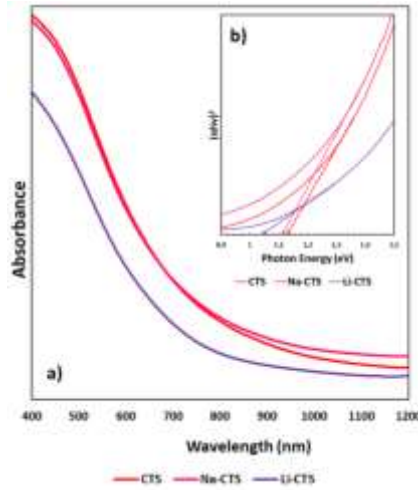


Figure 3. Pure CTS, Na doped CTS and Li doped CTS thin films **a)** Uv-Vis-IR absorbance spectrum, **b)** photon energy band gap values.

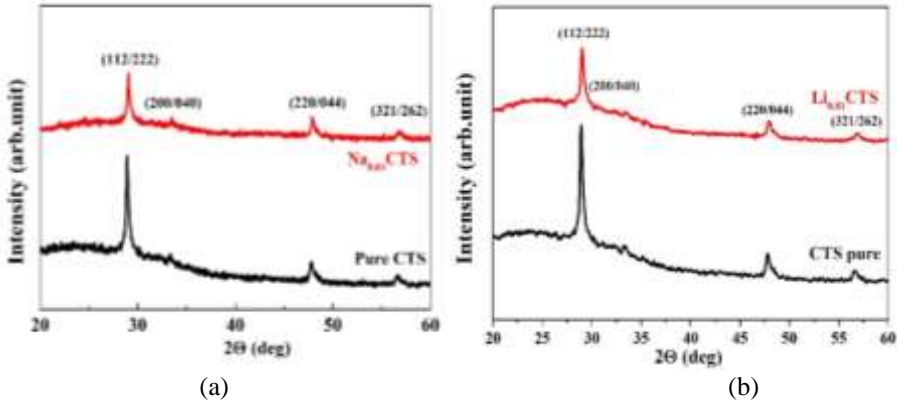


Figure 4. XRD patterns comparing for a) pure CTS, Na_{0.03} Doped and b) pure CTS, Li_{0.01} Doped CTS thin films were annealed for 10 min at 500°C with 50 mg of sulphur in evacuated oven.

Z-scan Nonlinearities of CTS, Na_{0.03} Doped CTS and Li_{0.01} Doped CTS Thin Films

The experimental findings of open and closed apertures, that are employed to evaluate nonlinear optical characteristics in z-scan curves, change depending on the sample location dependency of laser intensity. Data from both open and closed apertures were modelled using equations (2) and (3), respectively.

$$T_{open}(x) = (\beta I_0 L_{eff} / 2.83)(1/x^2) \tag{2}$$

$$T_{closed}(x) = 1 + (4\Delta\Phi_0 x / (x^2+9)(x^2+1)) \tag{3}$$

L_{eff} is specified as $(1 - e^{-\alpha L}) / \alpha$ [20] and closed aperture z-scan data was fitted to equation (3) where $x = z / z_0$ in which z is the location of thin films and z_0 is defined as $\pi\omega_0^2/\lambda$ and known as Rayleigh range. $\Delta\Phi_0$ has measured by following equation;

$$\Delta\Phi_0 = 2\pi / \lambda (n_2 I_0 L_{eff}) \tag{4}$$

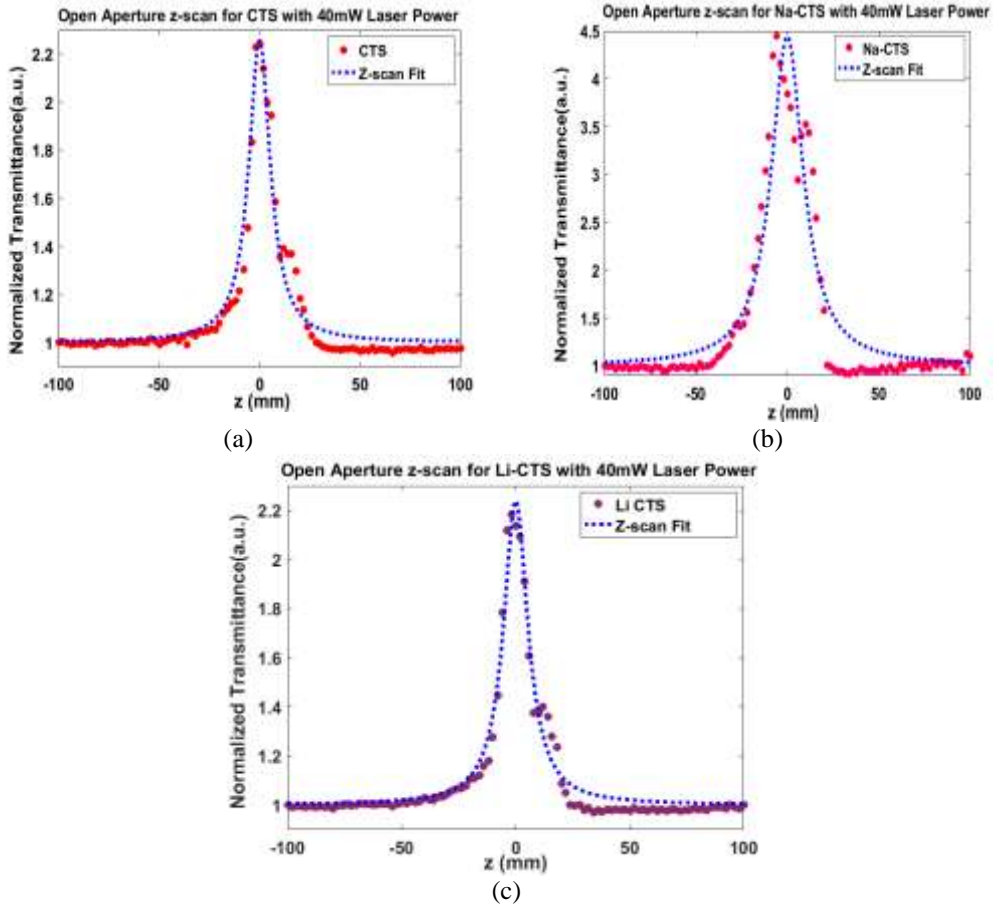


Figure 5. Open aperture z-scan plottings were obtained using 40 mW laser for a) pure CTS, b) Na doped CTS and c) Li doped CTS.

In equations, ω_0 is examined as the beam waist at the focusing point, λ is consistently referred as the wavelength, in laser intensity for beam is I_0 , and the linear absorption value represented as α [20]. Open aperture data in fs laser z-scan for CTS, Na doped CTS and Li doped CTS thin films have been fitted applying experimental data exhibits in fig. 5 (a-c). Numerical results for these thin films are exhibited in table 1.

Table 1. List of calculated β parameters for CTS, Na doped CTS and Li doped CTS thin films using fs laser z-scan method at a power intensity of 9.50×10^{11} (W/cm²).

Sample Name	α (abs)	β ($\times 10^{-11}$ cm/W)
Pure CTS	3.460	9.050
Na _{0.03} doped CTS	3.430	0.164
Li _{0.01} doped CTS	2.867	0.604

4. CONCLUSION

In this study, pulsed laser deposition technique was used to obtain pure CTS, Na_{0.03} Doped CTS and Li_{0.01} Doped CTS Thin Films. These thin films are generally produced for solar cells, diodes or transistors applications. Nonlinear optical properties of these thin films have been carried out and saturable absorbance behaviors were observed for thin films. Open aperture results show saturable absorption trend in 9.50×10^{11} W/cm² laser intensity. The nonlinear absorption coefficients (β) were observed between 9.050×10^{-11} cm/W for pure CTS thin film and 0.164×10^{-11} cm/W for Na_{0.03} doped CTS and Li doped CTS thin film, respectively,

Z-scan method serves as a promising method to study the nonlinearities in NPs depends on applications. Understanding these nonlinear optical characteristics will help you make more informed decisions about how to employ CTS thin films to open up new applications like lasing, waveguides, and other nonlinear devices will broaden the range of uses for technology.

ACKNOWLEDGEMENT

Authors kindly would like to thank

-Selçuk University Scientific Research Project (BAP) Coordination for the support with the number 13301022 and 22705063 projects,

-Selçuk University, High Technology Research and Application Center (İL-TEK) and SULTAN Center for infrastructures.

REFERENCES

1. Chierchia, R., et al., *Cu₂SnS₃ based solar cell with 3% efficiency*. *physica status solidi (c)*, 2016. 13(1): p. 35-39.
2. Zhang, H., et al., *Fabrication of highly crystallized Cu₂SnS₃ thin films through sulfurization of Sn-rich metallic precursors*. *Journal of Alloys and compounds*, 2014. 602: p. 199-203.
3. Chantana, J., et al., *Investigation of carrier recombination of Na-doped Cu₂SnS₃ solar cell for its improved conversion efficiency of 5.1%*. *Solar Energy Materials and Solar Cells*, 2020. 206: p. 110261.
4. Giaccherini, A., G. Montegrossi, and F. Di Benedetto, *Stability of naturally relevant ternary phases in the Cu–Sn–S system in contact with an aqueous solution*. *Minerals*, 2016. 6(3): p. 79.
5. Rahaman, S., et al., *Optimization and fabrication of low cost Cu₂SnS₃/ZnS thin film heterojunction solar cell using ultrasonic spray pyrolysis*. *Optical Materials*, 2022. 123: p. 111838.
6. Yadav, S.M. and A. Pandey, *Highly efficient and broadband hybrid photodetector based on 2-D layered graphene/CTS quantum dots*. *IEEE Transactions on Electron Devices*, 2019. 66(8): p. 3417-3424.
7. Fernandes, P., P. Salomé, and A. Da Cunha, *A study of ternary Cu₂SnS₃ and Cu₃SnS₄ thin films prepared by sulfurizing stacked metal precursors*. *Journal of Physics D: Applied Physics*, 2010. 43(21): p. 215403.
8. Vanalakar, S., et al., *Fabrication of Cu₂SnS₃ thin film solar cells using pulsed laser deposition technique*. *Solar Energy Materials and Solar Cells*, 2015. 138: p. 1-8.
9. Ashebir, G.Y., et al., *Solution-processed extremely thin films of Cu₂SnS₃ nanoparticles for planar heterojunction solar cells*. *Journal of Physics D: Applied Physics*, 2020. 53(11): p. 115101.
10. Olgar, M., *Improvement in the structural and optical properties of Cu₂SnS₃ (CTS) thin films through soft-annealing treatment*. *Superlattices and Microstructures*, 2020. 138: p. 106366.
11. Chen, Q., et al., *Study and enhance the photovoltaic properties of narrow-bandgap Cu₂SnS₃ solar cell by p–n junction interface modification*. *Journal of colloid and interface science*, 2012. 376(1): p. 327-330.
12. Gezgin, S.Y., A. Houimi, and H.Ş. Kılıç, *Production and photovoltaic characterisation of n-Si/p-CZTS heterojunction solar cells based on a CZTS ultrathin active layers*. *Optik*, 2019. 199: p. 163370.

13. Medishetty, R., et al., *Nonlinear optical properties, upconversion and lasing in metal–organic frameworks*. Chemical Society Reviews, 2017. 46(16): p. 4976-5004.
14. Hoque, M.I.U., et al., *One-dimensional Sn (IV) hydroxide nanofluid toward nonlinear optical switching*. Materials Horizons, 2020. 7(4): p. 1150-1159.
15. Gündoğdu, Y., H.Ş. Kılıç, and M. Çadırcı, *Third order nonlinear optical properties of CdTe/CdSe Quasi Type-II Colloidal Quantum Dots*. Optical Materials, 2021. 114: p. 110956.
16. Amina Houimi, S.Y.G., Hamdi Şükür Kılıç, *The effect of sodium (Na) doping on the performance of n-Si/Cu₂SnS₃ heterojunction solar cells deposited by PLD using a homemade target*. Optik, 2022. 169364.
17. Zhang, Y.-x. and Y.-h. Wang, *Nonlinear optical properties of metal nanoparticles: a review*. RSC advances, 2017. 7(71): p. 45129-45144.
18. Gezgin, S.Y., et al., *Determination of photovoltaic parameters of CIGS hetero junction solar cells produced by PLD technique, using SCAPS Simulation Program*. Submitted to Vacuum 2021.
19. Kılıç, H.Ş., et al., *Nonlinear optical properties of Cu₂ZnSnS₄ nanocrystal thin films and its constituents thin films*. Optical and Quantum Electronics, 2021. 53(1): p. 1-11.
20. Wang, X., et al., *Third-order nonlinear optical properties of a novel series of D-π-A pyrene-aldehyde derivatives*. Journal of Nonlinear Optical Physics & Materials, 2016. 25(02): p. 1650014.

Optimization of S-wave Prediction Method in Mahu Area and Its Influence on Calculation of Rock Mechanics Parameters

Song WANG¹, Lixiao XIAO^{2✉}, Huiyong YU¹, Jiayan LI¹, Jun HU³

¹ Engineering Technology Research Institute, Xinjiang Oilfield Company, PetroChina, Karamay-CHINA

² China University of Petroleum, Enhanced Oil Recovery Institute, The Unconventional Oil and Gas Institute, Beijing-CHINA

³ Beijing Sunshine GIEC Technology Co, Ltd, Beijing-CHINA

ABSTRACT

In view of the absence of S-wave velocity, an important geophysical parameter and the low accuracy of empirical formula in actual production, taking the Mahu area as an example, the Xu-White model was finally selected by screening and analyzing the theoretical model of S-wave prediction, the geological depositional setting and burial depth were considered, S-wave velocity curve was calculated according to mineral composition, porosity and fluid composition curves, and the influence of the accuracy of S-wave velocity prediction on the calculation results of rock mechanics parameters was studied. After verification with measured dipole acoustic data, indoor core mechanical measurement data, and fracturing operation data, compared with the results calculated by conventional empirical formula, the accuracy of Xu-White model was greatly improved. The model was generally applicable to the glutenite stratum in the Baikouquan Formation, Mahu area. This technology has proven to be highly effective in the accurate calculation of rock mechanics parameters and the fracturing scheme design of glutenite tight oil reservoir. It is of great significance to the study on the geology-engineering integration in the development of tight oil in Mahu area.

KEYWORDS - *S-wave prediction, rock mechanics parameters, acoustic logging, Xu-White model, tight oil, Mahu Area.*

1. INTRODUCTION

P-wave and S-wave velocities are important parameters for the interpretation of geophysical data. P-wave and S-wave velocities can be used to identify lithology, determine fluid properties, calculate porosity and predict fracture distribution, etc. The various parameters of rock mechanics, such as Poisson ratio, Young's modulus, shear modulus, bulk modulus and compressibility are also obtained by P-wave and S-wave velocities. The magnitude and direction of present in-situ stress can be predicted by combining with drilling data. Based on the prediction of P-wave and S-wave velocities, the characteristics of in-situ stress, borehole stability, sand production analysis and artificial fracturing scheme design are studied. The P-wave velocity comes from the time lag of conventional logging and it is easier to obtain, while the S-wave velocity derived from array acoustic logging is usually only performed in a few key wells in a block due to measurement cost. The P-wave and S-wave velocity curves of all wells are needed to predict the distribution of geological "sweet spots", accurately calculate rock mechanics parameters and in-situ stresses. In the past work, the S-wave velocity is usually calculated with polynomial regression and empirical formula. However, the rock physical properties of the stratum are not considered in calculation S-wave velocity, and result large errors. Therefore, obtaining accurate S-wave velocity curve is one of the key problems in oil and gas reservoir exploration and development.

Although it is extremely complex for the factors which affect the actual underground rock velocity, shear wave logging and conventional logging usually have similar response characteristics and certain correlation for the same rock sample or sample point. At present, the empirical formula method is the most commonly used method for S-wave velocity prediction, that is to use the relationship between p-wave and S-wave velocities for performing regression. There is a linear relationship between P-wave and S-wave velocities and the main representatives were Castagna et al^[1]. Han^[2] and Tosaya^[3] believed that the S-wave velocity had a linear relationship with porosity

and shale content. However, the empirical formulas for above calculating shear wave velocity were obtained only by laboratory tests, and the biggest problem of the formulas is that it does not consider the rock physical properties or it simplifies the rock physical model, resulting in large error and poor universality. Another type of S-wave velocity prediction method is the forward modeling based on P-wave velocity and rock physics model. Currently, methods such as Greenberg-Castagna^[4], Cemented^[5], MudRock, Unconsolidated^[6], Xu-White^[7], CriticalPhi^[8], Krief^[9], Self-consistent^[10], Vernik^[11] and SoftPorosity^[12-13] are the most commonly used. Among them, the first four models are suitable for medium and -high pore formations, while the last six models are suitable for medium and low pore formations. In practical work, an appropriate model is firstly selected according to the characteristics of strata and reservoirs in the study area. And then the relevant information of strata, including rock mineral type, content, pore type and porosity, particle contact relationship, fluid and saturation, temperature and pressure, etc, is input into the model to form a unique rock physical model in the study area^[14-17]. In the end, forward modeling is performed on this unique model to obtain accurate S-wave velocity data in the study area^[18]. This method effectively solves the drawbacks of the empirical formula methods, and the calculation results are more accurate. In recent years, it has been more and more widely used in S-wave velocity prediction.

2. OPTIMAL METHOD OF PREDICTING S-WAVE VELOCITY

The tight sand and conglomerate reservoir of the Triassic Baikouquan Formation in Mahu area is a key block in the production capacity construction of Xinjiang Oilfield in recent years, with the characteristics of large geological reserves and deep burial. The reservoir is mainly developed in the sand and conglomerate of sheet-like traction currents and underwater distributary channels in the front of the fan delta. The burial depth is 2500~3000 m, and the pore types are dominated by remaining intergranular pores and intragranular dissolved pores, which are generally characterized by medium-low porosity and permeability.

According to the lithology, reservoir physical properties, burial depth and other geological conditions of Triassic Baikouquan Formation in the study area, six models suitable for medium-low porosity formations were selected as the basis of S-wave velocity prediction. The measured S-wave velocity data of Well M15 and Well M131 were used for calibration and verification respectively, and as a result, the S-wave prediction method and petrophysical parameters suitable for the target layer in the area were optimized.

The comparison between the predicted S-wave velocity curves and the measured S-wave velocity curves of the Well M15 and the Well M131 by six petrophysical models are shown respectively in Figure 1 and Figure 2. From the perspective of the curve shape, the S-wave velocity curve predicted by the Xu-White method almost overlaps with the measured S-wave velocity with the highest similarity. The comparison of the error statistics and correlation coefficients between the predicted S-waves and the measured S-waves by six methods is shown in Table 1. From the perspective of data accuracy, the average relative error of the Xu-White method is only 2.8%, and the correlation coefficient square between the predicted S-wave and the measured S-wave reaches a level of 0.9101, which is ahead of other methods. The Xu-White method is more suitable for S-wave velocity prediction of Triassic Baikouquan Formation in Mahu area based on the comparison of logging curve morphology, error and correlation coefficient.

The Xu-White method is a sand-mudstone mixing model based on the Kuster-Toksöz theory, the differential effective medium (DEM) theory and the Gassmann equation^[19]. The influence of clay composition, pressure, cementation and other factors on acoustic wave is attributed to the difference of pore geometry and face ratio between shale and sandstone, considering the rock porosity and clay content to predict sound wave velocity. Assuming that rock pores are mainly composed of sandstone pores and mudstone pores, the ellipsoids with different aspect ratios are used to simulate these two kinds of pores^[20-23]. Because of the large aspect ratio, the pores closed to the spherical shape are often more stable and less prone to deformation, and they are called hard pores. The sandstone

contains relatively hard pores with an aspect ratio of 0.10 to 0.15, while the aspect ratio of clays is about 0.02 to 0.05. The elastic modulus of dry rock skeletons is obtained by using the Kuster-Toksöz model in Xu-White method. Assuming that the Poisson’s ratio of the rock skeleton does not vary with porosity, the solution of Kuster-Toksöz equation based on DEM theory is transformed into solving linear ordinary differential equations, so as to obtain the elastic modulus of the rock skeleton. Afterwards, the Gassmann equation is used to calculate the bulk modulus and shear modulus of fluid-saturated rocks, and then the S-wave and P-wave velocities are calculated by simulation. Due to taking into account factors such as the content of sand and mudstone, pore types and other differences, the Xu-White model is closer to the actual geological situation, so the accuracy of calculating S-wave velocity is higher than that of other models, which is more suitable for the prediction of S-wave velocity of the Baikouquan Formation in Mahu area.

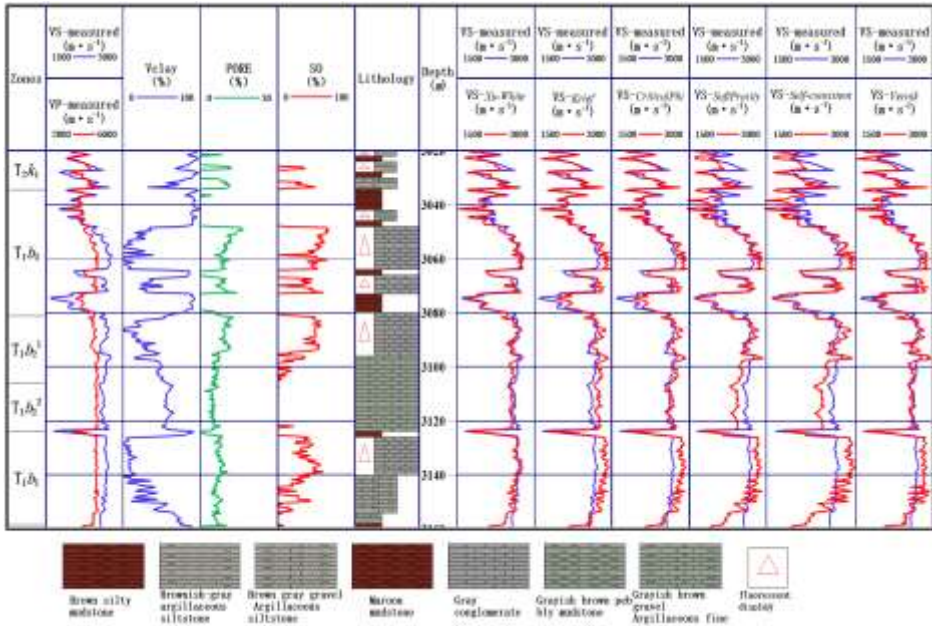


Figure 1. The comparison of curves of predicted and measured S-waves by different methods in Well M15

In order to further verify the applicability of the Xu-White model in Mahu area, the measured S-wave data of Well FN15 and Well XIA93 located in adjacent blocks of the study area were projected onto the P-wave velocity and S-wave velocity intersection plates of Well M15 and Well M131, as shown in Figure 3. The relationship of P wave and S wave of the two test Wells is exactly consistent with that of Well M15 and Well M131, and the value range is also the same, indicating that there has good applicability and accuracy of the S-wave velocity prediction method in the Baikouquan Formation in Mahu area and it can be used for S-wave velocity prediction of other wells in this region. As a consequence, the Xu-White model provides a data basis for geophysical reservoir prediction and precise calculation of rock mechanical parameters.

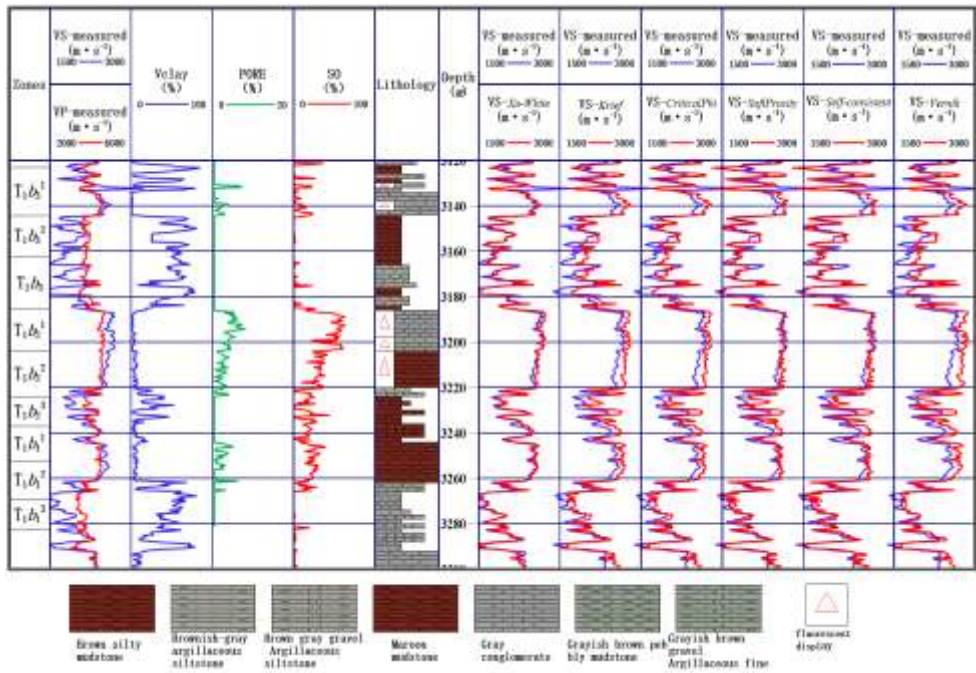


Figure 2. The comparison of curves of predicted and measured S – waves by different methods in Well M131

Table 1. The comparison of error statistics and correlation coefficients between predicted and measured S-waves by different methods

Method of prediction	Minimum Velocity (m·s ⁻¹)	Maximum velocity (m·s ⁻¹)	Average velocity (m·s ⁻¹)	Average absolute error(m·s ⁻¹)	Average relative error (%)	Correlation coefficient R ² (Dimensionless)
Measured S-Wave	1584.2	2784.9	2522.4	0.0	0.0	1.0000
Xu-White	1520.3	2807.5	2473.7	68.1	2.8	0.9101
Krief	1587.6	2949.9	2634.9	121.7	4.9	0.8892
CriticalPhi	1595.2	2943.3	2610.0	104.1	4.2	0.8882
SoftProsity	1421.5	2928.7	2479.0	140.5	5.7	0.8063
Self-consistent	1428.3	2978.1	2502.3	160.4	6.4	0.7830
Vernik	1472.6	2947.6	2544.9	98.0	4.0	0.8832

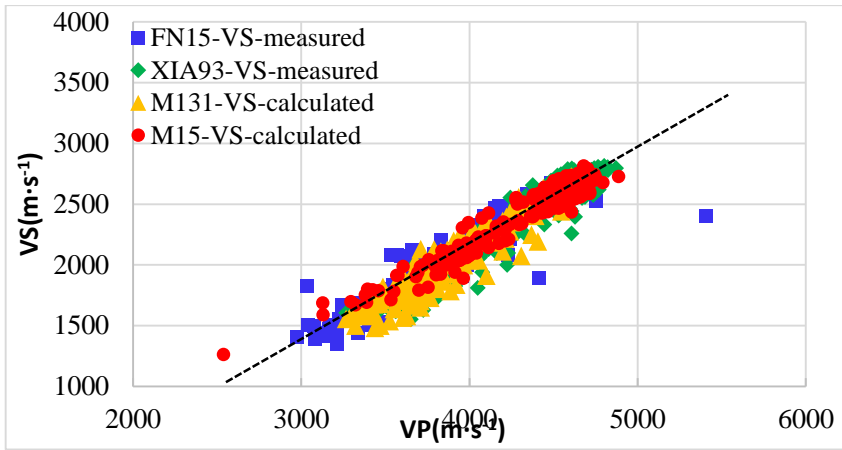


Figure 3. The multi – well verification for the S-wave velocity prediction methods in Baikouquan Formation in the Mahu Area

3. CALCULATION OF ROCK MECHANICS PARAMETERS AND ERROR ANALYSIS

The rock elastic parameters and the rock mechanical strength parameters are commonly used in engineering as rock mechanics parameters, of which the rock elastic parameters like Poisson's ratio and Young's modulus are independent parameters, and their calculation requires accurate P-wave velocity and S-wave velocity.

Poisson's ratio is the ratio of the transverse strain to the longitudinal strain:

$$\nu = \frac{V_p^2 - 2V_s^2}{2(V_p^2 - V_s^2)} \tag{1}$$

Young's modulus is the ratio of the applied axial stress to the normal strain:

$$E = \rho V_s^2 \frac{(3V_p^2 - 4V_s^2)}{(V_p^2 - V_s^2)} \tag{2}$$

The rock mechanical strength parameters include the uniaxial compressive strength, the internal friction coefficient and the formation fracture pressure. The uniaxial compressive strength is the ultimate failure strength under compression in one direction:

$$\text{Sandstone: } UCS = 1200e^{-0.036\Delta t} \tag{3}$$

$$\text{Mudstone: } UCS = 72.5V_p^3 \tag{4}$$

The coefficient of internal friction is the tangent of the inclination angle of the shear strength line in the $\sigma - \tau$ coordinate plane.

$$\mu = \tan \left[\arcsin \left(\frac{V_p - 1}{V_p + 1} \right) \right] \tag{5}$$

The fracture pressure of the formation is the maximum pressure that the formation can be tolerated when the formation fractures:

$$p_f = \frac{\nu}{1-\nu} S_v + \frac{1-2\nu}{1-\nu} \alpha p_p + \frac{E}{1-\nu^2} \varepsilon_x + \frac{\nu E}{1-\nu^2} \varepsilon_y \quad (6)$$

In the formula: ν , Poisson's ratio; V_p , the rock P-wave velocity, m/s; V_s , the rock S-wave velocity, m/s; E , Young's modulus, Pa; ρ , the rock bulk density, kg/m³; UCS , the rock uniaxial compressive strength, Pa; Δt , the acoustic time difference, m/s; μ , the internal friction coefficient; p_f , the formation fracture pressure, Pa; S_v , the overlying rock pressure, Pa; α , the Biot coefficient; p_p , the formation pressure, Pa; ε_x , ε_y , the construction coefficients.

The rock mechanics parameters are the key parameters in the fracturing design for the development of tight oil and gas reservoirs and shale oil and gas reservoirs, which are extremely important for the study of rock fractures, hydraulic fracture extension and fracture geometries. The S-wave velocity in traditional rock mechanics parameter calculation method is mainly calculated by empirical formulas related to lithology, or directly converted from the P-wave velocity through the data regression relationship between the limited measured P-wave velocity and the S-wave velocity. As a result, there are large errors due to the above calculation method of S-wave velocity, and it will directly affect fracturing design and construction of tight oil reservoirs in Mahu area. According to the actual data of the target layer in Well M15, the above conventional empirical method was used to calculate the S-wave velocity, and the optimized Xu-White rock physics model was used to predict the S-wave velocity curve for comparative analysis. Consequently, the rock mechanics parameters in Mahu area were respectively calculated and calibrated with the laboratory core mechanical measurement data. The results are shown in Figure 4.

As shown in Figure 4, the Poisson's ratio and formation fracture pressure are relatively small, while the Young's modulus is relatively large, which are calculated with the S-wave velocity obtained by the conventional method. For example, the Poisson's ratio of the mechanical experiment results in Well M15 with a depth of 3063.04 m is 0.239. The Poisson's ratio calculated with the S-wave velocity obtained by conventional method is 0.186, with a relative error of more than 20%. However, the Poisson's ratio obtained by the optimized Xu-White method for the S-wave velocity calculation is 0.234 with the relative error of 2%, and the calculation results are more accurate than that of the conventional method. The formation fracture pressures of the mechanical experiment results in the Well M15 are respectively 51.1MPa and 56.5MPa, with the depths of 3063.04 m and 3065.20 m. The formation fracture pressures calculated by the conventional method of S-wave velocity are 48.3 MPa and 50.9 MPa, with the relative errors all over 5%, while the formation fracture pressures calculated by Xu-White method are 50.9 MPa and 58.7 MPa, with relative errors of 0.4% and 3.9%, which also have a higher accuracy.

It is often required to hydraulic fracture for improving single-well production and even stage fracturing is also required when transforming longer horizontal well sections in low-porosity and permeability reservoirs, especially tight oil reservoirs. Young's modulus, Poisson's ratio, horizontal formation stress and other parameters have played an important role in the design of the downhole fracturing construction schemes, and with the help of them, the parameters such as construction pump pressure and fracturing fluid displacement can be calculated more accurately. Consequently, the length, width and height of the fractures produced in the fracturing process can be reasonably controlled. In the end, it can avoid the phenomenon that the target formation cannot be opened, or the pressure is too large and then cause the interlayer being pressed to develop fresh water channeling, and avoid resulting in unnecessary losses. Therefore, the fracturing operation parameters, fracturing scale and fracturing method of the reservoir can be reasonably designed by analyzing the formation stress and rock mechanical properties before hydraulic fracturing.

According to the calculation results of the optimized Xu-White method, the uniaxial compressive strength of the sand and conglomerate in the Baikouquan Formation in Mahu area is 70~120MPa, the Young's modulus is about 40 GPa, the Poisson's ratio is about 0.250, the internal friction coefficient is 0.8~0.9 and the formation fracture pressure is 47.0~55.0 MPa. At the same time, it is determined that the formation fracturing pressure at the depth of 3056 m in Well M15 is about 50.0 MPa in the actual fracturing process. The calculation results of rock mechanics show that the formation fracture pressure predicted by the conventional empirical method at the depth point is 47.5 MPa, and that predicted by the Xu-White method is 49.7 MPa, which is more consistent with the actual fracturing construction data.

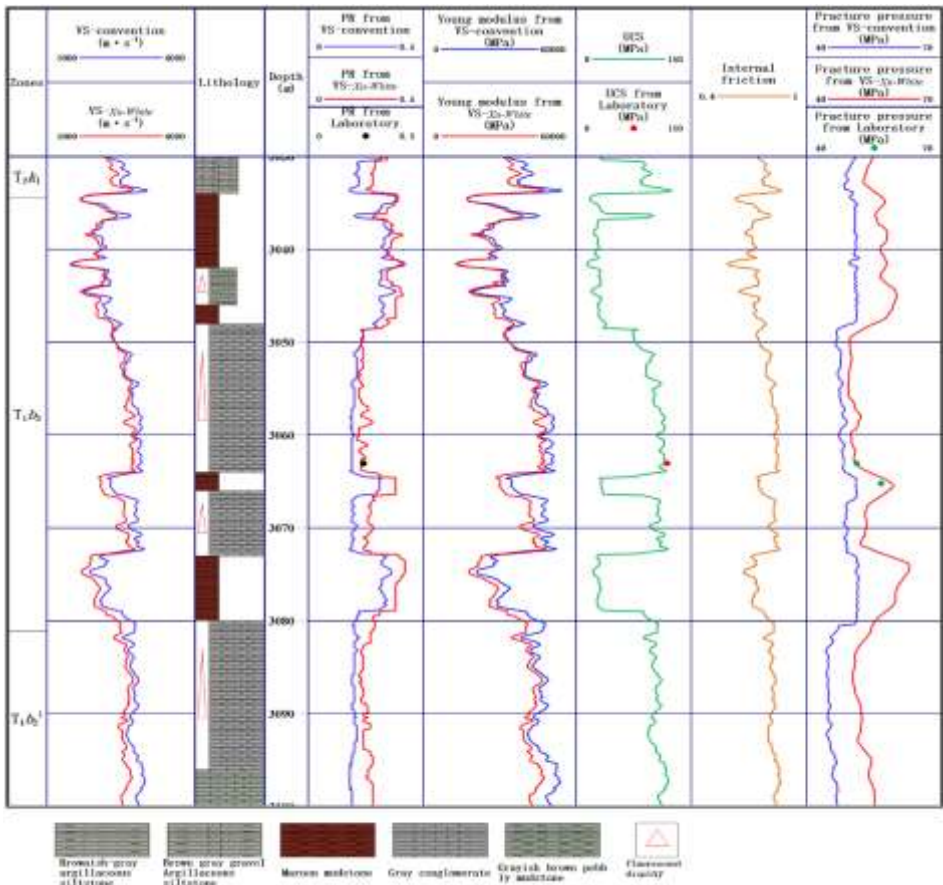


Figure 4. The profile of rock mechanics parameters calculated by two methods in Well M15

Through the above example calculations, the accuracy of the S-wave velocity determines the calculation accuracy of rock mechanics parameters, and further influences the fracturing scheme design of tight oil reservoir. For Mahu area, the S-wave velocity curve that is more in line with the actual formation characteristics can be obtained through the optimized Xu-White prediction model, by fully considering the formation rock types, shale content, pore types and porosity, and then high-precision rock mechanics parameters can be obtained as well. After multiple verifications of rock mechanics experiment and fracturing construction data, the Xu-White prediction model can depict the geological and mechanics characteristics of the actual formation more accurately and

realistically, which is helpful to optimize the scale and displacement of fracturing and other key construction parameters in order to improve the effectiveness of fracturing.

4. CONCLUSION

- (1) The rock mechanics parameters are greatly affected by the accuracy of S-wave velocity calculations, so it is necessary to optimize the appropriate S-wave velocity prediction method and parameters calculation method according to the different geological characteristics of research areas.
- (2) According to the comparison and analysis of the measured dipole acoustic wave data, the strict calibration of rock mechanics parameters and the inspection of fracturing construction results, the Xu-White S-wave velocity prediction method has good applicability in Mahu area to calculate rock elastic parameters with higher accuracy and better using for subsequent fracturing scheme design in tight oil reservoirs.
- (3) This paper preliminarily forms a complete set of technical system for high-precision S-wave prediction of rock physics, rock mechanics and fracturing scheme design, which plays a demonstration role in the integrated research of geological and engineering for the development of the tight oil reservoirs in Mahu area.

REFERENCES

- [1] Castagna J P, Batzle M L, Eastwood R L. Relationships between compressional-wave and shear-wave velocities in clastic silicate rocks[J]. *Geophysics*, 1985,50(4):571-581.
- [2] Han D, Nur A, Morgan D. Effects of porosity and clay content on acoustic properties of sandstones and unconsolidated sediments[J]. *Geophysics*, 1986,51(11):2093-2107.
- [3] Tosaya C, Nue A. Effect of diagenesis and clay on compressional velocities in rocks[J]. *Geophysical Research Letters*, 1982,9(1):5-8.
- [4] Greenberg M L, Castagna J P. Shear-wave velocity estimation in porous rocks: theoretical formulation, preliminary verification and applications[J]. *Geophysical Prospecting*, 1992,40(2):195-209.
- [5] Dvorkin J, Nur A, Yin H. Effective properties of cemented granular materials[J]. *Mechanics of Materials*, 1994,18(4):351-366.
- [6] Gassmann F. Uber die Elastizitat poroser Medien[J]. *Vier Der Natur Gesellschaft in Zurich*, 1951,96(4):1-23.
- [7] Xu S Y, White R E. A new velocity model for clay-sand mixtures[J]. *Geophysical Prospecting*, 1995,43(1):91-118.
- [8] Nur A, Marion D, Yin H. Wave velocities in sediments[OL]. *MRS Online Proceedings Library*, 1990,195(1):459-469.
- [9] Krief M, Garat J, Stellingwerff J, et al. A petrophysical interpretation using the velocities of P and S waves (full-waveform sonic)[J]. *The Log Analyst*, 1990,31(6):355-369.
- [10] Hill R. A self-consistent mechanics of composite materials[J]. *Journal of Mechanical Physics of Solids*, 1965,13(4):213-222.
- [11] Vernik L. Acoustic velocity and porosity systematics in siliciclastics[J]. *The Log Analyst*, 1998,39(4):27-35.
- [12] Ruiz F, Cheng A. A rock physics model for tight gas sand[J]. *The Leading Edge*, 2010,29(12):1484-1489.
- [13] Chen Y H, Hu J, Jiang LC, et al. Quantitative Prediction of Fractured Porosity by Using Conventional Logging Curves[J]. *Special Oil & Gas Reservoirs*, 2017,24(6):7-11.
- [14] Parvizi S, Kharrat R, Asef M.R, et al. Prediction of the Shear Wave Velocity from Compressional Wave Velocity for Gachsaran Formation[J]. *Acta Geophysica*, 2015,63(5):1231-1243.

-
- [15] Ai-Dousari M, Garrouch A A, Ai-Omair O. Investigating the dependence of shear wave velocity on petrophysical parameters[J]. Journal of Petroleum Science & Engineering, 2016, 146(4):286-296.
- [16] Yan F, Han D H. Effect of pore geometry on Gassmann fluid substitution[J]. Geophysical Prospecting, 2015,64(6):1575-1587.
- [17] Xiong X, Lin K, He Z. A method for S-wave velocity estimation based on equivalent elastic modulus inversion[J]. Oil Geophysical Prospecting, 2012, 47(5):723-727.
- [18] He F B, You J. Gas sand distribution prediction by prestack elastic inversion based on rock physics modeling and analysis[J]. Applied Geophysics, 2011,8(3):197-205.
- [19] Kuster G T, Toksöz M N. Velocity and attenuation of seismic waves in two phase media: Part1, Theoretical formulation[J]. Geophysics, 1974,39(5):587-606.
- [20] Jorstad A, Mukerji T, Mavko G. Model-based shear-wave velocity estimation versus empirical regressions[J]. Geophysical Prospecting, 2010,47 (5):785-797.
- [21] Zhang Y. Estimating Seismic Wave Velocity Using Xu-White Model[J]. Journal of Chengdu University of Technology: Natural Science Edition, 2005,32(2):8.
- [22] Shi S H, Deng Z W, Liu L P, et al. Uncertainty of shear wave velocity prediction by Xu-White model[J]. Coal Geology & Exploration, 2015,43(5):95-99.
- [23] Bai J Y, Song Z X, Xie S, et al. Error analysis of shear wave velocity prediction based on Xu-White model[J]. Xinjiang Oil and Gas, 2011, 7(3):6.

Investigation of interaction of some iron minerals with gamma rays using XCOM database

Osman GÜNAY^{1*}, Hakan AKYILDIRIM², Kadir GÜNOĞLU³, İskender AKKURT²

¹ Yildiz Technical University, Faculty of Electrical and Electronics Engineering, Department of Biomedical Engineering, Istanbul- TURKEY

² Suleyman Demirel University, Science Faculty, Physics Department, Isparta-TURKEY

³ Isparta Applied Science University, Technical Sciences Vocational School, Isparta- TURKEY
*o.gunay@yildiz.edu.tr

ABSTRACT

With the discovery of radiation and the effect of developing technology, radiation finds a wide range of uses. Due to the use of radiation in many areas, radiation protection methods have gained importance in order to reduce the harmful effects on humans and the environment. These methods are time, distance and shielding. One of these three principles, the shield, is the generality of different types of materials placed between a person or a system and radiation. In this study, it is aimed to determine the shielding properties by examining the interactions of hematite and magnetite minerals, which contain high iron element, with gamma radiation. The interactions of the minerals were determined theoretically using the web version of the XCOM photon section database.

KEYWORDS: hematite, magnetite, mass attenuation coefficient, XCOM database

1. INTRODUCTION

With the increasing use of gamma radiation in various applications such as industry, medicine, agriculture, nuclear reactors and particle accelerators, the exposure for longer duration of these radiations can cause very harmful effects on human health. Therefore, the use of shielding becomes a paramount thing to use these radiations without risk. A variety of materials can be used for protection against gamma rays radiations. To choose an appropriate type of shielding material, the energy of radiation must be taken in consideration. Indeed, the effectiveness of the shielding material is determined by the interactions between the incident radiation and the atoms of the absorbing medium. The interactions which occur depend essentially on the radiation energy, the chemical composition and the density of the material [1-3].

Above mentioned, it is seen that the radiation shielding parameters are very important to study in various fields and is potential useful in development of semi-empirical formulations of high accuracy. Especially the mass attenuation coefficient (μ_m) parameter, it is momentous to determination of these value for radiation shielding materials because of the theoretical data shows probability of interaction and this data can be used for development and characterizations the materials [4]. The mass attenuation coefficient is basic quantity to determining the attenuation of Xrays and gamma rays in matters and required for shield design [5].

Photoelectric effect, Compton scattering and Pair production are the main interaction mechanisms between photon radiation and atoms and nuclei of matter. The Photoelectric effect is dominant interaction process for low energy photon (≤ 100 keV), Compton scattering is the dominant interaction for medium energy photons ($100 \text{ keV} < E < 1022\text{keV}$) whereas Pair production is dominant for high energy photons (≥ 1022 keV). Photoelectric effect is a complete removal process of photon, whereas pair production generates electron and positron; positron annihilates with electron producing medium energy photons. Compton effect buildups photon of medium energy through multiple scattering, which modifies the application of attenuation coefficients using Lambert Beer's law for shielding and dosimetry [6-7].

In this study, the interaction mechanisms of the iron minerals magnetite and hematite with gamma radiation were investigated. The interactions studied are Photoelectric Absorption, Coherent Scattering, Incoherent Scattering and Pair Production in Nuclear Field and in Electron Field and

mass attenuation coefficient. These interactions were determined theoretically using the web version of the XCOM database.

2. THEORETICAL CALCULATION

Basically, 3 interactions take place during the passage of a photon through the material. These interactions occur in the form of photoelectric absorption, scattering (coherent scattering, incoherent scattering) and pair production. If a photon beam with an initial density of I_0 penetrates matter, it will be weakened and its intensity will decrease exponentially according to the exponential law:

$$I = I_0 e^{-\left(\frac{\mu}{\rho}\right)x} = I_0 e^{-\mu_m x} \tag{1}$$

This is called the Beer–Lambert law, where I is the transmitted intensity, μ is the linear attenuation coefficient in cm^{-1} ; ρ is the material density in g cm^{-3} , x is the thickness of the absorbing medium and μ_m is the total mass attenuation coefficient (cm^2g^{-1}) [8].

$$\mu_l/\rho = \sum_i w_i (\mu_l/\rho)_i \tag{2}$$

where ρ is the mass density of the sample and w_i and $(\mu_l/\rho)_i$ are the fraction by weight and mass attenuation coefficient of i th constituent, respectively. The mass attenuation coefficients for total and partial interactions have been obtained from the XCOM program [8]. Equation 1, this well-known mixture rule is valid with the assumption that the effects of molecular binding and the chemical and crystalline environment are negligible. For a chemical compound, the fraction by weight is given by [8]:

$$w_i = \frac{a_i A_i}{\sum_j a_j A_j} \tag{3}$$

where a_i and A_i are the number of formula units and the atomic weight of the i th element, respectively.

3. RESULTS AND DISCUSSION

Figure 1 and Figure 2 shows the photon interactions obtained from the XCOM program in the energy range of 1 keV- 10^3 MeV for the iron minerals magnetite and hematite. The dependence of (μ_m) on incident photon energy can be explained by the dominance of partial processes of interaction of photons with materials (Photoelectric Absorption, Coherent Scattering, Incoherent Scattering and Pair Production in Nuclear Field and in Electron Field) as shown in Figure 1 and 2. Those figures show that there are three energy ranges relative to the partial processes: low ($E < 0.1$ MeV), intermediate (0.1 MeV $< E < 10$ MeV) and high photon energy ($E > 10$ MeV). It can be seen from those figures that all partial processes depend on the incident photon energy and the chemical composition of materials. The results obtained for both minerals showed that the photoelectric absorption and total mass attenuation coefficient in the low photon energy region are higher than the other regions. In the middle incident photon energies, the total mass attenuation coefficient decreases gradually as the incident photon energy increases. This is because when the incident photon energy is between 100 keV and 10 MeV, the Compton Scattering process becomes the dominant mechanism (particularly inconsistent), with increasing incoming photon energy the partial mass attenuation coefficient slowly decreases. Finally, in the high energy region ($20\text{MeV} < E$), mass attenuation coefficient values slowly increase to almost constant. These behaviors are related to the Z -dependence of the cross section of the Pair Production, which is proportional to Z^2

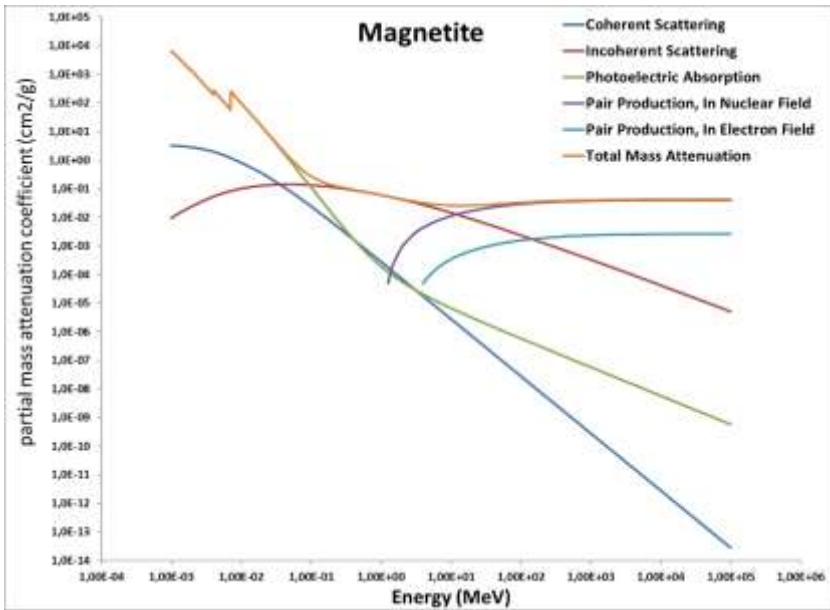


Figure 1. The variation of the total and partial mass attenuation coefficient versus the incident photon energy for magnetite.

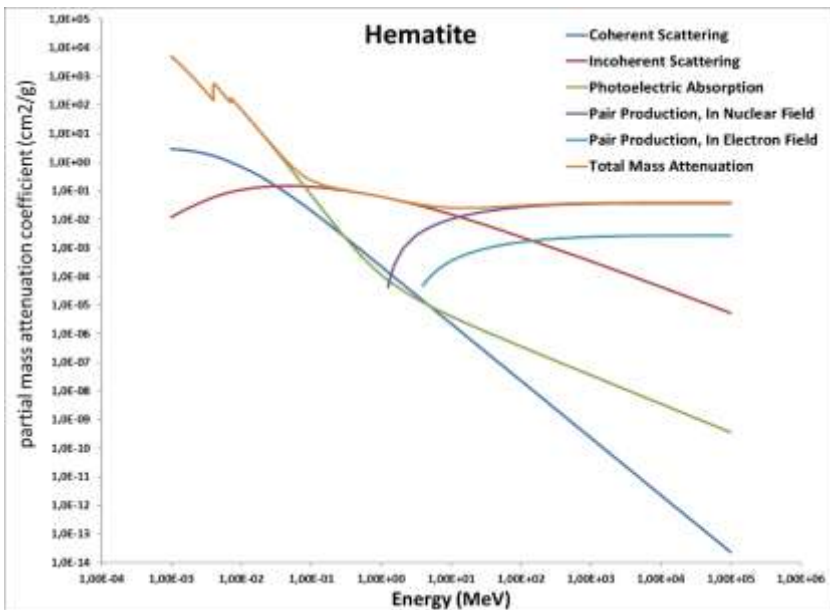


Figure 2. The variation of the total and partial mass attenuation coefficient versus the incident photon energy for hematite.

REFERENCES

[1]. Akkurt, I., 2009. Effective atomic and electron numbers of some steels at different energies. Ann. Nucl. Energy 36, 1702–1705.

- [2]. Akkurt, I., El-Khayatt, A.M., 2013a. The effect of barite proportion on neutron and gamma-ray shielding. *Ann. Nucl. Energy* 51, 5–9.
- [3]. Akkurt, I., El-Khayatt, A.M., 2013b. Effective atomic number and electron density of marble concrete. *J. Radioanal. Nucl. Chem.* 295, 633–638.
- [4] Singh, K., Singh, H., Sharma, V., Nathuram, R. and Khanna, A. 2002. Gamma-ray attenuation coefficients in bismuth borate glasses. *Nuclear Instruments and Methods in Physics Research Section B: Beam Interactions with Materials and Atoms*, 194, 1-6.
- [5] Mahadevappa, M. 2009, *MDCT Physics: The Basics-Technology, Image Quality and Radiation Dose*, Lippincott Williams and Wilkins, chapter 5.
- [6]. Akkurt I et al (2012) Photon attenuation coefficients of concrete including marble aggregates. *Ann Nucl Energy* 43:56–60
- [7] M. Berger, J. Hubbell, XCOM: photon cross sections on a personal computer, *Natl. Bur. Stand. Washington, DC (USA). Cent. Radiat. Res.* (1987) 1–28,
- [8].M.S. Seltzer Calculation of photon mass energy-transfer and mass energy absorption coefficients *Radiat. Res.*, 136 (1993), pp. 147-170

Study on dynamic variation law of stress field in a well area of Mahu and application of proppant selection

Ning CHENG¹, Lixiao XIAO^{2✉}, Song WANG¹, Wei TANG¹, Lin TANG³

¹ Engineering Technology Research Institute, Xinjiang Oilfield Company, PetroChina, Karamay-CHINA

² China University of Petroleum, Enhanced Oil Recovery Institute, The Unconventional Oil and Gas Institute, Beijing-CHINA

³ Beijing Sunshine GIEC Technology Co, Ltd, Beijing-CHINA

ABSTRACT

The volume fracturing of large-scale, close-cut horizontal wells in tight oil conglomerate reservoirs in Mahu Oilfield has achieved remarkable results. For this special lithologic tight oil reservoir, the pressure change of the reservoir is caused by the fracturing of horizontal wells and the development and production process, which in turn induces complex changes in the in-situ stress state of the reservoir. The pore pressure change, minimum principal stress change and bottom hole flow pressure change of horizontal wells during fracturing and production are simulated by means of integration of geology and engineering, and then the time change of the force acting on the proppant is calculated. The simulation results show that the minimum principal stress of the reservoir changes with the change of pore pressure during fracturing and production of a horizontal well in this well area, and presents the law of “increase, recover and decrease” during the whole development process; 32.5MPa decreased to 6MPa, the minimum principal stress decreased from the current 50.0MPa to 36.0MPa, and the force acting on the proppant increased from the current 17.5MPa to 30.0MPa, which was lower than the test limit of 35MPa for closed fracturing of quartz sand. Silica sand can be used as proppant in the zone.

KEYWORDS - Mahu tight oil, integration of geology and engineering, dynamic in-situ stress, quartz sand.

1. INTRODUCTION

Volume fracturing in horizontal wells has become an effective method for the development and production of tight conglomerate reservoir in Mahu oilfield, but the cost of fracturing has been increased because of large-scale volume fracturing. As a consequence, the urgent problem to be solved is how to control the cost of fracturing while maintaining the fracturing effect. The research results of the integration of geology and engineering has been widely used in Mahu area. And therefore, the difficulties in fracturing transformation of the tight conglomerate reservoir in Mahu oilfield are analyzed on the basis of strengthening geological understanding. In the meantime, A multi-aspect comprehensive research is also carried out through combining three-dimensional in-situ stress, rock mechanics analysis and laws of proppant migration and displacement. Afterwards, targeted technical measures such as fracturing technics of energy enhancement and storage and combinations of lower cost fracturing materials have been proposed, and a series of volume fracturing technology tests have been implemented in several blocks in Mahu area. In these oilfield tests, the quartz sand replaced the ceramics as the proppant partially or completely in several blocks, and achieved excellent results^[1-6].

An integrated 3D model with geological and engineering attributes has been established in several well blocks in Mahu area, which can be used to accurately simulate the fracture morphology of hydraulic fracturing and predict the fracturing effect of horizontal wells^[7-9]. As a result, the integrated 3D model is conducive to the realization of well location deployment, fracturing design and production dynamic prediction in 3D space. The simulation process of dynamic stress field is introduced in detail as taking a typical well group in a well block of Mahu area as an example. Firstly, an integrated numerical model is established based on the 3D model. What's more, the artificial fracture morphology is fitted according to the fracturing construction data with reference

to the microseismic monitoring results. Then, the artificial fractures are loaded into the integrated numerical model to simulate the dynamic variation of the stress field, pressure field and oil saturation field of the well group during fracturing and production. The dynamic variation of stress field has important guiding significance for the fracturing design of new well, re-fracturing and proppant optimization^[10-12].

2. DYNAMIC VARIATION LAWS OF IN-SITU STRESS FIELD IN FRACTURED WELLS

The study on the dynamic variation of the in-situ stress field in fractured wells is different from the conventional numerical simulation. In addition to the conventional simulation of production, pressure and saturation, the integrated numerical model must also be able to simulate the stress changes of the 3D in-situ stress field in the production process^[13-14]. What’s more, the complex morphology of artificial fractures is also able to be characterized completely in the integrated numerical model due to the large number of fracture series and large scale of fracturing in fracturing wells. In general, the width of hydraulic fracturing artificial fractures is often about a few millimeters or even smaller, and the mesh size is extremely small if the artificial fractures are represented by differential mesh method in conventional numerical simulation^[15]. As a result, it is extremely easy to cause the non-convergence problem of simulation calculations, and even its calculation speed and calculation efficiency are both extremely lower as the convergence of calculations. In the paper, finite element mesh method is utilized to characterize the artificial fractures in this conventional numerical model, which is composed of mesh elements with a triangular mesh inside and a rectangular mesh outside. The fractures are determined by the 2D plane and the width of a seam defined on the plane. The biggest advantage of finite element mesh is that it can solve the convergence of differential meshes representing artificial fractures while ensuring calculation accuracy and efficiency, and also characterize complex morphology of fractures^[16-18].

A well group is composed of 7 horizontal wells from Well 1 to Well 7 in the early evaluation stage of a well block in Mahu area with a well spacing 400 m. The 20/40 mesh ceramic grains were used as the main proppant, and a decent fracturing effect was achieved, as shown in Fig.1.

2.1 The establishment of integrated numerical model

When determining the mesh direction of the numerical model, it is necessary not only to consider the direction of the fault, the main seepage direction of the sedimentary phases and the arrangement direction of the well pattern, but also to consider the direction of the artificial fractures. Therefore, the mesh direction is consistent with the direction of the artificial fractures. The mesh data fields and geological parameters required for numerical simulation of reservoirs, such as porosity, permeability, saturation, and original in-situ stress field, are all depend on the 3D geological model and 3D in-situ stress model. Then, the block permeability curve and PVT data are imported into the numerical model. The numerical model of 7 wells as shown in Figure 1 adopted a mesh of 25 m×15 m×2 m, and the number of meshes is 124×136×29 with a total of 489056 meshes. The main geological reservoir parameters are shown in Table 1.

2.2 The import of artificial crack loading

The in-situ stress and rock mechanics profile of each section in 7 horizontal wells are extracted according to the 3D model. Combined with the micro-seismic monitoring results, the actual construction parameters are used to fit and simulate the length, height, width and diversion ability of artificial fractures. At the same time, the corresponding fracture parameters are added so as to form the fracture model with the finite element mesh, as shown in Figure.2.

Table 1. Table of main geological reservoir parameters.

Reservoir parameters	Average (range)
Effective thickness (m)	8 (2-15)
Permeability (mD)	1.1 (0.1-1.2)
Porosity(%)	10.25 (7.5-12)

Oil saturation (%)	56 (45-75)
Minimum principal stress (MPa)	50.7 (49-52)
Maximum principal stress (MPa)	65.2 (62-68)
Vertical stress (MPa)	76.1 (72-79)
Pore pressure (MPa)	36.7 (35.1-39.5)

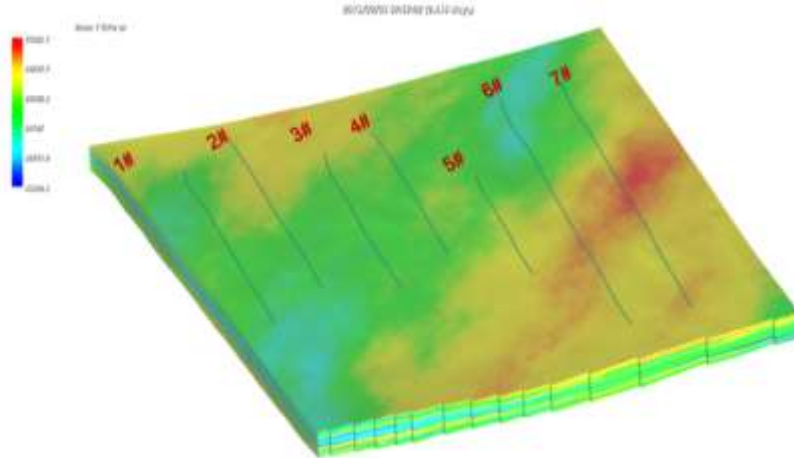


Figure 1. Numerical model of Well 1 to Well 7.

2.3 History Fitting

Different from conventional numerical simulations, the fracturing wells in Mahu area have the characteristics of large number of fracture series and large amount of fracturing fluid injection, which have a great impact on the original saturation field and pressure field. The peculiarity of the block allows that the pressure around the well had reached 60~70 MPa or even higher after the fracturing was completed. The water saturation in the near-wellbore zone became higher after fracturing, resulting in a period of initial high water cut and then followed by a rapid drop in water cut during the production process [19-21]. If the injection volume is not fitted, the model formation pressure will be lower than that in the actual formations and the water cut will be lower than that in the actual formations. As a consequence, the accuracy of the model will be seriously insufficient and result in large errors in the prediction results. So as to ensure that the initial pressure field and saturation field of the model are consistent with the actual situation, the total volume of the fracturing fluid into the well was used as the fluid volume in the model during the simulation calculation. Figure 3 showed the fitting curve of injection volume for each single well.

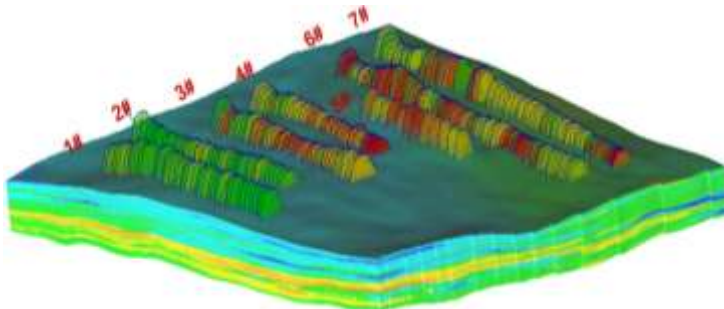


Figure 2. Numerical model of 7 wells added fracture parameters

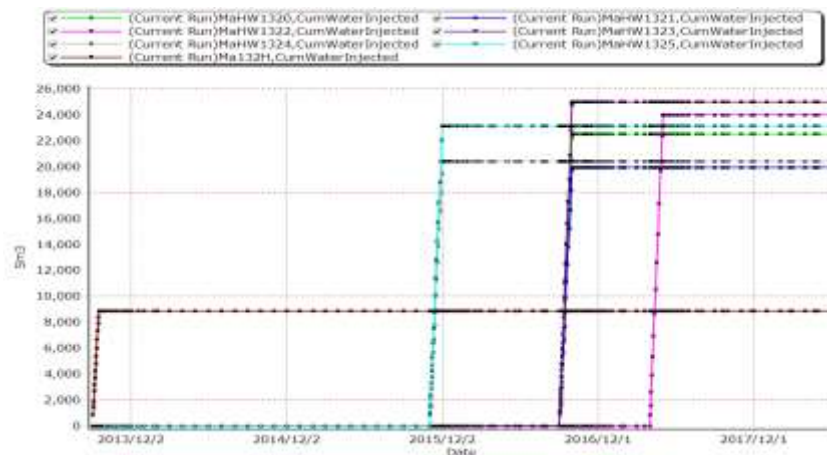


Figure 3. Fitting curve of injection volume for each single well

In the simulation of the production process, the model adopted a constant liquid volume to calculate and fit the daily oil production and the wellhead pressure. As seen in Figure 4, the data calculated with the model was in better agreement with the actual data from the historical fitting results.

2.4 Dynamic variation of stress field

As seen in Figure 4, the original average minimum principal stress from the Well 1 to Well 7 is about 52.0 MPa, while the average minimum principal stress has dropped to 49.0 MPa as of April 2021. The minimum horizontal principal stress around the Well 4, Well 5, Well 6 and Well 7 decreased significantly from 52.0 MPa to 47.0 MPa, with a decrease of 5.0 MPa. On the contrary, the minimum horizontal principal stress around the Well 1, Well 2, and Well 3 was slightly reduced by 0~2.0 MPa compared with the original value. The change of in-situ stress was consistent with the production situation of 7 wells in Table.2. The reason of large change in the minimum principal stress in the area of Well 5, Well 6 and Well 7 is due to the fact that the cumulative production volume in the area is much greater than the cumulative injection volume. However, the minimum principal stress near Well 1, Well 2 and Well 3 changed a little, mainly because that the in-situ stress increased due to the initial fracturing fluid injection, and then gradually recovered to the vicinity of original in-situ stress during the production process.

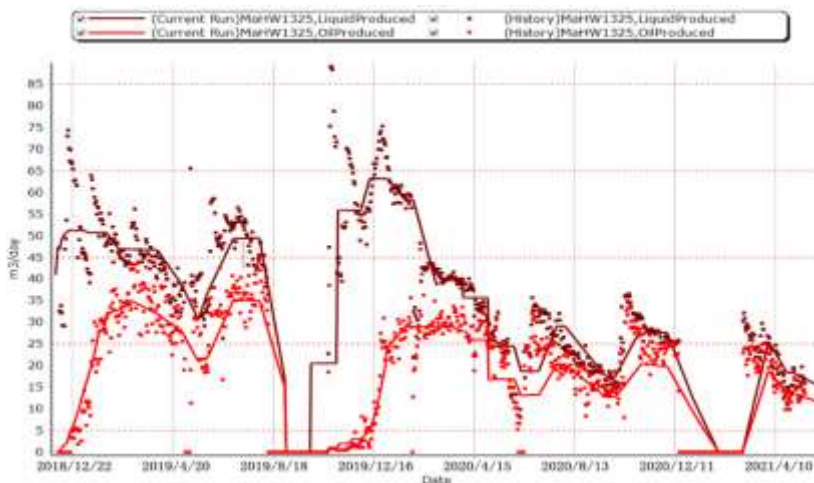


Figure 4. Fitting curve of daily liquid production and daily oil production in Well 5

Table 2. Injection and output statistics of per well

Well number	Cumulative oil production (m ³)	Total injection volume (m ³)	Total production volume (m ³)	Injection and production difference (m ³)
1	10180	22311	22262	49
2	10181	19781	17410	2371
3	5786	23957	8943	15014
4	10035	25931	15682	10249
5	16281	5659	34496	-28837
6	13766	20195	25425	-5230
7	17168	23020	28870	-5850

In order to visually display the changes of the in-situ stress and pore pressure of the 7 wells in the area, the in-situ stress and pore pressure of a mesh were selected for each of the 7 wells to approximately represent the in-situ stress and pore pressure of the well, and then the variation law was analyzed. The minimum principal stress of the 7 wells in the area recovered to the original minimum principal stress within 4 to 8 months after fracturing, which was consistent with the variation of pore pressure. Among them, the injection volume of Well 5 was the smallest, the time for the pore pressure recovering to the original value was the fastest, and the shortest time for the recovery of the minimum principal stress was 4 months. The variation law of the in-situ stress field, pore pressure and bottom-hole flowing pressure of the well group during the production process showed that the in-situ stress changes with the change of pore pressure and presented the trend of initial increase, mid-term recovery and last decrease. With the increase of oil recovery, the formation pore pressure decreased and the minimum principal stress also decreased in the later production period.

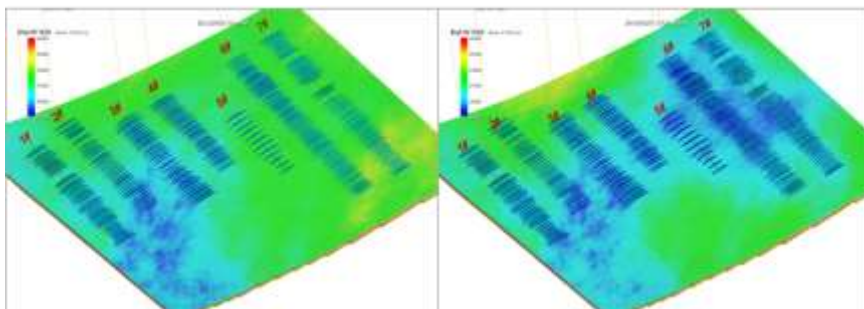


Figure 5. Variation of minimum horizontal principal stress field of each well:(a) Initial minimum horizontal principal stress field; (b) The minimum horizontal principal stress field in April 2021

2.5 Analysis of dynamic variation in proppant force

The force acting on the proppant is related to the state of stress and pore pressure. For the case where the main fracture is perpendicular to the direction of the minimum principal stress, the effective force on the proppant is less than the closure stress since the partial closure stress is borne by the liquid in the fracture during production. As a result, the force on the proppant is the difference between the minimum principal stress and the bottom-hole flowing pressure^[22]. Taking Well 1 as an example, the bottom-hole flowing pressure dropped from 32.5 MPa to 6 MPa, as well as the minimum principal stress dropped from 50.0 MPa to 36.0 MPa during the development process. Therefore, the force acting on the proppant had increased from 17.5 MPa to 30.0 MPa, and the quartz sand met the requirements for the proppant in this well area. The capacity of holding formation pressure has been improved due to the large volume of fluid injection in the horizontal well, such as Well 5. The well has a cumulative production of 1085 days with a cumulative oil production of 20807 t. At present, the daily oil production is 15 t and the wellhead pressure is 5.4 MPa, equivalent to the maximum effective force of 29.9 MPa. The long self-injection period and strong pressure holding capacity of horizontal wells provide conditions for the replacement of quartz sand.

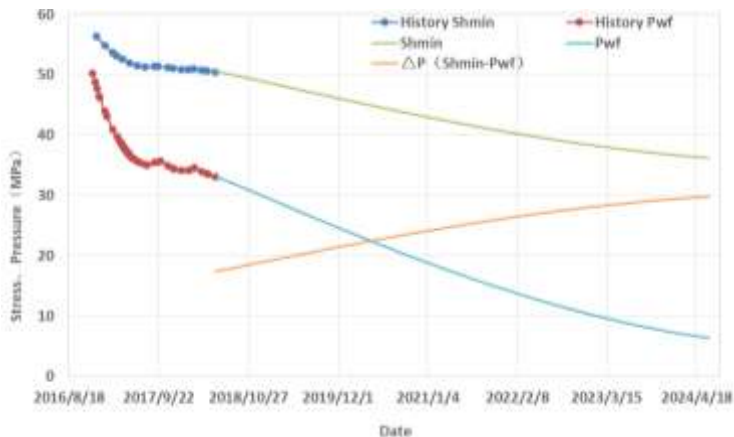


Figure 6. Variation curve of minimum principal stress and bottom-hole flowing pressure in Well 1

3. FIELD TEST EFFECTS

Taking the Mahu well area with the largest number of quartz sand test wells as an example, the depth of the middle of the reservoir in the block is 2568~3260 m, the formation pressure coefficient is 1.11~1.18, and the wellhead pressure drops to 0.5 MPa to stop the self-injection. The maximum

effective force is about 28.6 MPa during the self-injection period. The cumulative oil production of 15 test wells in the block for 270 days was counted. The average horizontal wells using quartz sand as proppant is 5024 t, while the horizontal wells using the ceramicsite as proppant is 5429.4 t, with an average daily production difference of 1.5 t/d. Considering the factor of horizontal section length, the cumulative oil production is converted to the cumulative oil production per meter. As a result, the average oil production per meter of the horizontal wells using quartz sand as proppant is 3.28 t/m, and that of using ceramicsite as proppant is 3.68 t/m, which indicated that there was no significant difference in the average oil production per meter of the horizontal wells with different proppants. The two wells of 12X6 and 12X7 in T₁b₃ layer of the well area have a buried depth of 3103~3209 m. The test well 12X6 using quartz sand as proppant has a horizontal section of 1612 m and the oil layer drilling rate of 91.7%, as well as the adjacent well 12X7 has a horizontal section of 1692 m and the oil layer drilling rate of 85.7%. Therefore, there are basically the same geological and physical properties of the two wells. The Well 12X6 fractured 41 clusters in section 21, with fracturing fluid volume 25785 m³ and quartz sand 1814 m³, and the Well 12X7 fractured 42 clusters in section 22 with fracturing fluid volume 24578 m³ and ceramicsite 1597 m³. The fracturing parameters of the two wells are basically the same except for the difference in sanding intensity. The Well 12X6 was put into production 1 month later than the Well 12X7, and it has been working for 590 days. Before being interfered by fracturing of other wells, there were no significant difference in the cumulative oil production and pressure of the Well 12X6 and the Well 12X7, and it can be shown in Figure 7 and Figure 8.

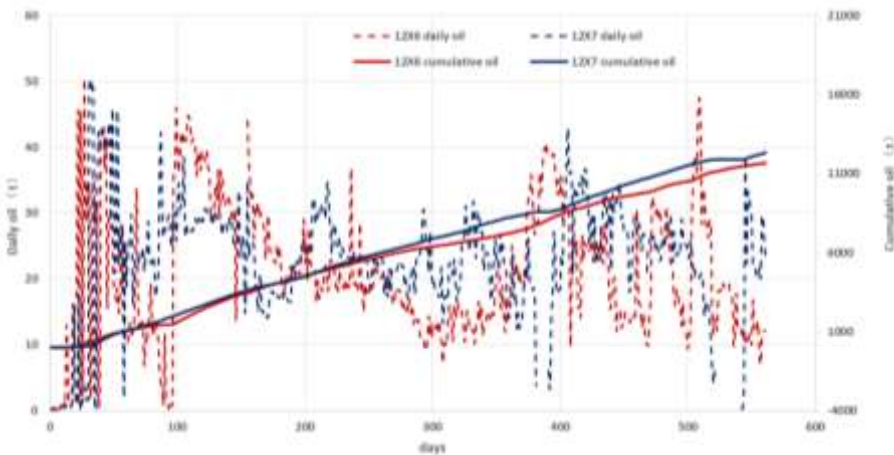


Figure 7. Comparison of cumulative oil production between 12X6 and 12X7



Figure 8. Comparison of pressure between MaHW12X6 and MaHW12X7

4. CONCLUSIONS

The results of integrated numerical simulation indicated that the minimum horizontal principal stress varies with the change of the formation pore pressure. With the increase of the oil recovery, the formation pore pressure decreases and the minimum horizontal principal stress decreases as well, which provides favorable conditions for the use of quartz sand as proppants. In view of the current field application situation, there is little difference in the fracturing effect of using quartz sand instead of ceramsite as proppants in this well area.

REFERENCES

- [1] Xu Jiangwen, Li Jianmin, Wu Yuanyue, Ding Kun. Exploration and Practice of Volume Fracturing Technology for Horizontal Wells in Mahu Tight Conglomerate Reservoir [J]. China Petroleum Exploration, 2019, 3(02).
- [2] Kou Shuangfeng, Chen Shaoning, He Le, Liao Kuo. The adaptability of quartz sand to fracturing in Sulige tight sandstone gas reservoirs [J]. Reservoir Evaluation and Development, 2019, 9(02):65-70.
- [3] Huang Tiankun, Hao Shiyan, Wei Dengfeng. Research on fracture resistance of fracturing proppant and its mathematical model [J/OL]. Chinese Journal of Applied Mechanics: 1-6[2019-06-05]. <http://kns.cnki.net/kcms/detail/61.1112.O3.20190202.2032.002.html>.
- [4] Lei Qun, Guan Baoshan, Cai Bo, Wang Xin, Xu Yun, Tong Zheng, Wang Haiyan, Fu Haifeng, Liu Zhe, Wang Zhen. Progress and development direction of reservoir stimulation technology [J]. Petroleum Exploration and Development, 2019, 46(03): 580-587.
- [5] Gao Xiping, Peng Junliang, Peng Huan, Wang Liang, Zhou Yuchao, Feng Yan. Experimental study on replacing ceramsite with quartz sand for shale gas fracturing [J]. Drilling and Production Technology, 2018, 41(05):35-37+41+9.
- [6] Yang Lifeng, Tian Zhuhong, Zhu Zhongyi, et al. Economic adaptability of quartz sand for fracturing of shale gas reservoirs [J]. Natural Gas Industry, 2018, 38(05):71-76.
- [7] Jin Chengzhi, He Jian, Lin Qingxiang, Mei Jian, Duan Yanqing. Fracturing stimulation based on geology-engineering integration to tight oil reservoirs in Block Fang 198-133, northern Songliao Basin [J]. China Petroleum Exploration, 2019, 24(2): 218-225.
- [8] Wang Xin, Yang Bin, Wang Rui. Beneficial exploration based on geology-engineering integration in low-saturation oil reservoirs of Tuha oil-field [J]. China Petroleum Exploration, 2017, 22(1): 38-45.

-
- [9] Zhang Jing, Luo Zhao, Xu Mingqiang, et al. Application of geology engineering integration in development of tight oil in Xinjiang oilfield[J]. China Petroleum Explo-ration, 2017, 22(1): 12-20.
- [10] Zhang Guangming, Liu He, Zhang Jin et al. Simulation of hydraulic fracturing of oil well based on fluid-solid coupling equation and non-linear finite element[J]. ACTA PETROL EI SINICA 2009 30 (1):113-116.
- [11] Shi Lianjie, et al. Variation of porous medium and fluids during the development of a low permeability reservoir in eastern Daqing [J]. Journal of Da Qing Petroleum Institute, 1999, 23 (2): 85-87.
- [12] Zhou Zhijun Liu Yongjian Ma Yingjian et al The theoretical model of fluid-solid coupling seepage in low permeability reservoirs [J]. Journal of Daqing Petroleum Institute, 2002, 26 (3): 29-32.
- [13] Gu S, Shi Y, Chen Z. Numerical Simulation of Fracture Permeability Change in Production of Pressure-sensitive Reservoirs with In-situ Stress Field[J]. The Open Petroleum Engineering Journal, 2015, 8(1):440-450.
- [14] Singh U K, Sahoo B C. Computing the 3D in-situ stress field from shut-in pressure data using statistical regression[J]. Geotechnical & Geological Engineering, 2000, 18(2):119-137.
- [15] Shakib J T, Ghaderi A, Shahri A A. Analysis of hydraulic fracturing in fractured reservoir: Interaction between hydraulic fracture and natural fractures[J]. Science, 2012, 239(4):393-404.
- [16] DanDan, Xu, Zhan Li, et al. Study on interaction between induced and natural fractures by extended finite element method[J]. Science in China: Physics, Mechanics, astronomy, 2017, 60(2):14.
- [17] Cherny S, Chirkov D, Lapin V, Muranov A, Bannikov D, Miller M, et al. Two-dimen- sional modeling of the near-wellbore fracture tortuosity effect. International Journal of Rock Mechanics and Mining Science 2009;46(6):992–1000.
- [18] Axelsson O, Barker V A. The Finite Element Method - ScienceDirect[J]. Finite Element Solution of Boundary Value Problems, 1984, 18(7):163-267.
- [19] Pater C, Beugelsdijk L. Experiments and numerical simulation of hydraulic fracturing in naturally fractured rock[C]. 40th U.S. rock mechanics symposium and 5th U.S.-Canada rock mechanics symposium. 2005.
- [20] Akulich A V, Zvyagin A V. Numerical simulation of hydraulic fracture crack propagation[J]. Moscow University Mechanics Bulletin, 2008, 63(1):6-12.
- [21] Adachi J I, Detournay E. Self-similar solution of a plane-strain fracture driven by a power-law fluid[J]. International Journal for Numerical & Analytical Methods in Geomechanics, 2010, 26(6):579-604.
- [22] Wu G, Xu Y, Yang Z, et al. Numerical simulation considering the impact of proppant and its embedment degree on fracture flow conductivity[J]. Natural Gas Industry, 2013, 33(5):65-68.

Evaluation of heavy metal distributions in surface waters and sediments of Eğirdir Lake

Alper ÖZSEVEN¹, İskender AKKURT², Kadir GÜNOĞLU³

¹ Suleyman Demirel University Medical Faculty, Isparta/TURKEY

² Suleyman Demirel University Science Faculty, Isparta/TURKEY

³ Isparta Applied Science University, Technical Sciences Vocational School, Isparta TURKEY

alperozseven@sdu.edu.tr

ABSTRACT

Eğirdir Lake is still one of the most irreplaceable natural habitat in the Göller District as well as the Isparta Province. Eğirdir Lake is still the fourth largest lake in Turkey which also provides drinking water. In this study, the heavy metal distributions in Isparta-Eğirdir Lake were determined. The water samples were taken from the surface of Eğirdir Lake and the sediment samples were taken from the bottom of Eğirdir Lake by using Van Veen sediment sampler which were stored in 2000 ml leak-proof polyethylene containers. Measurements were carried out in the spring and autumn of the year to explore the seasonal changes. Inductively coupled plasma mass spectrometry (ICP-MS) was used to analyse the heavy metal contents in soil and water samples. The relative abundance of the median concentrations of heavy metals in the surface water samples were in the order of As > Cr > Fe > Zn > Ni > Cu > Pb > Hg > Mn > Cd. On the other hand, the relative abundance of the median concentrations of heavy metals in the sediment samples were in the order of Mn > Ni > Zn > Cr > Cu > Pb > As > Fe > Cd > Hg. With the exception of As, all heavy metal measurement findings in Lake Eğirdir's surface waters were within the WHO-recommended limit. The median findings for both seasons showed that Eğirdir Lake may be regarded as being clear of Cd, Pb, and Zn pollution, according to the EPA's recommendation for sediment quality guidelines. On the other hand, the lake may be classified as being highly As, Mn, and Ni contaminated.

KEYWORDS: Eğirdir Lake, Heavy metals, Surface waters and sediments

1. INTRODUCTION

Certainly, water has been one of the most basic need and natural resources for humanity all through the history [1]. The main sources of water are lakes and rivers. Furthermore, with their sediments, rocks, soils, surrounds, and inhabitants, lakes comprise an ecological zone in addition to being a supply of freshwater. Heavy metals are seen as another significant concern that has to be carefully monitored. For living organisms, there are two types of metals: those that are necessary and those that are not. Some metals, such as Fe, Ni, Cu, Zn, Co, Mn, and Mo, are necessary for the efficient functioning of biological and metabolic processes in living beings at a specific level, but other non-essential metals are threatening to life [2,3]. Additionally, bio-essential metals have the potential to be harmful in concentrations greater than necessary to people and other living things [4]. Toxic heavy metals, on the other hand, are dangerous because they have a tendency to bioaccumulate and can become carcinogenic. Compounds accumulate in living things when they are ingested and stored more quickly than they are digested or eliminated. As Cd, Co, Cr, Cu, Hg, Fe, Mn, Ni, Pb, and Zn are accepted by the majority of communities as the primary causes of concern and require monitoring to avoid damaging effects on human organs and systems [5-9]. In this study, heavy metal concentrations of As, Cd, Cr, Cu, Fe, Hg, Mn, Ni, Pb, and Zn were investigated in sediment and water samples. The study was conducted at two distinct seasons of the year in order to examine the seasonal effect. The study was carried out at the beginning of June 2017 (the start of the summer season), when the lake's water level was at its highest, and at the beginning of November 2017 (the start of the winter season), when it was at its lowest level [10].

2. MATERIALS AND METHODS

İsparta is a city in the southwest of Turkey that has one of the largest agricultural areas and orchards of fruits and vegetables. The entire territory of that section of Anatolia, known as the Göller District, is home to a variety of water resources. The Eğirdir Lake, which covers an area of 457 km², is regarded as the most significant water resource in the region. Latitude 37° 50' 41"-38° 16' 55" N and longitude 30° 57' 43"-30° 44' 39" E are the location coordinates of the lake. Eğirdir Lake is the 2nd largest lake in Göller District and 4th in Turkey [11]. Most of the agricultural lands in this part of country are irrigated through Eğirdir Lake. Moreover, part of drinking water is still provided by Eğirdir Lake through the water pump stations (WPS) it hosts, in the time of aridity (Figure 1 yellow indicators) [12,13]. With the purpose of distributing the sampling points homogeneously over Eğirdir Lake, land exploration was conducted. Water pump stations belonging to the State Hydraulic Works (SHW) in Eğirdir Lake were taken into considerations in the process of determining the locations of 12 sampling points. Collecting samples were performed on days when the lake was smooth. The sediment samples were collected from the bottom of Eğirdir Lake using a Van Veen sediment sampler, which has dimensions of around 20x30x60 cm and a 250cm² grabbing area. The water samples were collected from the top of Eğirdir Lake and kept in 2000 ml leak-proof polyethylene containers (Figure 1, green needles). The detailed entire procedure about sampling and processing can be found in the previous studies [12,13]. Inductively coupled plasma mass spectrometry (ICP-MS) was used to analyse the heavy metal contents in bottom sediment and surface water samples (ACME LABS, Bureau Veritas Mineral, Canada). Statistical analyses were completed using the SPSS software version 22 (Armonk, NY: IBM Corp., USA). Descriptive statistics were used to evaluate the distribution forms of collected data. Frequency histograms were plotted for assessing the normal distribution of the sample results.



Figure 1 Eğirdir Lake, Outfall of Streams and Sampling Points

3. RESULTS AND DISCUSSIONS

The distributions of heavy metals in surface water and sediment samples are shown in Tables 1 and 2, respectively. The distribution of heavy metals in surface water samples was assessed using World Health Organization (WHO) guidelines, and the level of pollution in sediment samples was determined using U.S. Environmental Protection Agency (U.S. EPA) standards [14,15,16]. The list of the reference values recommended by these authorities were presented in Table 3 and Table 4, respectively.

Table 1 Measured heavy metal concentrations in surface water samples

	As		Cd		Cr		Cu		Fe		Hg		Mn		Ni		Pb		Zn	
	June	Nov.	June	Nov.	June	Nov.	June	Nov.	June	Nov.	June	Nov.	June	Nov.	June	Nov.	June	Nov.	June	Nov.
S1	7.20	14.20	<0.05	<0.05	7.30	8.30	0.40	0.50	<10.00	<10.00	<0.10	<0.10	<0.05	0.04	0.30	0.20	<0.20	<0.20	0.50	0.80
S2	8.50	15.80	<0.05	<0.05	7.90	9.00	0.50	0.50	<10.00	<10.00	<0.10	<0.10	<0.05	<0.05	0.60	0.40	<0.20	0.20	1.30	0.90
S3	8.50	16.50	<0.05	<0.05	8.10	9.20	0.40	0.40	<10.00	<10.00	<0.10	<0.10	<0.05	<0.05	0.60	0.30	<0.20	0.30	0.30	<0.50
S4	8.20	16.90	<0.05	<0.05	7.90	8.60	0.30	0.30	<10.00	<10.00	<0.10	<0.10	<0.05	<0.05	0.60	0.20	<0.20	<0.20	0.60	0.70
S5	7.60	11.20	<0.05	<0.05	8.40	10.00	0.40	0.50	12.00	<10.00	<0.10	<0.10	<0.05	0.07	0.60	<0.20	<0.20	1.80	<0.50	
S6	7.90	16.90	<0.05	<0.05	8.40	9.20	0.40	0.40	<10.00	<10.00	<0.10	<0.10	<0.05	<0.05	0.30	0.30	<0.20	<0.20	1.50	0.50
S7	7.40	10.90	<0.05	<0.05	8.00	9.20	0.30	0.40	<10.00	<10.00	<0.10	<0.10	<0.05	<0.05	0.50	0.20	<0.20	<0.20	<0.50	<0.50
S8	8.30	15.20	<0.05	<0.05	8.30	8.80	0.40	0.30	<10.00	<10.00	<0.10	<0.10	<0.05	<0.05	0.70	0.30	<0.20	<0.20	<0.50	0.60
S9	11.60	13.50	<0.05	<0.05	8.50	10.10	0.20	0.30	11.00	<10.00	<0.10	<0.10	<0.05	<0.05	0.30	<0.20	<0.20	<0.20	<0.50	<0.50
S10	11.40	10.50	<0.05	<0.05	8.10	10.30	0.20	0.30	<10.00	<10.00	<0.10	<0.10	<0.05	<0.05	<0.20	<0.20	<0.20	<0.20	<0.50	0.50
S11	10.70	9.70	<0.05	<0.05	7.50	9.50	0.20	0.20	<10.00	<10.00	<0.10	<0.10	<0.05	<0.05	<0.20	<0.20	<0.20	<0.20	<0.50	<0.50
S12	12.00	10.90	<0.05	<0.05	7.90	10.10	0.20	0.30	<10.00	<10.00	<0.10	<0.10	<0.05	<0.05	0.40	<0.20	<0.20	<0.20	<0.50	<0.50
Median	8.40	14.70			8.00	8.70	0.40	0.40	8.00				0.04	0.40	0.20			0.60	0.60	
(Min)	(7.20)	(9.70)			(7.30)	(8.30)	(0.20)	(0.10)	(8.00)				(0.04)	(0.04)	(0.20)			(0.20)	(0.40)	(0.40)
(Max)	(12.00)	(17.80)			(8.50)	(10.30)	(0.50)	(0.50)	(12.00)				(0.07)	(0.70)	(0.40)			(0.30)	(1.80)	(0.90)

All the values in table are in microgram per liter (µg/L)

Table 2 Measured heavy metal concentrations in sediment samples

	As		Cd		Cr		Cu		Fe		Hg		Mn		Ni		Pb		Zn	
	June	Nov.	June	Nov.	June	Nov.	June	Nov.	June	Nov.	June	Nov.	June	Nov.	June	Nov.	June	Nov.	June	Nov.
S1	15.10	10.60	0.58	0.27	40.40	31.30	59.68	52.27	5.31	2.33	46.50	40.50	895.00	609.00	72.40	52.50	17.54	17.96	80.00	58.20
S2	15.90	11.60	0.22	0.17	28.40	21.80	27.40	20.23	2.52	1.94	41.00	35.00	530.00	434.00	39.40	32.90	17.29	16.95	63.80	43.10
S3	13.50	9.80	0.99	0.18	28.80	34.70	17.28	20.96	1.59	2.44	39.00	42.00	399.00	583.00	34.00	70.90	9.83	17.26	53.10	56.00
S4	16.90	13.60	0.36	0.18	18.00	21.60	30.70	39.60	2.00	2.55	7.00	13.00	685.00	692.00	16.70	20.86	34.45	43.60	39.00	46.30
S5	20.00	13.70	0.13	0.12	27.10	29.50	21.60	23.90	2.23	2.77	50.00	18.00	598.00	643.00	50.60	61.20	17.83	22.41	43.90	54.10
S6	16.60	9.60	0.10	0.18	10.10	35.10	4.32	27.47	4.02	2.40	<0.50	48.00	577.00	582.00	7.50	67.60	4.55	17.06	66.70	53.70
S7	10.60	8.30	0.14	0.22	33.00	32.60	24.00	26.60	2.16	2.39	42.00	38.00	494.00	553.00	64.20	63.90	15.58	17.22	52.20	52.50
S8	14.90	8.20	0.66	0.18	30.10	34.90	11.93	26.22	1.51	2.42	55.00	38.00	390.00	597.00	52.60	63.86	8.81	17.05	29.90	54.00
S9	11.30	9.90	0.10	0.07	11.30	7.30	3.91	2.82	0.76	0.23	18.00	12.00	182.00	131.00	10.00	4.70	3.80	2.47	14.30	8.40
S10	18.90	17.60	0.12	0.09	17.50	17.50	35.51	32.36	1.74	1.71	33.00	38.00	501.00	374.00	20.50	19.20	29.23	33.91	37.90	28.60
S11	14.60	8.50	0.38	0.09	55.20	22.80	24.12	8.48	1.60	0.70	19.00	13.00	549.00	377.00	118.70	48.40	9.28	4.60	37.10	13.30
S12	14.30	11.20	0.11	0.07	25.90	20.60	15.70	13.87	1.45	1.33	24.00	33.00	308.00	287.00	48.80	42.50	9.52	9.76	32.50	26.10
Median	15.00	10.50	0.13	0.18	27.80	28.80	22.70	26.41	1.87	2.37	27.00	26.50	516.00	566.00	69.60	58.90	12.70	17.14	38.40	48.40
(Min)	(10.60)	(8.20)	(0.06)	(0.07)	(10.10)	(7.30)	(3.91)	(2.82)	(0.76)	(0.23)	(4.90)	(12.00)	(182.00)	(131.00)	(7.50)	(4.70)	(5.80)	(2.47)	(14.30)	(8.40)
(Max)	(20.00)	(17.60)	(0.22)	(0.27)	(40.40)	(35.30)	(59.68)	(54.60)	(6.02)	(2.77)	(66.00)	(49.00)	(895.00)	(692.00)	(118.70)	(70.90)	(34.60)	(43.60)	(80.00)	(58.20)

All the values in table are in milligram per kilogram (mg/kg) except for Fe and Hg. Fe and Hg results were given in % and microgram per kilogram (µg/kg) respectively.

In the surface water samples, the relative abundance of the median concentrations of heavy metals was distributed as follows: As > Cr > Fe > Zn > Ni > Cu > Pb > Hg > Mn > Cd. Surface waters' lowest seasonal average As, Cr, and Cu contents were 9.4 µg/L, 7.8 µg/L, and 0.15 µg/L, respectively, at sample stations S5, S1, and S9/S12. In contrast to the median value of 14.70 µg/L in November, the median As concentration in June was 8.40 µg/L. Additionally, the measured findings for the elements Cd, Fe, Hg, Mn, Ni, Pb, and Zn were below MDL and suggested levels. Based on the results, the S9 sampling points had the highest seasonal average As and Cr concentrations in surface waters, measuring 12.55 µg/L and 9.30 µg/L, respectively. The highest seasonal average results for Cd, Cu, Fe, Hg, Mn, Ni, Pb, and Zn were significantly below the recommended values and close to the MDL (Table 1). With the exception of As, all heavy metal measurement results in Eğirdir Lake surface waters fell within the WHO-recommended limit values. A particular emphasis should be placed on As outcomes as well. Except for S5 sampling point, the seasonal average As concentration was determined to be considerably above the WHO guideline, which is 10 µg/L. Additionally, compared to the June data, the As concentration was higher in November. The Şener et al. findings, which stated that the mean As content in Eğirdir Lake was 13 0.0025 µg/L, are well verified by these findings [11].

Table 3 WHO limits for drinkable-water [14]

Heavy metals	Guideline value (µg/L)
As	10
Cd	3
Cr	50
Cu	2000
Fe	NA
Hg	6
Mn	400
Ni	70
Pb	10
Zn	NA

Abbreviation: NA= not available

Table 4 Sediment Quality Guidelines recommended by EPA (mg/kg) [15,16]

Heavy metals	Not polluted	Moderately polluted	Heavily polluted
As	<3	3–8	>8
Cd	NA	<6	>6
Cr	<25	25–75	>75
Cu	<25	25–50	>50
Fe	NA	NA	NA
Mn	<300	300–500	>500
Ni	<20	20–50	>50
Pb	<40	40–60	>60
Zn	<90	90–200	>200

Abbreviation: NA= not available

The relative abundance of the median concentrations of heavy metals in the sediment samples were in the order of Mn > Ni > Zn > Cr > Cu > Pb > As > Fe > Cd > Hg. S9 sampling site had the lowest seasonal average of Cu, Cr, Fe, Mn, Ni, Pb, and Zn concentrations in bottom sediments. The Taşevi settlement and the Hoyran WPS are close to this sampling location. Additionally, the lowest seasonal average As, Cd, and Hg concentrations were found in sediment samples taken from the S7, S10, and S4 sampling stations, with values of 9.45 mg/kg, 0.15 mg/kg, and 9 mg/kg, respectively. On the other hand, the highest seasonal average concentrations for heavy metals in bottom sediments generated more complicated pattern. Cd, Cr, Cu and Mn concentrations were highest in S1 sampling point, which is close to the Çay Stream Outfall with values of 0.22 mg/kg, 39.95 mg/kg, 35.98 mg/kg and 801 mg/kg, respectively. Fe and Zn distributions were highest in S6 sampling point, which is near the Bedre Beach. Furthermore, the highest seasonal average of As, Hg, Ni and Pb concentrations were measured in S10, S8, S11 and S4 sampling points, respectively (Table 2). The median results for both seasons demonstrated that Eğirdir Lake can be regarded as being clear of Cd, Pb, and Zn pollution, according to the EPA's recommendation for sediment quality guidelines. On the other hand, the lake can be described as being severely As, Mn, and Ni polluted. Moreover, in relation to Cr element, the lake can be classified as moderately polluted. Besides, while the lake was non-polluted in the June with Cu, it turned to be moderately polluted in the November. The median Fe results for both seasons were lower than the average of Earth's crust, which is 5% [17]. It can be inferred from the current study results that the pollution level of the lake with Pb, Cu, Ni, Mn and Zn was increased with respect to the findings of Şener et al [11].

4. CONCLUSIONS

Eğirdir Lake is still one of the most unique natural wonders in the Göller District as well as the Isparta Province. In this detailed and updated study, the heavy metal distributions of Eğirdir Lake

were assessed. It could be stated that Eğirdir Lake water, which was investigated in the current study, were not significantly contaminated, only As concentrations were found to be slightly higher than the international recommendation. Generally, heavy metal pollution in Eğirdir Lake increased as compared to the findings of earlier studies, particularly in sediment samples.

REFERENCES

- [1] H. F. Çay, [1] H.S. Vuorinen, P.S. Juuti, T.S. Katko, *Water Supply*, 7 , 49 (2007) <https://doi.org/10.2166/ws.2007.006>
- [2] Stankovic, S. and Stankovic, A.R. (2013) Chapter 5: Bioindicators of Toxic Metals. In: Lichtfouse, E., Schwarzbauer, J. and Robert, D., Eds., *Green Materials for Energy, Products and Depollution*, Series Volume 3, Springer Netherlands, 151-228.
- [3] Wong CSC, Li X, Thornton I (2006) Urban environmental geochemistry of trace metals: a review. *Environ Pollut* 142:1-16
- [4] Hu H (2002) Human health and heavy metals exposure. In: McCally M (ed) *Life support: the environment and human health*. MIT Press, Cambridge, pp 65-82
- [5] Chen YC, Serrell N, Evers CD, Fleishman JB, Lambert FK, Weiss J, Robert P, Mason PR, Bank SM (2008) Methylmercury in marine ecosystems – from sources to seafood consumers. *Environ Health Perspect* 116(12):1706-1712
- [6] Lavery JT, Kemper MC, Sanderson K, Schultz GC, Coyle P, James G, Mitchell GJ, Seuront L (2009) Heavy metal toxicity of kidney and bone tissues in South Australian adult bottlenose dolphins (*Tursiops aduncus*). *Mar Environ Res* 67:1-7
- [7] Stankovic S, Jovic M, Stankovic RA, Katsikas L (2011) Heavy metals in seafood mussels. In: Lichtfouse E et al (eds) *Risks for human health in: environmental chemistry for a sustainable world: Volume 1.* , Chapter 9, pages 64, pp 311-375, ISBN-10: 9400724411, ISBN-13: 978-94007244119
- [8] Jovic M, Onjia A, Stankovic S (2012) Toxic metal health risk by mussel consumption. *Environ Chem Lett* 1:69-77
- [9] Markovic J, Joksimovic D, Stankovic S (2012) Trace elements concentrations determined in collected wild mussels in the coastal area of southeastern Adriatic, Montenegro. *Arch Biol Sci Belgrade* 64(1):265-275
- [10] Keskin, M. E. , Aksoy, Y. R. , Aksoy, A. S. & Yılmazkoç, B. (2017). Göl Seviye Tahmini: Eğirdir Gölü. *Mühendislik Bilimleri ve Tasarım Dergisi* , 5 (3) , 601-608 <https://doi.org/10.21923/jesd.340383>
- [11] Şener, Ş., Davraz, A. & Karagüzel, R. (2013) Evaluating the anthropogenic and geologic impacts on water quality of the Eğirdir Lake, Turkey. *Environ Earth Sci* 70, 2527-2544. <https://doi.org/10.1007/s12665-013-2296-0>
- [12] Özseven, A., & Akkurt, İ. (2020a). Evaluation of gross-alpha and gross-beta activity concentrations and assessment of excess lifetime cancer risk in waters of Eğirdir Lake, Turkey. *International Journal of Environmental Analytical Chemistry*, 1-13. <https://doi.org/10.1080/03067319.2020.1822352>
- [13] Özseven, A., Akkurt, I., & Günoğlu, K. (2020b). Determination of some dosimetric parameters in Eğirdir Lake, Isparta, Turkey. *International Journal of Environmental Science and Technology*, 17(3), 1503-1510. <https://doi.org/10.1007/s13762-019-02569-z>
- [14] World Health Organization (WHO), *Guidelines for drinking-water quality - 4th ed*, (WHO, Geneva, Switzerland, 2011)
- [15] U. S. Environmental Protection Agency (U.S. EPA). *Guidance for the Pollutational Classification of Great Lakes Harbor Sediments, Region V, Chicago, Illinois; 1977.*
- [16] Ali M.J.A , Al-Tamimi O. (2018) Ecological Indices of the Heavy Metals in the Soil of Shewasoor Sub-Basin, Kirkuk NE Iraq. *Open Science Journal* 3(1)
- [17] Mason B, Moore CB (1982) *Principles of geochemistry*, 4th edn. Wiley, New York

Nonlinear Optical Properties of IGZO Thin Films Prepared by Pulse Laser Deposition

Hamdi Şükür KILIÇ^{1,2*}, Yasemin GÜNDOĞDU^{2,3} and Serap YİĞİT GEZGİN¹

¹Department of Physics, Faculty of Science, University of Selçuk, Konya, TURKEY

²Directorate of Laser Induced Proton Therapy Application and Research Center, University of Selçuk, Konya, TURKEY

³Department of Computer Technologies, Kadınhanı Faik İçil Vocational High School, University of Selçuk, Konya, TURKEY

*hamdisukurkilig@selcuk.edu.tr

ABSTRACT

Semiconductor materials give opportunities to develop some novel product in high technology areas to present expected properties such as low energy consumption and high efficiency. Amorphous Indium Gallium Zinc Oxide (IGZO) semiconductor firstly developed in 2003 and after development of this very beneficial material, its structural, morphological, electrical and optical properties have been investigated and obtained results have been interpreted.

In this study, we have concentrated on nonlinear optical properties of IGZO which has been deposited as in the form of thin films. Firstly, by producing IGZO thin films in nano dimensional thicknesses using Pulsed Laser Deposition (PLD) method and non-linear optical (NL) properties of thin films have been determined using femtosecond(fs) laser z-scan technique. Linear absorbance range, nonlinear absorption coefficient, refractive index as well as third order susceptibility have been calculated and given in details.

KEYWORDS: *Nonlinear Optics, z-scan, pulsed laser deposition, optical susceptibility*

1. INTRODUCTION

Interaction of laser beam with material is a comprehensive subject and can mainly be divided into two main categories of linear and nonlinear interactions from the viewpoint of optics depending on laser beam intensity. In the case of higher laser intensities, materials give a nonlinear response to an intensive laser beam while linear optical phenomena are taken place in the case of lower laser intensities. Due to these facilities, a large number of work have been performed by several research groups all over the world and great results as well as technological outcomes have been given and reported in literature [1-3]. Investigation of materials depending on laser beam intensities at the focal point gains attraction as laser technologies develop and gives us some better and better possibilities as well as flexibilities to set different experimental conditions.

The main concept of photonics can be defined to be production and investigation of new technological materials showing high nonlinear effects. The most of materials at the present needs a certain laser intensity to induce nonlinear effects. Some novel structures to produce some new nonlinear optical properties can be expected in the future with different wavelength.

Novel as well as functional materials are required for the invention and development of photonics such as new diodes, sensors with several applications, biosensors as well as solar energy technologies. Conventional or nonlinear optical treatments may be needed to well characterise and define materials for better usage for novel applications. It is strongly believed that some new devices based on nonlinear phenomena in new photonics applications are needed but it is not commercially available yet [4]. The refractive index and absorption coefficient of materials can be divided into two parts as linear and complex. These can be given to be

$$n = n_0 + n_2 I \quad (1)$$

$$\alpha = \alpha_0 + \Delta\alpha \quad (2)$$

Where n_0 and α_0 are linear refractive index and absorption coefficient while n_2 and β are nonlinear refractive index and multiphoton absorption coefficient, respectively. Where n_2 is nonlinear refractive index of medium which can be increased or decreased as a function of light intensity and interprets some significant properties of material, but n_0 remains constant in the case of linear optics. Here, it would be better to mention that nonlinear refractive index, n_2 , is related to the real part, $\chi_{Re}^{(3)}$, of third order susceptibility while the nonlinear absorption coefficient, β , is related to imaginary part, $\chi_{Im}^{(3)}$, of $\chi^{(3)}$, susceptibility, which are proportional to the light intensity I ($\propto |E|^2$), i.e., it can be written as

$$n_2 \propto (\chi_{Re}^{(3)})I$$

$$\beta \propto (\chi_{Im}^{(3)})I$$

In the case of third order non-linear processes, the variation of susceptibility, the NL refractive index and the NL absorption coefficient are all depends on the intensity of laser beam. IGZO is one of the most important materials for semiconductor technology and can be used either in crystal structure or amorph structure depending on applications [5]. It is produced and used in amorphous form to develop technologies, especially a large number of study has been reported in literature [6] in amorphous structure and [7] in crystal form, and both form of material have been extensively investigated and used for Thin Film Transistor (TFT) technology. It is well interpreted that the deposition of a crystalline IGZO thin film can be constructed by a variety of methods and it was stated that only a-IGZO can be obtained at low temperature and crystallisation IGZO starts from 140 °C and the best crystallisation was obtained at 180 °C under optimized experimental conditions [7]. An open aperture z-scan experiment was performed to measure two photon absorption coefficient of a-IGZO thin film produced at room temperature and NL absorption coefficient and third order susceptibility of a-IGZO have been reported [6]. Crystallization characteristics of IGZO thin film have been extensively studied as a function of substrate temperature and the thickness of IGZO thin film [8]. In this work, Jo et al. have employed a RF deposition technique to deposit IGZO thin films and they have investigated crystalline structure of IGZO and then they have allowed annealing this thin film over an hour at 400-850 °C in a conventional furnace and they have reported that, a-IGZO thin film starts to become c-IGZO structure after 700 °C as thin film thickness goes down to about 10 nm [8]. In another work, Obonai et al. [9] has conducted a detailed work on the nonlinear optical properties of IGZO thin film produced by sputtering technique at room temperature as a function of different composition of components and have also investigated the effect of the change of composition on the performance of field effected transistor (FET). IGZO thin films were deposited on glass substrates by ultrasonic spray pyrolysis as a function of the substrate temperature by Jayaraman [10]. They have investigated physical properties of IGZO thin film and given results about structural, morphological, optical, and electrical properties of IGZO thin films. Three 425, 450 and 475 °C annealing temperatures were applied and some conclusions were made that IGZO thin films were produced as a crystalline form in hexagonal wurtzite structure and the substrate temperature changed the sizes of hexagonal IGZO nanoparticles as well as transmittance in UV-vis regions and it was concluded that IGZO films have transparent structure (> 70%) with a minimal resistivity [10].

In this study, we have worked out linear and nonlinear optical attitudes of IGZO semiconductor material and determined n , α , β , real, $\chi_{Re}^{(3)}$, and imaginary, $\chi_{Im}^{(3)}$, parts of $\chi^{(3)}$ as well as $\chi^{(3)}$ third order nonlinear susceptibility itself. Due to the knowledge of authors, no compact characterisation of IGZO thin film has not been studied yet, but it can be said that IGZO sample is a transparent semiconductor and commonly used in transistor technologies [11-13].

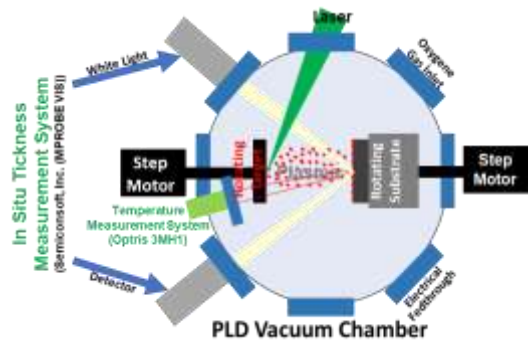
Therefore, it is believed that this work will give a significant contribution to IGZO literature about its nonlinear optical properties.

2. IGZO THIN FILM PRODUCTION

In this work we have given an extensive study either experimentally or theoretically to give some important data from IGZO semiconductor material to check whether we can produce some more photonics applications or not. Experimentally, firstly we have performed an experiment to produce IGZO, purchased from Kurt Lesker commercially, thin films by performing Pulsed Laser Deposition (PLD) and we have performed a number of tests to give some characteristic data about IGZO materials such as UV-Vis spectroscopy, Atomic Force Microscopy (AFM), Scanning Electron Microscopy (SEM), Profilometry and Z-Scan analysis to give linear absorption coefficient and band gap, surface morphology, compositional structure, thickness and either nonlinear properties (nonlinear two photon absorption coefficient and nonlinear refractive index) have been determined, respectively. All details of these procedure as well as results will be discussed below. PLD system (given in Fig.1) is used in connection with a Nd:YAG laser (Continuum, Minilite II, USA) system which produces laser beam at 1064 nm used to perform IGZO thin films in this work. Laser system produces laser pulses at 5 ns in duration with a tuneable repetition rate from 1 Hz to 15 Hz. Power delivered by laser per pulse is changed through a neutral density filter and measured after the filter at just before the focusing lens using a powermeter.



(a)



(b)

Figure 1: PLD system is shown as (a) photograph, (b) schematics of the components of vacuum system.

Soda lime glasses (SLG) were used as a substrate on which IGZO thin films were deposited. SLG substrates were first cleaned in an order of washing with soap foam, bath in acetone/isopropyl alcohol for fifteen minutes, cleaning in an ultrasonic bath and then dried in a nitrogen gas flow. a-IGZO films were deposited at room temperature (RT). The laser beam energy per pulse was set to 3 mJ and tightly focused on IGZO sputtering target surface by using an optical lens with a focal length of 40 cm. The background pressure in vacuum chamber before start experimenting was evacuated down to several 10^{-7} mbar. Then, a-IGZO sputtering target was ablated by applying laser pulses and a-IGZO thin films were grown in an O_2 atmosphere at 2×10^{-3} mbar. All details of our experimental system have been given in several report elsewhere in literature [5, 14-19].

3. RESULTS AND DISCUSSIONS

The morphology of a-IGZO thin films deposited on a SLG substrate was analysed by AFM microscopy technique. The optical absorption spectra of a-IGZO thin film deposited on SLG was measured using a UV-Vis spectrophotometer (JASCO, V-670 Spectrophotometer, Japan) and then

all results obtained have been discussed below. Absorption spectrum of a-IGZO is shown in Fig.2(a) representing absorbance of a-IGZO over a spectral range from 300 nm to 1500 nm. Linear absorption coefficient, α , of sample has been determined to be $\alpha = 0.157$. The absorption intensity in visible region is relatively higher than that in IR region for this a-IGZO thin film. The Tauc equation has been used to determine photon energy band gap values by using absorption spectrum as indicated in Eq. (3),

$$(\alpha h\nu)^2 = A(h\nu - E_g)^{1/2} \quad (3)$$

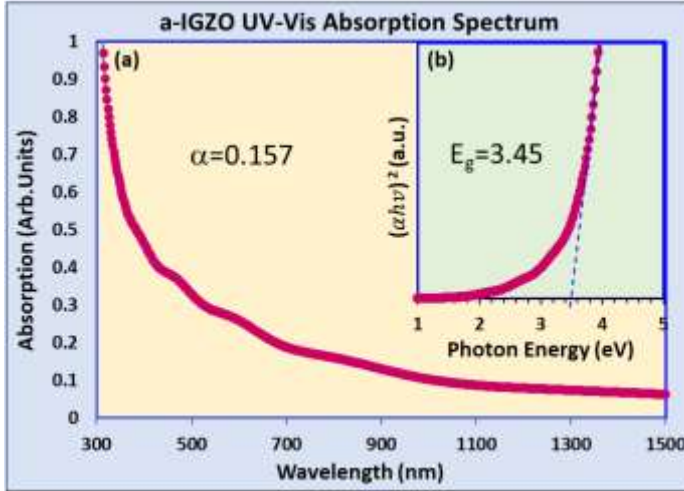


Figure 2: (a) Absorption spectrum of a-IGZO structure, (b) $(\alpha h\nu)^2$ energy diagram of a-IGZO material as a function of photon energy.

where E_g is band gap value for a-IGZO thin film, A is area illuminated and $h\nu$ is photon energy. All of these three parameters are constant during the time duration of experiment. E_g has been determined by straight line of $(\alpha h\nu)^2$ plotted against $(h\nu)$ in Tauc plot in Fig.2(b). The band gap has been determined by performing a calculation using Eq. (3) to be about 3.45 eV and this value has been used to determine nonlinear optical characteristics of a-IGZO thin film as is discussed below. In this study, experimental measurement has been obtained from z-scan experiment and theoretical analysis of experimental data have been performed. Data was analysed and both nonlinear two photon β absorption and nonlinear n_2 refraction index have been determined and then obtained results have been discussed below in detail.

Z-scan technique is a clever technique used to characterise several types of materials such as glasses, organic/inorganic crystals, polymers, semiconductors, some organic/inorganic molecules, liquid crystals, dielectric/metallic coatings, thin films, gases etc. [16, 20-31]. Experimental set-up for this work is shown in Fig.3 and details have been given elsewhere [21, 22, 32, 33]. A fs laser system was used to perform z-scan experiments consists of a Ti:Sapphire laser system from Quantronix, NY, USA, delivers laser pulses at 800 nm wavelength at 90 fs pulse duration @ 1, 2 and 3 kHz repetition rates. In our Z-Scan experimental system, we have an opportunity to measure both two photon nonlinear absorption coefficient and nonlinear refractive index simultaneously employing open and closed aperture detectors indicated as **DI** and **DII** as represented in Fig. 3. In the experimental procedure, we have used a reference detector to measure applied laser intensity just before focusing lens, after that laser beam focused by a long focal length lens along z axis.

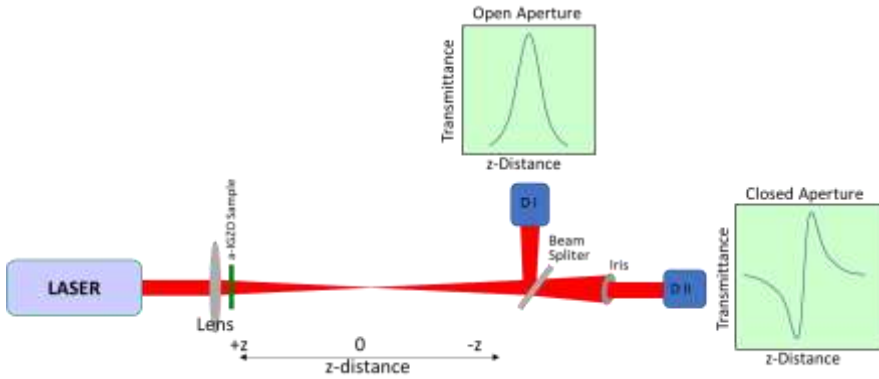


Figure 3: Experimental set-up for an open aperture Z-Scan system used in this work.

The sample under investigation moves along z-axis to pass through focal zone of laser beam back and forth to investigate the sample response to the light beam as a function of the light intensity. After gathering data from both detectors, we have used some MATLAB codes to fit data to theoretical equations and then determine this nonlinear absorption and refraction coefficients of material.

NL optical signal from **DI** open aperture detector has been measured and then fitted to Eq. (4)

$$T(z, \beta) = \frac{\beta I_0 L_{eff}}{2\sqrt{2}} \frac{1}{(1+z^2/z_0^2)} \quad (4)$$

where z is the position of sample and $z_0 = \pi \omega_0^2 / \lambda$ is Rayleigh range [34, 35]. $L_{eff} = 1 - e^{-\alpha L} / \alpha$ is effective length, where β is the effective NL absorption coefficient, ω_0 is the beam waist at the focal point, λ is laser wavelength and I_0 is the laser beam intensity at focal point [36].

Table 2. NL two photons absorption (TPA) coefficient (β) and NL refractive index (n_2) parameters of a-IGZO at a laser intensity of 1.43×10^{12} (W/cm²).

Sample Name	β ($\times 10^{-11}$ cm/W)	n_2 ($\times 10^{-16}$ cm ² /W)
a-IGZO	7.223	-6.0464

The effective NLO two photons absorption coefficient β value is obtained from open aperture z-scan transmittance using Eq. (4). Table 2 shows β parameters at the order of 10^{-11} cm/W for a-IGZO measured by using laser intensities about 10^{12} W/cm² intensity for fs laser pulses. Open and closed aperture z-scan curves for a-IGZO are shown in **figure 4a** and **figure 4b**. The curve in open aperture (figures 3a) shows characteristic saturable absorption (SA) behaviours [37, 38] which is found out that transmittance of laser beam through the sample under investigation increases as input laser intensity increases at focal point [39]. Closed aperture z-scan curve shown in figure 3b demonstrates no any good fit to theory for a-IGZO characteristics. The negative NL optical refractive index n_2 exhibits no clear self-defocusing effect obtained from Eq. (5) and shown in Table 2. n_2 parameter for a-IGZO thin film has been calculated as a negative parameter in order of 10^{-16} cm²/W [40]. Normalized transmittance z-scan curves from open and closed aperture detectors have been fitted and plotted using necessary codes in MATLAB programme produced in our laboratory [20-22]. After collection of experimental data *via* a closed apertured detector, the signal is fitted to an equation (Eq. (5)) of

$$T(z, \Delta\phi_0) = 1 + \frac{4\Delta\phi_0 z}{((z^2/z_0^2)+9)(z^2/z_0^2+1)} \quad (5)$$

where z is the position of medium and $\Delta\phi_0$ is phase shift. The closed aperture z-scan data gives the phase shift $\Delta\phi_0$ which is given to be $\Delta\phi_0 = (2\pi/\lambda)n_2I_0L_{eff}$. The experimental measurements of NL refractive index, n_2 , and NL-TPA coefficient, β , were carried out to calculate third-order NL optical susceptibility ($\chi^{(3)}$) of a-IGZO thin film. The third-order NL optical properties of a-IGZO have been calculated utilizing z-scan results which gives opportunity to calculate real and imaginary values by using following equations;

$$\chi_{Re}^{(3)}(esu) = 10^{-4} \frac{\epsilon_0 c^2 n_0^2}{\pi} n_2 \quad (6)$$

$$\chi_{Im}^{(3)}(esu) = 10^{-2} \frac{\epsilon_0 c^2 n_0^2 \lambda}{4\pi^2} \beta \quad (7)$$

According to the parameters in these equations, the vacuum permittivity and the velocity of light is symbolized as ϵ_0 and c , respectively. Calculated n_2 and β parameters have been utilized to identify the third order susceptibility of a-IGZO applying Eq. (8) and results have been shown in Table 3 [40-42].

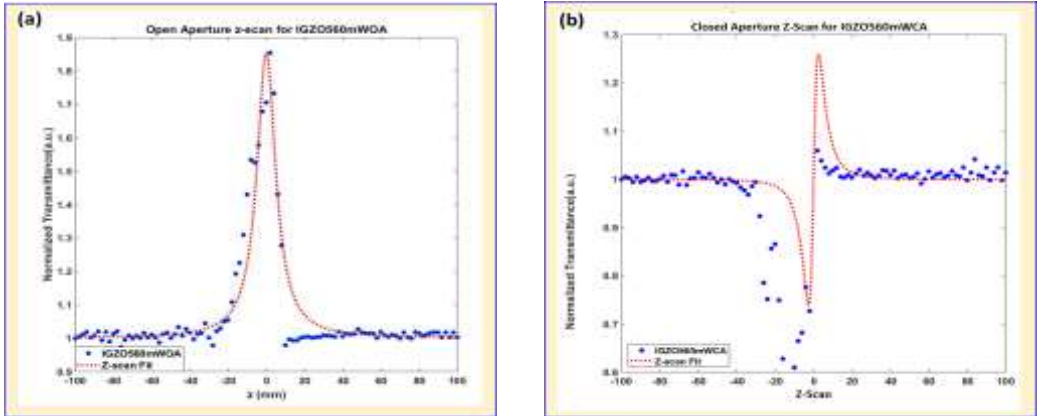


Figure 4: (a) a-IGZO open and (b) closed aperture normalized z-scan data have been plotted and a comparison of experimental and theoretical data has been presented.

$$|\chi^{(3)}| = \left[(\chi_{Re}^{(3)})^2 + (\chi_{Im}^{(3)})^2 \right]^{1/2} \quad (8)$$

Table 3. The real and imaginary parts of third order NL optical susceptibility of a-IGZO.

Sample Name	$\chi_{Re}^{(3)}(esu)$	$\chi_{Im}^{(3)}(esu)$	$\chi^{(3)}$
a-IGZO	-5.737×10^{-16}	4.363×10^{-14}	4.3634×10^{-14}

1. CONCLUSIONS

The data shows some NL optical properties of a-IGZO and presented performing fs laser z-scan technique. The open and closed aperture z-scan experimental results make possible to measure third order NL optical susceptibilities and NL refractive indices and NL two photons absorption coefficients [43]. These obtained data show that NL two photons absorption coefficient β and NL

refractive index n_2 of a-IGZO have been found to be good candidate of optical limiting devices applications.

The third order NL optical parameters of a-IGZO in terms of fs z-scan experimental procedure as well as real and imaginary parts are measured 10-16 esu and 10-14 esu. β , n_2 and $\chi(3)$ values for the sample have been calculated to be in orders of 10-11 cm/W, 10-16 cm²/W and 10-14 esu, respectively. Depending on NL optical results of a-IGZO is actively investigated by a number of scientists and they have been concluded as potential candidate for optical limiter [44, 45] and optical switches [46] for photonics applications.

ACKNOWLEDGEMENT

Author would like to kindly acknowledge;

Selçuk University Scientific Research Project (BAP) Coordination for the support with the number 20401018, 19401140, 18401178, 15201070 and 13301022 projects,

Selçuk University, High Technology Research and Application Center (İL-TEK) and SULTAN Center for infrastructures.

REFERENCES

- [1] Menzel, R., Photonics: linear and nonlinear interactions of laser light and matter. 2013: Springer Science & Business Media.
- [2] Banerjee, P.P., Nonlinear optics: theory, numerical modeling, and applications. 2003: CRC Press.
- [3] Li, C., All-optical switch based on nonlinear optics, in Nonlinear Optics. 2017, Springer. p. 279-386.
- [4] Light, H., Optical Science and Engineering for the 21st Century. 1998, National Academy Press, Washington DC.
- [5] GEZGİN, S.Y., Y. GÜNDOĞDU, and H.Ş. KILIÇ, Electrical Properties of The Heterojunction Diode Produced Based on IGZO Thin Film. Afyon Kocatepe Üniversitesi Fen Ve Mühendislik Bilimleri Dergisi, 2021. 2021(2): p. 257-265.
- [6] Sanal, K., et al. Nonlinear properties of IGZO thin films prepared by RF magnetron sputtering. in Nanophotonic Materials XI. 2014. SPIE.
- [7] Wang, X., et al., Preparation and Properties of Crystalline IGZO Thin Films. Membranes, 2021. 11(2): p. 134.
- [8] Jo, J., et al. The influence of annealing temperature and film thickness on crystallization behaviors of IGZO thin films. in 2015 22nd International Workshop on Active-Matrix Flatpanel Displays and Devices (AM-FPD). 2015. IEEE.
- [9] Obonai, T., et al., Relation between crystallinity and constituent distribution of an IGZO thin film. Japanese Journal of Applied Physics, 2019. 58(9): p. 091003.
- [10] Jayaraman, V.K. and A.M. Álvarez, Effect of substrate temperature on structural, morphological, optical and electrical properties of IGZO thin films. Physica E: Low-dimensional Systems and Nanostructures, 2017. 86: p. 164-167.
- [11] Hosono, H., How we made the IGZO transistor. Nature Electronics, 2018. 1(7): p. 428-428.
- [12] Han, K., et al., Indium-Gallium-Zinc-Oxide (IGZO) Nanowire Transistors. IEEE Transactions on Electron Devices, 2021. 68(12): p. 6610-6616.
- [13] Rios, R., et al., A physically based compact model for IGZO transistors. IEEE Transactions on Electron Devices, 2021. 68(4): p. 1664-1669.
- [14] Yiğit Gezgin, S. and H.Ş. Kiliç, Determination of electrical parameters of ITO/CZTS/CdS/Ag and ITO/CdS/CZTS/Ag heterojunction diodes in dark and illumination conditions. Optical and Quantum Electronics, 2019. 51(11): p. 1-22.
- [15] Yiğit gezgin, S., A. Houimi, and h.ş. kiliç, Comparison of electrical and photovoltaic parameters of the hetero-junction solar cells based on CZTS and CIGS ultrathin films. Materials Technology, 2021: p. 1-13.

- [16] Kılıç, H.Ş., et al., Nonlinear optical properties of Cu₂ZnSnS₄ nanocrystal thin films and its constituents thin films. *Optical and Quantum Electronics*, 2021. 53(1): p. 1-11.
- [17] Gezgin, S.Y. and H.Ş. Kılıç, The electrical characteristics of ITO/CZTS/ZnO/Al and ITO/ZnO/CZTS/Al heterojunction diodes. *Optik*, 2019. 182: p. 356-371.
- [18] Gezgin, S.Y., et al., The effect of CZTS ultrathin film thickness on the electrical characteristic of CZTS/Si heterojunction solar cells in the darkness and under the illumination conditions. *Silicon*, 2021. 13(10): p. 3555-3567.
- [19] Gezgin, S.Y., A. Houimi, and H.Ş. Kılıç, Production and photovoltaic characterisation of n-Si/p-CZTS heterojunction solar cells based on a CZTS ultrathin active layers. *Optik*, 2019. 199: p. 163370.
- [20] Gundogdu, Y., et al., Copper-based thiospinel quantum dots as potential candidates for nonlinear optical applications. *Optics & Laser Technology*, 2022. 148: p. 107752.
- [21] Gündoğdu, Y., H.Ş. Kılıç, and M. Çadırcı, Third order nonlinear optical properties of CdTe/CdSe Quasi Type-II Colloidal Quantum Dots. *Optical Materials*, 2021. 114: p. 110956.
- [22] Çadırcı, M., et al., Nonlinear optical properties of core shell type II quantum dot structures. *Optics & Laser Technology*, 2020. 128: p. 106246.
- [23] Zhang, H., et al., Z-scan measurement of the nonlinear refractive index of graphene. *Optics letters*, 2012. 37(11): p. 1856-1858.
- [24] Ramteke, S., et al., Novel report on SHG efficiency, Z-scan, laser damage threshold, photoluminescence, dielectric and surface microscopic studies of hybrid inorganic ammonium zinc sulphate hydrate single crystal. *Optics & Laser Technology*, 2018. 104: p. 83-89.
- [25] Kumar, S.A., J. Senthilselvan, and G. Vinitha, Third order nonlinearity and optical limiting behaviors of Yb: YAG nanoparticles by Z-scan technique. *Optics & Laser Technology*, 2019. 109: p. 561-568.
- [26] KILIÇ, H.Ş., et al., Femtosaniye laser Z-Scan tekniği ile malzemelerin Nonlineer optik karakterizasyonu. *Selcuk University Journal of Engineering Sciences*, 2016. 15(2): p. 44-59.
- [27] He, T., et al., Z-scan determination of third-order nonlinear optical nonlinearity of three azobenzenes doped polymer films. *Optics communications*, 2007. 275(1): p. 240-244.
- [28] Couris, S., et al., An experimental investigation of the nonlinear refractive index (n₂) of carbon disulfide and toluene by spectral shearing interferometry and z-scan techniques. *Chemical Physics Letters*, 2003. 369(3-4): p. 318-324.
- [29] Battaglin, G., et al., Z-scan study on the nonlinear refractive index of copper nanocluster composite silica glass. *Applied Physics Letters*, 2001. 78(25): p. 3953-3955.
- [30] Ayare, N.N., et al., Z-scan and DFT approach for investigating the NLO properties of imidazole fused anthraquinone dyes. *Journal of Photochemistry and Photobiology A: Chemistry*, 2020. 390: p. 112327.
- [31] Ali, Q.M. and P. Palanisamy, Z-scan determination of the third-order optical nonlinearity of organic dye Nile blue chloride. *Modern Physics Letters B*, 2006. 20(11): p. 623-632.
- [32] Kılıç, H.Ş., et al., Femtosaniye laser Z-Scan tekniği ile malzemelerin Nonlineer optik karakterizasyonu. *Selçuk-Teknik Dergisi*, 2016. 15(2): p. 44-59.
- [33] Kılıç, H.Ş., et al., Nonlinear optical properties of Cu₂ZnSnS₄ nanocrystal thin films and its constituents thin films. *Optical and Quantum Electronics*, 2021. 53(1): p. 1-11.
- [34] Ajami, A., et al., Two-photon absorption cross section measurements of various two-photon initiators for ultrashort laser radiation applying the Z-scan technique. *JOSA B*, 2010. 27(11): p. 2290-2297.
- [35] Vivacqua, M., D. Espinosa, and A. Martins Figueiredo Neto, Application of the Z-scan technique to determine the optical Kerr coefficient and two-photon absorption coefficient of magnetite nanoparticles colloidal suspension. *Journal of Applied Physics*, 2012. 111(11): p. 113509

-
- [36]Wang, X., et al., Third-order nonlinear optical properties of a novel series of D- π -A pyrene-aldehyde derivatives. *Journal of Nonlinear Optical Physics & Materials*, 2016. 25(02): p. 1650014.
- [37]Wang, C., et al., Polymers containing fullerene or carbon nanotube structures. *Progress in Polymer Science*, 2004. 29(11): p. 1079-1141.
- [38]Mishra, S., H. Rawat, and S. Mehendale, Reverse saturable absorption and optical limiting in C60 solution in the near-infrared. *Applied physics letters*, 1997. 71(1): p. 46-48.
- [39]Kulyk, B., et al., Penta (zinc porphyrin)[60] fullerenes: Strong reverse saturable absorption for optical limiting applications. *Applied Surface Science*, 2020. 533: p. 147468.
- [40]Zidan, M., et al., Investigation of optical nonlinearity of C60 doped acetylenedicarboxylic acid polymer. *Optics & Laser Technology*, 2015. 68: p. 60-66.
- [41]Geethakrishnan, T. and P. Palanisamy, Z-scan determination of the third-order optical nonlinearity of a triphenylmethane dye using 633 nm He-Ne laser. *Optics Communications*, 2007. 270(2): p. 424-428.
- [42]Singh, V. and P. Aghamkar. Z-scan: A simple technique for determination of third-order optical nonlinearity. in *AIP Conference Proceedings*. 2015. AIP Publishing LLC.
- [43]Ganeev, R., et al., Nonlinear optical characteristics of C60 and C70 films and solutions. *Optics communications*, 2000. 185(4-6): p. 473-478.
- [44]Sun, J., et al., Remarkable nonlinear optical response of pyrazine-fused trichalcogenasumanenes and their application for optical power limiting. *Journal of Materials Chemistry C*, 2018. 6(48): p. 13114-13119.
- [45]Veisi, M., S.H. Kazemi, and M. Mahmoudi, The effects of intersystem and reverse intersystem crossing on the optical limiting properties of C60. *Journal of Applied Physics*, 2020. 127(10): p. 103102.
- [46]Dong, Y., et al., Passive optical switches based on endohedral fullerenes. *Optical Materials*, 2016. 53: p. 14-18.

Türkiye'de Yapay Zeka Alanında Lisansüstü Tezlerde Güncel Konular (1984-2021)

Hasan ŞAHİN^{1*}, Halit ÖZTEKİN²

¹ Bursa Technical University, Industrial Department, Bursa-TURKIYE

² Sakarya University of Applied Sciences/Computer Engineering, Sakarya, TÜRKİYE

*h.sahin@btu.edu.tr

ÖZET

Lisansüstü eğitim sürecinin en önemli çıktısı tezlerdir. Bu tezlerde ele alınan konular, o bilim dalındaki bilgi birikiminin kapsamına ilişkin önemli sonuçlar ortaya koymaktadır. Ulusal ve uluslararası alanda bilimsel çalışmaların taranması ile ilgili olarak yapılmış yüksek lisans ve/veya doktora tezlerini analiz eden birçok araştırmaya rastlamak mümkündür. Bu araştırmada Türkiye’de doğrudan yapay zeka ile ilgili anabilim dallarında hazırlanmış ve Yükseköğretim Kurulu Başkanlığı (YÖK) Tez Merkezi’nde 974 Yüksek lisans tezi, 296 doktora, 18 Tıpta uzmanlık 4 sanatta yeterlilik ve 2 diş hekimliği olmak üzere 1294 lisansüstü tez incelenmiştir. Araştırmanın temel amacı bu tezlerde odaklanılan konu ve yöntemleri tespit etmektir. Bu amaçla 2022 yılına kadar (1984-2021) yayımlanmış tezlerinin genel profilini belirlemeye çalışılmıştır. Tezler özgün dil, yıl, üniversite, enstitü, anabilim dalı, konu, uygulama alanı ve yöntem açısından incelenmiştir. Araştırmada nitel yöntem kullanılmış, YÖK Tez Merkezi’nde paylaşılan tez künyeleri ve özetlerinden edinilmiş veriler, içerik analizi tekniği ile analiz edilmiştir. Yapılan analizler sonucunda yapay zeka konusunda yapılan tezlerin çoğunlukla Bilgisayar Mühendisliği, Elektrik Elektronik Mühendisliği, Endüstri Mühendisliği, İnşaat Mühendisliği, Makine Mühendisliği, İşletme, Mekatronik Mühendisliği ve Mimarlık Anabilim Dalı’nda çalışıldığı ortaya çıkmıştır. Ayrıca tezlerde en çok araştırılan konunun Bilgisayar Mühendisliği Bilimleri-Bilgisayar ve Kontrol ve en yaygın kullanılan yöntemin yapay sinir ağları, makine öğrenmesi ve derin öğrenme olduğu belirlenmiştir.

ANAHTAR KELİMELER: *Yapay Zeka, Yüksek Lisans Tezi, Doktora Tezi, Türkiye*

Hot Topics in Postgraduate Theses on Artificial Intelligence in TURKIYE (1984-2021)

ABSTRACT

In online education, which is becoming more and more widespread, it is critical for the quality of education to evaluate and grade the assignments or exams that students upload to the system. However, it is time consuming to determine how well the circuit drawings prepared for the digital logic course, which is a fundamental course in computer engineering and similar disciplines, are not only correct, but also compatible with the truth table. Content-Addressable Memory (CAM), also known as Associative Memory, is a data storage and retrieval unit. Typically used instead of the conventional memories in fast-paced and time-sensitive applications such as address lookup in internet routers, databases, and pattern recognition. CAMs implement the search process by comparing the content itself with a key instead of finding the address like the conventional memories. Unlike conventional memories where the search process is done sequentially and takes multiple clock cycles to find the desired data, the parallelism property of the CAMs allows them to search for the data (content) within the memory unit in a single clock cycle. A logic circuit evaluation engine is an application that can be used as an educational tool that helps to evaluate hand-drawing or digital-drawing logical circuit designs. The increase in the speed of the evaluation process helps the application to be more efficient, especially if there is a large number of designs. In this paper, a comparison between an FPGA-based logic circuit evaluation engine using CAM versus Random-

Access Memory (RAM) is made in order to demonstrate the advantages of using CAMs over the conventional memories based on their discussed results.

KEYWORDS: *Artificial Intelligence, Master Thesis, PhD Thesis, Turkey*

1. GİRİŞ

Yapay zeka; insan gibi düşünen, insan gibi davranan, akılcı (rasyonel) düşünen ve akılcı davranan canlıların zekice olarak kabul edilen davranışlarına sahip bilgisayar sistemleridir ve makine öğrenmesi bu anlamda yapay zekanın son evresi olarak kabul edilmektedir (Howard, 2019). Yapay zekâ teknolojileri, endüstriyel süreçlerin verimliliğini ve etkinliğini artırmak için kullanılmak üzere tasarlanmıştır (Şahin, 2021). Bilgi işlem ve bilgi işleme tekniklerindeki hızlı ilerleme, bilgisayarların çıkarım, analiz ve karar verme gibi akıllı insan davranışlarını simüle ederek görevleri gerçekleştirmesini sağlamayı amaçlayan yapay zekanın (AI) ilerlemesini ve uygulamalarını hızlandırmıştır (Topol, 2019). Yapay zeka kavramı, “insan zekasının sinir sistemi, gen yapısı gibi fizyolojik ve nörolojik yapısının ve doğal olayların modellenerek makineler (bilgisayar ve yazılımlara) aktarılması” olarak tanımlanmaktadır (Pomerol, 1997). Yapay zekâ, canlıların ve insanın davranış biçiminden esinlenerek sistemlerin modelleme çalışmasının genel adıdır (Sucu ve Ataman, 2020). Günümüzde ve gelecekte yapay zekâ üzerine söylenecek birçok şey bulunmaktadır (Nabiyev, 2012). Yapay zekâ insan zekasıyla karşılaştırıldığında, yapay zekânın daha fazla kalıcı olduğu kolaylıkla kopyalanabilir ve geniş kitlelere ulaştırılabilir olduğu görülebilir (Demir, 2018) ve bazı tıbbi sistemler, potansiyel hastalıkları tespit etmede veya büyük bir veri setini analiz ederek karar vermede insan uzmanlara yardımcı olabilir (Zhu, 2020). Güçlü yapay zekâ karşıtları makinelerin kalıtsal olarak insandan farklı olduklarını savunarak, asla sevgi duyamayacaklarını, öğrüyü ve yanlışı sağduyulu bir şekilde ayırt edemeyeceklerini, insan gibi düşünemeyeceklerini savunurlar. Bununla birlikte taraftarları ise insan beyninin tek başına düşünemeyen şuurlu olmayan bileşenlerden oluşup, bir araya geldiklerinde düşünen ve şuurlu olduklarını söyleyerek aynı fenomenin makine için de geçerli olabileceğini savunurlar (Şen ve Yurtoğlu, 2020).

Türkçe kaynaklarda Yapay Us ve Suni Zeka olarak da bilinen Yapay Zekanın çağdaş bir bilim dalı olarak gelişmesi 1956 yılında C. Shannon, M. Minsky ve J. McCarthy'nin çabaları ve katkıları ile başlamıştır. “Yapay Zeka” adı ilk kez 1956 yılında ABD’de bir Makine Zekası konferansında kullanılmış bir kavramdır (Allahverdi, 2002). Yapay zekanın amacı insan zekasına sahip bilgisayarlar geliştirmek, insanın zeki davranışları ile benzeyen makineler yapmaktır. 1956’lı yıllardan günümüze özellikle de bilgisayar donanım ve yazılımı, robotlarda görme, tanıma, örüntü ve konuşma algılama, öğrenme, bilişsel modelleme, bilgiye erişim, bilgi arama, oyun teorisi, gibi uygulamalarda kullanılmış binlerce akademik yayın, araştırma projesi ve doktora çalışmasına sahne olmuştur.

Yapay zeka ile uğraşan bilim adamları bir anlamda bilgisayar programlarının problemleri çözerken gösterdiği yaklaşımın bir insanın davranışına benzemesi olarak kabul edilen bilgisayar sistemleri geliştirmekle uğraşmaktadırlar (Allahverdi, 2002). Yapay zeka, insanlarda zeka ile ilgili zihinsel fonksiyonları bilgisayar modelleri yardımıyla inceleyip bunları formel hale getirdikten sonra yapay sistemlere uygulamayı amaçlayan bir araştırma alanıdır (Nabiyev, 2012). Çağdaş dünyada bilgisayar ve bilgisayar sistemleri yaşamın vazgeçilmez parçası haline gelmiştir. Elimizdeki cep telefonlarından, evlerimizdeki buzdolapları, bulaşık makinası, çamaşır makinasına kadar bir çok makine bilgisayar sistemleri ile çalışmaktadır. İş dünyasından kamu çevrelerine, çevre ve sağlık sektöründen askeri sistemlere kadar hemen hemen her alanda bilgisayardan faydalanmak gereklilik haline gelmiştir. Bunun tersini düşünmek bile teknolojinin nimetlerini hiçe saymak olarak görülebilir (Öztemel, 2012).

Özetle yapay zeka; “insan gibi düşünen, insan gibi davranan, akılcı (rasyonel) düşünen ve akılcı davranan” (Atalay ve Çelik, 2017), canlıların zekice olarak kabul edilen davranışlarına sahip bilgisayar sistemleridir ve makine öğrenmesi bu anlamda yapay zekanın son evresi olarak kabul edilmektedir. Yapay zekâ uygulamalarının en başında günümüzde insansı robotlar gelmektedir

(Selwyn 2019). Özellikle gelişen teknoloji ve yeni doğan ihtiyaçlarla birlikte yapay zekâ ve insansı robotlara ilgi her geçen gün artmaktadır (Öztürk, Şahin, 2018).

YZ kavramını ilk duyduğumuzda ister akademisyen, öğretmen, öğrenci olsun ister işadami olsun birçok kişi üzerinde oldukça fazla merak uyandırmaktadır. Bu merakın nedeni olarak aslında zeka gibi soyut kavramın yapay olarak nitelendirilmesi olarak açıklanabilir. Yapay zekanın uyandırmış olduğu bu merakın nedeni olarak içeriği yada temsil ettiği konular hakkında birçok kişinin ciddi bir bilgiye sahip olmamasından da kaynaklanabilir. Yapay zeka ile birlikte daha çok duyulan ifadeler ise uzman sistemler, yapay sinir ağları, bulanık mantık, genetik algoritmalar, makine öğrenmesi, etmen tabanlı sistemlerdir (Allahverdi, 2002). Bunun yanında yapay zeka konuları ile ilgilenen bilgisayar mühendisliği, endüstri mühendisliği, felsefe, bilişsel bilim, elektronik bilimler gibi birçok disiplini bulunmaktadır. Yapay zeka konusunda son zamanlarda Türkçe yayınlanmış bazı yayınlar olsa da henüz yeteri düzeyde olmadığını söyleyebilir. Bu çalışma da Türkiye’de doğrudan yapay zeka ile ilgili anabilim dallarında hazırlanmış ve Yükseköğretim Kurulu Başkanlığı (YÖK) Tez Merkezi’nde yayınlanmış 1294 lisansüstü tez incelenmiştir. Bu tezlerde odaklanılan konu ve yöntemler tespit edilerek 2022 yılına kadar (1984-2021) yayınlanmış tezlerin genel profilini belirleme amacı taşımaktadır.

Tablo 1. Geçmiş Yıllarda Yapılan Çalışmaların Özeti (Topal ve Şahin, 2016)

Yazar (Yıl)	Yıllar	Konu
Sekreter ve Akyüz (2003)	1995-2002	Pazarlama Araştırmaları
Arı ve ark. (2009)	1990 - 2005	Pazarlama Ve Yönetim Alanı
Benligiray (2009)	1983–2008	İnsan Kaynakları Yönetimi
Kayabaşı (2010)	2010	Lojistik
Yalçın (2011)	1941-2010	Jeoloji
Çiltaş (2012)	2012	Matematik Eğitimi
Gömleksiz ve Bozpol (2013)	2013	Eğitim Programları Ve Öğretim Alanı
Bakır (2013)	1994-2012	Pazarlama
Alkan 2014	1984-2012	Muhasebe
Baş ve ark. (2014)	2002-2012	Entelektüel Sermaye
Bozyiğit (2016)	2014-2015	Türkiye’deki Lojistikle İlgili Lisans Bölümleri
Çelik (2016)	2000-2015	Yenilikçilik
Topal ve Şahin (2016)	2000-2015	Tedarik Zinciri Yönetimi
Bu çalışma	1984-2021	Yapay zeka

2. LİTERATÜR ARAŞTIRMASI

Yapay zekâ insan zekâsının ileri teknoloji ile kopyalanmış, mantıklı ve matematiksel kararlar verebilen teknoloji sistemidir (Topakkaya, Eyibaş, 2019). Yapay zekanın sezgisel karar vermeyi yönlendiren taklit edebilme ve çoğaltabilme gibi insana özgü nitelikleri gerçekleştirebilmesi oldukça zor görülmektedir. Gelecekte yapay zekanın insan-yapay zeka iş birliğinde karar verme sürecinde insan yerine geçebilmesi tartışılan konular arasında yer almaktadır (Jarrahi, 2018).

Yapay zeka, insan tarafından yapıldığında zeka olarak adlandırılan akıllı davranışların makineler tarafından da yapılabilmesidir. Yapay zeka aslında insan aklının nasıl çalıştığını gösteren bir kuram şeklinde de açıklanabilir. Yapay zekanın makineleri daha akıllı hale getirmek, zekanın ne olduğunu anlamak ve makineleri daha faydalı olacak şekilde geliştirme amacı vardır (Tektaş ve ark., 2002).

Teknolojik gelişmeler sonucu ortaya çıkan inovatif ürünlerden biri de kollobratif robotlar olarak bilinmektedir. Günümüzde fabrikalarda işçilerin yardımcıları niteliğinde görev yapan bu robotlar üretim süreçlerindeki hem hız ve verimliliği artırmakta hemde maliyetleri düşürmektedirler (Kurt, Bozokulu, 2019). Bu teknolojik gelişmelerin yanında ayrıca ses tanıma ve anlama ile konuşulan tüm içerikler mikrofon tarafından dijitalleşir bir duruma getirilir ve bu sesler, harflere dönüşmekte, kelimeler ise algılanmaya yönelik çalışmaya başlamaktadır. Bireysel yönde kullanılan Google Asistan, Siri, Cortana, Now ve Echo önemli örnekler olarak gösterilebilir. Kurumsal ortamlara

bakıldığında şirket santral sistemlerinde sesli yanıtlama özellikleri ve çağrı merkezlerinde insan olamadan sadece sesli müşteri hizmetleri, sesli imza tarzı uygulamalar olarak görülebilmektedir. Başka bir teknoloji ise görüntü işlemedir. Burada kamera sayesinde çeşitli görüntüler ortaya çıkmaktadır. Bu yönde de bilişim gücü dijital yönde algılanmaktadır. Kameranın pikselleri dijital ortamda bir kod şeklinde gösterilmektedir. Bu pikselleri anlamada yapay zeka teknolojilerinin algoritmaları kullanılmaktadır. Görüntü işleme ile ilgili olarak sürücüsüz araçta verilen konum bilgisi ile aracın sensörler ile etrafını algılayıp aracı doğru konuma götürmesi güzel bir örnek olarak gösterilebilir. Ayrıca güvenlik kameralarının tehlikeli durumları algılayıp alarma geçmesi oluşabilecek tehlikeyi önlemesi oldukça önemlidir. Bunun yanında cep telefonlarındaki kameralarda yer alan tanı cihazları da sağlık açısından gerekli tespitler noktasında geliştirilmiş faydalı algoritmalarıdır. Ayrıca doğal dil işleme ile cümlelerde arama yapma, başka dile çevirme gibi algoritmaların geliştirilmesi de günlük hayatımızda kullandığımız örneklerdir. Google'ın arama motorunda Skype'ta konuşan kişinin konuştuğu dili algılayıp başka bir dile çevirebilme özelliği bulunmaktadır. Belki de en dikkat çekici olan muhakeme özelliğidir. Muhakeme esnasında karşı düşünceye sahip olan kişi dinlenir ve bir yargıya varılır. Yapay zeka bu nokta da olayı değerlendirip rasyonel bir çıkarımda bulunması beklenmektedir (Sucu, Ataman, 2020).

DoNotPay İngiliz-Amerikalı bir girişimci olan Joshua Browder tarafından kurulmuş bir hukuk hizmetleri sohbet robotudur. Chatbot başlangıçta park cezalarına itiraz etmek için inşa edilmiştir, ancak daha sonra diğer hizmetleri de içerecek şekilde genişletilmiştir. Bir "robot avukat" olan DoNotPay, her üç ayda bir 36 ABD doları abonelik maliyetiyle yasal hizmetler sunmak için yapay zeka kullanan indirilebilir bir mobil uygulama olarak bilinmektedir (Adhikari, 2020). Günümüzde robotlar, oldukça fazla kullanım alanı bulmaktadırlar. Bu sayede insanların mesleki alanları içerisinde kendine yer bulmaya başlamıştır (Selwyn, 2019). Caliburger adında bir burger firması, Miso Robotics firmasındaki mutfak bölümüne entegre ettikleri Flippy adı verilen robot ile işbirliği yapmışlardır. Bu sayede yemek hazırlatan hamburger şefi olarak çalışan bir robot tasarlamışlardır. Ayrıca bu yönde engelliler için de robot kullanımı sayesinde günlük hayatı daha da kolaylaştıracağına düşünerek turizm de seyahatlerde de tercih edilmeye başlanmıştır (Sucu, Ataman, 2020).

Günümüzde yapay zeka uygulamaları ile yapay zekaya entegre edilen robotik teknolojilerin insanlığın hizmetine daha fazla dahil olduğu görülmektedir. Yapay zekayı diğer teknolojik gelişmelerden farklı kılan öğrenebilen bir algoritmaya sahip olmasıdır. İnsanlığın yaratılmasından günümüze kadar olan süreçte en büyük eşiklerden biri olarak yapay zekânın geliştirilmesi kabul edilebilir (Kafalı, 2019).

Genel olarak insan zekâsı soyut ve somut kavramlar arasındaki ilişkiyi kurabilme, muhakeme etme, soyut düşünme ve zihinsel işlevlerini amaca yönelik kullanabilme olarak tanımlanmaktadır. İnsan sahip olduğu zekâsı ile bazı nesnelere arasındaki ilişkileri görebilmekte, kaliteyi anlayıp ve değişik nesnelere nasıl birbirleriyle ilişkili olduklarını ortaya koyacak şekilleri tanımlayabilmektedir (Topakkaya, Eyibaş, 2019).

Literatür incelendiğinde, pazarlama, insan kaynakları, jeoloji, sürdürülebilirlik ve sosyal sorumluluk, lojistik, muhasebe, entelektüel sermaye, yenilikçilik gibi farklı konularda araştırmalar yapıldığı görülmüştür. Yüksek lisans ve doktora düzeyinde yapılan bu araştırmalarda genellikle verilerin toplanmasında doküman analizi, verilerin çözümlenmesinde içerik analizi, betimsel analiz, frekans analizi, tipolojik analiz vb. yöntemlerin kullanıldığı tespit edilmiştir. Literatürde yapay zeka konusunda yapılan lisansüstü çalışmalar incelendiğinde daha çok yapay sinir ağı, makine öğrenmesi, derin öğrenme konularında çalışıldığı tespit edilmiştir. Bu araştırma ile yapay zeka konusuyla ilgili yapılan lisansüstü tezlerinin mevcut durumunu ortaya koymanın yanı sıra ileri çalışma önerileriyle alana farklı bakış açıları sunma açısından literatüre katkı sağlanacağı düşünülmektedir.

Sekreter ve Akyüz (2003), çalışmasında, 1995-2002 yılları arasında, yurt dışındaki önemli dergilerde pazarlama araştırmaları alanında yayınlamış makalelerin, uygulamış oldukları araştırma yöntemlerine ilişkin bir yazın taraması yapmıştır. Arı ve ark., (2009) Gazi üniversitesinde 1990 ile

2005 yılları arasında pazarlama ve yönetim alanında yazılmış olan yüksek lisans tezleri incelenmiştir. Benligiray (2009) 1983–2008 yılları arasındaki insan kaynakları yönetimi alanında toplam 2216 lisansüstü tezin yapıldığı tespit edilmiştir. Kayabaşı (2010), çalışmasında müşteriler tarafından lojistik faaliyetlere yönelik şikâyetlerinin araştırılması amaçlanmış ve bu amaçla, içerik analizi ile anket yöntemi kullanılarak elde edilen veriler analiz edilmiştir. Yalçın (2011) 1941-2010 yılları arasında 26 öğretim üyesinin danışmanlığında 140 tez yapıldığını ve İstanbul Üniversitesi'nde jeoloji konusunda tamamlanmış olan doktora tezlerini ilgili konu, danışman öğretim üyesi ve tamamlanma yılı gibi kriterler çerçevesinde incelemiştir. Altuntaş Ve Türker (2012), 2007-2010 yılları arasında sürdürülebilirlik ve sosyal sorumluluk adları ile rapor yayınlayan 17 firma belirlenmiş ve Türk iş dünyası için henüz yeni bir uygulama alanı olan sürdürülebilir tedarik zincirlerinin, Türkiye'de stratejik olarak nasıl kavramsallaştırıldığı ve uygulandığını analiz etmektedir. Bakır (2013) 1994-2012 yılları arasında pazarlama konusunda yapılmış 184 doktora tezinin genel bir profilini ortaya çıkarmış ve bu doğrultuda tezler, öncelikle yayınladığı yıl, yazar adı, danışman adı, üniversite, bilim dalı, veri toplama yöntemi ve veri analiz yöntemleri açısından incelenmiştir.

Alkan, 2014, yaptığı çalışma da 1984-2012 yılları arasında muhasebe alanında yazılan ve erişime açık 656 lisansüstü tezi seçmiş ve seçmiş olduğu tezleri içerik analizi yöntemi kullanılarak konularına, kullanılan yöntem, geliştirilen öneri ve alana katkı gibi belirli kriterlere göre incelemiştir. Baş vd. (2014) 2002-2012 yılları arasında Türkiye'de entelektüel sermaye alanında yazılmış olan ve anahtar kelimeleri bulunan lisansüstü (yüksek lisans ve doktora) tez çalışmalarının içerik analizi yöntemiyle incelenmiştir. Çelik, (2016), çalışmasında 2000-2015 yılları arasında Türkiye'de yenilikçilik konusunda yapılan doktora tezlerinin genel profilini belirlemeyi amaçlamaktadır. Çalışma yenilikçilik konusunda yapılan 100 doktora tezini kapsamakta ve tezler özgün dil, yıl, üniversite, enstitü, anabilim dalı, konu, uygulama alanı ve yöntem açısından incelenmiştir.

3. ARAŞTIRMANIN AMACI VE YÖNTEMİ

Bu araştırmanın amacı, yapay zeka konusunda Türkiye'deki üniversitelerde yürütülen lisansüstü tezlerinin genel bir profilini ortaya çıkarmak ve bu tezlerde kullanılan yöntemlerin yıllar içerisindeki dağılımını tespit etmektir. Bunu gerçekleştirmek için araştırmaya konu olan lisansüstü tezleri belirli kategoriler çerçevesinde analiz edilmiştir. Yapay zeka konusunda kaç adet lisansüstü tez yapılmıştır? Yapılan tezlerin özgün dillerine göre dağılımları, üniversitelere, enstitülere ve anabilim dallarına göre dağılımları, konulara ve uygulama alanlarına göre dağılımları ve daha çok hangi yöntemlerin kullanıldığı şeklinde sorulara cevaplar aramaktadır.

Araştırma kapsamında bulunan tezlerin tespit edilmesi ile ilgili olarak Yüksek Öğretim Kurumu Tez Merkezi'den yararlanılmıştır. Araştırma kapsamında bu tezlerin güncel ve hatasız olduğu kabul edilmiştir. Araştırmanın ana küntlesini Türkiye'de yapay zeka konusunda yapılan lisansüstü tezler olarak belirlenmiş olup, örneklem 1987-2021 yılları arasında yapılan lisansüstü tezler olarak seçilmiştir.

Nitel araştırma, “gözlem, görüşme ve doküman analizi gibi nitel veri toplama tekniklerinin kullanıldığı, algıların ve olayların doğal ortamda gerçekçi ve bütüncül bir biçimde ortaya konmasına yönelik nitel bir sürecin izlendiği araştırma” olarak tanımlamak mümkündür (Yıldırım ve Şimşek, 2008). Nitel araştırma, disiplinler arası bütüncül bir bakış açısını esas alarak, araştırma problemini yorumlayıcı bir yaklaşımla incelemeyi benimseyen bir yöntemdir. Üzerinde araştırma yapılan olgu ve olaylar kendi bağlamında ele alınarak, insanların onlara yükledikleri anlamlar açısından yorumlanır (Altunışık ve ark., 2010). Geleneksel olarak görüşme, gözlem, doküman inceleme ve odak grup çalışmasını içeren nitel araştırma yöntemleri araştırdıkları merkezi temaya göre farklılık gösterebilmektedir (Dedeoğlu, 2002).

Araştırma kapsamında incelenen konuyla ilgili olgu ve olaylar hakkında bilgi içeren yazılı belgelerin analiz edilmesiyle veri sağlanmasına doküman incelemesi denilmektedir. Araştırma yapılan alanla

ilgili pek çok bilgi görüşme ve gözlem yapmaya gerek kalmaksızın belge inceleme yoluyla elde edilebilir. Bu sayede araştırmacı zaman ve kaynak tasarrufu sağlamış olur. Hangi dokümanın önemli olduğu ve veri kaynağı olarak kullanılabileceğine araştırma konusuna bakarak karar vermek gerekir (Yıldırım ve Şimşek, 2008).

Araştırmada Yüksek Öğretim Kurumu Tez Merkezinin web sayfasından yapay zeka anahtar kelimeleri ile taramalar yapılmış olup, bu alanda yapılmış 1294 lisansüstü teze ulaşılmıştır. Elde edilen veriler tablolar yardımıyla özgün dil, yıl, üniversite, enstitü, anabilim dalı, konu ve yönetime göre sınıflandırılmıştır.

Tablo 2. Yapay Zeka ile ilgili Lisans Programları ve Bağlı Buldukları Üniversiteler

Üniversite Adı	Program Adı	Süre	Kontenjan
Ankara Üniversitesi (Devlet)	Yapay Zeka Ve Veri Mühendisliği	4	25
Hacettepe Üniversitesi (Ankara) (Devlet)	Yapay Zeka Mühendisliği (İngilizce)	4	40
İstanbul Teknik Üniversitesi (Devlet)	Yapay Zeka Ve Veri Mühendisliği (İngilizce)	4	40
Bahçeşehir Üniversitesi (İstanbul) (Vakıf)	Yapay Zeka Mühendisliği (İngilizce) (Ücretli)	4	27
	Yapay Zeka Mühendisliği (İngilizce) (Burslu)	4	8
	Yapay Zeka Mühendisliği (İngilizce) (%50 İndirimli)	4	21
Ostim Teknik Üniversitesi (Ankara) (Vakıf)	Yapay Zeka Mühendisliği (Burslu)	4	6
	Yapay Zeka Mühendisliği (%50 İndirimli)	4	34
Tobb Ekonomi Ve Teknoloji Üniversitesi (Ankara) (Vakıf)	Yapay Zeka Mühendisliği (İngilizce) (Ücretli)	4	10
	Yapay Zeka Mühendisliği (İngilizce) (Burslu)	4	10
	Yapay Zeka Mühendisliği (İngilizce) (%50 İndirimli)	4	10

Türkiye’de yapay zeka üzerine uzmanlaşmak isteyen öğrenciler için tezli ve tezsiz olarak toplamda 15 üniversitede yüksek lisans bölümü bulunmaktadır. Yapay zeka, veri bilimi, veri analitiği, büyük veri ve iş zekası gibi konulara ağırlık veren yüksek lisans bölümleri Tablo 3’te yer verilmiştir.

Tablo 3. Yapay Zeka ile ilgili Lisansüstü Programlar ve Bağlı Buldukları Üniversiteler

Üniversite Adı	Bölüm Adı	Tezli	Tezsiz
Abdullah Gül Üniversitesi	Veri Bilimi Yüksek Lisans	X	
Akdeniz Üniversitesi	Veri Analitiği Ve Yönetimi Yüksek Lisans		X
Bahçeşehir Üniversitesi	Büyük Veri Analitiği Ve Yönetimi / Yapay Zeka Yüksek Lisans	X	X
Çankaya Üniversitesi	Veri Analitiği Yüksek Lisans	X	X
Dokuz Eylül Üniversitesi	Veri Bilimi Yönetimi Ve Analizi Yüksek Lisans	X	X
Galatasaray Üniversitesi	Veri Bilimi Yüksek Lisans		X
İstanbul Teknik Üniversitesi	Büyük Veri Ve İş Analitiği Yüksek Lisans		X
İzmir Bakırçay Üniversitesi	İş Zekası Ve Veri Analitiği Yüksek Lisans		X
Koç Üniversitesi	Data Science Veri Bilimi Yüksek Lisans		X
Marmara Üniversitesi	Veri Mühendisliği Yüksek Lisans	X	
Özyeğin Üniversitesi	Veri Bilimi Yüksek Lisans / Yapay Zeka Yüksek Lisans	X	X
Sabancı Üniversitesi	Veri Analitiği Yüksek Lisans		X
Ted Üniversitesi	Uygulamalı Veri Bilimi Yüksek Lisans	X	X
Üsküdar Üniversitesi	Yapay Zeka Yüksek Lisans	X	X
Yeditepe Üniversitesi	Veri Bilimi Yüksek Lisans	X	X

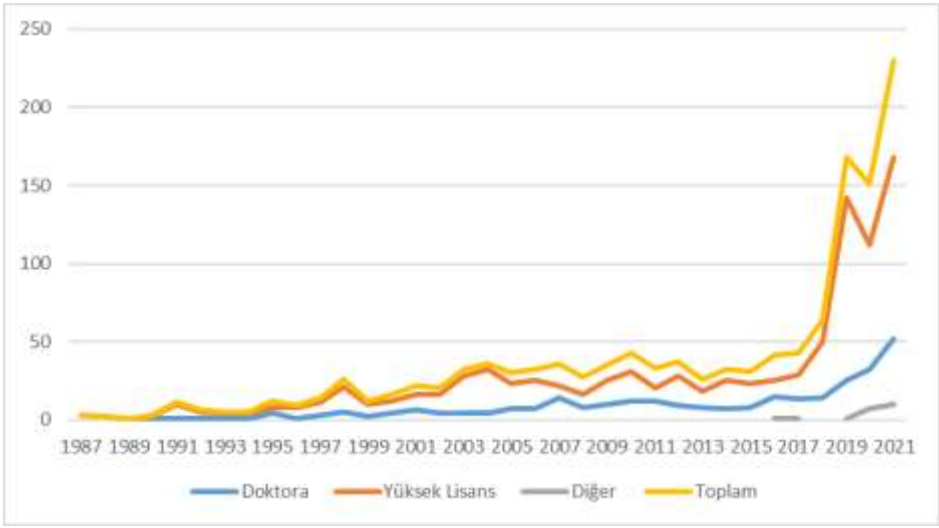
4. BULGULAR

Yüksek Öğretim Kurumu Ulusal Tez Merkezinden elde edilen verilere göre Türkiye’de yapay zeka konusunda toplam 1294 adet lisansüstü teze ulaşılmıştır. Araştırma kapsamında 1294 adet lisansüstü tez seçilmiştir.

Özgün dillere göre dağılım incelendiğinde yaklaşık olarak %70,79 Türkçe, %29,06 İngilizce olduğu görülmektedir. 2019, 2020 ve 2021 yıllarında 549 çalışma yapılmış olup bu çalışmalardan 262'si Türkçe olarak hazırlandığı görülmektedir. Ayrıca tüm yıllar içinde %42,43'ü 2019, 2020 ve 2021 yıllarında hem Türkçe ve İngilizce olacak şekilde hazırlandığı görülmektedir. Yapılan tezlerinin Gazi, İstanbul Teknik, Orta Doğu Teknik, Sakarya, Selçuk ve Yıldız Teknik Üniversitesi tarafından hazırlandığı tespit edilmiştir.

Tablo 4. Yapay Zeka Alanında Yapılan Lisansüstü Tezlerin Özgün Dillere Göre Dağılımı

Yıl	Doktora	Yüksek Lisans	Diğer	Toplam
1987		3		3
1988		2		2
1989	1	0		1
1990	1	2		3
1991	1	10		11
1992	1	5		6
1993	1	4		5
1994	1	4		5
1995	4	8		12
1996	1	8		9
1997	3	11		14
1998	5	21		26
1999	2	10		12
2000	4	12		16
2001	6	16		22
2002	4	16		20
2003	4	28		32
2004	4	32		36
2005	7	23		30
2006	7	25		32
2007	14	22		36
2008	8	16	3	27
2009	10	25		35
2010	12	31		43
2011	12	20	1	33
2012	9	28		37
2013	8	18		26
2014	7	25		32
2015	8	23		31
2016	15	25	1	41
2017	13	29	1	43
2018	14	50		64
2019	25	142	1	168
2020	32	112	7	151
2021	52	168	10	230
Toplam	296	974	24	1294



Şekil 1. Yapay Zeka Alanında Yapılan Lisansüstü Tezlerin Özgün Dillere Göre Dağılımı

Yapay zeka alanında yapılan lisansüstü tezlerin yıllara göre dağılımı Şekil 1’de görülmektedir. Şekil 1 incelendiğinde yapay zeka alanında yapılan lisansüstü tezlerde 2017 yılından sonra bir artış görülmektedir. 2017 yılına kadar yapılan çalışmaların belli seviyede artarken bu yıldan sonra büyük bir artış olduğu görülmektedir. 2017 yılında daha çok yüksek lisans çalışmalarında artış, 2020 yılından sonra da doktora çalışmaları artmaya başlamıştır.

Tablo 5. Yapay Zeka Alanında Yapılan Lisansüstü Tezlerin Üniversitelere Göre Dağılımı

Üniversite	2010	2011	2012	2013	2014	2015	2016	2017	2018	2019	2020	2021	Toplam	%
Ankara Üniversitesi		1					1	1	1	4	1	4	16	1,24
Bahçeşehir Üniversitesi	2				2				5	4	9	3	37	2,86
Boğaziçi Üniversitesi	1		1			1	1	1	2	5	2	1	23	1,78
Çukurova Üniversitesi			1		1		3		2	4	2		16	1,24
Dokuz Eylül Üniversitesi	2	2	1				1	1	1	5	4	9	27	2,09
Ege Üniversitesi	3	1					3	1	1	1	2	7	24	1,85
Erciyes Üniversitesi	3	4	1	2	1	2		1	1	1	3	10	43	3,32
Fırat Üniversitesi	2	1	2				1	1	1	3	1	5	34	2,63
Gazi Üniversitesi	7	2	1	1	3		1		1	4	2	4	57	4,40
Gaziantep Üniversitesi		1		1		1	1			1	2	2	14	1,08
Hacettepe Üniversitesi	1		1			1	1	2	1	2	3	2	18	1,39
İstanbul Aydın Üniversitesi			1	1	1	1	1	1	2	1	5	4	18	1,39
İstanbul Teknik Üniversitesi	3	2	4	3	4	5	1	8	11	30	13	26	175	13,52
İstanbul Üniversitesi	1	1			1	2	1	1	4	4	3	7	36	2,78
Karadeniz Teknik Üniversitesi		1	1		1	3	1	1		2	1	5	26	2,01
Marmara Üniversitesi	1	1	2	1	1	1		1	1	3	7	5	39	3,01

Üniversite	2010	2011	2012	2013	2014	2015	2016	2017	2018	2019	2020	2021	Toplam	%
Ondokuz Mayıs Üniversitesi	1	1	3	1	1	1		1		3	4	3	19	1,47
Orta Doğu Teknik Üniversitesi	2	1	2		4	3	4		3	3	2	2	66	5,10
Sakarya Üniversitesi	4	2		1	1	3	3	2	1	2	6	1	54	4,17
Selçuk Üniversitesi	3		3	4	1	1	1		2	8	2	2	52	4,02
Süleyman Demirel Üniversitesi		2	1		2	1		1	1		2	2	25	1,93
Yıldız Teknik Üniversitesi	1		2	2	2	1	3	4	1	6	6	6	48	3,71

Yapay zeka alanında yapılan lisansüstü tezlerin üniversitelere göre dağılımı Tablo 5’de verilmiştir. Tablo 5 incelendiğinde en çok İstanbul Teknik Üniversitesi, daha sonra sırasıyla Orta Doğu Teknik, Gazi, Sakarya ve Selçuk Üniversitelerinde çalışma konusu olduğu görülmektedir. Bu çalışmalar daha çok 2019, 2020 ve 2021 yıllarında olduğu tespit edilmiştir.

Tablo 6. Yapay Zeka Alanında Yapılan Lisansüstü Tezlerin Enstitüye Göre Dağılımı

Enstitü	Frekans	%
Bilişim	19	1,47
Biyo-Medikal Mühendislik	1	0,08
Biyoteknoloji	1	0,08
Dış ticaret	1	0,08
Dış hekimliği	2	0,15
Eğitim araştırma	1	0,08
Eğitim bilimleri	11	0,85
Ekonomi ve Sosyal Bilimler	1	0,08
Enerji	1	0,08
Enformatik	4	0,31
Fen bilimleri	899	69,47
Güzel Sanatlar	9	0,70
İşletme	1	0,08
Lisansüstü Eğitim	65	5,02
Mühendislik ve Fen Bilimleri	27	2,09
Nükleer Bilimler	2	0,15
Sağlık Bilimleri	17	1,31
Sosyal Bilimler	214	16,54
Tıp	16	1,24
Yurt dışı enstitü	2	0,15
Toplam	1294	100

Tablo 6 incelendiğinde ise yapay zeka alanında lisansüstü çalışmalarının yaklaşık %69,47 oranında Fen Bilimleri ve yaklaşık % 17 oranında ise Sosyal Bilimler Enstitülerinde çalışıldığı, bunun yanında %22,33 ile Bilgisayar Mühendisliği anabilim dalında ve %10,59 oranında ise Elektrik Elektronik Mühendisliği anabilim dalında çalışıldığı görülmektedir. Bunun yanında Endüstri, İnşaat ve Makine Mühendisliği anabilim dallarında da yapay zeka alanında lisansüstü çalışmaları yapıldığı görülmektedir.

Tablo 7. Yapay Zeka Alanında Yapılan Lisansüstü Tezlerin Anabilim Dallarına Göre Dağılımı

AnaBilim Dalı	2010	2011	2012	2013	2014	2015	2016	2017	2018	2019	2020	2021	Toplam	%
Bilgisayar Mühendisliği	15	8	8	5	10	12	6	12	15	36	30	43	289	22,33
Bilişim Sistemleri	1	0	1	0	1	2	0	0	1	3	1	3	16	1,24
Elektrik Ve Elektronik Mühendisliği	4	6	3	2	3	2	11	7	11	11	10	23	137	10,59
Elektronik Ve Haberleşme Mühendisliği	0	1	1	1	0	1	0	0	1	4	4	3	17	1,31
Elektronik-Bilgisayar Eğitimi	1	1	0	2	1	0	0	0	1	1	0	0	16	1,24
Endüstri Mühendisliği	3	0	4	3	1	2	0	2	3	8	7	6	80	6,18
İktisat	0	1	0	0	2	0	0	0	0	3	3	4	16	1,24
İnşaat Mühendisliği	2	5	3	1	1	1	2	2	4	8	0	6	69	5,33
İstatistik	1	0	2	1	1	0	1	1	0	2	1	2	14	1,08
İşletme	2	1	0	3	2	1	5	1	6	6	16	15	76	5,87
Makine Mühendisliği	1	2	1	1	0	0	1	2	1	3	4	2	48	3,71
Matematik	0	2	1	2	0	2	0	0	0	0	1	2	14	1,08
Mekatronik Mühendisliği	0	0	1	1	2	0	1	1	1	7	2	7	23	1,78
Mimarlık	2	1	0	1	0	0	2	1	2	2	4	6	43	3,32
TOPLAM	43	33	37	26	32	31	41	43	64	16 8	15 1	23 0	129 4	100,0 0

Tablo 8’de ise konularına göre lisansüstü tezleri incelendiğinde tezlerinin daha bilgisayar mühendisliği bilimleri-bilgisayar ve kontrol, elektrik ve elektronik mühendisliği, endüstri ve endüstri mühendisliği ile ilgili olduğu, bunun yanında işletme, inşaat mühendisliği, makine mühendisliği, mimarlık üzerine olduğu tespit edilmiştir.

Tablo 8. Yapay Zeka Alanında Yapılan Lisansüstü Tezlerin Konulara Göre Dağılımı

Konu	..	2010	2011	2012	2013	2014	2015	2016	2017	2018	2019	2020	2021	Toplam	%
Bilgisayar Mühendisliği Bilimleri-Bilgisayar ve Kontrol	..	19	10	11	9	14	13	9	18	22	52	39	60	390	30,14
Bilim ve Teknoloji	..	0	1	0	0	0	0	1	0	2	5	4	12	29	2,24
Eğitim ve Öğretim	..	1	0	1	0	1	0	1	1	0	3	2	2	19	1,47
Ekonomi	..	0	1	0	0	1	0	0	0	0	3	4	6	17	1,31
Elektrik ve Elektronik Mühendisliği	..	3	5	3	2	3	3	12	5	10	16	11	27	153	11,82
Endüstri ve Endüstri	..	3	0	4	3	1	2	1	3	3	9	8	6	83	6,41

Konu	2010	2011	2012	2013	2014	2015	2016	2017	2018	2019	2020	2021	Toplam	%
Mühendisliğ i														
Felsefe	0	0	0	0	0	2	0	0	0	2	5	1	13	1,00
İnşaat Mühendisliğ i	1	4	3	1	1	1	2	2	4	9	0	4	64	4,95
İstatistik	1	0	2	1	1	1	1	1	0	2	1	2	16	1,24
İşletme	2	1	0	2	2	0	4	1	4	5	15	16	73	5,64
Jeodezi ve Fotogrametri	0	1	0	0	0	0	0	0	1	1	3	3	16	1,24
Makine Mühendisliğ i	1	2	1	1	0	0	1	2	1	2	4	2	51	3,94
Matematik	0	2	1	2	0	2	0	0	0	0	1	2	15	1,16
Mekatronik Mühendisliğ i	0	0	1	1	2	0	0	0	1	5	1	6	17	1,31
Mimarlık	3	1	0	1	1	1	2	1	2	2	5	6	47	3,63
Mühendislik Bilimleri	1	1	0	0	0	2	0	1	1	1	7	5	25	1,93
TOPLAM	43	33	37	26	32	31	41	43	64	168	151	230	1294	100,00
%	3,32	2,55	2,86	2,01	2,47	2,40	3,17	3,32	4,95	12,98	11,67	17,77	100,00	

Tablo 9 incelendiğinde ise yapılan lisansüstü tezlerin yapay sinir ağları yaklaşık olarak %18,32 ile en çok tercih edilen yöntem olurken, nitel araştırma %10,05 ile tercih edilen bir yöntem olmuştur. Bunun yanında model önerisi, makine öğrenmesi, uzman sistem tasarımı ve derin öğrenme gibi yöntemler de yapay zeka alanında yapılan lisansüstü tezlerde yöntem olarak kullanıldığı tespit edilmiştir.

Tablo 9. Yapay Zeka Alanında Yapılan Lisansüstü Tezlerinin Çalışılan Yönteme Göre Dağılımı

Yöntem	2010	2011	2012	2013	2014	2015	2016	2017	2018	2019	2020	2021	Toplam	%
Algoritma Tasarımı	1	4	4	2	3	2	4	4	1	0	0	6	48	3,71
Anfis	2	2	0	1	1	3	2	1	1	0	0	0	24	1,85
Anket Yöntemi	0	0	0	0	0	0	1	1	1	8	7	11	31	2,40
Bulanık Mantık	5	1	5	4	1	1	2	0	5	5	1	5	69	5,33
Derin Öğrenme	0	0	0	0	0	0	0	4	3	18	19	31	75	5,80
Destek Vektör Makinesi	0	0	0	0	1	3	0	2	1	0	0	4	13	1,00

Yöntem	2010	2011	2012	2013	2014	2015	2016	2017	2018	2019	2020	2021	Toplam	%
Doğal Dil İşleme	0	0	0	0	1	2	0	1	0	3	0	5	20	1,55
Etmen Tabanlı Sistem	6	1	2	1	0	0	1	0	0	1	0	3	28	2,16
Genetik Algoritma	4	1	2	0	3	1	1	3	3	3	0	0	50	3,86
Görüntü İşleme	0	0	0	0	0	0	0	0	0	6	2	5	15	1,16
Makine Öğrenmesi	1	1	2	0	1	1	3	2	5	19	20	39	98	7,57
Model Önerisi	2	1	1	2	2	4	5	8	9	14	12	18	110	8,50
Nicel Araştırma	0	0	0	0	2	0	0	0	0	0	1	16	22	1,70
Nitel Araştırma	2	0	2	0	2	2	3	3	10	13	22	48	130	10,05
Robot Tasarımı	0	0	0	0	1	2	0	0	2	2	0	0	13	1,00
Sistem Tasarımı	0	0	2	0	1	1	0	0	0	1	7	1	16	1,24
Uzman Sistem	1	0	1	0	4	0	0	0	0	1	3	1	83	6,41
Veri Madenciliği	1	0	1	1	1	1	0	0	0	0	2	3	15	1,16
Yapay Sinir Ağları	10	14	10	7	5	1	11	7	12	30	16	22	237	18,32
Yapay sinir ağları ve Bulanık Mantık	2	4	1	1	0	1	2	0	1	3	0	1	27	2,09
TOPLAM	43	33	37	26	32	31	41	43	64	168	151	230	1294	100,00
%	3,32	2,55	2,86	2,01	2,47	2,40	3,17	3,32	4,95	12,98	11,67	17,77	100,00	

5. SONUÇ ve ÖNERİLER

Bu araştırmada Türkiye’deki üniversitelerde 1987-2021 yılları arasında yapay zeka alanında yapılan lisansüstü tezler içerik analizi yöntemiyle incelenerek, tezlerin mevcut durumları ortaya konulmaya çalışılmıştır. Elde edilen sonuçlara göre, Türkiye’de yapay zeka alanında yapılan lisansüstü tezlerin çoğunlukla özgün dilinin Türkçe olduğu, en fazla tezin 2019, 2020 ve 2021 yıllarında yazıldığı tespit edilmiştir. Ayrıca en fazla yapay zeka alanında lisansüstü tez yapan kurumun İstanbul Teknik Üniversitesi ve Orta Doğu Teknik Üniversitesinde olduğu, yapılan tezlerin fen bilimler enstitüsünde Bilgisayar Mühendisliği anabilim dalında çalışıldığı görülmüştür. Araştırmaların yapay sinir ağları, nitel araştırma, model önerisi, derin öğrenme ve makine öğrenmesi yöntemlerin kullanıldığı tespit edilmiştir. Tezlerde en sık araştırılan bilgisayar mühendisliği bilimleri-bilgisayar ve kontrol, elektrik ve elektronik mühendisliği, endüstri ve endüstri mühendisliği konularının olduğu görülmüştür.

Yapay zeka alanında yapılan mevcut tezlere genel bir bakış sağlama niteliğinde olan bu araştırmanın, geçmiş araştırmaları toplu bir şekilde ortaya koymasının yanı sıra gelecek araştırmalara da ışık tutarak yapay zeka konusunun geliştirilmesine katkı sağlaması beklenmektedir. Konuyla ilgili daha detaylı olarak lisansüstü tezler incelenerek karşılaştırmalar yapılabilir.

Araştırmanın Kısıtları ve Gelecek Araştırmacılara Öneriler

Bu araştırmada yalnız YÖK Tez Merkezi’nde paylaşıma açılmış tezlerin incelenmiş olması, araştırmanın en büyük kısıtıdır. Gelecekte bu konuya ilgi duyabilecek araştırmacıların YÖK Tez Merkezi’nde henüz paylaşılma açılmamış tezlere de ulaşarak daha kapsamlı bir değerlendirme yapmasının faydalı olacağı düşünülmektedir. Öte yandan bu araştırmanın en azından her on yılda bir tekrar edilmesinin hem Yapay zeka tezlerinde sıkça ve nadiren ele alınan konular hakkında hem de odaklanılan konuların trendi hakkında faydalı bilgiler sunabileceği böylece tez hazırlayan

öğrencilere ve akademik danışmanlara fikir verebileceği düşünülmektedir. Konuya ilgi duyabilecek araştırmacıların bir başka araştırmada da Türkiye'de yapay zeka ile ilgili yazılmış bilimsel makaleleri benzer bir yöntemle inceleyerek makalelerde en çok ve en az ele alınan konuları değerlendirmelerinin Türkiye'deki yapay zeka literatürünün başka bir boyutuna ışık tutabileceği tahmin edilmektedir.

KAYNAKÇA

- Adhikari, R. (2020), "Robot Lawyer Faces Legal Troubles of Its Own", Erişim Adresi: <https://www.technewsworld.com/story/86956.html>, Erişim Tarihi: 03.02.2021
- Alkan, G. (2014). Türkiye'de Muhasebe Alanında Yapılan Lisansüstü Tez Çalışmaları Üzerine Bir Araştırma (1984- 2012), Muhasebe ve Finansman Dergisi, 61, 41-52.
- Allahverdi, N. (2002). Uzman Sistemler: Bir Yapay Zeka Uygulaması. Atlas Yayın Dağıtım.
- Altunışık, R., Coşkun, R., Bayraktaroğlu, S., & Yıldırım, E. (2010). Sosyal Bilimlerde Araştırma Yöntemleri SPSS Uygulamalı (6. Baskı). Sakarya: Sakarya Yayıncılık.
- Altuntaş, C. & Türker, D. (2012). Sürdürülebilir Tedarik Zincirleri: Sürdürülebilirlik Raporlarının İçerik Analizi, Dokuz Eylül Üniversitesi Sosyal Bilimler Enstitüsü Dergisi, 14/3, 39-64
- Arı, S. G., Armutlu, C., Tosunoğlu N. G. & Toy, B. Y. (2009). Nicel Araştırmalarda Metodoloji Sorunları: Yüksek Lisans Tezleri Üzerine Bir Araştırma, Ankara Üniversitesi Siyasal Bilgiler Fakültesi Dergisi, 64/4, 16-37.
- Atalay, M., & Çelik, E. (2017). Büyük veri analizinde yapay zekâ ve makine öğrenmesi uygulamaları, Mehmet Akif Ersoy Üniversitesi Sosyal Bilimler Enstitüsü Dergisi, 9(22), 155-172.
- Bakır, N. O. (2013). Pazarlama Alanında Yapılan Doktora Tezlerinin Kategorik Olarak Değerlendirilmesi (1994 - 2012), Öneri, 10/40, 1-13
- Baş, M., Yangil, F. M. & Aygün, S. (2014). Entelektüel Sermaye Alanında Yapılan Lisansüstü Tez Çalışmalarına Yönelik Bir İçerik Analizi: 2002-2012 Dönemi, Uluslararası Yönetim İktisat ve İşletme Dergisi, 10/23, 207-226.
- Benligiray, S. (2009). Türkiye'de İnsan Kaynakları Yönetimi Alanında Yapılan Lisansüstü Tezler ve Bu Tezlerde İncelenen Temaların Analizi: 1983-2008 Dönemi, Eskişehir Osmangazi Üniversitesi İİBF Dergisi, 4/1, 167-197.
- Çelik, N. (2016). Yenilikçilik Konusunda Yapılan Doktora Tezlerinin İçerik Analizi Yöntemiyle Değerlendirilmesi, Uluslararası Ekonomi ve Yenilik Dergisi, 2/1, 29-42
- Dedeoğlu, A. Ö. (2002). Tüketici Davranışları Alanında Kalitatif Araştırmaların Önemi Ve Multidisipliner Yaklaşımlar, D.E.Ü.İ.İ.B.F. Dergisi, 17/2, 75-92.
- Demir, A. (2018). Ölümsüzlük ve yapay zekâ bağlamında trans-hümanizm. AJIT-e: Bilişim Teknolojileri Online Dergisi, 9(31), 95-104.
- Howard, J. (2019). Artificial intelligence: Implications for the future of work. American Journal of Industrial Medicine, 62(11): 917-926.
- Jarrahi, M. H. (2018). Artificial intelligence and the future of work: Human-AI symbiosis in organizational decision making. Business horizons, 61(4), 577-586.
- Kafalı, H. (2019). Yapay zekâ, toplum ve din'in geleceği. Ondokuz Mayıs Üniversitesi İlahiyat Fakültesi Dergisi, (46), 145-172.
- Kayabaşı, A. (2010). Elektronik (Online) Alışverişte Lojistik Faaliyetlere Yönelik Müşteri Şikayetlerinin Analizi Ve Bir Alan Araştırması, İşletme Araştırmaları Dergisi 2/2, 21-42.
- Kurt, D. & Bozoklu, Ü. (2019). Robot Ekonomisinin Yükselişi . Sosyal Bilimler Metinleri, 2019 (1) , 25-47
- Nabiyev, V. V. (2012). Yapay zeka: insan-bilgisayar etkileşimi. Seçkin Yayıncılık.
- Öztemel, E. (2012). Yapay sinir ağları. Papatya yayınları.
- Öztürk, K., & Şahin, M. E. (2018). Yapay sinir ağları ve yapay zekâ'ya genel bir bakış. Takvim-i Vekayi, 6(2), 25-36.

- Pomerol, J. C. (1997). Artificial intelligence and human decision making. *European Journal of Operational Research*, 99(1): 3-25.
- Sekreter, M. S., & Akyüz, G. (2003). Pazarlama arařtırmalarında kullanılan ölçeklere ilişkin bir yazın taraması (1995-2002). *Akdeniz İİBF Dergisi*, 3(6), 123-150.
- Selwyn, N. (2019). Should robots replace teachers? AI and the future of education. Indianapolis: John Wiley & Sons.
- Sucu, İ. & Ataman, E. (2020). Dijital Evrenin Yeni Dünyası Olarak Yapay Zeka Ve Her Filmi Üzerine Bir Çalıřma. *Yeni Medya Elektronik Dergisi*, 4 (1), 40-52.
- Şahin, H. (2021). İnsan Değeri ve Yapay Zekâ. Recep Yıldız ve Eyüp Sabri Kala (Ed.). *İnsan Sosyal Hizmette İnsan Değeri içinde*, (s. 189-207). Bursa: Ekin Yayınevi.
- Şahin, H., & Topal, B. (2016). Türkiye’de tedarik zinciri konusunda yapılan doktora tezlerinin genel profilinin içerik analizi yöntemiyle belirlenmesi. *International Journal of Social Science*, Autumn II, 50, 471-482.
- Şen, Y. F., & Yurtođlu, D. (2020). Teknoloji ve Güvenlik İliřkisi Bađlamında Yapay Zekânın İstihbarat Analizindeki Önemi. *Güvenlik Çalıřmaları Dergisi*, 22(1), 24-48.
- Tektař, M., Akbař, A. ve Topuz, V. (2002), Yapay zekâ tekniklerinin trafik kontrolünde kullanılması üzerine bir inceleme. *Uluslararası Trafik ve Yol Güvenliđi Kongresi ve Fuarı*, Ankara, Türkiye.
- Topakkaya, A., & Eyibař, Y. (2019). Yapay zekâ ve etik iliřkisi. *Felsefe Dünyası*, 70(1), 81-99.
- Topol, E. J. (2019). High-performance medicine: The convergence of human and artificial intelligence. *Nature Medicine*, 25(1), 44–56.
- Yalçın, M. N. (2011). İstanbul Üniversitesi’nde Jeoloji Konusunda Tamamlanmıř Doktora Tezleri ve Yer Bilimlerine Katkıları, *İstanbul Yerbilimleri Dergisi*, 24/1, 1-18
- Yıldırım, A., & Şimřek, H. (2008). *Sosyal Bilimlerde Nitel Arařtırma Yöntemleri* (6. Baskı). Ankara: Seçkin Yayıncılık.
- Zhu, H. (2020). Big data and artificial intelligence modeling for drug discovery. *Annual Review of Pharmacology and Toxicology*, 60, 573–589.

Determination of Ra-226 concentration at Suadiye beach in Istanbul

Osman GÜNAY*

Yıldız Technical University, Faculty of Electrical and Electronics Engineering, Department of Biomedical Engineering, İstanbul-TURKEY,

*ogunay@yildiz.edu.tr

ABSTRACT

Human beings are constantly exposed to ionizing natural radiation. Natural radiation is found in rocks, soils and sand particles. One of the natural radiations that people are exposed to is radium (Ra-226). Determining the natural radiation level is very important for human health. In this study, radium dose level was determined in Suadiye beach sand samples in Istanbul. The radium dose level in the sand samples on this beach varies between 24.57 and 31.26 Bq/kg, with an average of 27.68 Bq/kg. The calculated dose level was compared with the radium level in other beach sands around the world. Radium dose level at the beach was found to be lower than the world average.

KEYWORDS - Natural Radioactivity, İstanbul, Beach

1. INTRODUCTION

Radiation has always existed in nature. Generally, natural radiation is examined in two separate categories as cosmic and terrestrial radiation. There are basically three different radiations that make up the terrestrial radiation source. These are Ra-226, Th-232 and K-40. Terrestrial radiation level is very important for determining the radiation exposure of humans. For this reason, numerous studies have been conducted on both radiation protection and terrestrial radiation determination [1-15].

The main purpose of this study is to determine the Ra-226 radiation dose concentration level in Suadiye Beach in Istanbul.

2. MATERIALS AND METHODS

In this study, Ra-226 concentrations were determined in the sand samples of the Suadiye beach in Istanbul. For this, approximately 1000 grams of sand samples were taken from 4 different points at equal intervals from the beach. These sand samples were first dried in the furnace in the laboratory, then sieved and purified from macro and micro impurities. then placed in airtight containers and kept for 40 to 50 days. After this stage, the radiation dose was calculated by using the NaI (TI) gamma detector to determine the Ra-226 dose level of the sand sample.

Gamma radiation measurement experimental setup is shown in figure-1. The measurement level of gamma doses experimental set includes Spectrometer, Amplifier, MCA and Computer in general terms.

The calibration curve is shown in Figure 2. The calibration of the experimental setup was made using Co-60 and Cs-137 sources.

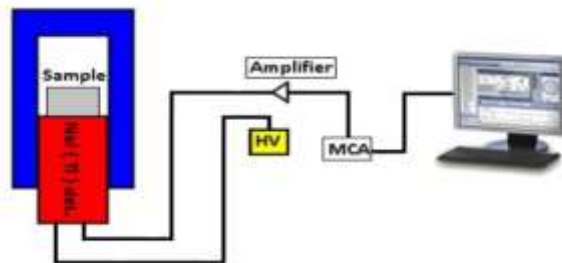


Figure 1. Experimental setup

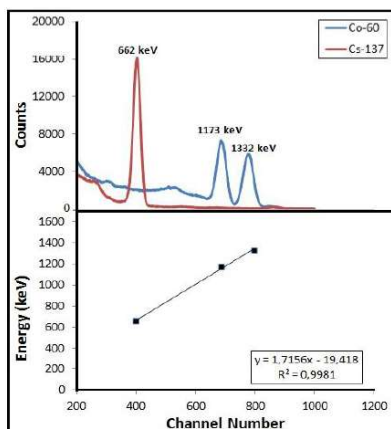


Figure 2. The gamma spectrum

3. RESULTS AND DICCUSSION

Ra-226 radiation concentrations are shown in table-1. The Ra-226 concentration was found to be the lowest at sample-4 with 24.57 ± 2.74 Bq/kg, and the highest at sample-3 with 31.26 ± 1.58 Bq/kg. The average Ra-226 concentration was calculated as 27.66 ± 1.19 Bq/kg. In fig-3, Ra-226 concentrations according to the sampling points are shown.

In a similar study conducted in Vietnam[16], the concentration of Ra-226 in the soil was 43 Bq/kg, in a study conducted in Yemen 48 Bq/kg [17], in a study in India 27 Bq/kg [18], in a study in Iraq 14 Bq/kg[19] and in a study in Pakistan 26 Bq/kg[20]. The results obtained as a result of this study are similar to the results of studies conducted in other countries.

Table 1. Ra-226 Concentration

Sampling Point	Ra-226 Concentration (Bqkg ⁻¹)
Sampling-1	28.80±0.96
Sampling-2	25.99±1.87
Sampling-3	31.26±1.58
Sampling-4	24.57±2.74
Mean	27.66±1.19

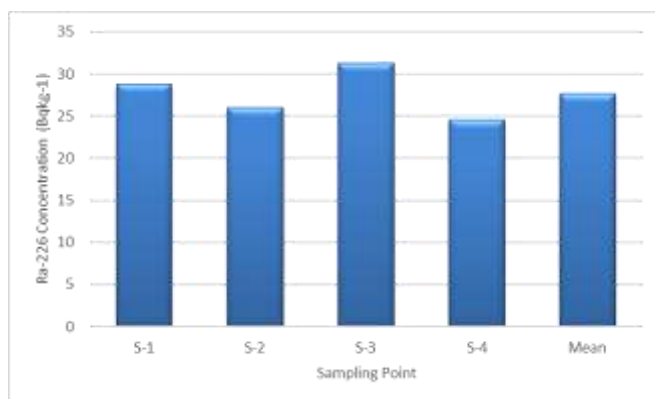


Figure 3. Ra-226 Concentration

4. CONCLUSION

In this study, Ra-226 radiation dose level in 4 different sand samples taken from Suadiye beach in Istanbul was determined using NaI(Tl) gamma detector. The Ra-226 radiation dose concentration found as a result of the study was compared with similar studies conducted in different countries. It has been observed that the average of the results obtained from this study and the average of the results obtained from the studies conducted in other countries are close to each other.

REFERENCES

- [1] Choudhary, M. D., Akkurt, I., Almisned, G., & Tekin, H. O. (2022). Radiation shielding properties for titanium dioxide added composites. *Emerging Materials Research*, 1-7.
- [2] Akkurt, I., & Tekin, H. O. (2020). Radiological parameters of bismuth oxide glasses using the Phy-X/PSD software. *Emerging Materials Research*, 9(3), 1020-1027.
- [3] Al-Obaidi, S., Akyıldırım, H., Gunoglu, K., & Akkurt, I. (2020). Neutron shielding calculation for barite-boron-water. *Acta Phys. Pol. A*, 137(4), 551.
- [4] Aközcan S, Kūlahcı F, Günay O, Özden S (2021) Radiological risk from activity concentrations of natural radionuclides: cumulative hazard index. *J Radioanal Nucl Chem* 327(1):105–122. <https://doi.org/10.1007/s10967-020-07474-1>
- [5] Akkurt I, Tekin HO (2020) Radiological parameters of bismuth oxide glasses using the Phy-X/PSD software. *Emerging Materials Research* 9(3):1020–1027. <https://doi.org/10.1680/jemmr.20.00209>
- [6] Akkurt I, Gunoglu K, Arda SS (2014) Detection efficiency of NaI (Tl) detector in 511–1332 keV energy range. *Science and Technology of Nuclear Installations*.
- [7] AKKURT I., N. Ayten UYANIK, Kadir GÜNOĞLU (2015).“ *International Journal of Computational and Experimental Science and Engineering* 1–1, 1–11 <https://doi.org/10.22399/ijcesen.194376>
- [8] Çelen YY, Evcin A (2020) Synthesis and characterizations of magnetite–borogypsum for radiation shielding. *Emerging Materials Research* 9(3):770–775. <https://doi.org/10.1680/jemmr.20.00098>
- [9] Çelen YY (2021) . *Emerging Materials Research* 10–2. (2021) <https://doi.org/10.1680/jemmr.21.00043>
- [10] Çelen YY, Evcin A, Akkurt I, Bezir NÇ, Günoğlu K, Kutu N (2019) Evaluation of boron waste and barite against radiation. *Int J Environ Sci Technol* 16(9):5267–5274. <https://doi.org/10.1007/s13762-019-02333-3>
- [11] El-Agawany F.I., Karem Abdel-Azeem Mahmoud, Hakan Akyıldırım, El-Sayed Yousef, Huseyin Ozan Tekin, Yasser Saad Rammah. (2021). *Emerging Materials Research* 10–2, 227 <https://doi.org/10.1680/jemmr.20.00297>
- [12] Günay O (2018) Assessment of lifetime cancer risk from natural radioactivity levels in Kadikoy and Uskudar District of Istanbul. *Arab J Geosci* 11(24):782
- [13] Günay O, Saç MM, İçedef M, Taşköprü C (2018) Natural radioactivity analysis of soil samples from Ganos fault (GF). *Int. J. Environ. Sci. Technol* 16:1735–1472
- [14] Günay O, Eke C (2019) Determination of terrestrial radiation level and radiological parameters of soil samples from Sariyer-Istanbul in Turkey. *Arab J Geosci* 12(20):1–10. <https://doi.org/10.1007/s12517-019-4830-1>
- [15] Kulali F (2020) Simulation studies on the radiological parameters of marble concrete. *Emerging Materials Research* 9(4):1341–1347. <https://doi.org/10.1680/jemmr.20.00307>
- [16] Huy NQ, Hien PD, Luyen TV et al (2012) Natural radioactivity and external dose assessment of surface soils in Vietnam. *Radiat Prot Dosim* 151(3):522–531
- [17] Harb S, El-Kamel AEH, Abbady AEB, Saleh II, El-Mageed AIA (2012) Specific activities of natural rocks and soils at quaternary intraplate volcanism north of Sana’a, Yemen. *J. Med. Phys. Assoc. Med. Phys. India* 37(1):54

- [18] Reddy U, Ningappa C, Sannappa J (2017) Natural radioactivity level in soils around Kolar Gold Fields, Kolar district, Karnataka. India J Radioanal Nucl Chem 314:2037–2045
- [19] Ahmed AI, Akrawy DT (2005) Measurement of natural radioactivity in soil samples from bekhma, Kurdistan region, Iraq. International Journal of Recent Research and Review, 8(4).
- [20] Akhtar N, Tufail M, Ashraf M, Mohsi IM (2005) Measurement of environmental radioactivity for the estimation of radiation exposure from saline soil of Lahore. Pakistan Radiat Meas 39:11–14

Determination of ^{226}Ra radioactivity level in Goztepe Beach

Osman GÜNAY*

Yıldız Technical University, Faculty of Electrical and Electronics Engineering, Department of Biomedical Engineering, İstanbul-Turkey,

*ogunay@yildiz.edu.tr

ABSTRACT

Terrestrial natural radiation consists of radium, thorium and potassium. In this study, the radium (Ra-226) radioactivity level in Göztepe Beach, one of the important beaches of İstanbul, was determined. In the study, sand samples were taken from four different points of Göztepe beach and the dose level of radium was determined by gamma spectroscopy system. The lowest radium dose was 27.63 ± 0.76 , while the highest radium dose was 49.19 ± 2.21 . The average dose of radium is 35.96 ± 1.57 .

KEYWORDS - Natural Radioactivity, İstanbul, Beach

1. INTRODUCTION

Terrestrial natural radiation consists of radium, thorium and potassium. There are different ratios of these three radioactive substances in the soil depending on the structure of the soil. These substances, which constitute natural radiation, are not only found in the soil, but also in the structure of the sand. It is very important to determine the radioactivity level in the sand since the beaches are used a lot especially in the summer season. Researchers have done many studies on radiation, natural radiation in soil and natural radiation in sand[1-15].

In this study, the radium (Ra-226) radioactivity level in Göztepe Beach, one of the important beaches of İstanbul, was determined.

2. MATERIALS AND METHODS

In this study, firstly, 4 points to be sampled from Göztepe beach were determined. Approximately 750 grams of sand samples were taken from these 4 points. After the sand samples were dried in the laboratory, they were sieved for purification. The prepared sand samples were placed in containers and kept for about 1 month. After one month, the radium radioactivity concentration was determined with a NaI(Tl) detector and the average was calculated.

The experimental setup with gamma spectrometry is shown in figure-1 and the calibration curve is shown in figure-2.

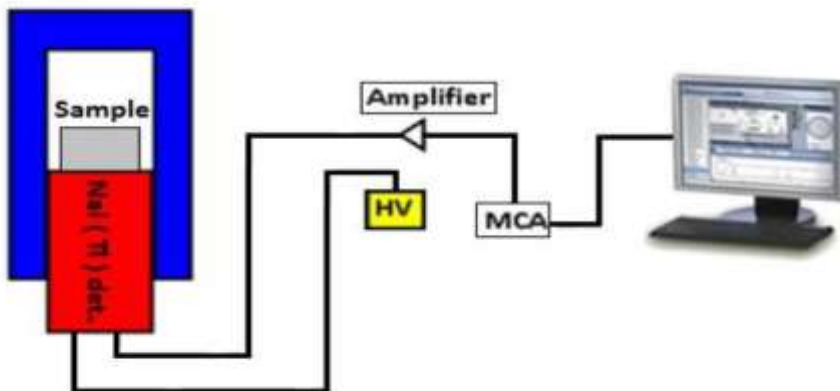


Figure 2. Experimental setup

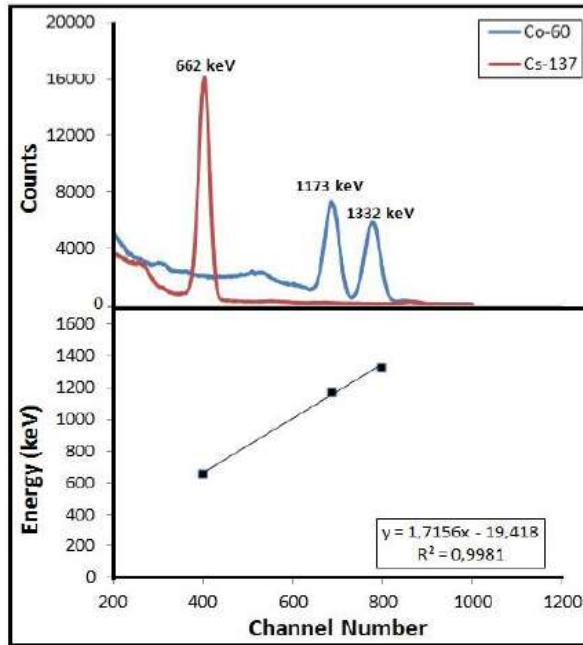


Figure 2. The gamma spectrum

3. RESULTS AND DICCUSSION

Ra-226 radioactivity dose levels at Göztepe beach are shown in table-1. Ra-226 radioactivity dose level at sampling point 1 was 27.63 ± 0.76 bq/kg, at sampling point 2 was 49.19 ± 2.21 Bq/kg, at sampling point 3 was 35.97 ± 0.89 Bq/kg, and at sampling point 4 was 31.07 ± 0.93 Bq/kg . The mean Ra-226 dose level was calculated as 35.96 ± 1.57 Bq/kg (fig-3).

Table 1. Ra-226 Concentration

Sampling Point Ra-226 Concentration	Ra-226 Concentration (Bqkg ⁻¹)
Goztepe-1	27.63 ± 0.76
Goztepe -2	49.19 ± 2.21
Goztepe -3	35.97 ± 0.89
Goztepe -4	31.07 ± 0.93
Mean	35.96 ± 1.57

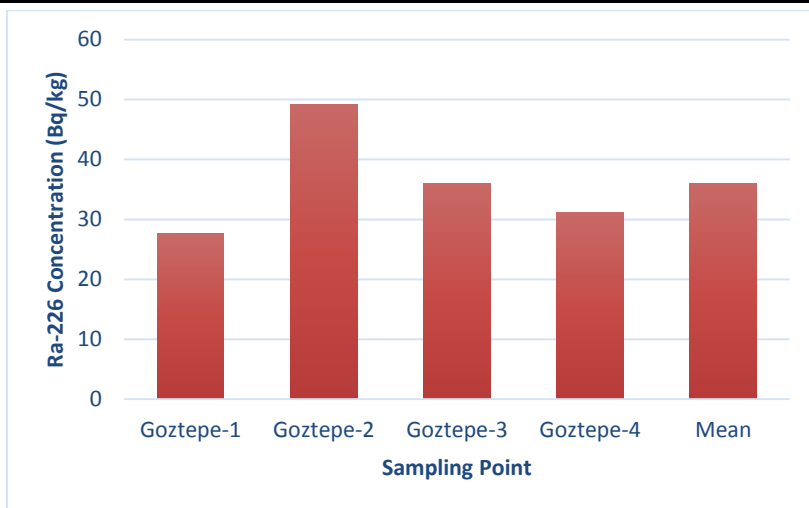


Figure 3. Ra-226 Concentration

4. CONCLUSION

In this study, Ra-226 radiation dose level in 4 different sand samples taken from Goztepe beach in Istanbul was determined using NaI(Tl) gamma detector. The mean Ra-226 dose level was calculated as 35.96 ± 1.57 Bq/kg.

REFERENCES

- [1].Choudhary, M. D., Akkurt, I., Almisned, G., & Tekin, H. O. (2022). Radiation shielding properties for titanium dioxide added composites. *Emerging Materials Research*, 1-7.
- [2].Akkurt, I., & Tekin, H. O. (2020). Radiological parameters of bismuth oxide glasses using the Phy-X/PSD software. *Emerging Materials Research*, 9(3), 1020-1027.
- [3].Al-Obaidi, S., Akyıldırım, H., Gunoglu, K., & Akkurt, I. (2020). Neutron shielding calculation for barite-boron-water. *Acta Phys. Pol. A*, 137(4), 551.
- [4].Aközcan S, Kùlahcı F, Günay O, Özden S (2021) Radiological risk from activity concentrations of natural radionuclides: cumulative hazard index. *J Radioanal Nucl Chem* 327(1):105–122. <https://doi.org/10.1007/s10967-020-07474-1>
- [5].Akkurt I, Tekin HO (2020) Radiological parameters of bismuth oxide glasses using the Phy-X/PSD software. *Emerging Materials Research* 9(3):1020–1027. <https://doi.org/10.1680/jemmr.20.00209>
- [6].Akkurt I, Gunoglu K, Arda SS (2014) Detection efficiency of NaI (Tl) detector in 511–1332 keV energy range. *Science and Technology of Nuclear Installations*.
- [7].AKKURT I., N. Ayten UYANIK, Kadir GÜNOĞLU (2015).“ *International Journal of Computational and Experimental Science and Engineering* 1–1, 1–11 <https://doi.org/10.22399/ijcesen.194376>
- [8].Çelen YY, Evcin A (2020) Synthesis and characterizations of magnetite–borogypsum for radiation shielding. *Emerging Materials Research* 9(3):770–775. <https://doi.org/10.1680/jemmr.20.00098>
- [9].Çelen YY (2021) . *Emerging Materials Research* 10–2. (2021) <https://doi.org/10.1680/jemmr.21.00043>
- [10]. Çelen YY, Evcin A, Akkurt I, Bezir NÇ, Günoğlu K, Kutu N (2019) Evaluation of boron waste and barite against radiation. *Int J Environ Sci Technol* 16(9):5267–5274. <https://doi.org/10.1007/s13762-019-02333-3>

-
- [11]. El-Agawany F.I., Karem Abdel-Azeem Mahmoud, Hakan Akyildirim, El-Sayed Yousef, Huseyin Ozan Tekin, Yasser Saad Rammah. (2021). *Emerging Materials Research* 10–2, 227 <https://doi.org/10.1680/jemmr.20.00297>
- [12]. Günay O (2018) Assessment of lifetime cancer risk from natural radioactivity levels in Kadikoy and Uskudar District of Istanbul. *Arab J Geosci* 11(24):782
- [13]. Günay O, Saç MM, İçedef M, Taşköprü C (2018) Natural radioactivity analysis of soil samples from Ganos fault (GF). *Int. J. Environ. Sci. Technol* 16:1735–1472
- [14]. Günay O, Eke C (2019) Determination of terrestrial radiation level and radiological parameters of soil samples from Sariyer-Istanbul in Turkey. *Arab J Geosci* 12(20):1–10. <https://doi.org/10.1007/s12517-019-4830-1>
- [15]. Kulali F (2020) Simulation studies on the radiological parameters of marble concrete. *Emerging Materials Research* 9(4):1341–1347. <https://doi.org/10.1680/jemmr.20.00307>

Detection of Anomalies via Robust Artificial Neural Networks and Gaussian Mixture Models

Mehmet Ali KAYGUSUZ¹ and Vilda PURUTÇUOĞLU^{2*}

¹ Anadolu University, Department of Economics, Eskişehir, TURKEY

² Middle East Technical University, Department of Statistics, Ankara, TURKEY

*vpurutcu@metu.edu.tr

ABSTRACT

Robust regression is an alternative approach to the classical regression when data are contaminated with outliers, and it can be used for the purpose of detection of influential observations. Recently, a robust artificial neural network (RNN) has been proposed. This new form of neural network applies the Huber loss function in the classification problem. We consider that this network model can be effective to detect anomalies in the data as an alternative of Gaussian mixture model (GMM). Because from our previous analyses, we have seen that GMM is successful for the classification of the protein-protein interaction data, specifically, when the data have outlier observations. Hence, in the study, we perform both RNN and GMM for the classification in order to detect the outliers in protein-protein interaction datasets while comparing the results with an autoencoder neural network structure in RNN. Accordingly, we evaluate them under different dimensional biological systems' data with distinct topologies and numbers of observations.

KEYWORDS: *Robust statistics, Classification, Artificial neural networks, Biological data*

1. INTRODUCTION

Traditionally, the artificial neural networks or shortly neural networks have been shown strong power to approximate high-dimensional functions and to truly classify/label the associated data. In the process of labelling, besides the neural networks, different machine learning approaches have been used too. But, this task can be computationally challenging for complex high dimensional biological data. Because this data type has very complex structure and the numbers of parameters p are much more higher than the numbers of observations n . The robust neural network (RNN) is a special type of artificial neural networks which use Huber loss function in clustering the data and in detecting abnormal observations.

Previously, RNN has been proposed to make labelling for high dimensional data by Smith et al. (1993). Then, it has been studied by Beliaikov et al. (2011) to detect outlier values on high dimensional regression. More recently, the empirical risk minimization function (Mehri et al., 2018) for RNN has been provided by Weng et al. (2021).

On the other side, the Gaussian mixture model (GMMs) is another classification method for high dimensional data. This method basically considers that clusters in the data are composed of a mixture of Gaussian distribution with predefined weights in such a way that we can find cluster successfully by capturing the underlying elements of mixtures (Peel and McLachan, 2000). In recent analyses, it has been shown that GMM can be a promising method to identify the outliers in biological systems' datasets. In the application of moderate protein-protein interaction systems (Kaygusuz et al., 2022), it has been seen that GMM performs better than artificial neural network when the data have outliers. Hence, in this study, we compare both the performance of RNN and GMM to investigate the gain in accuracy via the robustified version of artificial neural network over GMM under various biological networks.

Accordingly, we organize our study as follows: We present the robust artificial and autoencoder neural networks and empirical risk minimization function for RNN in the second section. Here, we briefly describe GMM too. In the third section, we represent different biological networks which are simulated under various topologies, numbers of observations and genes when the systems have outliers. Finally, fourth section is left for conclusion and future studies.

2. THEORY AND METHODS

2.1. Robust artificial neural networks

Artificial neural network is based on a collection of connected units or nodes, called artificial neurons, which loosely model the neurons in a biological brain. Each connection, like the synapses in a biological brain, can transfer a signal to other neurons. An artificial neuron receives signals and processes and sends them to neurons which are connected to those. The "signal" at a connection is a real number, and the output of each neuron is computed by some non-linear function of the sum of its inputs. These connections are called edges. Neurons and edges have weights which are adjusted in the learning procedure of neural networks. The robust neural network (RNN) is a specific neural network which uses the Huber loss activation function in the calculation of weights. The Huber statistics is one of the well-known robust statistics to overcome the limitation of traditional parametric and non-parametric methods in statistical analyses (Huber and Rochetti, 1998).

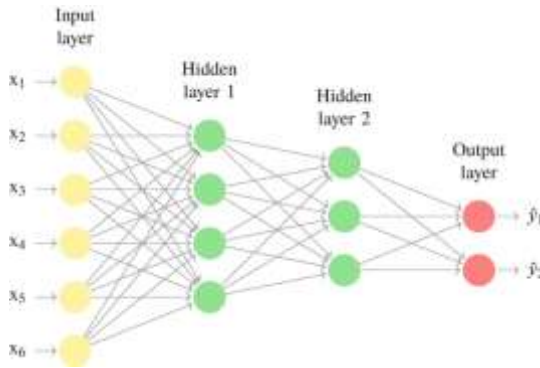


Figure 1. An example of architecture of artificial neural network with multiple hidden layers (Dixon et al., 2020).

In the mathematical modeling of RNN, as seen in Figure 1 and Equation (1), $x(t)$ indicates the input vector, $y(t)$ denotes the output vector which is the output from the j th hidden layer and $h(x)$ vector shows a hyperbolic tangent (\tanh) activation function. Here, in place of $h(x)$, the classical neural network uses typically sigmoid or rectified linear activation (ReLU) activation functions.

$$h_j(x) = \tanh \left(\sum_{i=1}^n w_{ji}^{(l)} x_i(t) + w_{j0}^{(l)} \right) \quad (1)$$

in which $w_{ij}^{(l)}$ is the input of the hidden layers weights vector and $w_{j0}^{(l)}$ is a hidden layer bias vector. Thus, the estimated output layer transfer function can be shown as the following form.

$$f_i(x) = f \left(\sum_{j=1}^n w_{ij}^{(H)} h_j(x) + w_{i0}^{(H)} \right), \quad (2)$$

where $w_{jl}^{(l)}$ is the input to hidden layer, $w_{ij}^{(H)}$ presents the hidden to output layers' weights and finally, $w_{i0}^{(H)}$ refers to the output layer bias vector. All weights are obtained via a weight vector $w = (w_{jl}^{(l)}, w_{ij}^{(H)})$.

2.2. Auto-encoder neural network

The autoencoder is a special type of architecture for neural networks whose outputs are same as their inputs. Thus, this network type can be used to learn a compressed raw data. It compresses the input and the decoder attempts to recreate this input from the compressed version provided by the encoder as simply shown in Figure 2. Hereby, this structure is used to reduce the noise in data. Through the process of compressing input data, encoding it, and then reconstructing it as an output, autoencoders allow to reduce dimensionality. Moreover, autoencoders can be trained as a classification machine learning problem, in particular, when we have very limited input data.

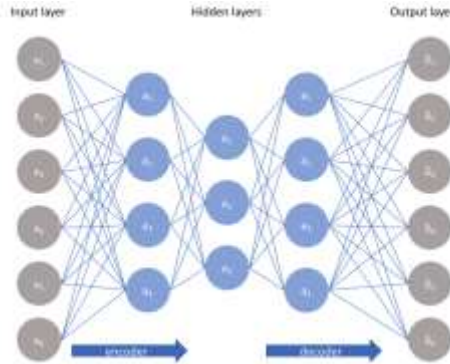


Figure 2. An example of the architecture of auto-encoder neural network with three hidden layers (<https://www.jeremyjordan.me/autoencoders/>).

Furthermore, regularized autoencoders are very useful for learning representations of the classification task and they apply different activation functions such as sigmoid and ReLu while computing the weights between nodes like RNN. Moreover, autoencoders are also generative models which can randomly create new data similar to input data. Traditionally, autoencoder neural networks minimize a function $L(x, g(f(x)))$, where is L is a loss function penalizing $g(f(x))$ to be dissimilar to x with L_1 -norm of their difference. Therefore, we can define the regularized auto-encoder neural networks as follows.

$$L(x, g(f(x))) + \lambda \sum_{i=1} |a_i^{(h)}| \tag{3}$$

in which λ is a L_1 -regularization parameter and a denotes an activation function for the h th layer. Thus, we can define the activation function for the auto-encoder neural networks as below.

$$a^{(h)} = f(z^{(h)}) \text{ and } z^{(h)} = w^{(h-1)}x + b^{(h-1)} , \tag{4}$$

where $w^{(h-1)}$ is a weighted matrix for the $(h - 1)$ th layer of autoencoder neural networks and $b^{(h-1)}$ is a bias vector of the $(h - 1)$ th layer of the auto-encoder neural networks. In our assessment, we construct RNN via auto-encoder structures so that their outcomes can be comparable with the Gaussian mixture model’s outcomes.

2.3. Empirical risk minimization

The empirical risk function is a function to compare the performance of robust classification neural networks and gives theoretical bounds for performances of the multilayer neural networks. Here, the risk function of a classifier is a measure of the average performance that can be defined as follows.

$$r_D(f) = E_{(X,Y) p_D} [L(X, Y, f_\theta)], \tag{5}$$

where (X, Y) is the input dataset, L describes the loss function, $E(\cdot)$ represents the expectation and p_D indicates the true data generating distribution. Hence, $L(X, Y, f_\theta)$ can be written as $\phi(f_\theta, Y)$ for the natural risk via

$$r_D^{auto}(f_\theta) = E_{(X,Y) p_D} [\max_{f \in F(M,C)} \phi(f_\theta, Y)] \tag{6}$$

while the empirical risk can be computed with Monte Carlo mean of $(X_1, Y_1), \dots, (X_n, Y_n)$ pairs for n number of observations.

2.4. Gaussian mixture model

Gaussian mixture model (GMM) is a special type of machine learning algorithm for classification of mixed data in many different areas, including, genetics, finance and signal progressing analyses. Basically, it uses to classify data into different categories based on the probability distribution. GMM applies either hard clustering or soft clustering on query data. In hard clustering, GMM assigns query data points to the multivariate normal components that maximize the component posterior probability given the data. Hence, in GMM, it is assumed a (multivariate) Gaussian distribution for each component k whose parameter θ , i.e., $f_k(x; \theta_k) \sim N(\mu_k, \Sigma_k)$, while clusters are centered at

the mean vector μ_k , and with scale parameter determined by the covariance matrix Σ_k . The parameter estimation of covariance matrix is done by means of an eigen-values of the form $\sum_k \lambda_k D_k A_k D_k^T$ where λ_k is a scalar value controlling the volume of the ellipsoid, A_k shows a diagonal matrix specifying the shape of the density contours with the determinant $\det(A_k) = 1$, and D_k presents an orthogonal matrix which determines the orientation of the corresponding ellipsoid. Here, $(\cdot)^T$ indicates the transpose of the given matrix.

Hereby, GMM is an unsupervised learning algorithm whose cluster parameters are generally estimated by the expectation-maximization (EM) algorithm (Dempster et al., 1977; McLachlan and Peel, 2000) via mixtures of Gaussian distributions with iterative approach. In calculation, we accept that $x = \{x_1, x_2, \dots, x_i, \dots, x_n\}$ is a sample of n independent identically distributed observations. The distribution of every observation is specified by a probability density function through a finite mixture model with G number of mixture components, which takes the following form

$$f(x_i, \Psi) = \sum_{k=1}^G \pi_k f_k(x_i; \theta_k), \tag{7}$$

where $\Psi = \{\pi_1, \dots, \pi_{G-1}, \theta_1, \dots, \theta_G\}$ are the parameters of the mixture model, $f_k(x_i; \theta_k)$ is the k th component density for observations x_i with parameter vector θ_k , and $(\pi_1, \dots, \pi_{G-1})$ refer to the mixing weights or probabilities such that $\pi_k > 0$, and $\sum_{k=1}^G \pi_k = 1$. In the computation, it is accepted that G is fixed and mixture model parameters are unknown in general. Therefore, we need to estimate it with the likelihood equation $(\Psi; x_1, \dots, x_n) = \sum_{i=1}^n \log f_k(x_i; \Psi)$. Direct estimation of the log-likelihood function is very complex and as stated before, the maximum likelihood estimator is obtained via the EM algorithm.

3. ANALYSES

3.1. Data description

In the application of RNN and GMM in protein-protein interaction (PPI) networks, we use different simulated datasets. We generate data by the following scenarios:

We generate system with 10 and 20 proteins from multivariate normal distribution where each protein has 50 observations. In the first 10-protein system, we simulate multivariate normally distributed data whose 8 proteins have random topology and 2 proteins form scale-free topology (Dataset 1). In the second dataset (Dataset 2), we simulate 20 proteins which have 4 proteins from scale-free structure and accordingly, the remainings are from random network structure. Then, we label them via 0 and 1 to present outlier and non-outlier proteins. By this way we have 2 systems having outliers under mixture of normal distributions while outliers' ratios are not greater than % 25 of the data.

We simulate mixture data similar to the above scenarios, but, with the following composition: 8 proteins are taken from scale-free networks and 2 proteins are generated from random network data (Dataset 3). Similarly, in the fourth dataset (Dataset 4), we get 20 proteins where 16 of them are from scale-free network and 4 proteins are simulated from random network structures. We also label them as 0 and 1 to denote outlier and non-outlier proteins in our assessment of clustering performances of RNN and GMM.

3.2. Results

In this part, we present the scatter plots of RNN and GMM to detect outliers when we have different numbers of proteins ($p=10$ and 20) under 50 numbers of observations ($n=50$) and 4 different scenarios. In the plots, the outliers are shown by red colours in RNN which are generated under auto-encoder structures and by circle signs in GMM. Figures 3-6 present these plots for all datasets, respectively. In these plots, the independent variables are plotted on the x-axis while the dependent variable is plotted on the y-axis. Here, if y-values are greater than 2, we can say that the associated observations are outliers.

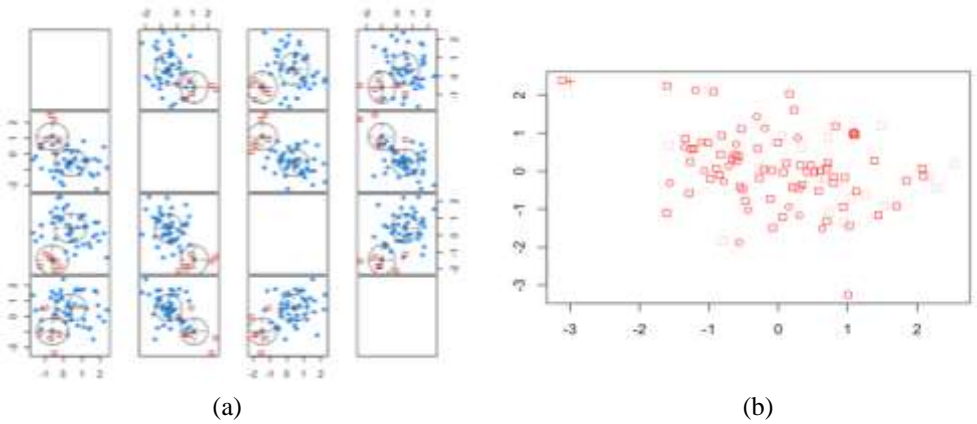


Figure 3. Scatter plots of robust neural network (a) and Gaussian mixture model (b) to detect anomalies under Dataset 1.

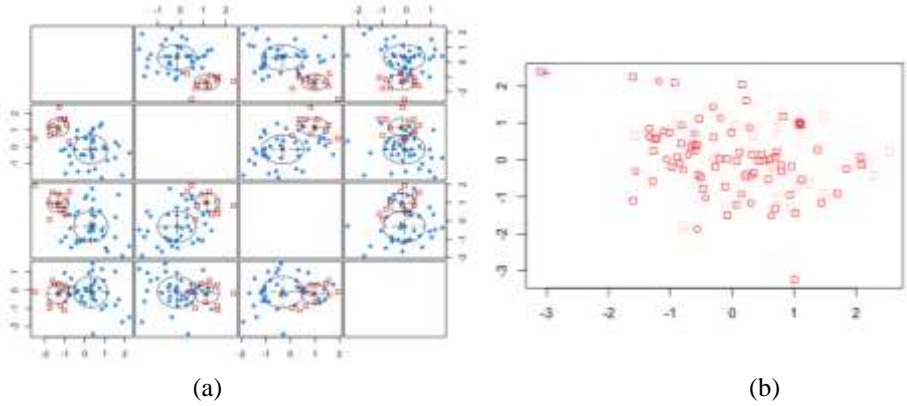


Figure 4. Scatter plots of robust neural network (a) and Gaussian mixture model (b) to detect anomalies under Dataset 2.

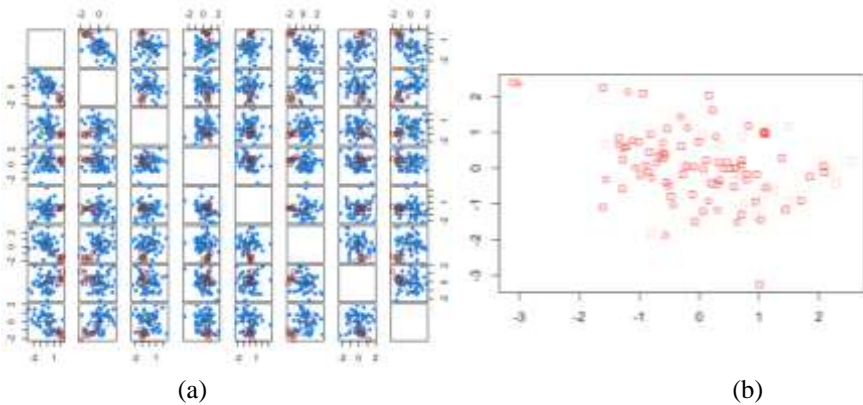


Figure 5. Scatter plots of robust neural network (a) and Gaussian mixture model (b) to detect anomalies under Dataset 3.

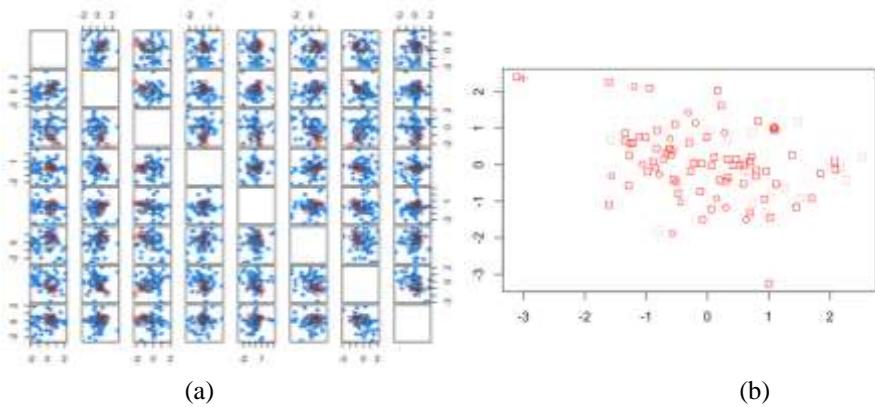


Figure 6. Scatter plots of robust neural network (a) and Gaussian mixture model (b) to detect anomalies under Dataset 4.

On the other hand, we summarize our analyses in Table 1. In this calculation we compare their accurate labels over the given p . From the results it is seen that in majority of the scenarios GMM outperforms than RNN and correctly identifies the true classes.

Table 1. Number of correctly identified outlier classes in 4 datasets via RNN and GMM approaches.

Networks	Dataset	RNN	GMM
$n=50, p=10$	Dataset 1	7	6
	Dataset 2	5	12
$n=50, p=20$	Dataset 3	4	5
	Dataset 4	4	4

4. CONCLUSION

In this work, we have studied robust neural networks and Gaussian mixture models for protein-protein interaction data to detect outlier proteins. In the robust neural network, the architecture has been constructed via the auto-encoder structure. Then, both approaches have been applied to 4 simulated datasets whose dimensions and topologies are different. From the assessment, we have seen that the Gaussian mixture model has had better accuracy than the robust neural network in most of the generated scenarios. Therefore, we consider that the first method is more promising than the latter ones for the detection of outlier proteins.

As the future studies, we think to generate a comprehensive simulation studies to analyze both approaches with more details. In this analysis, we will take into account the effects of dimensions, and changes in observations per protein. Finally, we consider that in place of Huber statistics, other robust statistics can be used as the activation function of the robust neural networks to improve the accuracy.

REFERENCES

[1] G. Beliakov, A. Kelarev, J. Yearwood, Robust artificial neural networks and outlier detection. Technical Report (2011). *arXiv preprint arXiv:1110.0169*

-
- [2] A. P. Dempster, M. L. Nan, B. R. Donald, Maximum likelihood from incomplete data via the EM algorithm. *Journal of the Royal Statistical Society: Series B*, 39, 1 (1977): 1-22.
- [3] M. F. Dixon, I. Halperin, P. Bilokon, *Maching Learning in Finance: From Theory to Practice*, Springer, 2020.
- [4] K. Eckle, J. Schmidt-Hieber, A comparison of deep networks with ReLU activation function and linear spline-type methods. *Neural Networks*, 110 (2019), 232-242.
- [5] J. Feng, H., Xu, S. Mannor, S. Yan, Robust logistic regression and classification. *Advances in Neural Information Processing Systems*, 27(2014).
- [6] P. J. Huber, E. Ronchetti, *Robust Statistics*, John Wiley and Sons, New York, 1981.
- [7] P. J. Huber, Robust estimation of a location parameter. In *Breakthroughs in statistics* (pp. 492-518). Springer, New York, 1992.
- [8] P. J. Huber, Robust statistics. In *International encyclopedia of statistical science* (pp. 1248-1251), Springer, Berlin, 2011.
- [9] M. A. Kaygusuz, M. Göğebakan, S. Akoğul, V. Purutçuoğlu, Bootstrap in Gaussian Mixture models and Performance assesement. *The 6th International Conference in Mathematics Proceeding*, 2022.
- [10] M. Kohler, A. Krzyzak, S. Langer, Estimation of a function of low local dimensionality by deep neural networks (2019), *arXiv preprint arXiv:1908.11140*.
- [11] G. J. McLachlan, T. Krishnan, *The EM algorithm and extensions*. John Wiley and Sons, 2007.
- [12] M. Mohri, A. Rostamizadeh, A. Talwalkar, *Foundations of machine learning*. MIT Press, 2018.
- [13] D. Peel, G. MacLahlan, *Finite mixture models*, John Wiley and Sons, 2000.
- [14] D. J. Smith, T. C. Bailey, A. G. Munford, Robust classification of high-dimensional data using artificial neural networks. *Statistics and Computing*, 3, 2 (1992), 71-81.
- [15] B. Wang, S. Webb, T. Rainforth, Statistically robust neural network classification. In *Uncertainty in Artificial Intelligence* (pp. 1735-1745). PMLR, 2021.

Conditional Randomization Test for Causal Additive Models in Biological Networks

Mehmet Ali KAYGUSUZ¹ and Vilda PURUTÇUOĞLU^{2*}

¹ *Anadolu University, Department of Economics, Eskişehir, TURKEY*

² *Middle East Technical University, Department of Statistics, Ankara, TURKEY*

**vpurutcu@metu.edu.tr*

ABSTRACT

Causal models are the popular probabilistic tools to analyze and visualize conditionally independent relationships between random variables. The random forest and classification and regression trees are some of the popular models under this branch. In this work, we consider the causal additive models (CAMs) which are the structural equations having additive forms between variables and error terms. Besides their flexibilities in the interpretation due to the additivity, the parameters of these models are identifiable from the distribution. But, from previous studies in the construction of the biological networks, it has been shown that when the number of parameters is considerably bigger than the number of observations, their accuracies can decrease. In order to solve this problem, we have performed the conditional randomization test to choose the core proteins in the system. From the results in bench-mark systems, we have observed that the test is successful in decreasing the dimension of the networks and thereby, improves the accuracy of the random forest model. Hence, in this study, we aim to extent this analysis by specifically performing boosting algorithm in the conditional randomized test and apply a knockoff filter criterion in the construction of the optimal model. By this way, we consider to decrease the computational time without losing from accuracy. We think that the proposal idea can be also adapted to other complex regression problems where the high dimension and correlations are the major challenges in modeling the data.

KEYWORDS – *Multiple testing, causal models, generalized additive models.*

1. INTRODUCTION

The causal additive models (CAMs) are one of the useful model groups which can describe the conditional relationships between random variables (Pearl, 2009). The random forest, classification and regression trees method are some of the well-known causal additive models. Hence, these models are special type of generalized additive models too (GAMs) which can capture non-linearity in independent variables (Hastie and Tibshirani, 1993; Wood, 2017; Meier et al., 2009).

Conditional randomization tests (CRTs) are very flexible to define relationship between variables since they don't have any distributional assumption about the model. Nonetheless, when the number of parameter (p) is more than the number of observation (n), their computations can be challenging. In this study, mainly, we combine both CAMs and CRTs to improve the performance of causal model by decreasing the dimension of the variables by CRT. As the causal additive models, we apply the random forest since it is one of the successful alternatives in CAMs. Moreover, we propose the boosting algorithm for CAMs to find computationally attractive selection procedure in CRTs since the boosting algorithm is focused on iteratively combining weak learners while building a strong learner that can predict more accurate outcomes. Therefore, this algorithm can reduce the error on the training stage of machine learning methods too (Freund, 2019). Within this algorithm, the selection procedure can be done by distinct criteria. In our analyses, we perform the knockoff filter method (Candes et al., 2018; Barber and Candes, 2015) as it can effectively control the false discovery rate of the estimated models.

On conclusion, we organize our paper as follows: The Second Section presents CAMs and CRTs to define relationship between variables. Here, we also represent boosting algorithm and knockoff filter while improving the power of CRTs. In the third section, we conduct the simulation analyses and evaluate our results. Finally, the fourth section is left for conclusion and future studies.

2. METHODS

2.1 Causal additive models

Causal models are mathematical models representing causal relationships between variables. Therefore, these models are applied in different areas such as genetics, epidemiology, econometrics (Peters et al., 2013; 2014; 2017). Causal additive models (CAMs) proposed by Buehlmann et. al. (2014) exhibit structural equations which are additive in the variables and error terms as the following form.

$$X_j = f_j(X_{PA_D(j)}, \varepsilon_j), \quad (j = 1, \dots, p) \tag{1}$$

where $X_{PA_D(j)}$ shows the set of parents for node j in *directed acyclic graphs*, f_j denotes a function while $j=1, \dots, p$, and ε_j shows the error. This model has some limitations when the number of parameters (p) exceeds the number observations (n). Hence, additive structural equation models with Gaussian errors are suggested by Buehlmann et al. (2014) to capture nonlinearities in the data and to deal with the problem of high dimension. This extended model is presented in Equation (2).

$$X_j = \sum_{k \in PA_D(j)} f_{j,k}(X_k) + \varepsilon_j \tag{2}$$

in which $\varepsilon_1, \dots, \varepsilon_p$ are independent with $\varepsilon_j \sim N(0, \sigma_j^2)$ while $\sigma_j^2 > 0$. Here, $E[f_{j,k}(X_k)] = 0$ for all j, k . Furthermore, $f_{j,k}(\cdot)$ is a smooth function from $\mathbb{R} \rightarrow \mathbb{R}$. Accordingly, it can be written as Equation (3) with coefficients for structural equations models.

$$X_j = \sum_{k \in PA_D(j)} \beta_{j,k} X_k + N_j. \tag{3}$$

In Equation (3), $\varepsilon_1, \dots, \varepsilon_p$ are independent with $\varepsilon_j \sim N(0, \sigma_j^2)$ for $\sigma_j^2 > 0$ similar to Equation (2).

2.2. Conditional randomization tests

The conditional randomization tests (CRTs) are introduced by Candes et al. (2018) without any assumption of dependent variable Y . They merely assume that the conditional distribution of random variables, let (X, Y, Z) , is known. But, the detection of the conditional distribution can be challenging, in particular, for high dimensional data. Thus, it is accepted that the conditional distribution of $X|Z$ is known and $Q(\cdot|Z)$ shows the distribution of X given $Z = z$, conditional on Z_1, \dots, Z_n . Therefore, CRT generates X values from datasets which have the following distribution:

$$X_1^{(1)} \sim Q(\cdot | Z_i) \tag{4}$$

where it is obtained independently from every $i = 1, \dots, N$ and independently from real values of X_i 's and Y_i 's. Thereby, we can write $(X|Y=y, Z=z) \stackrel{d}{=} (X|Z=z) \sim Q(\cdot|z)$. while $(= \stackrel{d}{})$ indicates the equality in distribution. Hence, we can present $(X^{(1)}, Y, Z) = (X, Y, Z)$ for all $(X^{(1)} = X_1^{(1)}, \dots, X_n^{(1)})$ and for all null hypotheses which state the equality of distribution. If we have a difference between two sides of equation, we can reject the hypothesis of the equality of distribution. Then, we repeat this procedure k times in such a way that $(X_i^{(k)}|X, Y, Z) \sim Q(\cdot | Z_i)$ is obtained independently for $i = 1, \dots, N$ and $k = 1, \dots, K$. In here, we assume that the conditional distribution

of (X, Y, Z) , $(X^{(1)}, Y, Z)$, ..., $(X^{(k)}, Y, Z)$ are identically distributed and ex-changeable by the null hypotheses. Thus, any statistics of $T(X, Y, Z)$ is also exchangeable too via $T(X, Y, Z), T(X^{(1)}, Y, Z), \dots, T(X^{(k)}, Y, Z)$. So, the step of CRT can be listed as below:

- i) Data step: (X_i, Y_i) , where X is the independent variable and Y shows the dependent variable for $i = 1, \dots, n$ observations, are defined. Then, $T(X, Y, Z)$ is computed as the test statistics to check conditional relationship between X and Y . Finally, $k \in (1, \dots, K)$ copies the sample $X^{(k)} L(X_i, Y_i)$ for all to compute $T(X^{(k)}, Y, Z)$.
- ii) Calculation step: The p -value is computed by $p = \frac{\{1 + \sum_{k=1}^K 1\} \{T(X^{(k)}, Y, Z) \geq T(X, Y, Z)\}}{1 + K}$. Here, the p -values are obtained by true X vector versus the values of the CRT copies.

2.3. Boosting procedure for causal additive models

Boosting is an ensemble learning method that combines a set of weak learners into a strong learner to minimize training errors (Schapire, 1999; Freund and Schapire, 2019). In boosting, a random sample of data is selected, fitted with a model and then, trained sequentially—that is, each model tries to compensate for the weaknesses of its precedes. Therefore, boosting is a method used in machine learning to reduce errors in predictive data analysis. A generalized additive model is fitted by using a boosting algorithm based on component-wise base-learners. The base-learners can either be specified via the formula object or via the base learner argument. In this calculation, GAMBoost algorithm is used to fit a generalized additive model by likelihood based boosting. It is particularly suitable for models with a large number of predictors with potentially non-linear influence. It provides a smooth functional estimates of covariate influenced-functions together with confidence bands and approximate degrees of freedom.

2.4. Knockoff filter for causal additive models

Barber and Candès (2015) propose a novel model selection procedure by using false discovery rate control for low dimensional regression. Later, this idea is extended by Candès et al. (2018) by suggesting the conditional randomization test for logistic regression. Their selection procedure is based on three stages. The first step is to make knockoff copies of conditional variables. Then, we calculate the importance of variables. Finally, in the third step, we make model selection depending on the false discovery rate control of type 1 error. Due to the exchangeability and sufficiency properties of knockoff filter, they can be applied in causal additive models effectively.

3. APPLICATION

In the analyses, we use two simulated datasets. In the first data, we define four variables ($p=4$) and in the second data, we use eight variables ($p=8$). Then, we assign 100 observations for each variable ($n=100$) in both datasets. Later, we apply the boosting algorithm for random forest model and we find 2-1, 1-4, 3-4, 2-3, and 3-1 relationships for edges of the first dataset (i.e., $p=4$). For the second dataset, these pairwise edges are found as 6-5, 2-1, 8-7, 5-8, 1-4, 3-4, 2-3, 6-7, 5-7, 1-6, 3-1, 3-6, 7-4, 8-4, 5-4, 2-4, 1-5 and 2-6.

Then, we perform the knockoff filter as the model selection criterion in the random forest whose main edges are defined by boosting algorithm. We take 0.1 as the knockoff filter value, i.e., false discovery rate, for both datasets. It means that among all the paired connections, 10% of these are truly null, i.e., there is no edge between the selected nodes in the given dataset. Thereby, in the first dataset, solely the (2-1)-pair has the p -value 0.126 implying that the edge is not significant, and the remainings are found truly. On the other hand, for the second dataset, we find that among the selected 18 edges, (6-5), (8-7) and (6-7) pairs have higher p -values via 0.223, 0.177 and 0.121, respectively, based on the false discovery criterion that is set to 0.1 as stated. Moreover, from both datasets, we

observe that the computational time is reduced sharply via the proposal prediction of the system's structure. For the first dataset, thanks to the boosting algorithm, the calculation is completed as 3 times faster and for the second dataset, it is finished as 5 times faster. Finally, when we compare the correctly estimated edges in both systems with the true systems' connections, we find that the estimated edges exist in the actual systems too. Therefore, we conclude that the inference of the edges via CRT based on boosting algorithm and knockoff filter selection criterion give promising results for the construction of estimated systems.

4. CONCLUSION

In this work, shortly, we have proposed an alternative model selection procedure for causal additive models by using conditional randomization test (CRT) since it is very useful to decide relationship between variables. Accordingly, in the construction of the systems, we have performed random forest method in the family of causal additive models and have applied the boosting algorithm within the CRT to estimate the connected edges. Finally, we have selected the optimal model via the knockoff filter approach which controls the false discovery rate of all connected pair of genes. From the findings, we have seen that the proposal procedure of analysis can successfully estimate the major edges in the actual systems and significantly decrease the computational time since it focuses on the major edges which have higher strengths between genes. We consider that due to the efficiency of the time, this approach can be applied for realistically large systems, at least, to detect the main connections.

As the continue of this analysis, we will investigate the performance of the proposal strategy is inference of other networks models such as random networks and modular networks besides the scale-free ones and under various sample sizes n and dimensions p .

REFERENCES

- [1] P. Bühlmann, J. Peters, J. Ernest, CAM: Causal additive models, high-dimensional order search and penalized regression. *The Annals of Statistics*, 42, 6, (2014), 2526-2556.
- [2] R. F. Barber, E. J. Candès, Controlling the false discovery rate via knockoffs. *The Annals of Statistics*, 43, 5 (2015), 2055-2085.
- [3] E. Candès, Y. Fan, L. Janson, J. Lv, Panning for gold: 'model-X' knockoffs for high dimensional controlled variable selection. *Journal of the Royal Statistical Society: Series B*, 80, 3 (2018), 551-577.
- [4] Y. Freund, R. Schapire, N. Abe, A short introduction to boosting. *Journal-Japanese Society For Artificial Intelligence*, 14 (2019), 771-780.
- [5] L. Meier, S. Van de Geer, P. Bühlmann, High-dimensional additive modeling. *The Annals of Statistics*, 37, 6B (2009), 3779-3821.
- [6] J. Pearl, *Causality*. Cambridge University Press, 2009.
- [7] J. Peters, D. Janzing, B. Schölkopf, Causal inference on time series using restricted structural equation models. *Advances in Neural Information Processing Systems*, 26 (2013).
- [8] J. Peters, J. M. Mooij, D. Janzing, B. Schölkopf, Causal discovery with continuous additive noise models, *Journal of Machine Learning Research*, 15 (2014), 2009-2053.
- [9] J. Peters, D. Janzing, B. Schölkopf, *Elements of causal inference: foundations and learning algorithms*, MIT Press, 2017.
- [10] R. E. Schapire, Theoretical views of boosting. In *European conference on computational learning theory* (pp. 1-10). Springer, Berlin, Heidelberg, 1999.
- [11] S. N. Wood, *Generalized additive models: an introduction with R*. CRC Chapman and Hall, 2017.

Research on temperature distribution of heavy oil reservoir in situ heated by electromagnetic radiation

Jiexian XIAO¹, Deli GAO^{1*}, Zhengxu WANG², Xuelin DONG¹ and Qingfeng GUO²

¹ MOE Key Laboratory of Petroleum Engineering, China University of Petroleum, Beijing, CHINA

² CNPC Engineering Technology R&D Company Limited, Beijing, CHINA

* gaodeli_team@126.com

ABSTRACT

Heavy oil, as one of the unconventional oil and gas resources, is increasingly gaining more concerns from all over the world. However, the steam injection recovery applied broadly is gradually being abandoned due to low efficiency and large amounts of greenhouse gas emissions. Therefore, a radio frequency (RF) heating technology used in vertical well is proposed which mobilizes heavy oil by using RF electromagnetic wave (RF-EMW) rather than steam. To accurately investigate the temperature distribution of heavy oil reservoir in situ heated by electromagnetic radiation, an electromagnetic-thermal coupling model is established initially. The model considers the thermal properties change the heavy oil reservoir with temperature. Afterward, the model is validated by experimental data. Finally, the influence of several key factors on the reservoir temperature are discussed. Calculation results display that the maximum heating radius of the RF heating technology is up to 10m, which indicates that this technology has obvious technical advantages. The model considering the varying specific heat brings about lower reservoir temperature around the wellbore, and the maximum temperature in the condition of constant thermal conductivity is obviously higher than that in the case of varying thermal conductivity. In addition, in the premise of constant frequency (50MHz) and output power (10kW), the reservoir temperature based on RF heating can be enhanced by increasing the relative permittivity of reservoir, porosity, electrical conductivity and saturation of water. The research results are intended to provide important guidance for the field application of RF heating technology.

KEYWORDS - Heavy oil, RF heating, Influencing factors, Temperature distribution, Numerical simulation

1. INTRODUCTION

With the decrease of conventional crude oil, heavy oil is being exploited increasingly by a major thrust of petroleum companies [1-3]. While the high viscosity of heavy oil is the main factor leading to low oil production [4,5]. Several practices have demonstrated that increasing temperature helps to reduce the crude oil viscosity [6]. Fig. 1 shows the viscosity change with temperature for the heavy oil sample from the WanT 1 Oilfield, Xinjiang of China [7].

Current thermal recovery technologies include steam flooding, SAGD and combustion. But those methods have gradually exposed the technique flaws of low profit, high carbon emission and environmental disruption. Therefore, it is urgent to develop new mining technologies. In recent years, RF heating method appears and considered to be a viable technology for extracting heavy oil. It can effectively deliver more thermal energy to reservoir and extract oil from reservoirs cracks where steam method is ineffective. Besides, the RF heating process does not emit carbon dioxide to the atmosphere [8-10].

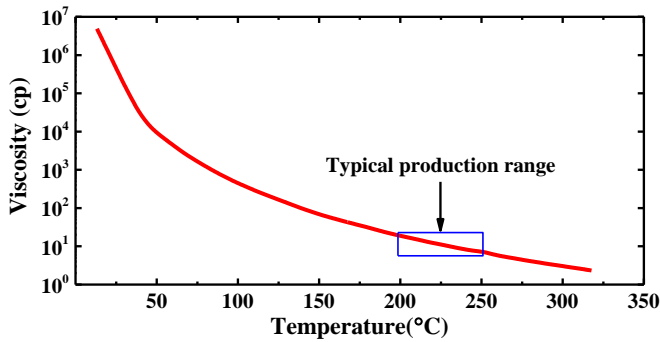


Figure 1. The relationship between viscosity and temperature.

The use of RF-EMW was firstly mentioned by Ritchey to obtain oil from bitumen [11]. Later, some researchers carried out extensive numerical simulation researches on RF heating technology, and some simulation results show that this novel method is technically feasible [12-14]. The COMSOL Multiphysics software is used to calculate the oil production rate. The simulation results can guide the design of pilot tests for the RF heating process [15]. Wang and Gao studied various heating patterns of RF heating based on the multi-antenna [16]. They also used the waveguide to transmit EMW to the heavy oil blocks and comprehensively analyzed the factors influencing the reservoir temperature [17]. The numerical simulation describing the processes of RF and electric heating was done and the conclusion was obtained that RF heating was more applicable for the heavy oil reservoir with different properties [7]. An RF heating with antenna array for horizontal and vertical wells was proposed to improve heating power and area [18].

But in the previous investigations some mathematical models assumed that the reservoir properties were constant, which failed to fit actual heating. This is due to the effects of temperature on the reservoir properties during the RF heating process. This problem was rarely considered in the current literatures and might result in some inaccurate simulation results.

Therefore, to address this problem, this paper considered the reservoir properties changes with temperature, and the corresponding 2D axisymmetric geometry model and mathematical model were established for obtaining the temperature results. Simulation values were also compared with the experimental temperature data. Furthermore, the performance of RF heating was evaluated based on the simulation results. The effects of relative permittivity, specific heat, electrical conductivity, thermal conductivity, water saturation and reservoir saturation on the reservoir temperature distributions were also investigated. The research purpose was to promote the development of RF technology.

2. MECHANISM OF RF HEATING

As one of several heating methods, RF technology depends on the abilities of different materials to absorb electromagnetic energy. The heavy oil reservoir is mainly composed of oil, water and rock. In general, the water called lossy medium owns a strong ability to absorb EM energy. Due to polarization effects in water present in the reservoir, the EM energy is dissipated into thermal energy, causing the increased temperature of oil and rocks. Actually, the oil is heated indirectly, which is shown in Figure 2. Moreover, the water is made up of the polar molecules, and the torques are exerted on those polar molecules. The dipole moments align the polar molecules with the oscillating electric fields [19,20]. Ultimately, the polar molecular collision causes the friction heat generation.

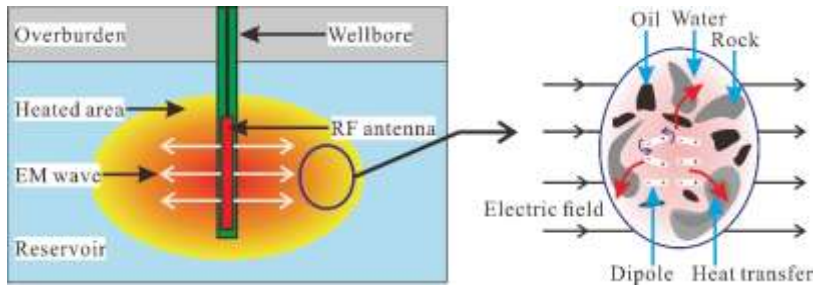


Figure 2. Schematic diagram of RF heating mechanism.

3. MODEL DESCRIPTION

3.1. Geometric Model

For RF heating technology, the antenna is regarded as an important component because it can radiate EM wave into oil-bearing formation and provide EM energy. Considering the actual situation, the antenna shape should make it accommodate to the narrow borehole space. Only in this way can the flexible movement operations be successfully done. Accordingly, in this paper the dipole antenna with linear appearance is adopted as the radiating element that emits RF-EMW, and the corresponding geometry model is shown in Figure 3. The dipole antenna is composed of two arms, and there is a gap between them. The coordinate origin of the whole geometric model is in the antenna center, and Table 1 details its dimensions.

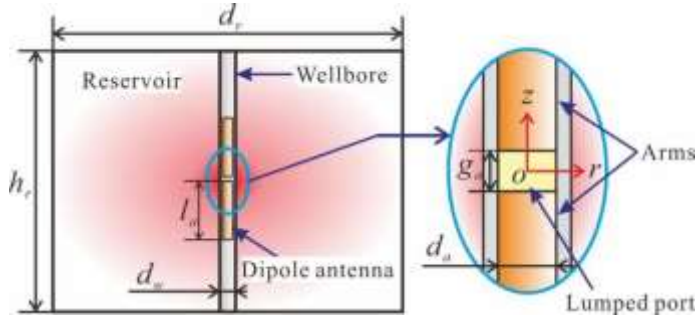


Figure 3. Geometric model of reservoir and dipole antenna.

Table 1. Geometric model size

Parameters	Unit	Value
Reservoir thickness (h_r)	m	15
Reservoir diameter (d_r)	m	20
Wellbore diameter (d_w)	m	0.2
Arm length of antenna (l_a)	m	4.0
Antenna diameter (d_a)	m	0.01
Gap between two arms (g_a)	m	0.01

3.2. Reservoir Properties

During the heavy oil is heated, the thermal conductivity and specific heat change dynamically resulting from temperature rise. According to the experimental data from the Refs [21] and [22], the least square and fitting methods are employed to describe the relationship between reservoir properties and temperature. When the value of temperature is in the range of 250-500K, the expressions are given as Eqs. (1) and (2), respectively. The relative errors are 0.92% and 0.66%, which indicates the correlations have high accuracy.

$$c(T) = -0.001(T + 273.15)^2 + 2.186(T + 273.15) + 132.423 \tag{1}$$

Where, c is specific heat in J/kg/°C and T is reservoir temperature in °C.

$$k(T) = 1.2 \times 10^{-6}(T + 273.15)^2 - 4.48 \times 10^{-4}(T + 273.15) + 0.179 \tag{2}$$

Where, k is thermal conductivity in W/m/°C.

According to the Archie’s formula[23, 24], the electrical conductivity of reservoir is given:

$$\sigma \approx \sigma_w \Phi^{m_1} S_w^{n_1} \tag{3}$$

Where, σ is electrical conductivity in S/m, σ_w is electrical conductivity of water in S/m, Φ is porosity in dimensionless, S_w is water saturation, m_1 is the cementation factor of rock in dimensionless, n_1 is saturation exponent in dimensionless.

Besides, the reservoir density is calculated by the volume-averaged method:

$$\rho = (1 - \Phi)\rho_s + S_w\Phi\rho_w + (1 - S_w)\Phi\rho_o \tag{4}$$

Where, ρ denotes reservoir density in kg/m³, the subscript s , w and o is for rock, water and oil, respectively. The reservoir properties are listed in Table 2.

Table 2. Parameters of reservoir properties.

Parameters	Unit	Value
Relative permeability of reservoir (μ_r)	-	1.0
Density of water (ρ_w)	kg/m ³	1000
Conductivity of water (σ_w)	S/m	0.5
Density of rock (ρ_s)	kg/m ³	2100
Density of oil (ρ_o)	kg/m ³	980
Porosity of reservoir (Φ)	-	25%
Frequency of EMW (f)	MHz	50
Water saturation (S_w)	-	20%
Saturation exponent (n_1)	-	2.0
Initial reservoir temperature (T_{const})	°C	30
Cementation factor of rock (m_1)	-	2.0
Relative permittivity of reservoir (ϵ_r)	-	12

3.3. Heating model

Helmholtz equation is firstly derived [25] based on the Maxwell equations:

$$\nabla^2 \vec{E} + k_c^2 \vec{E} = 0 \tag{5}$$

Where, \vec{E} is electric field in V/m, k_c is wave number in 1/m.

k_c is complex and also called “complex wave number”, it is expressed as:

$$k_c = \omega \sqrt{\mu \epsilon_c} \tag{6}$$

Where, μ is reservoir permeability in H/m, ω is angular frequency in rad/s, ϵ_c is complex permittivity. So the value of k_c is:

$$k_0 = \omega \sqrt{\epsilon_0 \mu_0} \tag{7}$$

Where, μ_0 denotes permeability in H/m, ϵ_0 is permittivity in F/m. Their values are $4\pi \times 10^{-7}$ H/m and 8.85×10^{-12} F/m, respectively.

The expressions of ϵ_c and ω are:

$$\epsilon_c = \epsilon - j \frac{\sigma}{\omega} \tag{8}$$

$$\omega = 2\pi f \tag{9}$$

Where, ϵ is permittivity of lossy medium in F/m, j is imaginary unit, f is wave frequency in Hz.

The Eq. **Hata! Başvuru kaynağı bulunamadı.** can be obtained after substituting Eqs. **Hata! Başvuru kaynağı bulunamadı.-Hata! Başvuru kaynağı bulunamadı.** into Eq. **Hata! Başvuru kaynağı bulunamadı.:**

$$\nabla^2 \vec{E} + \frac{\mu}{\mu_0} k_0^2 \left(\frac{\epsilon}{\epsilon_0} - \frac{j\sigma}{2\pi f \epsilon_0} \right) \vec{E} = 0 \tag{10}$$

And then Eq. **Hata! Başvuru kaynağı bulunamadı.** becomes:

$$\mu_r^{-1} \nabla^2 \vec{E} + k_0^2 \left(\epsilon_r - \frac{j\sigma}{2\pi f \epsilon_0} \right) \vec{E} = 0 \tag{11}$$

Substituting the Eq. **Hata! Başvuru kaynağı bulunamadı.** into Eq. **Hata! Başvuru kaynağı bulunamadı.**, electrical field distribution equation can be obtained (Eq. **Hata! Başvuru kaynağı bulunamadı.**).

$$\nabla \times (\nabla \times \vec{E}) = \nabla (\nabla \cdot \vec{E}) - \nabla^2 \vec{E} \tag{12}$$

$$\nabla \times \mu_r^{-1} (\nabla \times \vec{E}) - k_0^2 \left(\epsilon_r - \frac{j\sigma}{2\pi f \epsilon_0} \right) \vec{E} = 0 \tag{13}$$

The heat converted by EM energy is [25]:

$$Q = \frac{1}{2} \text{Re}[(\sigma - 2\pi f j \epsilon_r) \vec{E} \cdot \vec{E}^*] \tag{14}$$

Where, Q is heat in W/m^3 .

FEM is used to compute the mathematical model. To improve calculation accuracy, the meshes in the outer surfaces of the dipole antenna and the reservoir area around the wellbore are discretized densely (Figure 4).

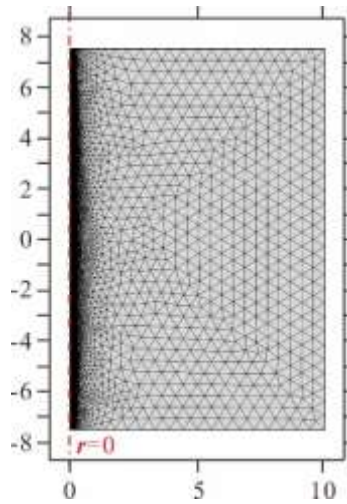


Figure 4. Mesh discretization of geometric model in rz plane.

3.4. Model Validation

An experimental setup is designed to verify the validity of the mathematical model. Figure 5 displays the compute values and experimental results of temperature distribution. The comparison indicate that the simulation results are in line with the experimental values. the relative errors of all points are within the range of 3.04% to 4.37%. The errors can be caused by the several reasons: (1) the oil sand is Inhomogeneous due to manual operation; (2) water vapor appears causing temperature change; (3) there are several measurement errors. So the established model considers the key factors and it can be concluded that the silumation results are feasible.

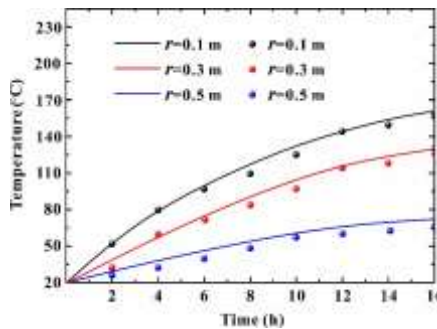


Figure 5. Numerical values (solid lines) and experimental results (symbols).

4. RESULTS AND DISCUSSION

The performance of RF heating is evaluated in this section, and the EM frequency and output power are 10kW and 50MHz respectively throughout the heating process

4.1. Evaluation of RF Heating with Vertical Well

Figure 6 shows the simulation results after 6 months of heating. The part of this 3D model is cut away to show the internal structure clearly.

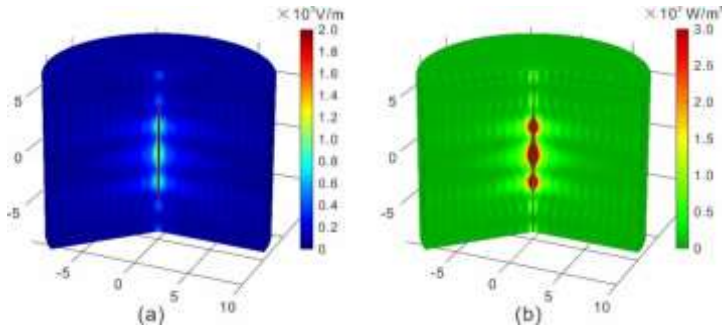


Figure 6. Electrical field (left) and electric power dissipation density (right) distribution.

The electrical field distribution in the reservoir is shown in Figure 6-(a), It is noticed that the areas of high electrical field intensity are located near the two antenna arms, especially in the areas near the midpoint of two arms, due to EMW attenuation. Besides, the electric field distribution with the corrugated shape within the reservoir indicates that EMW has penetrated the reservoir. Figure 7 shows the temperature fields after 6 months of heating. The distributions of temperature field and electric power dissipation density are similar. The higher temperature is reached along the wellbore or in the vicinity of antenna arms. This is because that the most EM energy is absorbed by the reservoir near the antenna, but the remaining EM energy is less and continue to transmit to the distant reservoir area.

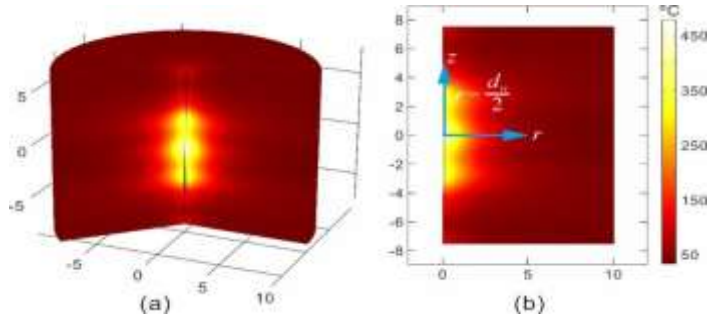


Figure 7. Temperature distribution ((a) 3D view and (b) sectional view).

Figure 8 draws the temperature distribution marked in the Figure 7-(b). The r-axis is located in the middle of the two arms and the z-axis is along the wall of wellbore ($r=dw/2$). From Figure 8-(a), we can observe that the temperature drops gradually with the r-axis, and the heating radius is greater than 10m. Besides the temperature curve symmetrically distributes along the r-axis, there are three local maximum values and four local minimum values, and the maximum temperature value appears in the r-direction (Figure 8-(b)). It is worth noting that the calculated results in Sect. 4.1 are based on the dynamic change of the specific heat and thermal conductivity of the reservoir with temperature.

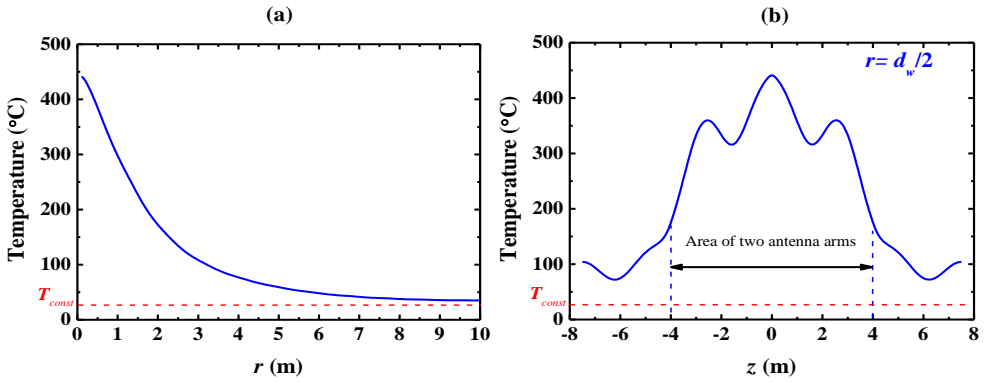


Figure 8. Temperature distributions along the radial direction (left) and wellbore (right).

4.2. Effects of Reservoir Properties on Reservoir Temperature

Under the premise of the constant output power and EM frequency, the effects of reservoir properties on temperature distribution are analysed in this section. Initially, the temperature distribution in the case of unchanged value of specific heat and thermal conductivity is compared with that in the condition of the varying values with temperature. Afterwards the effects of relative permittivity, electrical conductivity of water, water saturation and reservoir porosity on the temperature distribution during the RF heating process are analyzed according to a single variable method, and finally, the reasons for the above analyses are explained in detail.

(1) Effect of Specific Heat of Reservoir

Considering the two cases of constant (case 1) and changed values (case 2) of specific heat, the temperature curves are drawn in Figure 9, in which the constant value of specific heat is set to 800J/(kg·°C). Obviously the maximum temperature along the wellbore in the condition of the constant value is higher. In Figure 9-(a), we can also see that within 2.5m distance of wellbore, the temperature near the wellbore for case 1 is slightly high than that for case 2. With the increase of radial distance, two temperature curves drop and trend to coincide. In Figure 9-(b), the wellbore temperature near the area of two antenna arms are higher than that of other areas, and the constant specific heat contributes to higher wellbore temperature. But the temperature values outside the antenna region for the cases 1 and 2 are almost equal. In brief, the numerical model of this paper considering the varying specific heat can result in lower reservoir temperature near the area of antenna.

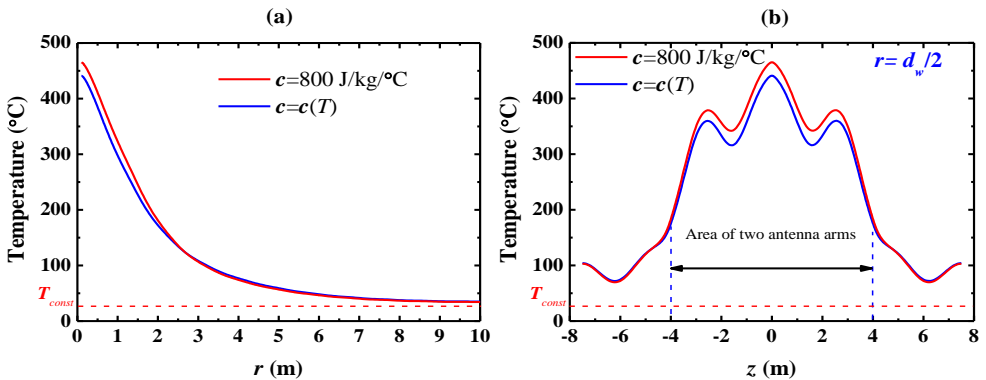


Figure 9. Effects of specific heat of reservoir on temperature curves.

(2) Effect of Thermal Conductivity

Figure 10 displays the effect of thermal conductivity of reservoir on temperature curves during 6 months of heating. Here the constant value of thermal conductivity is set to $0.2\text{W}/(\text{m}\cdot^\circ\text{C})$, and the varying thermal conductivity with temperature refers to Eq. [Hata! Başyuru kaynağı bulunamadı.](#). Similar to the results shown in Figure 9, the constant thermal conductivity results in higher wellbore temperature. From Figure 10-(a), it is apparent that within 1.0 m radial distance, the wellbore temperature for unchanged value of thermal conductivity (case a) is greatly high than that for varying value of it (case b). Besides, within the range of 1-3m, the temperature curve of the case a is below that of the case b, and as the increase of radial distance, the two temperature curves tend to coincide. The degree of temperature increase within the antenna region shown in Figure 10-(b) is obviously higher than that in the both ends of wellbore. Therefore, the numerical model in this paper based on the varying thermal conductivity can lead to apparently lower reservoir temperature near the wellbore.

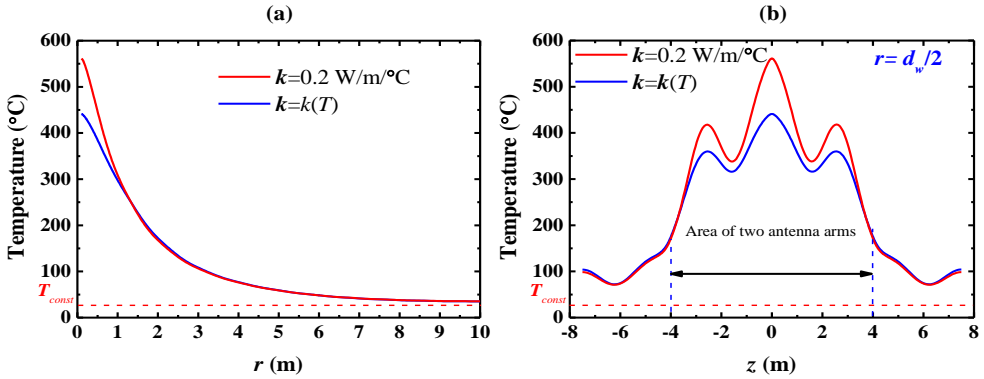


Figure 10. Effects of thermal conductivity of reservoir on temperature curves.

4.2.1 Effect of Relative Permittivity of Reservoir

This Sects. 4.2.3-4.2.6 mainly focus on the studies on the effects of relative permittivity, electrical conductivity of water, water saturation and reservoir porosity on the reservoir temperature profiles. Because this meets the actual situation during the RF heating process. Therefore, the results are more convincing and have important guiding significance.

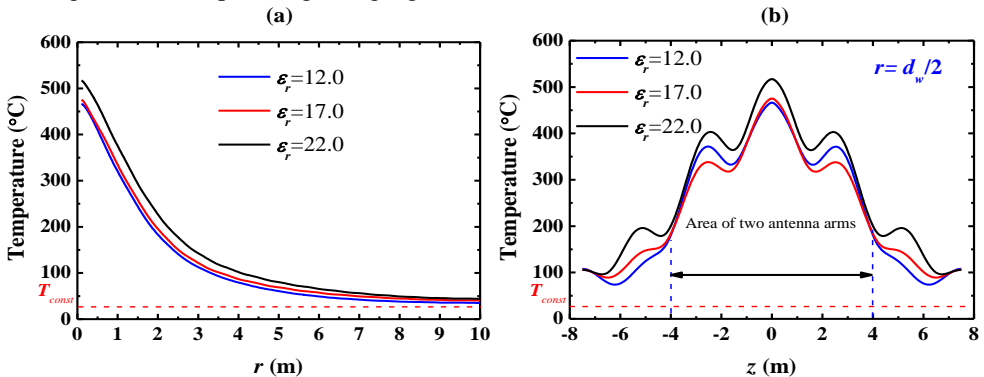


Figure 11. Effects of relative permittivity of reservoir on temperature curves.

The effects of relative permittivity of reservoir on temperature curves are presented in the Figure 11. When the relative permittivity increases from 17 to 22, the reservoir temperatures at any points of the r-axis grow. Figure 11-(b) shows that the relative permittivity of reservoir has a greater influence on wellbore temperature distribution. The temperature values along the wellbore rises when the

relative permittivity changes from 17 to 22, As its value becomes 12, the maximum temperature drops slightly, however, the temperature becomes high within the area of 1.0-3.8m. The results indicate that higher relative permittivity of reservoir contributes to high maximum temperature but lower relative permittivity can result in high temperature in the local position of the wellbore.

4.2.2 Effect of Electrical Conductivity of Water

Through comparing the curves shown in Figure 12, the increase of the electrical conductivity of water remarkably brings about a rise in reservoir temperature near the antenna area. When the conductivity is the value of 0.9 S/m, the maximum wellbore temperature is up to 620°C, which indicate that the high electrical conductivity of water has good absorbing property for EMW and then causes higher temperature. It is worth noting that the continued high temperature appears near the antenna or along the wellbore, which may pose a greater challenge to the antenna and wellbore stability. So some effective measures need to be taken to maintain the temperature within a reasonable range, for example, employing the intermittent heating mode.

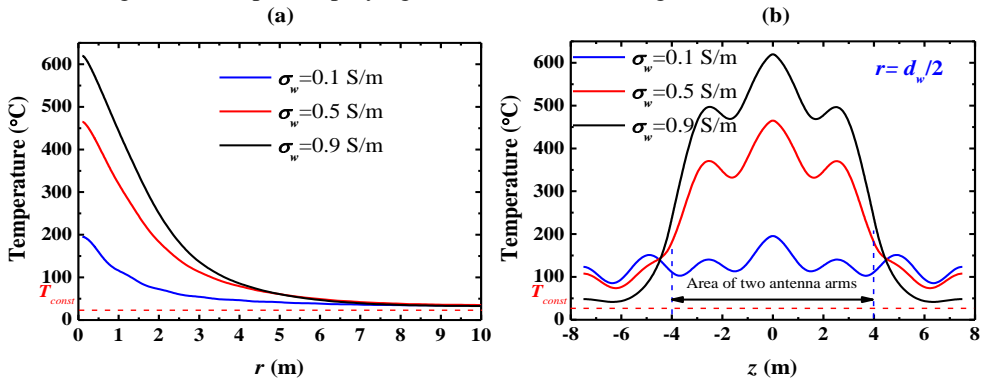


Figure 12. Effects of electrical conductivity of water on temperature curves.

4.2.3 Effect of Water Saturation

Furtherly, Figure 13 shows the influences of different water saturations on temperature curves. Higher value of water saturation brings about high maximum wellbore temperature, but the curve for high water saturation drops sharply as the increasing radial distance. In fact, the other change laws shown in the Figures 13-(a) and (b) are similar with the temperature curves revealed in Figures 12-(a) and (b).

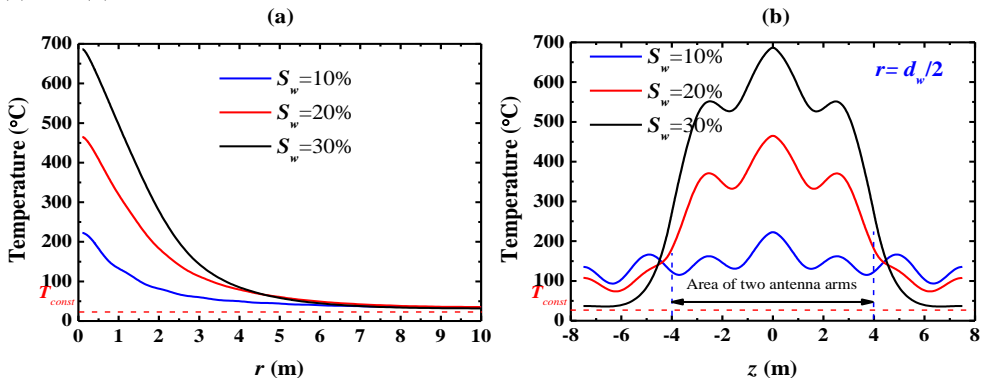


Figure 13. Effects of water saturation on temperature curves.

4.2.4 Effect of Reservoir Porosity

From the Figure 13, it can be seen that the effects of porosity on temperature are obvious. The maximum temperature is 653°C when the porosity is 35%, however the maximum temperature decreases to 268°C as the porosity is 15%. Meanwhile, as the increase of radial distance, the temperature values of three curves trend to the initial temperature, and their temperature values are about 35°C in the position of $r=10$ m (outer boundary of the reservoir) (Figure 14-(a)). However, within the range of 4.5-7.5m (or -7.5- -4.5m), the temperature values in the condition of lower reservoir porosity become high (Figure 14-(b)). So the analyses above manifest that the reservoir with higher porosity can improve the temperature near the antenna arms, but it fails to increase the temperature near the two ends of the wellbore.

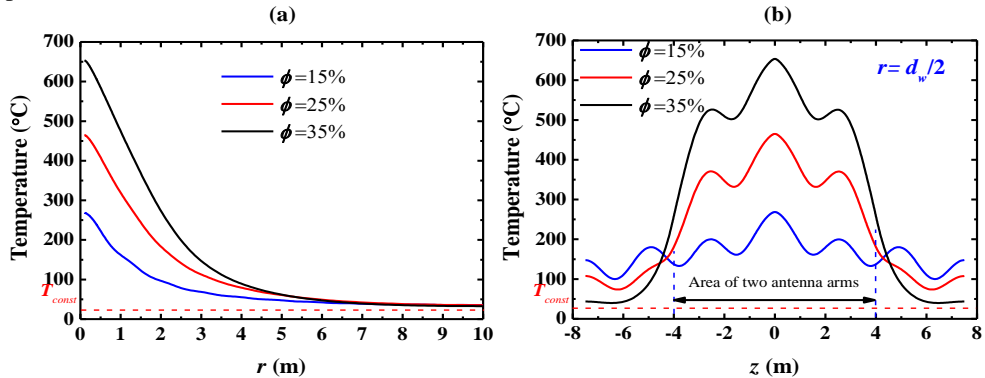


Figure 14. Effects of reservoir porosity on temperature curves.

5. CONCLUSION

From this study, the following main conclusions are drawn: (1) the maximum reservoir temperature in the condition of the constant specific heat is slightly higher than that in the case of the varying specific heat. The numerical model considering the varying specific heat can result in lower reservoir temperature near the area of antenna; (2) the constant thermal conductivity can improve greatly maximum wellbore temperature. So, the numerical model based on the varying thermal conductivity can lead to apparently lower reservoir temperature near the wellbore. Besides, the degree of temperature increase within the antenna region is obviously higher than that in the both ends of wellbore; (3) when the EM frequency (50MHz) and output power (10kW) are constant, the reservoir temperature can be enhanced by increasing the relative permittivity of reservoir, water saturation and reservoir porosity. Moreover, the reservoir temperature near the area of antenna arms ascends obviously with the increasing electrical conductivity of water during the RF heating. In fact, high porosity and water saturation help to improve the water content. Therefore, the conclude can be drawn that the water content and electrical conductivity of water play an important role in affecting the reservoir temperature distribution.

REFERENCES

- [1] Mao, X., Liu, Y., Guan, W. et al. Experimental and numerical simulation on the influence of anisotropic fracture network deformation to shale gas percolation. Arab J Geosci 11, 615 (2018). DOI: 10.1007/s12517-018-3973-9
- [2] Song, L., Ning, Z. & Duan, L. Research on reservoir characteristics of Chang7 tight oil based on nano-CT. Arab J Geosci 11, 472 (2018). DOI: 10.1007/s12517-018-3842-6
- [3] Huang, L., Ning, Z., Wang, Q. et al. Enhanced gas recovery by CO2 sequestration in marine shale: a molecular view based on realistic kerogen model. Arab J Geosci 11, 404 (2018). DOI: 10.1007/s12517-018-3762-5

-
- [4] Yunpeng, H., Lei, W., Wei, D. et al. A rate decline model for acidizing and fracturing wells in closed carbonate reservoirs. *Arab J Geosci* 12, 249 (2019). DOI: [10.1007/s12517-019-4348-6](https://doi.org/10.1007/s12517-019-4348-6)
- [5] Meng, Y., Li, X., Jiang, M. et al. Experimental research on three dimensional flow characteristics of multiple horizontal fractures utilizing an innovative experiment apparatus. *Arab J Geosci* 11, 243 (2018). DOI: [10.1007/s12517-018-3589-0](https://doi.org/10.1007/s12517-018-3589-0)
- [6] Ali S.: Heavy oil—evermore mobile[J]. *Journal of Petroleum Science and Engineering*, 2003, 37:5–9. DOI: [10.1016/S0920-4105\(02\)00307-8](https://doi.org/10.1016/S0920-4105(02)00307-8)
- [7] Wang, Z.; Gao, D.; Diao, B.; Tan, L.; Zhang, W.; Liu, K.: Comparative performance of electric heater vs. RF heating for heavy oil recovery. *Applied Thermal Engineering*. 2019.114105 (2019). DOI: [10.1016/j.applthermaleng.2019.114105](https://doi.org/10.1016/j.applthermaleng.2019.114105)
- [8] Abraham, T.; Afacan, A.; Dhandharia, P.; Thundat, T.: Conduction and Dielectric Relaxation Mechanisms in Athabasca Oil Sands with Application to Electrical Heating. *Energy & Fuels*. 30(7), 5630-5642 (2016). DOI: [10.1021/acs.energyfuels.6b00954](https://doi.org/10.1021/acs.energyfuels.6b00954)
- [9] Saeedfar, A.; Lawton, D.; Osadetz, K.: Directional RF Heating for Heavy Oil Recovery Using Antenna Array Beam-Forming. In: *SPE Canada Heavy Oil Technical Conference*, Calgary, Alberta, Canada (2016). DOI: <https://doi.org/10.2118/180695-MS>
- [10] Hu, L.; Li, H.; Babadagli, T.; Ahmadloo, M.: Experimental Investigation of Combined Electromagnetic Heating and Solvent Assisted Gravity Drainage for Heavy Oil Recovery. In: *SPE Canada Heavy Oil Technical Conference*, Calgary, Alberta, Canada (2016). DOI: <https://doi.org/10.2118/180747-MS>
- [11] Ritchey, H.W.: Radiation heating: USA Patent Application, Serial No. 2,757,738 (1956).
- [12] Bridges, J.E.; Krstansky, J.J.; Taflove, A.; Sresty, G.: The IITRI In Situ RF Fuel Recovery Process. *Journal of Microwave Power*. 18(1), 3-14 (1983).
- [13] Sresty, G.; Dev, H.; Snow, R.; Bridges, J.: Recovery of Bitumen From Tar Sand Deposits With the Radio Frequency Process. *SPE Reservoir Engineering*. 1(1), 85-94 (1986). DOI: <https://doi.org/10.2118/10229-PA>
- [14] Kasevich, R.S.; Price, S.L.; Faust, D.L.; Fontaine, M.F.: Pilot Testing of a Radio Frequency Heating System for Enhanced Oil Recovery From Diatomaceous Earth. In: *SPE 69th Annual Technical Conference and Exhibition*, New Orleans, LA, USA (1994). DOI: <https://doi.org/10.2118/28619-MS>
- [15] Ramcharan, T.; Hosein, R.; Jupiter, A.: The Viability of Oil Extraction from Trinidad Tar Sands by Radio Frequency Heating-A Simulation Approach. In: *SPE Trinidad and Tobago Section Energy Resources Conference*, Port of Spain, Trinidad and Tobago (2016). DOI: <https://doi.org/10.2118/180830-MS>
- [16] Wang, Z.; Gao, D.; Liu, K.; Tan, T.; Wang, Z.; Li, W.: Study on Radio Frequency Heating Pattern of Heavy Oil Reservoir Based on Multi-Antenna Configuration. In: *SPE International Heavy Oil Conference and Exhibition*, Kuwait City, Kuwait (2018). DOI: <https://doi.org/10.2118/193774-MS>
- [17] Wang, Z.; Gao, D.: A Simulation Study on the High-Frequency Electromagnetic Heating Heavy Oil Reservoir and Analysis of Influencing Factors. *ARAB J SCI ENG*. <https://doi.org/10.1007/s13369-019-03898-4> (2019).
- [18] Wang, Z.; Gao, D.; Fang, J.: Numerical simulation of RF heating heavy oil reservoir based on the coupling between electromagnetic and temperature field. *Fuel*. 220, 14-24 (2018). DOI: [10.1016/j.fuel.2018.02.012](https://doi.org/10.1016/j.fuel.2018.02.012)
- [19] Davletbaev, A.; Kovaleva, L.; Babadagli, T.: Mathematical modeling and field application of heavy oil recovery by Radio-Frequency Electromagnetic stimulation. *J. Petrol. Sci Eng*. 78(3), 646-653 (2011). DOI: [org/10.1016/j.petrol.2011.07.006](https://doi.org/10.1016/j.petrol.2011.07.006)
- [20] Abernethy, E.R.: Production increase of heavy oils by electromagnetic heating. *Journal of Canadian Petroleum*. 15(3), 91-97 (1976). DOI: [10.2118/76-03-12](https://doi.org/10.2118/76-03-12)

- [21] Haike, Y.; Yang, Z.; Zhongliang, Z.; Riheng, H.: Specific heat capacity of oil sands minerals and heavy oils. *Oilfield Chemistry*. 5(2), 134-137 (1988).
- [22] Qian, Z.; Yanwei, L.; Laibin, X.: Analysis of testing method and influencing factors of asphalt mixture thermal conductivity coefficient. *J. Xi'an Univ. of Arch. & Tech. (Nat Sci Edn)*. 46(2), 199-203 (2014).
- [23] Archie, G.E.: The Electrical Resistivity Log as an Aid in Determining Some Reservoir Characteristics. *Transactions of the AIME*. 146(1), 54-62 (1942). DOI: 10.2118/942054-G
- [24] Sun, J.: Archie's formula: historical background and earlier debates. *Progress In Geophysics*. 22(2), 472-486 (2007).
- [25] Von H.A.: *Dielectrics and Waves*. Xi'an Jiaotong University Press, Xi'an (2011).

Experimental Approach for Natural Radioactivity Measurement

Yusuf CEYLAN

³ Selçuk University, Science Faculty, Physics Department, Konya-TURKEY

* yceylan@selcuk.edu.tr

ABSTRACT

Radiations are existed since creation of universe due to the long life time of radionuclid. They are found in soil, rocks, water, air, vegetation, building material, food in small amounts and also from space as cosmic rays. In this study, measurement technique of measurement natural radioactivity for ^{226}Ra , ^{232}Th and ^{40}K concentrations were detailed.

KEYWORDS: Natural radioactivity, Gamma spectroscopy,

Humans are exposed to radiation from both natural and artificial sources in their living environments. Knowing the level of natural radioactivity in any region is important not only for people to recognize the natural radioactivity levels of their habitats, but also to detect any possible changes in radioactivity levels. Significant contributions to environmental radiation are due to radioactive elements such as ^{238}U , ^{232}Th and ^{40}K . Uranium and thorium concentrations in soils are high in local areas and cosmic rays are more intense at high altitudes [1]. External exposure due to natural environmental radioactivity and gamma radiation is largely dependent on geological and geographic conditions and appears at different levels in the territory of any area in the world [2].

The main purpose of environmental radiation measurements is to determine the type and dose of radiation that people receive from environmental sources and to assess the risk to be posed. In this, the environmental concentrations of radionuclides, which constitute natural sources of radiation, and the effect of radiation on biological systems, particularly in humans, need to be determined. In addition, the relationship between the radionuclides in the environment and the dose of radiation received by humans from these sources should also be determined. Only after such an investigation can it be decided whether a region is suitable for living in terms of natural radiation.

The radioactivity concentrations of ^{226}Ra , ^{232}Th and ^{40}K in soil samples were determined using a gamma ray spectrometry consists of a 3"x3" NaI(Tl) detector connected to Multi-Channel-Analyser (MCA). The spectrum is analyzed using the MAESTRO32 obtained from ORTEC. The schematic view of the experimental system has been shown in Figure 1.

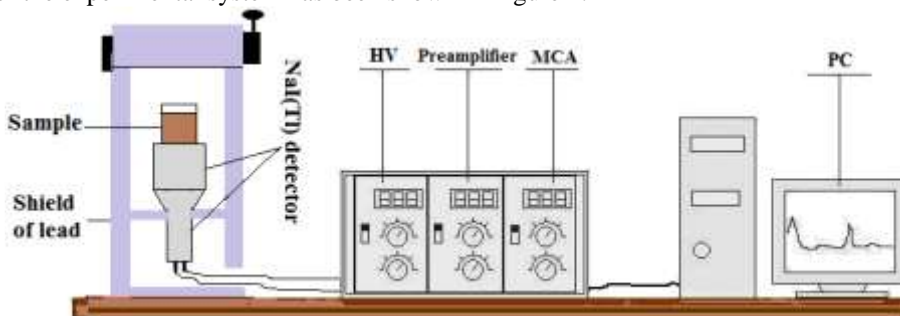


Figure 1. Schematic view of gamma Spectrometer and electronic units

The spectrum is analyzed using the MAESTRO32 obtained from ORTEC. The measurement was based on recording natural radioactivity quantities of three natural long-live elements: ^{226}Ra , ^{232}Th

and ^{40}K which are considered the photopeaks at 1760, 2610 and 1461 keV respectively, in the natural γ -ray spectrum [3,4].

The activities for the natural radionuclides were calculated using the following relation [3]

$$A(\text{Bq} / \text{kg}) = \frac{N}{\varepsilon \cdot \gamma \cdot t \cdot m} \quad (1)$$

where A is the activity of the radionuclide in Bq/kg, N is the net peak area under the most prominent photo peaks calculated by subtracting the respective count rate from the background spectrum obtained for the same counting time. The net count rate in the measurement is calculated from the background subtracted area of prominent gamma ray peaks. ε is the detector efficiency of the specific gamma ray, γ the absolute transition probability of gamma decay, t the counting time (s) and m the mass of the sample (kg).

REFERENCES

- [1]. Anagnostakis M. J; E.P. Hinis, S.E. Simopoulos, et al. Natural Radioactivity Mapping of Greek Surface Environment International, 1996, Vol. 22, Suppl. 1, S3- S8, Editor: J.P. McLaughlin, E.S. Simopoulos, F. Steinhäusler.
- [2]. Ravisankar, R., Chandrasekaran, A., Vijayagopal, P., et al. Natural radioactivity in soil samples of Yelagiri Hills, Tamil Nadu, India and the associated radiation hazards, Radiation Physics and Chemistry, 2012, 81, 1789-1795.
- [3]. Akkurt I. and Gunoglu, K., 2014. Natural Radioactivity Measurements and Radiation Dose Estimation in Some Sedimentary Rock Samples in Turkey. Science and Technology of Nuclear Installations Volume 2014, Article ID 950978
- [4]. Akkurt, I., Oruncak, B., Gunoglu, K., 2010. Natural radioactivity and dose rates in commercially used marble from Afyonkarahisar – Turkey. International Journal of the Physical Sciences Vol. 5 (2), p:170-173.
- [5]. UNSCEAR (2000) United Nations Scientific Committee on the Effects of Atomic Radiation. Report to the General Assembly, with scientific annexes, Sources and effects of ionizing radiation Annex B, New York. ,

A p3D Discrete Fracture-Matrix Simulation for Production Data Analysis in Vertically Fractured Well in Tight Gas Reservoirs

Chengwei ZHANG^{1,2}, Shiqing CHENG^{1,2*}, Wei ZHANG³, Lang ZHU^{1,2}, Tingting JIANG⁴,
Longquan HU³, Dengke SHI^{1,2}, Sha LU⁴

¹State Key Laboratory of Petroleum Resources and Engineering, China University of Petroleum, Beijing,
No.18 Fuxue Road, Changping District, Beijing, China

²China University of Petroleum, Beijing, No.18 Fuxue Road, Changping District, Beijing, China

³Research Institute of Exploration and Development of Changqing Oilfield Company, PetroChina, Xi'an 710018, China

⁴No.2 Gas Production Plant of Changqing Oilfield Company, PetroChina, Yulin 719000, China

*corresponding author@ chengsq973@163.com

Abstract

Unconventional gas reservoirs^[1,6] have played a most important part in use of unconventional resources, especially for tight gas. Therefore, the production performance analysis of fractured well in tight gas reservoir is important for us to study. However, until now, most of researchers only focused on 2D fracture model. To overcome this limitation, this work proposes a p3D fracture model to improve this situation. Considering that discrete fracture and matrix model is very useful for us^[5]. In this paper, a Discrete fracture–matrix method based on numerical simulation model (DFM-PDA). And it also provides an accurate code for the simulation of gas flow, including non-linear gas properties coupling in unconventional fractured gas reservoirs. Numerical examples and field cases are presented to test the validity and show the capabilities of the proposed approach.

Keywords-Discrete fracture matrix simulation; Production data analysis (PDA); Vertically fractured well; Tight sandstone gas reservoir; P3D fracture modeling

1 INTRODUCTION

The development of tight sandstone gas reservoirs synthesizes a number of advanced technological achievements in a variety of territories, especially hydraulic-fracturing. Until now, it is the only technology that can make the production from the low and ultralow-permeability unconventional plays possible^[1,2,6]. Because of the big value of thickness about real tight gas sandstone reservoirs, such as Shenmu gas field, the 2D fracture models cannot accurately simulate complex 3D fracture systems. Recently, some researchers have studied 3D fractured reservoirs by use of p3D DFM model. Lots of research effort has been devoted to developing numerical methods to accurately model fluid flow in fractures (p3D/3D)^[3-10]. In this paper, we develop a p3D DFM model to simulate the polygonal fractures about fractured well in tight sandstone gas reservoirs. Our simulator is verified by a good match of the simulation result with the actual field data in the case of simple vertical fracture.

2 EVALUATION OF SIMULATION RESULTS

2.1 Results

The proposed approach FVM-TPFA approach for the modeling of gas recovery from discrete fracture-matrix is validated against actual field data. In this study, we use the advanced generator DISTMESH to construct p3D grid^[7]. Based on 2D triangular grid, we extrude it into 3D layered grid. The case study for real gas fluids are investigated. To demonstrate the applicability of the proposed FVM-TPFA solution to production conditions typical of field operations, a field example is considered in this section. The data used in this case is a vertically fractured gas well in the Shenmu gas field of China. Fig. 10 gives the comparison of the interpretation results of well A1. As Fig. 1(a) and 1(b) show, the solution results of proposed FVM - TPFA approach are compared against the data from real gas field. Good agreement between results generated using the proposed method and that from data from WellA1. It is found in Fig.10 for all in which an excellent match is also observed among real field data and simulation data.

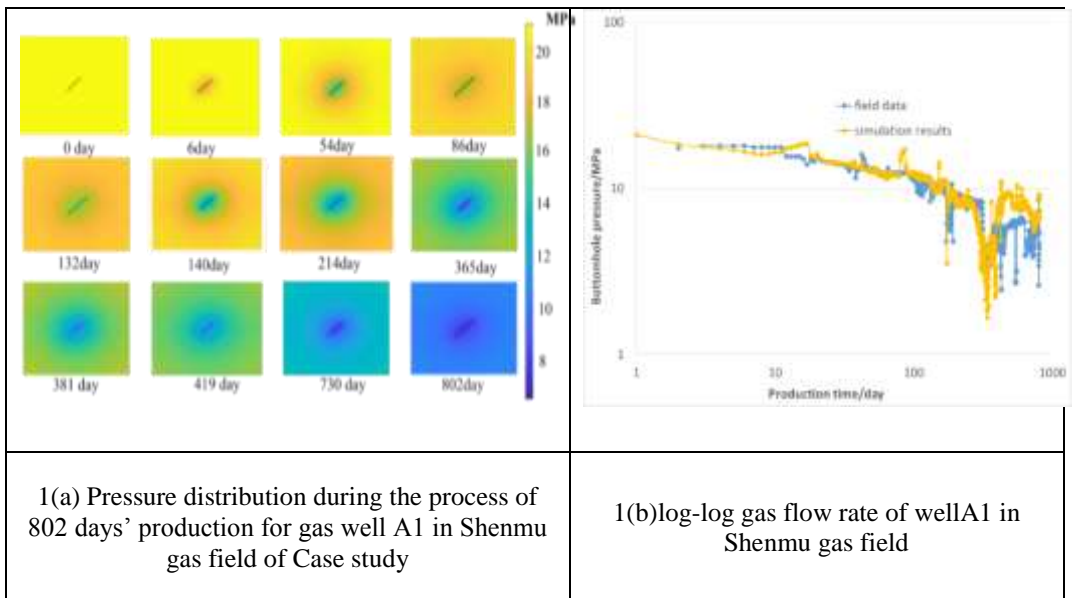


Figure. 1 Comparison of gas flow rate for Case between DFM-PDA, real field data of gas well A1 from Shenmu gas field

2.2 Sensitivity Study

Based on p3D fracture model, this sensitivity analysis concentrates on the effect of p3D parameters, including length of hydraulic fracture and aperture of hydraulic fracture on the Bottom-hole pressure's behavior. As shown in Figure. 2(a), the more HF's length increases, the farther pressure spreads. With HF's length increasing, the pressure's drop gradually. Therefore, the increase of hydraulic fracture's length can be beneficial to the improvement of reservoir's properties. As Figure. 2(b) shows, the more HF's aperture increases, the farther pressure spreads. Therefore, the increase of hydraulic fracture's length can be beneficial to the improvement of reservoir's properties.

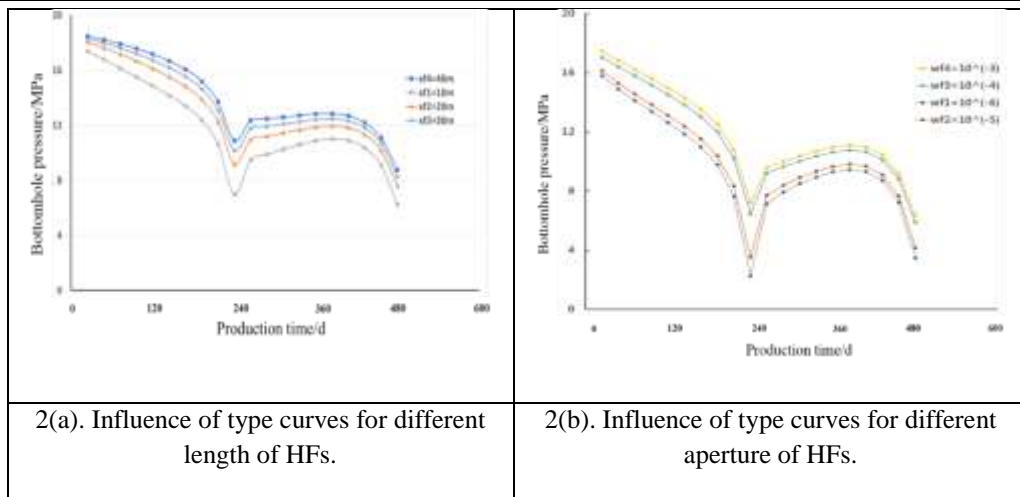


Figure.2 Influence of type curves for different parameters.

3 CONCLUSIONS

In this study, this work proposes a most useful method for simulating vertically fractured wells in tight gas reservoirs. Some conclusions can be drawn as follows:

- (1) The FVM-TPFA solution derived in this work is a generalized formulation applicable to natural gas reservoirs is very useful for us to analyze the production data on fractured well in tight gas sandstone reservoir.
- (2)The good agreement between predictions given by proposed solution and reported field data.
- (3) A general tight gas framework, DFM-PDA is developed and verified. This method can easily use and extend DFM-PDA to analyze practical giant tight gas problem with height and non-linear gas properties, like Shenmu gas field.

Acknowledgement

This work was supported by No.2 Gas Production Plant of PetroChina Changqing Oilfield Company, China (2016ZX05047-004 and 2016ZX05030).

REFERENCES

[1] Bai, J. , Liu, H. , Wang, J. , Xie, L. & Li, X. (2018). Dynamic and quantitative Sensitivity analysis on the efficient development of tight oil . International Journal of Computational and Experimental Science and Engineering , 4 (1) , 16-23 . DOI: 10.22399/ijcesen.368539

[2]Cao, N. , Li, H. & Liu, M. (2018). Effect of Stress Sensitivity on Production of Tight Heterogeneous Reservoir . International Journal of Computational and Experimental Science and Engineering , 4 (3) , 30-33 . DOI: 10.22399/ijcesen.444575

[3] Du X, Cheng L, Chen J. et al. Transient Pressure and Production Analysis of Fractured Horizontal Well with Elliptical SRV in Composite Shale Reservoir[C]. Presented at the 6th

International Conference on Computational and Experimental Science and Engineering held in Antalya, Turkey, 23-27 October 2019.

- [4]Hui, Mun-Hong, Kamath, Jairam, Narr, Wayne, Gong, Bin, and Robert Edward Fitzmorris. "Realistic modeling of fracture networks in a giant carbonate reservoir." Paper presented at the International Petroleum Technology Conference, Dubai, U.A.E., December 2007. doi: <https://doi.org/10.2523/IPTC-11386-MS>
- [5]Karimi-Fard, M., Durlofsky, L. J., and K. Aziz. "An Efficient Discrete-Fracture Model Applicable for General-Purpose Reservoir Simulators." *SPE J.* 9 (2004): 227–236. doi: <https://doi.org/10.2118/88812-PA>
- [6]Kent A. Bowker; Barnett Shale gas production, Fort Worth Basin: Issues and discussion. *AAPG Bulletin* 2007; 91 (4): 523–533.
- [6]Peaceman, D.W.. "Interpretation of Well-Block Pressures in Numerical Reservoir Simulation(includes associated paper 6988)." *SPE J.* 18 (1978): 183–194. doi: <https://doi.org/10.2118/6893-PA>
- [7]Persson P O, Strang G. A simple mesh generator in MATLAB[J]. *SIAM review*, 2004, 46(2): 329-345.
- [8]Xu Y. Implementation and application of the embedded discrete fracture model (EDFM) for reservoir simulation in fractured reservoirs[D]. , 2015.
- [9] Yang C, Cheng L, Li H, et al. Numerical Simulation of Water-Induced Fracture in Low Permeability Reservoirs[C]. 6th International Conference on Computational and Experimental Science and Engineering.
- [10]Zhang, S. , Liu, H. & Bai, J. (2019). Numerical simulation study on the bottom-water invasion in the carbonate gas reservoir with high angle fractures and high permeability zones . *International Journal of Computational and Experimental Science and Engineering* , 5 (2) , 80-85 . DOI: 10.22399/ijcesen.535713